Magneto-optic Effects in 2D Quantum Materials

Muzamil Shah

Laboratory for Quantum Technologies, Department of Physics, Syed Babar Ali School of Science and Engineering, Lahore University of Management Sciences

August, 2021

دو جہتی کوانٹم مادوں میں مقناطیسی نوریات کے مظاہر

مزمل شاہ

تجربہ گاہ برائے کوانٹم ٹیکنالوجیز، شعبۂ طبیعیات

سید بابر علی سکول برائے سائنس اور انجینئرنگ، لمز

اگست ۲۰، ۲۰۲۱


بسم الله الرحمن الرحيم

خلاصہ

اس مقالے کا بنیادی مقصد دو جہتی کوانٹم مادوں میں مقناطیسی نوریات کے مظاہر کی دریافت ہے۔ کسی مقناطیسی میدان میں مادہ اور روشنی کے تعامل کے نتیجے میں روشنی کے تقطیبی خواص کے مطالعے کو مقناطیسی نوریات میں شمار کیا جاتا ہے۔ اِن خصوصیات کا استعمال بصری مواصلاتی ٹیکنالوجی، مقناطیسی میدانوں کی پیمائش اور لیزر کے شعبوں میں ہوتا ہے۔ اس مقالے میں کچھ ایسے ہی مشاہدات پیش کیے گئے ہیں۔ ہم نے اس مقالے کو آسانی کی خاطر تین حصوں میں تقسیم کیا ہے۔

پہلے حصے میں ہم نے دو جہتی کوانٹم مادوں کے خواص کو سمجھنے کے لیے طبیعیات کے بنیادی تصورات کا جائزہ لیا ہے جن میں مقامیاتی بینڈ نظریہ، مقامیاتی متغیرات، وقتی استرداد کا توازن اور مقامیاتی حاجز کا تعارف شامل ہے۔ ہم نے گریفین اور سلیسین (بالترتیب کاربن اور سیلیکان کے دو جہتی بہروپ) کی برقیاتی خصوصیات کی ڈراک طبیعیات سے جانچ پڑتال کی اور ان سے منسلک توانائی کے انتشار کے کلیے بھی اخذ کیے جو جدید تحقیق میں بنیادی نوعیت کے حامل اور کوانٹم مادوں کے جامع اور تفصیلی جائزے کے لیے ناگزیر ہیں۔

دوسرے حصے میں ہم نے مقناطیسی نوریات کے نتیجے میں ہونے والی روشنی کی گردش کا مطالعہ کیا گیا جو بالترتیب روشنی کی انعکاس اور ترسیلی جیومیٹری سے منسلک ہیں۔ یہ گھومنے کا عمل دو طرح سے بیان کیا جاتا ہے۔ جب مادے پر روشنی گر کر واپس پلٹ جائے تو اس کو گردشِ کر، جبکہ یہی عمل اگر اس طرح واقع ہو کہ روشنی مادے میں سے آرپار گزر جائے، تو اس کو گردشِ فاراڈے کہتے ہیں۔ ان مظاہر کو نیم کلاسیکی اصولوں اور قواعد کے مطابق سیلیسین اور اس کے مماثل مادوں (جرمانین اور ٹنیین) میں پرکھا گیا ہے۔ ان مادوں کی نمایاں اور ممتاز خوبیوں میں سرفہرست خوبی، سپن مدارتی تعامل کا موجود ہونا ہے جو مادہ کے خواص میں

تبدیلی کے لیے ایک نئی جہت مہیا کرتی ہے۔ ہم نے دریافت کیا ہے کہ ۵ ٹیسلا کے مقناطیسی میدان میں حیران کن حد تک بڑی گردشِ کر دیکھی جاتی ہے۔ جبکہ اس طرح کے تجربات میں عمومی طور پر دوسرے مادوں میں گردش محض ۵ یا ۶ ڈگری تک ہوتی ہے۔ مزید یہ کہ مقناطیسی اور برقی محرکات کی موجودگی میں مقامیاتی حاجز میں ان رجحانات کا تجزیہ، معمولی اور غیر معمولی مقامیاتی صورتوں کے درمیان کوانٹم مرحلہ وار منتقلی کی راہ ہموار کرتا نظر آتا ہے۔ امید ہے کہ یہ کھوج طبیعیات کے معروف مضمون کوانٹم تھیوری کے گوناگوں کرشمات کو انسانی عقل و فہم کے مزید قریب لانے میں مدد دے گی۔

اس مقالے کا تیسرا اور آخری حصہ گوس ہانشین اور فوٹانک سپن ہال کے نتیجے میں وجود پذیر طولی اور زاویائی تبدیلیوں کے لیے مختص کیا گیا ہے۔ دو جہتی ٹوپولوجیکل مادے پر روشنی گرنے سے نت نئے بدلتے زاویوں کی تحقیق سے بائیو سینسرز کے ارتقا میں جدت لائی جا سکے گی اور مقناطیسی قوت ناپنے والے آلات کو بھی مزید بہتر بنایا جا سکے گا۔ طولی تبدیلی سے مراد روشنی کی مسلسل لہروں کا اپنے نقطہ ٹکراؤ کی بجائے طولی فاصلہ طے کر کے منعکس ہونا جبکہ زاویاتی تبدیلی روشنی کا اپنے سطح وقوع سے باہر نکل جانا ہے۔ ہم نے ان رجحانات کا مطالعہ دو جہتی کوانٹم مادوں میں برقی اور مقناطیسی محرکات کی موجودگی میں کیا ہے۔ خالص نظریاتی بنیاد پر وضع کیے گیے کلیوں کے تجزیے سے یہ بات سامنے لائی گئی ہے کہ ان رجحانات (مثبت یا صنفی) کی مقدار کوانٹم مادوں میں بڑھ جاتی ہے۔ مزید یہ کہ ان کی مقدار کو زاویہ انعطاف کے رد و بدل (بروسٹر زاویہ کے قرب میں) سے قابو کیا جا سکتا ہے۔

Abstract

Recent developments in quantum materials with emergent properties are opening alternative avenues for materials engineering on demand. In quantum materials, collective electrons demonstrate various macroscopic behavior, typically in the presence of external stimuli i.e., electromagnetic fields. The main theme of this thesis is to explore magneto-optic phenomena in two-dimensional quantum materials which show promise for optical communication technology, remote sensing of magnetic fields, and other laser applications.

The central body of this work explores magneto-optic effects and mechanical beam shifts in these 2D quantum materials. For the sake of clarity, we have divided the thesis into three parts. First, we focus on some basic concepts of condensed matter physics which are important for understanding this thesis. The theoretical pursuit involves topological band theory, topological invariants, the description of the classical and quantum Hall effects, time-reversal symmetry, and introduction to 2D and 3D topological insulators. We discuss the electronic properties of graphene and silicene by studying their low-energy Dirac physics using tight-binding approximations. We also derive the energy dispersion in the presence of a magnetic field. To drive topological quantum phase transition between trivial and non-trivial states, we utilize the electric and magnetic fields as a control knob. Furthermore, we focus on the transport properties providing the theoretical framework.

Second, we focus on the magneto-optic responses of 2D silicene and hybridized topological insulators. The behavior of these quantum materials under the influence of external fields, for example, electric and magnetic fields, is dictated in a highly non-trivial manner including the possibility of topological phase transitions. The presence of strong spin-orbit interaction in silicene and its analogues,

germanene and tinene, also leads to the opening of a gap in the energy spectrum and spin-splitting of the bands in each valley. We use a semiclassical treatment to describe the Faraday rotation (FR) and magneto-optic Kerr effect (MOKE) which can be modulated both electrically and magnetically. We derive analytical expressions for the valley and spin-polarized FR and MOKE for arbitrary polarization of incident light in the terahertz regime. All in all, very large FR and MOKE can be achieved.

We also discuss the magneto-optic response of topological insulator (TI) thin films exposed to quantizing, external magnetic fields. We theoretically investigate quantum phase transitions from topologically non-trivial to trivial states and vice versa in three-dimensional hybridized topological insulators ultra-thin films. The interplay between the hybridization of the top and bottom surface states (SSs) and Zeeman energy also gives rise to topological and normal insulating phases. Therefore, by tuning the Zeeman energy, we can drive the phase transition between these two phases. Furthermore, we impinge a Gaussian beam on the surface of the 3D TI to study FR MOKE in the presence of an external magnetic field, while explicitly taking into account the hybridization between the top and bottom Dirac SSs of the TI film.

The third part of the thesis is devoted to Goos-Hänchen and photonic spin Hall shifts for light beams impinging on the surface of 2D quantum material-substrate systems in the terahertz regime. We show that giant positive and negative quantized spatial and angular beam shifts can be obtained by tuning the angle of incidence in the vicinity of the Brewster angle. We demonstrate that the in-plane and transverse spatial spin-dependent shifts are quantized due to the Landau level (LL) quantization of the magneto-optic conductivities.

List of publications during Ph.D. thesis work

1. Muzamil Shah and Muhammad Sabieh Anwar, "Magneto-optical effects in the Landau level manifold of 2D lattices with spin-orbit interaction," Opt. Express 27, 23217-23233 (2019).

2. Muzamil Shah and Muhammad Sabieh Anwar, "Magneto-optic modulation of lateral and angular shifts in spin-orbit coupled members of the graphene family," OSA Continuum, 3, 878 (2020).

3. Muzamil Shah and Muhammad Sabieh Anwar, "Quantized and topological photonic spin Hall effects in the graphene family in the presence of magnetic fields," OSA Optical Sensors and Sensing Congress (2020).

4. Muzamil Shah, Ali Akbar, Muhammad Sajid and Muhammad Sabieh Anwar, " Transitional Faraday and Kerr effect in hybridized topological insulator thin films" Opt. Mat. Express 11, 525-538 (2021).

5. Muzamil Shah and Muhammad Sabieh Anwar, "Valley and spin polarized quantized spin dependent photonic shifts in topological silicene," Physics Letters A, 127342 (2021).

6. Muzamil Shah, Muhammad Sajid and Muhammad Sabieh Anwar, "Quantized Goos-Hänchen shifts on the surface of hybridized topological insulator thin films," Physica E: Low-dimensional Systems and Nanostructures, p. 114819 (2021).

7. Muzamil Shah, Mudasir Shah and Ali Akbar, "Magnetically tunable Goos-Hanchen shifts in topological quantum materials," CLEO OSA (2021).

8. Muzamil Shah, Muhammad Sajid and Mudasir Shah, "Magnetic field and Fermi energy modulated quantized Imbert-Fedorov shifts in Graphene," JOSA B 9, 2736-2741 (2021).

9. Muzamil Shah and Muhammad Sajid, "Surface state dependent giant quantized photonic spin Hall effect in a magnetic topological thin film " submitted to Physica E: Low-dimensional Systems and Nanostructures, (2021).

10. Muzamil Shah and Muhammad Sabieh Anwar, "dc and ac transport in two-dimensional ferrovalley materials,"in preparation (2021).

Acknowledgement

Alhamdulilah, Praise be to the Allah and all my respect for the Holy Prophet Muhammad (peace be upon him), the foundation of knowledge and guidance for all. First and foremost, I would like to thank my advisor, Dr. Muhammad Sabieh Anwar for his scholarly guidance, generous encouragement, thought provoking discussions and pleasant attitude. Without his insight and support, this thesis would not have been possible. He was always available for helping me in my research problem personally or by virtually. His commitment to my professional development and academic growth has not only given me the necessary skills to conduct physics research, but has also made this a very enjoyable journey.

I would also like to thank the members of my advisory committee: Dr. Adam Zaman Chaudhry and Dr. Ata Ulhaq. Their oversight, insight and feedback were valued. In particular, I would like to thank Dr. Ata Ulhaq for many discussions during my time as their research assistant and for the opportunity to work closely together. In addition, I would like to thank those who comprised my examination committee. I am also thankful to Dr. Muhammad Faryad for useful advices he gave me and the discussions we had out of his busy schedule. My special thanks go to my fellows, Asif Zaman, Azeem Iqbal, Warda and the whole Physlab team. I must acknowledge my friend Dr. Ali Akbar. He is the guy responsible for clarifying most of my questions and for correcting several of my mistakes.

Last but not the least, I wish to express my deep gratitude towards my loving parents Daji and BiBi to keep supporting and praying for the best of me until now. Finally, I would like to give a big thanks to my brothers and sisters for their support in my education. In particular, I owe a debt of gratitude to my wife for her patience, understanding and encouragement throughout the duration of my studies.

In the last, I would like to acknowledge financial support from the National Research program for Universities (NRPU), scheme number 10375 funded by the Higher Education Commission of Pakistan.

Dedicated to Daji and BiBi

Contents

1 Introduction **27**

1.0.1 A brief introduction to quantum materials 27
1.0.2 Band theory and topology 31
1.0.3 Berry's phase 34
1.0.4 Berry curvature 37
1.0.5 The classical Hall effect 39
1.0.6 Drude model 41
1.0.7 Landau levels 43
1.0.8 The Integer quantum Hall effect and chiral edge states . . . 46
1.0.9 Topological invariants and the quantum Hall effect 51
1.1 Topological insulators 52
1.1.1 Time-reversal symmetry and Kramers's theorem 52
1.1.2 Spin-orbit coupling 55
1.1.3 Quantum spin Hall effect 59
1.1.4 Topological insulators in two dimensions 59
1.1.5 From two to three dimensions 62
1.1.6 Three dimensional hybridized topological insulator 64
1.1.7 Concluding remarks 65

2 Electronic properties of 2D quantum materials **67**

2.1 Introduction 67
2.2 Electronic properties graphene 68

2.2.1 Momentum space description 72
2.2.2 Eigenfunctions of the graphene Hamiltonian 75
2.2.3 Magnetic field effects in graphene 76
2.2.4 The associated eigenfunctions of graphene in the presence of magnetic field 79
2.3 The electronic properties of staggered 2D semiconductor materials . 80
2.3.1 Impact of an electric field 87
2.3.2 Topological qunatum phase transition in 2D quantum materials 88
2.3.3 Two-component spinor wave functions of 2D quantum materials 92
2.3.4 Landau level quantization 93
2.3.5 Wave functions 98
2.4 3D hybridized topological insulator ultra-thin films in a magnetic Field 100
2.4.1 Wave functions 105

3 Quantized magneto-transport in 2D quantum materials 106
3.0.1 Introduction 106
3.1 Linear response theory 109
3.1.1 Kubo's prescription for linear response theory 110
3.1.2 Kubo formula for optical conductivity 112
3.1.3 Optical conductivity of the two-dimensional electron gas . . 115
3.2 Magneto-optical conductivity of the graphene family 118

4 Magneto-optic polarization re-orientation effects in 2D quantum materials 129
4.1 Faraday and Kerr rotation for the Landau level manifold of 2D lattices with spin-orbit interaction 130
4.1.1 Background and motivation 130

4.1.2 Fresnel coefficients . . . 133
4.1.3 Phenomenological description of the magneto-optic effects . 137
4.1.4 Results and discussion . . . 138
4.1.4.1 Electric field modulated Faraday rotation and ellipticity . . . 138
4.1.4.2 Magnetic field modulated Faraday and Kerr rotation 142
4.1.4.3 Effect of chemical potential . . . 144
4.1.5 Impact of angle of incidence . . . 146
4.1.6 Role of temperature and scattering . . . 146
4.1.7 Response in the semiclassical limit . . . 147
4.1.7.1 Probing topological quantum phase transitions via Faraday rotation . . . 149
4.1.7.2 Dependence on the silicene-substrate system . . . 150
4.2 Polarization manipulation with hybridized topological insulator thin films . . . 154
4.2.1 Background and motivation . . . 154
4.2.2 Geometry of the the magneto-optic effects and conductivities 156
4.2.3 Results and discussion . . . 157
4.2.3.1 Magnetic field effect on Faraday and Kerr rotations 157
4.2.3.2 Doping control of magneto-optic response . . . 163
4.2.3.3 Semiclassical approximation . . . 166

5 Mechanical beam shifts in 2D quantum materials 169
5.1 Magneto-optic modulation of lateral and angular shifts in spin-orbit coupled members of the graphene family . . . 170
5.1.1 Background and motivation . . . 170
5.1.2 Model and theory . . . 173
5.1.3 Results and discussion . . . 176
5.1.3.1 Magnetic field modulated Goos-Hanchen . . . 176
5.1.3.2 Tuning the electric field . . . 183

5.1.3.3 Effect of chemical potential variation 186
5.1.3.4 Semiclassical approximation, again! 188
5.1.3.5 Valley and spin polarized beam shifts 188
5.1.3.6 Dependence on the incident photonic energy 190
5.2 Quantized Goos-Hänchen shifts on the surface of hybridized topological insulator thin films 191
5.2.1 Background and motivation 191
5.2.2 Goos-Hänchen shifts 192
5.2.3 Results and Discussion 193
5.2.3.1 Effect of magnetic field on angular and spatial GH shifts 193
5.2.3.2 Impact of Zeeman potential on angular and spatial beam shifts 198
5.2.3.3 Chemical potential modulated angular and spatial beam shifts 199

6 The photonic spin Hall effect in topological silicene 204
6.1 Background and motivation 204
6.2 General theoretical model 206
6.3 Results and Discussion 208
6.3.1 Effect of magnetic field 208
6.3.2 Electric field modulated photonic spin Hall effect 213

7 Summary and outlook 216
7.1 Summary 216
7.2 Future Directions 220

List of Figures

1.1 The hexagonal cobweb for the quantum materials' family. 28
1.2 The classification of various type of 2D quantum materials based on their structures and topology. Here TMD=Transition metal dichalcogenide, BP=Black phosphorus and H-BN=Boron nitride. . 29
1.3 The band structures of metals, semiconductors and insulators, respectively. Each blue dot represents two electrons with opposite spins. 31
1.4 Topologically different objects (a sphere and donut) can be classified according to their genus (g). 32
1.5 (a) Smooth deformation, (b) not a smooth deformation. 34
1.6 Classical Hall effect. Electrons move to the left in the conductor. The magnetic field is directly out of the page, represented by black circles. 39
1.7 Representation of 2DEG electrons in a magnetic field moving in circular orbits with skipping trajectories. The diagram gives a classical picture. 42
1.8 (a) The quantum Hall state and equidistant Landau levels separated by $\hbar\omega_c$. 45

1.9 (a) Illustration of longitudinal and transverse resistivities as functions of the magnetic field. (a) Classical Hall effect behavior and (b) the IQHE. The red color. shows the ρ_{xx} while the green line denotes the Hall resistivity ρ_{xy}, which exhibits plateaus quantized in exact multiples of h/e^2. 46
1.10 (a) The formation of a chiral extended edge state. (b) Representation of the Landau levels. 50
1.11 Representation of helical edge states in a two-dimensional topological insulator. 60
1.12 Representation of helical edge states in quantum spin Hall system. . 62
1.13 (a) The conduction and valence bands of a 3D solid. The shaded regions represent the bands in the bulk while the black lines are the bands at the surface of the 3D solid. The conduction (valence) band is symmetric (antisymmetric). (b) The degeneracy of the electron spins is lifted due to the SOC. The conduction band becomes antisymmetric and the valence band becomes symmetric (+). The red and blue lines are the edge states at the boundary of the bands. Here backscattering is not possible. (c) Further increasing the SOC leads to more changes and the electrons at the edges can be backscattered. The purpose of the Möbius strips indicates the number of topological twists in the band structure. 63
1.14 Schematic of a 3D TI with the top (Red) and bottom (Blue) surface states Dirac systems and of its quasi-2D counterpart (right). 65

2.1 The basis vectors in the hexagonal lattice of graphene with primitive vectors a_1 and a_2 ($a = 1.42$ A) and the position vectors δ_1, δ_2 and δ_3 are position vectors. On the right, we also show the three sp^2 orbitals forming σ bonds and a p_z orbital forming a π bond across neighbours. 69

2.2 Linear dispersion relation of graphene.: (a) Band structure of monolayer graphene. (b) Contour plot of band structure in (a). 72
2.3 The first Brillouin zone of graphene. The cones indicate the K and K' valleys. 74
2.4 Landau levels evolution of graphene as a function of magnetic field B for $|n| \leq 5$, (a) for the K valley and (b) K' valley. 78
2.5 (a) The un-buckled structure of the staggered 2D semiconductor monolayer. (b) Illustration of the buckled honeycomb lattice of of the staggered 2D semiconductors which is distorted due to large ionic radius of a silicon atom and generates a staggered sublattice potential E_z. 81
2.6 SOC in the staggered 2D materials. (a) The nearest-neighbor force F_1 vanishes, while the next-nearest-neighbor force $\vec{F}_{\parallel}$ is non-zero in the horizontal plane. (b) The next-nearest-neighbor non-zero force $F_{\perp}^{A}$ equals negative $F_{\perp}^{B}$ in the perpendicular direction. The dark and light atoms correspond to atoms in the two staggered planes respectively. 83
2.7 The staggered 2D semiconductor honeycomb lattice. (a) The six next-nearest neighbor atoms of sublattice A at site i $(i = 1, ..., 6)$ are shown with number. The $R_j^{'}$ is the vector connecting the sublattice A at site i with its six next-nearest neighbors. (b) Next-nearest-neighbour hopping on the honeycomb lattice with $v_{ij} = \pm$. . 85
2.8 The electronic energy dispersion of the staggered 2D monolayer for the K valley corresponding to three different topological regimes: (a) TI ($\Delta_z = 0$), (b) TI ($\Delta_z = 0.5\Delta_{so}$), (c) VSPM ($\Delta_z = \Delta_{so}$) and (d) BI ($\Delta_z = 2\Delta_{so}$) respectively. The solid blue (dashed red) curves are for spin up (down). 91

2.9 The staggered 2D semiconductor Landau level energies as a function of the external magnetic field B for three distinct topological regimes, TI, VSPM and BI for both spin up and down ($\sigma_z = \pm 1$). (a) For $\Delta_z = 0$ the energy spectrum is gapped due to SOC energy, and we have a TI phase. (b) For $\Delta_z \neq 0$ but $\Delta_z < \Delta_{so}$, the degeneracy is lefted but the spctrum is still gapped and we have a TI phase. (c) When $\Delta_z = \Delta_{so}$, the energy spectrum becomes gappless giving rise to a the valley-spin polarized metal (VSPM) regime. (d) For $\Delta_z > \Delta_{so}$, the energy gap re-opens giving rise to a phase transition from VSPM to a BI phase. 97

2.10 Landau level energies as a function of the external magnetic field B for three distinct topological regimes, TI, CNP and NI for top and bottom SSs ($\tau_z = \pm 1$). (a) For $\Delta_z = 0$ the energy spectrum is gapped due to Hybridization energy, and we have a TI phase. (b) For $\Delta_z \neq 0$ but $\Delta_z < \Delta_H$, the degeneracy is lefted but the spctrum is still gapped and we have a TI phase. (c) When $\Delta_z = \Delta_H$, the energy spectrum becomes gappless giving rise to a Dirac point called charge Neutrality point (CNP). (d) For $\Delta_z > \Delta_H$, the energy gap re-opens giving rise to a phase transition from CNP to a NI phase. 103

3.1 Schematic representation of the graphene family conductivity in terms of inter-band and intra-band transitions between energy bands. 107

3.2 Feynman bubble for conductivity. 109

3.3 Schematic representation of the allowed transitions between LLs for two different chemical potentials in the K valley. (a) $\mu_F = 0$ and (b) $\mu_F \neq 0$. 119

3.4 Schematic representation of the allowed transitions between LLs for three different magnetic fields in the K valley for magnetic field (a) 1 T (b) 3 T (c) 5 T. Blue lines represent Landau levels for spin up ($\sigma =\uparrow$) and red lines represent Landau level for spin down ($\sigma =\downarrow$). The same color scheme applies for the Landau levels transitions. . . 125

3.5 Longitudinal and transverse Hall conductivities as a function of photonic energy for different magnetic fields in the TI regime. (a) Longitudinal conductivities in the K and K' valleys, respectively. (b) and (c) Hall conductivities in the K valley and K' valleys, respectively. Longitudinal and transverse Hall conductivities as a function of photonic energy for magnetic field of 1 T in different topological regimes. (d) Longitudinal conductivities in the K and K' valleys, respectively. (e) and (f) Hall conductivities in the K valley and K' valleys, respectively. The parameters used are Δ_z=8 meV, $\Delta_z = 0.5\Delta_{so}$ and chemical potential $\mu_F = 0$. 126

4.1 Overview of magneto-optic effects in 2D quantum material. 132

4.2 Schematic view of a monochromatic plane wave impinging on the surface of staggered 2D quantum material. 134

4.3 Schematic view of magneto-optic Kerr and Faraday effects on the surface of staggered 2D quantum material. 138

4.4 Faraday, Kerr rotation and ellipticity of silicene-substrate system as a function of photon energy electric and magnetic fields. (a) The s polarized Faraday rotation and (b) ellipticity as a function of incident photon energy in the K valley with modulation of the external electric field for the three distinct topological regimes, TI, VSPM, and BI for a magnetic field of 1 T. The spectral peaks are labeled 1 through 6 and their origin is identified in the main text. The spectrum are vertically shifted by 15° among themselves for clearer viewing. Furthermore, in this figure we use $\Delta_z = \Delta_{so}/2$ (TI) and $\Delta_z = 2\Delta_{so}$ (BI). (c) The s polarized Kerr rotation as a function of incident photon energy in the K' valley with modulation of the external magnetic field for the TI regime for three different values of B =1, 3 and 5 T. (d) The maximum Faraday, Kerr rotation and ellipticity as a function of the magnetic field in the K valley for the single transition $\Delta_{-10,K,\uparrow}$. The parameters used are Δ_z=8 meV, $\theta_1 = 30°$, $\Gamma = 0.01\Delta_{so}$, refractive index $n_2 = 1.84$ and chemical potential $\mu_F = 0$. 139

4.5 (a) Schematic representation of the allowed transitions between LL's for three different values of chemical potential μ_F =0, 10 and 22 meV; (b) and (c) the s polarized Kerr rotation as function of incident photon frequency in K and K' valleys with modulation of the chemical potential in the TI regime for a magnetic field of 1 T, respectively. (d) The s polarized Faraday rotation as function of incident photon energy in K valley for different incident angles for a single transition in the TI regime. (e) The s polarized Faraday rotation as function of incident photon energy in K for different temperatures for a single transition in the TI regime. (f) The s and p polarized Kerr rotation as function of incident photon frequency in the semiclassical limit for n-type and p-type silicene ($\mu_F = 56$ and -56 meV), respectively. The solid line represents the s polarized and the dashed line p polarized. The parameters used are Δ_z=8 meV, $\theta = 30°$, $\Gamma = 0.01\Delta_{so}$ and refractive index $n_2 = 1.84$. 143

4.6 (a) Schematic representation of the allowed transitions between LL's for chemical potential $\mu = 0.2$. (b) and (c) the s polarized Faraday rotation contour plots as function of x in K valley for $\mu = 0$ and 1.25, repectively, where $x = \Delta_z/\Delta_{so}$ and $\mu = \mu_F/\Delta_{so}$. The parameters used are $\theta = 30°$, $\Gamma = 0.01\Delta_{so}$ and refractive index $n_2 = 1.84$. 148

4.7 Faraday and Kerr rotation of silicene-substrate system as a function of photon energy for three different relative permittivities. (a) The s polarized and (b) p polarized Faraday rotation as a function of incident photon energy in the K valley with modulation of relative permittivities in the TI regime for a magnetic field of 1 T. (c) The s polarized and (d) p polarized Kerr rotation as a function of incident photon energy in the K valley with modulation of relative permittivities in the TI regime for a magnetic field of 1 T, for the two transitions. The parameters used are $\theta_1 = 30°$, $\Gamma = 0.01\Delta_{so}$ and chemical potential $\mu_F = 0$. 151

4.8 Faraday and Kerr rotation of silicene-substrate system as a function of photon energy for three different relative permeabilitis. (a) The s polarized and (b) p polarized Faraday rotation as a function of incident photon energy in the K valley with modulation of relative permeabilitis in the TI regime for a magnetic field of 1 T. (c) The s polarized and (d) p polarized Kerr rotation as a function of incident photon energy in the K valley with modulation of relative permeabilities in the TI regime for a magnetic field of 1 T, for the two transitions. 152

4.9 Faraday and Kerr ellipticities as a function of incident photon energy for three different relative permittivities. (a) The s polarized and (b) p polarized Faraday ellipticities as function of incident photon energy in the K valley with modulation of relative permittivities in the TI regime for a magnetic field of 1 T. (c) The s polarized and (d) p polarized Kerr ellipticities as a function of incident photon energy in the K valley with relative permittivities in the TI regime for a magnetic field of 1 T, for the two transitions. The parameters used are $\theta_1 = 30°$, $\Gamma = 0.01\Delta_{so}$ and chemical potential $\mu_F = 0$. . . . 153

4.10 (a) and (b) Longitudinal and transverse Hall conductivities as a function of photonic energy for different magnetic fields in the QSHI regime for top and bottom SSs, respectively. (c)-(f) Modulus of the s and p polarized magneto-transmission and reflection coefficients for TI thin film-substrate system as a function of the incident photonic energy for different magnetic fields in the QSHI regime for top and bottom SSs, respectively. The parameters used for this simulation are Δ_H=4 meV, $\Delta_z = 0.5\Delta_H$, $\theta_\psi = 30°$, $\eta = 0.15\Delta_H$, refractive index $n_2 = 1.84$, and chemical potential $\mu_F = 0$. 160

4.11 Kerr and Faraday rotation of TI thin film-substrate system as function of photonic energy for different values of magnetic field. (a) The p polarized and (b) s polarized Kerr rotation for magnetic field strength of 1, 3 and 5 T, in the QSHI regime. (c) The s polarized Faraday rotation for magnetic field strength of 1, 3 and 5 T, in the QSHI regime. (d) and (e) The s and p polarized Kerr rotation with modulation of the external Zeeman field interaction, for the QSHI ($\Delta_z = 0.5\Delta_H$), CNP ($\Delta_z = \Delta_H$) and BI ($\Delta_z = 2\Delta_H$) at a magnetic field of 1 T. (f) The s polarized Faraday rotation as function of the incident photonic energy with modulation of the external Zeeman field interaction, for the QSHI, CNP and BI at a magnetic field of 1 T. The parameters used for this simulation are Δ_H=4 meV, $\theta_\psi = 30°$, $\eta = 0.15\Delta_H$, refractive index $n_2 = 1.84$ and chemical potential $\mu_F = 0$. 162

4.12 (a) and (b) Optically allowed inter-band and intra-band LL transitions satisfying the selection rule $\Delta n = \pm 1$ for top and bottom SSs in the QSHI regime. (c) and (d) Real parts of the optical conductivities for p-type and n-type TIs thin film-substrate system as a function of the incident photonic energy in the QSHI regime. (e) and (f) the p polarized Kerr rotation in the QSHI regime with n-type and p-type doping for a magnetic field of 1 T, respectively. (e) and (f) the p polarized Kerr rotation in the QSHI regime with n-type and p-type doping for a magnetic field of 1 T, respectively . 164

4.13 (a) The real part of the longitudinal and (b) transvers Hall conductivity as a function of incident photonic energy in the semiclassical limit for two transitions for n-type doping. (c) the p polarized Kerr rotation and (d) the s polarized Faraday rotation as a function of incident photonic energy in the semiclassical limit. 167

5.1 Schematic representation of the Poynting vector direction in different parts of a beam ABCD. 171

5.2 Schematic representation of the beam reflection at a 2D staggered material-substrate interface in the presence of external electric and magnetic fields are shown for partial reflection (PR) and total internal reflection (TIR) conditions. The spatial and angular GH shifts for (a) PR and (b) TIR. The incident, classically predicted and reflected beams are denoted by a, b and c respectively. 174

5.3 Schematic representation of the allowed transitions between LL's for three different magnetic fields in the K valley at (a) 1 T (b) 3 T (c) 5 T. Blue lines represent Landau levels for spin up ($\sigma =\uparrow$) and red lines represent Landau level for spin down ($\sigma =\downarrow$). The same color scheme applies for the Landau levels transitions. (d) Longitudinal conductivity as a function of photon frequency. The parameters used are Δ_{so}=8meV, $\Delta_z = 0.5\Delta_{so}$ and chemical potential $\mu_F = 0$. . 178

5.4 Modulus and phase of the s and p polarized reflection coefficients for 2D staggered graphene-substrate system as a function of incident angle for different magnetic fields in K valley for PR: (a) R_{ss}, (b)R_{pp}, (c) ϕ_{pp} and (d) ϕ_{ss}. The parameters used are Δ_{so}=8meV, $\Gamma = 0.2\Delta_{so}$, refractive index $n_2 = 1.84$ and chemical potential $\mu_F = 0.179$

5.5 The p polarized spatial and angular GH shifts for charge neutral staggered graphene-substrate system as a function of incident angle for different magnetic fields in the K valley in the TI regime for PR and TIR. (a) The p polarized spatial GH shifts for PR, (b) the p polarized angular GH shifts for PR, (c) the p polarized spatial GH shifts for TIR and (d) the p polarized angular GH shifts for TIR. The dashed lines represents the values of θ_B and θ_C for the native dielectric substrate. The parameters used are identical across all figures, unless stated otherwise. 181

5.6 (a) Longitudinal conductivity as a function of incident photon frequency and the p polarized spatial and angular GH shifts for the staggered graphene-substrate system as a function of incident angle for magnetic field $B = 1$ T in the K valley in three distinct topological regimes and four different chemical potentials. The incidence is external PR, while (b) and (c) show the p polarized spatial and angular GH shifts with modulation of the external electric field, for the TI, VSPM, and the BI at a magnetic field of 1 T. (d) Schematic representation of the allowed transitions between LL's for three different values of chemical potential μ_F=0, 10 and 22 meV, and (e) and (f) are the p polarized spatial and angular GH shifts with modulation of the chemical potential in the TI and classical regimes for a magnetic field of 1 T. 184

5.7 The valley and spin-polarized spatial and angular GH shifts for staggered 2D material-substrate system as a function of incident angle for K and K' valleys in the TI regime. (a) The spatial GH shifts for both spins and for both valleys, (b) the p polarized angular GH shifts for both spins and valleys. The spatial and angular GH shifts for staggered 2D material-substrate system as a function of photon energy in the K valley for different magnetic and electric fields. (c) the p polarized spatial and angular GH shifts for three different magnetic fields in the TI regime, (d) the spatial and angular GH shifts for $B = 1$ T in three distinct topological regimes. The p polarized response is shown only. 189

5.8 Schematic illustration of the GH shifts of a light beam reflected from a TI-substrate interface. 192

5.9 Real part of the (a) longitudinal and (b) transverse Hall conductivities as a function of the photonic energy for different strengths of the applied magnetic field in the TI regime for top and bottom SSs. Variations of the modulus of (c) the TE and (d) TM polarized normalized magneto-reflection coefficients for the TI thin film-substrate system with the incident photonic energy for different strengths of the magnetic field in the TI regime for top and bottom SSs. Variation of (e) the $\phi_{TM,TM}$ and (f) $\phi_{TE,TE}$ with the incident angle. Parameters used for TI SSs are Δ_H= 4 meV, $\Gamma = 0.15\Delta_z$, refractive index $n_2 = 1.84$, and chemical potential $\mu_F = 0$. 195

5.10 Magnetic field modulated TM polarized spatial and angular GH shifts on the surface of the TI thin film substrate-system versus photonic energy ($\hbar\omega$) and θ_ψ for two different values of B for top and bottom SSs. (a) The TM polarized spatial GH shifts and (b) the TM polarized angular GH shifts for $B = 1$ T. (c) The TM polarized spatial GH shifts and (d) the TM polarized angular GH shifts when $B = 3$ T. 196

5.11 TM polarized spatial and angular lateral shifts on the surface of the TI thin film substrate-system as a function of the incident photonic energy and incident angle for two different topological regimes for top and bottom SSs. (a) The TM polarized spatial GH shifts and (b) the TM polarized angular GH shifts for $B = 2.3$ T in the CNP phase. (c) The TM polarized spatial GH shifts and (d) the TM polarized angular GH shifts for $B = 2.3$ T in the BI state. 199

5.12 (a) and (b). MO allowed inter-band and intra-band LL transitions for top and bottom SSs in the TI regime and for $B = 1$ T. (c) and (d). Real parts of the MO conductivities for n-type and p-type TIs thin film-substrate system as a function of the incident photonic energy in the TI regime. (e) and (f). The TM polarized spatial and angular GH shifts with modulation of the chemical potential in the TI regime for $B = 1$ T. 200

5.13 Chemical potential modulated TM polarized spatial and angular GH shifts on the surface of TI thin film substrate-system as a function of photonic energy and incident angle for two different chemical potential for both top and bottom SSs in the TI regime. (a) The TM polarized spatial and (b) angular GH shifts for n-type doping. (c) The TM polarized spatial and (d) angular GH shifts for p-type and magnetic of $B = 1$ T. 202

6.1 Schematic of the LHCP and RHCP spatial in-pane and transverse photonic spin Hall effect. 207
6.2 Schematic representation of the allowed transitions between LLs for (a) three different magnetic fields 1, 2 and 3 T for the QSHI regime in the K valley and (b) for three distinct topological regimes in the K valley for $B = 1$ T. 210
6.3 (a) Magnetic field modulated longitudinal conductivity as a function of the incident photon energy for different magnetic fields in the K valley for the QSHI regime. (b) Electric field modulated longitudinal conductivity as a function of the incident photon energy for three distinct topological regimes in the K valley for $B = 1$ T. (c) and (d) magnetic field modulated in-plane and transverse spatial shifts. (e) and (f) electric field modulated in-plane and transverse spatial shifts in distinct topological regimes. The parameters used are Δ_{so}=8 meV, $\Delta_z = 0.5\Delta_{so}$, $\theta_\psi = 61.9^\circ$ and chemical potential $\mu_F = 0$. 212
6.4 Magnetic field modulated LHCP (a) in-plane and (b) transverse PSHE as a function of the incident photon energy and the incident angle for both spins in the K valley. The applied magnetic field is 1 T. 213
6.5 Electric field modulated (a) LHCP in-plane and (b) RHCP transverse PSHE in the VSPM state as a function of the incident photon energy and the incident angle for both spins in the K valley. Electric field modulated LHCP (c) in-plane and (d) transverse PSHE in the BI phase. The applied magnetic field is 1 T. 214

List of Abbreviations

GH	Goos-Hänchen
PSHE	Photonic spin Hall effect
SC	Superconductor
2D	Two dimensional
TMDC	Transition metal dichalcogenide
IQHE	Integer quantum Hall effect
BS	Band structure
2DEG	Two dimensional electron gas
LL	Landau level
TKNN	Thouless, Kohmoto, Nightingale, and den Nijs
TIs	Topological insulators
TR	Time reversal
SOC	Spin-orbit coupling
BIs	Bulk insulators
QAHE	Quantum anomalous Hall effect
QSHI	Quantum spin Hall insulator
TRS	Time-reversal symmetry

SSs	Surface states
3D	Three-dimensional
BZ	Brillouin zone
TQPTs	Topological quantum phase transitions
BC	Berry curvature
CN	Chern number
VSPM	Valley spin metal polarized
CNP	Charge neutrality point
EM	Electromagnetic
MO	Magneto-optic
THz	Terahertz
MOKE	Magneto-optic Kerr effect
FR	Faraday rotation
TIR	Total internally reflected
PR	Partial reflected
TE	Transverse-electric
TM	Transverse-magnetic
LHCP	Left-handed circularly polarized
RHCP	Right-handed circularly polarized
TBG	Twisted bilayer graphene

Organization of thesis

The current thesis is organized as follows. In Chapter 1, we present some basic concepts which are important for understanding this thesis. We briefly introduce the quantum materials that we study, which are graphene, silicene, two-dimensional transition metal dichalcogenides, topological insulators, etc. We also present the basic band theory and topology. We furtherly enhance the discussion by connecting the topology and the integer quantum Hall effect via the Berry curvature and the Chern number. We also explore several novel phenomena e.g., time reversal symmetry and spin-orbit coupling for the two and three-dimensional topological insulators.

In Chapter 2, we discuss the lattice structure and derive the low energy Hamiltonian using a tight-binding approximation for quantum materials, in particular the energy spectrum of the graphene and silicene in the presence of electric and magnetic fields. In Chapter 3, we develop the description of magneto-optical conductivities for the 2D quantum systems admitting the Hamiltonian already derived in Chapter 2. Particularly, we explore spin and valley-polarized longitudinal and Hall conductivities with particular attention to the topological quantum phase transitions which can be tuned by an external electric field.

Subsequently in the following chapters, the magneto-optical conductivities are utilized for the investigation of the spin and valley-polarized magneto-optic responses in 2D quantum materials. In Chapter 4, we describe the physics underlying the spin and valley-polarized magneto-optic rotation and ellipticity in the silicene and 3D hybridized topological insulators. In Chapter 5, we investigate the Goos-Hänchen (GH) phenomenon in the staggered 2D quantum materials and hybridized topological insulators in the presence of perpendicular electric and magnetic fields. Finally, Chapter 6 is devoted to an analysis of the photonic spin Hall effect (PSHE) in these fascinating and versatile low dimensional quantum systems.

Chapter 1

Introduction

1.0.1 A brief introduction to quantum materials

With rapid advancement in contemporary technologies over the last decades, traditional systems such as nanostructures, thin films have been exhausted in terms of their maximum tunability, the potential for miniaturization, and device manufacturing. This in turns influenced and shifted the focus of the physics and materials science communities to search for materials with exotic yet flexible properties at unprecedented dimensions and time scales, leading to the burgeoning fields in condensed matter physics *e.g.*, valleytronics, spintronics, magnonics, and optoelectronics to name a few. Quantum materials offer a similar prospect for the future technology with broad functionalities. Owing to the quantum mechanical interactions at play at sub-atomic levels, it would not be wrong to say that all materials are quantum in nature, yet it is believed that there are certain conditions that must be met for a material to be qualified as a '*quantum*' material.

According to Ref. [1], a material is deemed quantum when the wavefunctions of electrons are wrapped up like a complicated knot. Furthermore, novel emergent phenomena are often seen due to the interaction of electronic states. The term emergent is used to evoke cooperative behavior of a large number of microscopic constituents, like charges and atoms resulting in phenomena that are qualitatively different than the behaviors of the individual constituents. In other words, a sys-

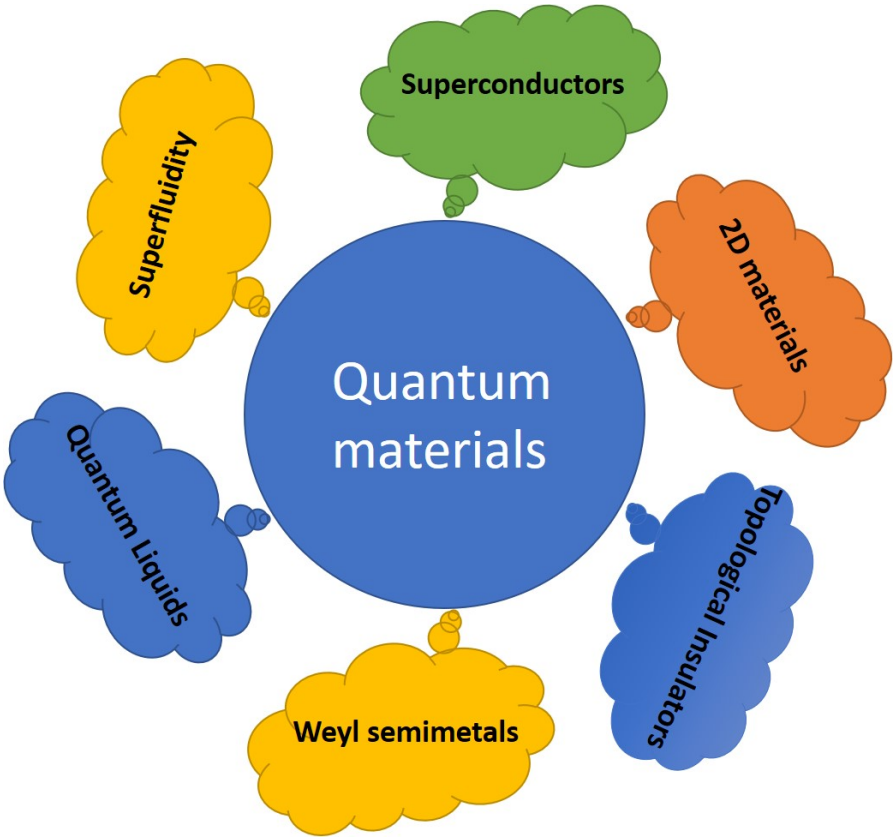

Figure 1.1: The hexagonal cobweb for the quantum materials' family.

tem with strongly correlated electrons, the rich variety of topologically ordered states, the existence of Dirac fermions or interactions between electrons, spins, magnons, polariton, phonons, etc. are also considered to be defining characteristics for a material to be quantum.

These interactions between excitations lead to the emergence of new properties. Quantum materials give rise to exotic and often remarkable properties like relativistic spin-orbit interaction, electron-electron interactions [2], quantum confinement [3, 4], quantum fluctuations [5], quantum entanglement [6], quantum coherence [7] and the topology of wavefunctions [8]. Examples of these unusual quantum properties include high-temperature superconductors (SCs) [9, 10], triplet super-

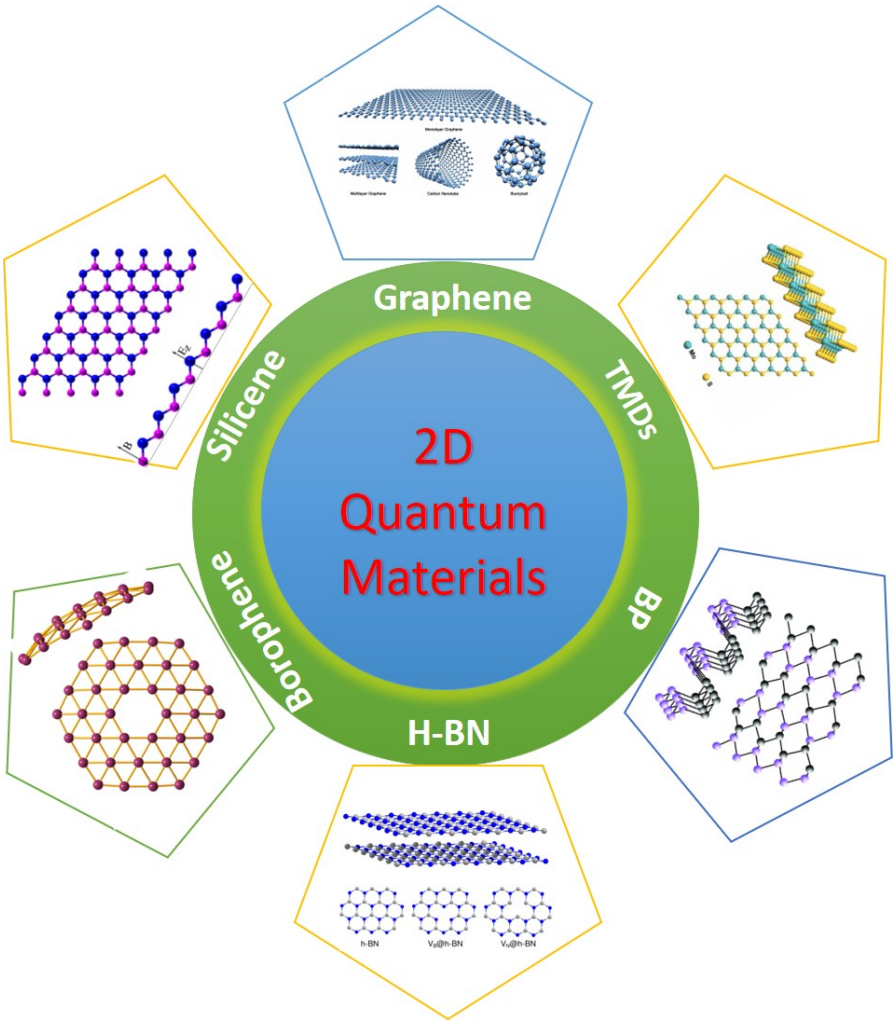

Figure 1.2: The classification of various type of 2D quantum materials based on their structures and topology. Here TMD=Transition metal dichalcogenide, BP=Black phosphorus and H-BN=Boron nitride.

conductivity [11, 12], integer and fractional quantum Hall effects [13, 14], the quantum spin Hall effect in 2D materials [15, 16], quantized quantum anomalous Hall effects [17] in quantum topological insulators [17, 18], quantum spin liquids [19], superfluid transport and spin superfluidity [20], to name just a few. Examples of some quantum materials are outlined in Fig 1.1.

Over the past decades, two-dimensional (2D) quantum materials have attracted much attention, both experimentally and theoretically. This paradigm shift began with the discovery of the integer quantum Hall effect and the physical realization of quantum semiconductor devices and structures (quantum wells, quantum wires, quantum dots, and superlattices) in 1980 [13, 14]. These wonder materials display the exclusive hallmarks of topological order, including dissipation-less quantum transport and the observation of the fractional quantum Hall effect [21]. These 2D materials include a wide range of new quantum materials, originally discovered in condensed matter physics systems, for example, graphene, staggered 2D semiconductors (i.e. silicene, germanene, stanene) [22, 23, 24, 25], 2D transition metal dichalcogenides (TMDCs) [26, 27], topological insulators and topological semimetals [21, 28], Dirac-Weyl semimetals [29, 30], and their artificial analogs [31, 32]. Probably one of the most celebrated quantum materials is graphene, also called a "wonder material" [33, 34]. While graphene has already been identified as a potential superstar by the electronics industry due to its distinguished electrical and optical properties, the discovery has also sparked a growing scientific interest to search for Dirac physics in materials other than graphene, which also demonstrate versatile performances and potential applications in electronic [35], spintronic [36], valleytronic [37], spinoptronic [38], optoelectronic [38], and plasmonic [39] devices. Some representative 2D quantum materials are enlisted in Fig. 1.2.

It is pertinent here to review some basic concepts in condensed matter physics which are recurrent throughout this thesis and will provide the necessary theoretical background to the reader. We set up the discussion with a brief review of quantum materials based on topology and the band theory of solids. The discussion is furthered by developing a connection between the topology and the integer quantum Hall effect (IQHE) through the Berry curvature and the Chern number. Finally, we will explore topological insulators in two and three dimensions. Topological insulators are aptly described in the books [40, 41].

1.0.2 Band theory and topology

The electronic band structure of a solid describes the range of energy levels that can be occupied by an electron of a given momentum k. The gap between energy levels is a region where no electronic states can exist. Materials can be classified into different classes based on their band gaps. Three main categories: metals, semiconductors, and insulators are shown in Fig. 1.3. Systems that display an energy gap in the electronic band structure (BS) between the highest level (filled) in the valence band and the lowest energy band (empty) in the conduction band are typically classified as insulators (often called band insulators) or semiconductors depending on the size of their bandgap. Referring to the insulator in Fig. 1.3, to excite one of the most energetic electrons from the valance band to the conduction band a finite amount of energy (E_g) is needed.

The bandgap of a material is also one of the distinguishing features to classify the system into topologically equivalent groups. Important information about the system can be extracted from the topology of the wavefunctions constituting the energy bands. In mathematical language, topology is concerned with geometrical

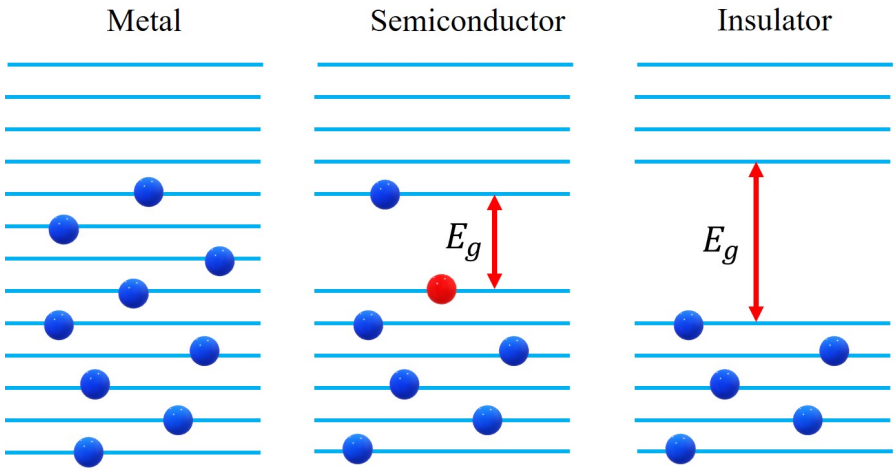

Figure 1.3: The band structures of metals, semiconductors and insulators, respectively. Each blue dot represents two electrons with opposite spins.

properties of objects that are insensitive under continuous deformations [42]. A simple example for explaining this concept is that of a sphere and a donut. It is observed that the two surfaces are topologically different as one cannot be continuously transformed to the other. For example, one can deform smoothly the sphere into the shape of a disc or a bowl but it cannot be smoothly deformed into a donut without scooping material out of it. On the other hand, the donut can be transformed into a coffee cup where the hole in the donut becomes the handle of the cup. In the language of topology, the sphere and bowl are in the same topological class while the donut and cup are in separate classes.

Furthermore, the sphere and a donut are distinguished by an integer topological invariant based on the number of holes in the manifold. This quantity is a topological invariant and is termed as genus. In the above example, the sphere has a genus $g = 0$ and a donut has a genus $g = 1$. Both of these objects are shown in Fig. 1.4. The associated topological invariants can be determined for geometrical surfaces utilizing a beautiful theorem known as the Gauss-Bonnet theorem. The Gauss-Bonnet theorem states that the integral of Gaussian curvature K over

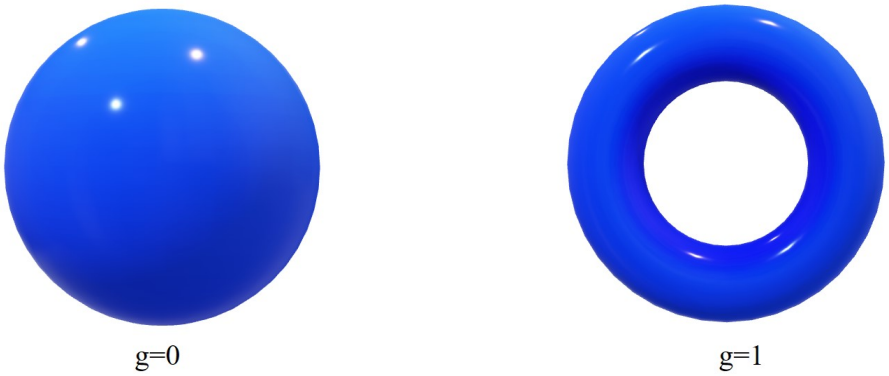

Figure 1.4: Topologically different objects (a sphere and donut) can be classified according to their genus (g).

a closed 2D surface is

$$\chi = \frac{1}{2\pi} \int_S K dA, \tag{1.1}$$

where χ is called the Euler characteristic, a global quantity describing the shape of the topological space and this is also quantized. For a sphere $\chi = 2$, where $K = 1/R^2$. The Euler characteristic of the surface is related to the genus by $\chi = 2 - 2g$ [43].

The question that arises here is: how can topology be utilized to distinguish different phases of matter? We will first discuss the topological classification of insulators. For example, two insulators are topologically equivalent if one can be smoothly transformed into the other by adiabatically tuning the bandgap such that the system always remains in the ground state as depicted in Fig. 1.5. The bandgap must be finite throughout the transformation. Figs. 1.5 (a) and (b) illustrate smooth and unsmooth deformation of BSs in an insulator. Fig. 1.5(a), illustrates the fact that two topologically inequivalent classes can be deformed smoothly in to one another while in Fig. 1.5(b), we show that the bandgap changes from + to −, which is not a smooth deformation. The occupied states of a band insulator can be viewed from a topological perspective [21, 28]. To identify the topological order of a material different classification scheme has emerged in the past few decades [44, 45]. From this, it is understandable, that topologically inequivalent insulator must involve a phase transition and the energy gap must vanishes (we will discuss these phase transitions in the subsequent chapters in detail).

The idea of topology was first introduced in solid-state physics for describing the integer quantum Hall effect (IQHE) [13] (which we discuss in detail in the following Section). In IQHE, the two-dimensional electron gas (2DEG) forms discrete Landau levels (LLs) which are spaced apart by the cyclotron frequency $\hbar\omega_c$. The IQHE shows band gaps and at the same time, exhibits non-zero transverse (or Hall) conductivity which is quantized in integer values of e^2/h. After the discovery of the IQHE, scientists realized that insulators and semiconductors indeed require

another sub-classification based on topology i.e., the fundamental origin of the IQHE is due to the topological nature of the bulk states. Therefore, bulk states can be distinguished by a topological invariant and different quantum phases are characterized and classified by these topological invariants [45, 46, 47]. One such topological invariant is the winding or the Chern number [21, 48]. This number is related to the Berry phase of Bloch wave functions. In the following sections, we will link Berry's phase and the Chern number.

1.0.3 Berry's phase

The Berry phase is an important concept of topological band theory and was first proposed in 1980 by Berry for quantum systems undergoing cyclic evolutions [49]. It is a quantum mechanical effect that arises due to the cyclic evolution of quantum

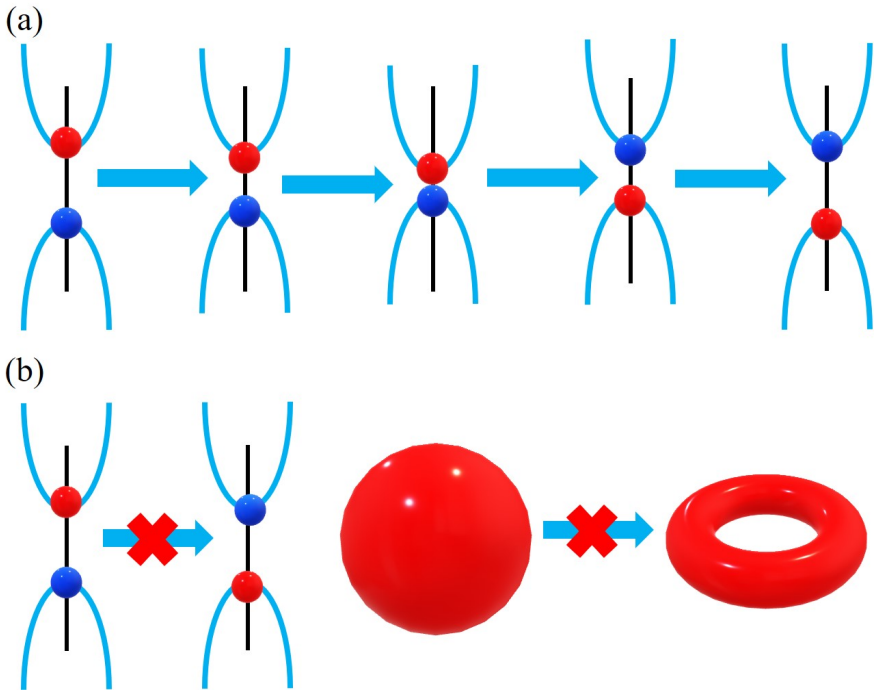

Figure 1.5: (a) Smooth deformation, (b) not a smooth deformation.

systems subjected to adiabatic disturbance. The adiabatic theorem states that if a quantum system evolves in time from some initial state i to some final state f and the evolution with time is very slow relative to the rate of transition, then the quantum system starting off in an eigenstate remains in the instantaneous eigenstate of the Hamiltonian. This problem can be casted in mathematical language.

Suppose a physical system with a general time-varying Hamiltonian depending on a set of time-dependent external parameters (e.g. magnetic field, electric field, flux and strain) labelled as $\boldsymbol{R}(t) = (R_1, R_2, ...)$ is initially in one of its eigenstates $|n(\boldsymbol{R}(0))\rangle$ [50]. Now if the system evolves adiabatically, then according to the quantum adiabatic theorem [51, 52], the system evolution can be written mathematically as

$$\hat{H}(\boldsymbol{R}(t))|n(\boldsymbol{R}(t))\rangle = E_n(\boldsymbol{R}(t))|n(\boldsymbol{R}(t))\rangle, \tag{1.2}$$

showing that the system remains in the instantaneous eigenstate $|n(t)\rangle$ as we are interested in the adiabatic evolution of the system, the evolution is sufficiently slow in time. The system picks up a phase $\theta(t)$ which is derived next.
The total wave-function of the quantum system at time t is given by

$$|\Psi_n(t)\rangle = e^{-i\theta(t)}|n(\boldsymbol{R}(t))\rangle. \tag{1.3}$$

The time evolution of the system can be described by the time-dependent Schrödinger equation:

$$\hat{H}|\Psi(t)\rangle = i\hbar\frac{d}{dt}|\Psi(t)\rangle, \tag{1.4}$$

which can therefore be written with the help of the ansatz in Eq. (1.3) as

$$E_{\mathrm{n}}(\boldsymbol{R}(t))|n(\boldsymbol{R}(t))\rangle = \hbar\frac{d\theta}{dt}|n(\boldsymbol{R}(t))\rangle + i\hbar\frac{d}{dt}|n|\boldsymbol{R}(t)\rangle. \tag{1.5}$$

Assuming orthonormality $\langle n(\boldsymbol{R}(t))|n(\boldsymbol{R}(t))\rangle = 1$, we obtain

$$E_n(\boldsymbol{R}(t)) = i\hbar\left\langle n(\boldsymbol{R}(t))|\frac{d}{dt}|n(\boldsymbol{R}(t))\right\rangle + \hbar\frac{d\theta}{dt}, \tag{1.6}$$

whose solution is given by

$$\theta(t) = \frac{1}{\hbar}\int_0^t E_n\left(\boldsymbol{R}\left(t'\right)\right)dt' - i\int_0^t \left\langle n\left(\boldsymbol{R}\left(t'\right)\right)\left|\frac{d}{dt'}\right|n\left(\boldsymbol{R}\left(t'\right)\right)\right\rangle dt'. \tag{1.7}$$

The first term of the above represents the dynamical phase and the second part is called the Berry phase γ. The total wave function can be written as

$$|\psi(t)\rangle = \exp\left(\frac{1}{\hbar}\int_0^t E_n\left(\boldsymbol{R}(t')\right)\right)\exp(i\gamma_n)|n\left(\boldsymbol{R}\right)\rangle. \tag{1.8}$$

All in all, the Berry phase can be written as:

$$\gamma_n = i\int_0^t \left\langle n(\boldsymbol{R}(t'))\left|\frac{d}{dt}\right|n(\boldsymbol{R}(t'))\right\rangle dt^{'}, \tag{1.9}$$

It is convenient to remove the time and instead express the Berry phase in terms of evolution in the particular space $\boldsymbol{R}$,

$$\gamma_n = i\int_C \langle n(\boldsymbol{R}(t'))|\nabla_{\boldsymbol{R}}|n(\boldsymbol{R}(t'))\rangle\cdot d\boldsymbol{R}, \tag{1.10}$$

where we have used $d/dt' = \nabla_{\boldsymbol{R}}\cdot d\boldsymbol{R}/dt'$ to re-express the above equation. Subsequently, we can define the Berry connection or Berry vector potential as follows

$$\boldsymbol{A}_n(\boldsymbol{R}) = -i\left\langle n(\boldsymbol{R})|\nabla_{\boldsymbol{R}}|n(\boldsymbol{R})\right\rangle. \tag{1.11}$$

The Berry phase can also be expressed as a path integral in the parameter space as

$$\gamma_n = \int_C d\boldsymbol{R}\cdot\boldsymbol{A}_n(\boldsymbol{R}). \tag{1.12}$$

Obviously the Berry connection $\boldsymbol{A}_n(\boldsymbol{R})$ is gauge dependent. Therefore, under a gauge transformation we can write

$$|n(\boldsymbol{R})\rangle \to e^{i\xi(R)}|n(\boldsymbol{R})\rangle, \tag{1.13}$$

where $\xi(\boldsymbol{R})$ is some smooth and a single-valued function. The Berry connection transforms in the usual way as below

$$A_n(\boldsymbol{R}) \to A_n(\boldsymbol{R}) - \frac{\partial}{\partial\boldsymbol{R}}\xi(\boldsymbol{R}). \tag{1.14}$$

The Berry phase γ_n is modified by the gauge transformation through an additional contribution

$$-\int_C \frac{\partial}{\partial \boldsymbol{R}}\xi(\boldsymbol{R})\cdot d\boldsymbol{R} = \xi[\boldsymbol{R}(0)] - \xi[\boldsymbol{R}(\tau)], \tag{1.15}$$

where τ is a long time (period) after the path C has been wholly traversed. Many people concluded that through a smart choice $\xi(\boldsymbol{R})$ could cancel the Berry phase in Eq. (1.10), but that reasoning was incorrect.

Consider a closed path C, such that $\boldsymbol{R}(0) = \boldsymbol{R}(\tau)$. Due to the single-valued nature of our eigenstates basis, $|n\left(\boldsymbol{R}(\tau)\right)\rangle = |n\left(\boldsymbol{R}(0)\right)\rangle$. Gauge transformations must also maintain this property, therefore

$$e^{i\xi[\boldsymbol{R}(0)]}|n[\boldsymbol{R}(0)]\rangle = e^{i\xi[\boldsymbol{R}(\tau)]}|n[\boldsymbol{R}(\tau)]\rangle, \tag{1.16}$$

which is only possible if $\xi\left(\boldsymbol{R}(\tau)\right) - \xi\left(\boldsymbol{R}(0)\right) = 2\pi n$, where n is an integer ($n \in \mathcal{Z}$). So, under a closed path, the Berry phase can be cancelled only if it is an integer multiple of 2π.

1.0.4 Berry curvature

The curl of the Berry vector potential is known as the Berry curvature and is given by

$$\Omega_n^{\alpha\beta}(\boldsymbol{R}) = \nabla \times \boldsymbol{A}_n(\boldsymbol{R}) = \frac{\partial}{\partial R^\alpha}A_n^\beta(\boldsymbol{R}) - \frac{\partial}{\partial R^\beta}A_n^\alpha(\boldsymbol{R}). \tag{1.17}$$

The Berry curvature is just like a magnetic field in the momentum space. From Eq. (1.11), we have

$$\boldsymbol{A}_n^\beta(\boldsymbol{R}) = -i\langle n(\boldsymbol{R})|\frac{\partial}{\partial R^\beta}|n(\boldsymbol{R})\rangle, \tag{1.18}$$

taking derivative with respect to R^α, we obtain

$$\frac{\partial}{\partial R^\alpha}A_n^\beta(\boldsymbol{R}) = i\langle n(\boldsymbol{R})|\frac{\partial}{\partial R^\beta}|n(\boldsymbol{R})\rangle + i\langle n(\boldsymbol{R})|\frac{\partial^2}{\partial R^\alpha \partial R^\beta}|n(\boldsymbol{R})\rangle. \tag{1.19}$$

In a similar manner, we can write

$$\frac{\partial}{\partial R^\beta} A_n^\alpha(\boldsymbol{R}) = i\langle n(\boldsymbol{R})|\frac{\partial}{\partial R^\alpha}|n(\boldsymbol{R})\rangle + i\langle n(\boldsymbol{R})|\frac{\partial^2}{\partial R^\beta \partial R^\alpha}|n(\boldsymbol{R})\rangle. \tag{1.20}$$

From the properties of partial derivatives, we can write

$$\frac{\partial^2 f(x,y)}{\partial x \partial y} = \frac{\partial^2 f(x,y)}{\partial y \partial x}. \tag{1.21}$$

Utilizing Eq. (1.21), the Berry cuvature in Eq. (1.17) can be re-written as

$$\Omega_n^{\alpha\beta}(\boldsymbol{R}) = i\langle\frac{\partial}{\partial R^\alpha} n(\boldsymbol{R})|\frac{\partial}{\partial R^\beta}|n(\boldsymbol{R})\rangle - i\langle\frac{\partial}{\partial R^\beta} n(\boldsymbol{R})|\frac{\partial}{\partial R^\alpha}|n(\boldsymbol{R})\rangle. \tag{1.22}$$

Using the complete state $\sum_{n'} |n'(\boldsymbol{R})\rangle\langle n'(\boldsymbol{R})|$ relation, this can be expressed as

$$\langle\frac{\partial}{\partial R^\alpha} n(\boldsymbol{R}) \mid \frac{\partial}{\partial R^\beta} n(\boldsymbol{R})\rangle = \sum_{n'\neq n}\langle\frac{\partial}{\partial R^\alpha} n(\boldsymbol{R})|n(\boldsymbol{R})\rangle|n'(\boldsymbol{R})\rangle\langle n'(\boldsymbol{R})|\frac{\partial}{\partial R^\beta} n(\boldsymbol{R})\rangle. \tag{1.23}$$

Consider

$$\frac{\partial}{\partial R^\alpha}\langle n(\boldsymbol{R})|\hat{H}|n'(\boldsymbol{R})\rangle = 0. \tag{1.24}$$

$$\begin{aligned}
\langle n(\boldsymbol{R})|\frac{\partial}{\partial R^\alpha}\hat{H}|n'(\boldsymbol{R})\rangle &= -\langle\frac{\partial}{\partial R^\alpha} n(\boldsymbol{R})|\hat{H}|n'(\boldsymbol{R})\rangle - \langle n(\boldsymbol{R})|\hat{H}|\frac{\partial}{\partial R^\alpha} n'(\boldsymbol{R})\rangle \\
&= -E_{n'}\langle\frac{\partial}{\partial R^\alpha} n(\boldsymbol{R})|n'(\boldsymbol{R})\rangle - E_n\langle n(\boldsymbol{R})|\frac{\partial}{\partial R^\alpha} n'(\boldsymbol{R})\rangle \\
&= (E_n - E_{n'})\langle\frac{\partial}{\partial R^\alpha} n(\boldsymbol{R})|n'(\boldsymbol{R})\rangle.
\end{aligned} \tag{1.25}$$

From above we can write

$$\langle\frac{\partial}{\partial R^\alpha} n(\boldsymbol{R})|n'(\boldsymbol{R})\rangle = \frac{\langle n(\boldsymbol{R})|\frac{\partial}{\partial R^\alpha}\hat{H}|n'(\boldsymbol{R})\rangle}{(E_n - E_{n'})}. \tag{1.26}$$

Similarly,

$$\langle n'(\boldsymbol{R})|\frac{\partial}{\partial R^\beta} n(\boldsymbol{R})\rangle = \frac{\langle n'(\boldsymbol{R})|\frac{\partial}{\partial R^\beta}\hat{H}|n(\boldsymbol{R})\rangle}{(E_n - E_{n'})}. \tag{1.27}$$

Finally, Eq. (1.22), can be written in more compact form as

$$\Omega_n^{\alpha\beta}(\boldsymbol{R}) = i\sum_{n'\neq n}\frac{\langle n|\frac{\partial}{\partial R^\alpha}\hat{H}|n'\rangle\langle n'|\frac{\partial}{\partial R^\beta}\hat{H}|n\rangle - \langle n|\frac{\partial}{\partial R^\beta}\hat{H}|n'\rangle\langle n'|\frac{\partial}{\partial R^\alpha}\hat{H}|n\rangle}{(E_n - E_{n'})^2}. \tag{1.28}$$

The advantages in writing the Berry curvature in summation form is that no differentiation on the wave function is involved, therefore it can be evaluated under any gauge-choice. Next, in the following Section, we systematically introduce the classical and quantized versions of the Hall effect to begin with.

1.0.5 The classical Hall effect

Understanding the underlying physics of the Hall effect provides a convenient platform for our discussion of the quantum Hall effect. Fig. 1.6, shows the setting. A magnetic field B is applied perpendicular to the solid is shown and pointing out of the page. The electrons are trapped in the two-dimensional (2D) plane of the conductor and current I is made to flow in the x-direction. The trapped charge carriers feel a magnetic force toward one side of the conductor and thus accumulate a net positive charge on the other side of the sample. Due to the separation of charge carriers, a Hall voltage is developed across the conductor. The inducing of the Hall voltage V_H in the y-direction is known as the Hall effect after Edwin Hall, who discovered it in 1879. Due to the applied magnetic field, the electrons undergo circular motion due to the Lorentz force in a direction perpendicular to

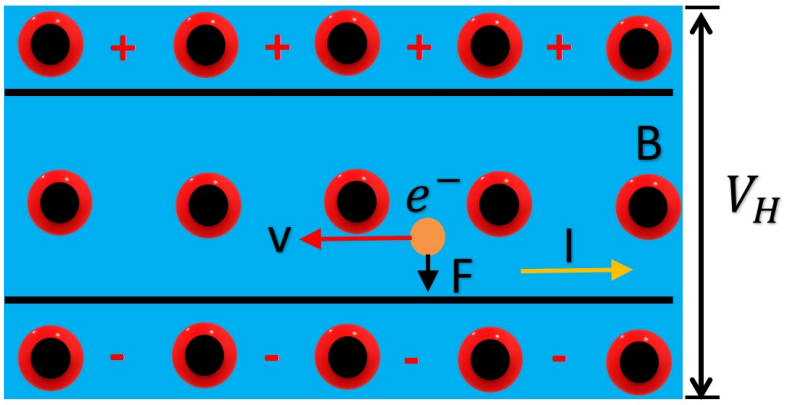

Figure 1.6: Classical Hall effect. Electrons move to the left in the conductor. The magnetic field is directly out of the page, represented by black circles.

the magnetic field. The charge polarization at both sides of the conductor builds up until the electric force E acting on the electrons in one direction is balanced by the magnetic force B on them in the opposite direction. In steady-state,

$$qE = qvB, \tag{1.29}$$

where m is the mass, q is the charge and v is the drift velocity of the electron. The relationship between the electric field E and Hall voltage is

$$E_H = \frac{V_H}{w}, \tag{1.30}$$

where w is the width of the conductor. Solving Eq. (1.30), for the Hall voltage we obtain

$$V_H = Bwv. \tag{1.31}$$

Consider that the conductor contains n mobile charge carriers per unit volume. The total current flowing through the conductor can be written as

$$I = nevA. \tag{1.32}$$

Here A is the cross-sectional area of the conductor. Utilizing Eqs. (1.29) and (1.30) in Eq. (1.32) one finally obtains the following expressions for the Hall voltage

$$V_H = \frac{IBw}{neA} \tag{1.33}$$

From Eq. (1.29), it is straight forward to determine the cyclotron frequency with which the electron goes around the circle;

$$\omega_c = \frac{eB}{m}. \tag{1.34}$$

1.0.6 Drude model

In order to understand some of the core ideas involved in the theory of the quantum Hall effect, it is instructive to discuss the semi-classical Hall effect for a finite sized two-dimensional electron gas (2DEG) subjected to a perpendicular external magnetic field B as shown in Fig. 1.7. For this purpose, we employ the Drude model which considers the 2DEG as a gas of electrons, electromagnetically responding to longitudinal electric and transverse magnetic fields and subject to particle scattering. Due to the Lorentz force, the charge carriers are moving in circular orbits having momentum $\vec{p}$. The Lorentz force can be written as

$$\frac{d\vec{p}}{dt} = -e\left(\vec{E} + \frac{\vec{p}}{m} \times \vec{B}\right) - \frac{\vec{p}}{\tau}, \tag{1.35}$$

where τ is the scattering rate, which captures the effect of the electron friction with impurities. Eq. (1.35) is the simplest model of charge transport, in which we treat the charge carriers as if they are classical billiard balls (ignoring electron-electron interactions etc.).

The conductivity of the 2DEG system can be obtained from equilibrium solutions of the equation of motion, $d\vec{p}/dt = 0$, as follows

$$eE_x = -eBv_y - \frac{mv_x}{\tau}, \tag{1.36}$$

$$eE_y = eBv_x - \frac{mv_y}{\tau}. \tag{1.37}$$

The current densities along the x and y directions are related to the velocities by the following relations

$$J_x = nev_x = \frac{en\tau}{m}\left(eE_x + eBv_y\right) \tag{1.38}$$

and

$$J_y = nev_y = \frac{en\tau}{m}\left(-eE_y - eBv_x\right). \tag{1.39}$$

The current flowing in the y direction is zero because the current cannot flow out of the sample in the y direction. From (1.39), we can write

$$J_y = nev_y = \frac{en\tau}{m}\left(-eE_y - eBv_x\right) = 0. \tag{1.40}$$

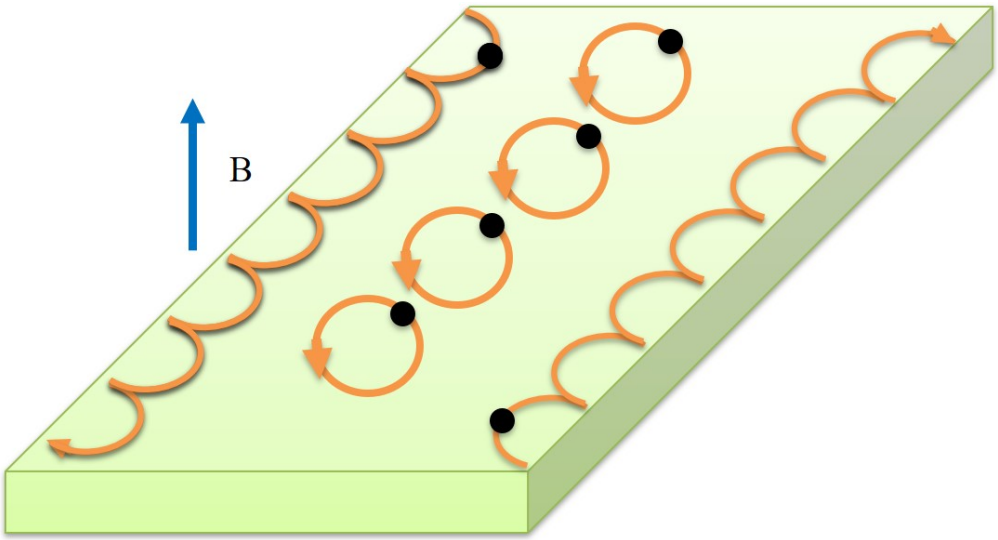

Figure 1.7: Representation of 2DEG electrons in a magnetic field moving in circular orbits with skipping trajectories. The diagram gives a classical picture.

We can write

$$E_y = Bv_x = -\frac{eB\tau}{m}E_x. \tag{1.41}$$

The Hall coefficient can be defined as

$$R_H = \frac{E_y}{J_x B}, \tag{1.42}$$

where $J_x = \sigma_0 E_x = ne^2\tau E_x/m$ and the Drude conductivity $\sigma_0 = ne^2\tau/m$. Using Eq. (1.41) in Eq. (1.42), the Hall coefficient in the standard form can be written as

$$R_H = -\frac{eB\tau E_x/mc}{ne^2\tau E_x B/m} = -\frac{1}{ne}. \tag{1.43}$$

We can re-write Eq. (1.38) and (1.39) relating the current density and the electric field

$$\begin{pmatrix} J_x \\ J_y \end{pmatrix} = \begin{pmatrix} \sigma_0 & \sigma_0\omega_c\tau \\ -\sigma_0\omega_c\tau & \sigma_0 \end{pmatrix} \begin{pmatrix} E_x \\ E_y \end{pmatrix}, \tag{1.44}$$

which is the tensorial form of Ohm's law in a 2DEG. The explicit expression for the conductivity tensor is given by

$$\sigma = \begin{pmatrix} \sigma_{xx} & \sigma_{xy} \\ -\sigma_{xy} & \sigma_{yy} \end{pmatrix} = \sigma_0 \begin{pmatrix} 1 & \omega_c\tau \\ -\omega_c\tau & 1 \end{pmatrix}, \tag{1.45}$$

with $\sigma_{xx} = \sigma_{yy} = \sigma_0$ and $\sigma_{xy} = \sigma_{yx} = \omega_c\tau$. The resistivity can be defined as the inverse of the conductivity. From the above expression, one may immediately read off the resistivity tensor as

$$\rho = \begin{pmatrix} \rho_{xx} & \rho_{xy} \\ -\rho_{xy} & \rho_{yy} \end{pmatrix} \tag{1.46}$$

The off-diagonal component of the resistivity tensor is called the Hall resistivity and is given by

$$\rho_{xy} = \frac{\omega_c\tau}{\sigma_0} = \frac{\omega_c\tau}{ne^2\tau/m} = \frac{eB\tau/mc}{ne^2\tau/m} = \frac{B}{nec}, \tag{1.47}$$

where ρ_{xy} is proportional to the magnetic field B. Similarly, the diagonal resistivity is given by

$$\rho_{xx} = \frac{m}{ne^2\tau} \tag{1.48}$$

showing that ρ_{xx} depends on the scattering time τ. In the limit $\tau \to \infty$, $\rho_{xx} = 0$. In the following section, we approach the 2D conductivity in a quantum mechanical picture before we come back to the resistivity again.

1.0.7 Landau levels

Before we review the integer quantum Hall effect we will first look at a non-relativistic 2DEG fermion in an external magnetic field. In order to understand the quantum mechanical picture, we start with the Hamiltonian of the free electron given by

$$\hat{H} = \frac{\hat{p}^2}{2m}. \tag{1.49}$$

Introducing the Landau gauge for the magnetic vector potential $A = (-yB, 0, 0)$, which is related to B through the relation $B = \nabla \times A$ and utilizing the Peierls substitution, the mechanical momentum is replaced by the canonical momentum in the following fashion [53],

$$\hbar k \to \hbar k - \frac{e}{c}A, \tag{1.50}$$

allowing the Hamiltonian to be written as

$$\hat{H} = \frac{1}{2m}\left(\hat{p}_x - \frac{eBy}{c}\right)^2 + \frac{\hat{p}_y^2}{2m}. \tag{1.51}$$

The Hamiltonian commutes with p_x so it is obivious that p_x is a good quantum number. The trial wave-functions is

$$\psi(x,y) = \frac{e^{ikx}}{\sqrt{L}}\chi(y), \tag{1.52}$$

where L is the length of the 2DEG. The momentum along the x direction can be defined as $p_x \equiv hk$. Making the usual substitution, we can express our Hamiltonian as

$$\begin{aligned}
\hat{H}\psi(x,y) &= \left[\frac{\hat{p}_y^2}{2m} + \frac{(hk - eBy/c)^2}{2m}\right]\frac{e^{ikx}}{\sqrt{L}}\chi(y) \\
&= \left[\frac{\hat{p}_y^2}{2m} + \frac{e^2B^2}{2mc^2}\left(y - \frac{hkc}{eB}\right)^2\right]\frac{e^{ikx}}{\sqrt{L}}\chi(y) \\
&= \left[\frac{\hat{p}_y^2}{2m} + \frac{e^2B^2}{2mc^2}\left(y + kl_B^2\right)^2\right]\frac{e^{ikx}}{\sqrt{L}}\chi(y) \\
&= \left[\frac{\hat{p}_y^2}{2m} + \frac{m\omega_c^2}{2}\left(y - y_0\right)^2\right]\frac{e^{ikx}}{\sqrt{L}}\chi(y),
\end{aligned} \tag{1.53}$$

where $\omega_c = eB/m$ is the cyclotron frequency, $y_0 = -\hbar k/(eB)$ and $l_B = \sqrt{\hbar/eB}$ is defined as the magnetic length. From Eq. (1.53), we note that we are dealing with a simple harmonic oscillator (SHM) with a shifted origin y_0. The energy levels of the non-relativistic fermions of 2DEG are discrete and given by

$$E_n = \hbar\omega_c\left(n + \frac{1}{2}\right). \tag{1.54}$$

where n is an integer denoting Landau quantum number. The energy dispersion is therefore given by discrete Landau levels spaced apart by $\hbar\omega_c$ as shown in Fig. 1.8.

In the classical picture, the Lorentz force is responsible for the circular orbits of electrons in a magnetic field and the trapped charge carriers at the edges trying to move in circular orbits with skipping trajectories. It is obvious that the SHM

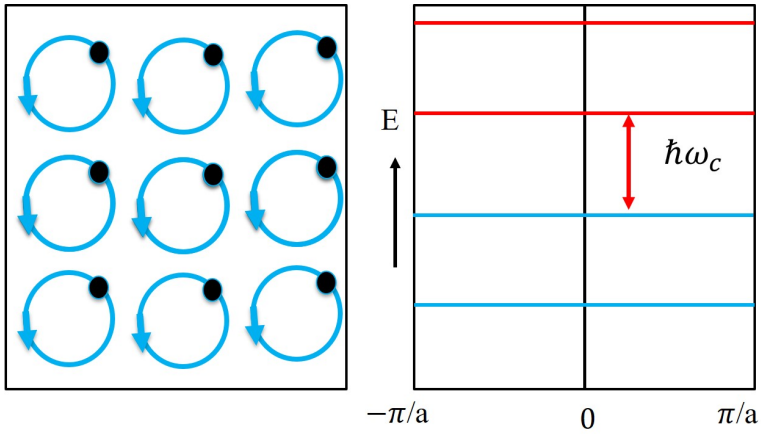

Figure 1.8: (a) The quantum Hall state and equidistant Landau levels separated by $\hbar\omega_c$.

interpretation seems reasonable. For $n = 0$ LLs the wave function is a Gaussian centered at $y_0 = -kl_B^2$, given by

$$\psi(x,y) = \frac{e^{ikx}}{\sqrt{\sqrt{\pi}L_x l_B}} e^{-\frac{1}{2l_B^2}(y+l_B^2)^2} = \frac{e^{ikx}}{\sqrt{\sqrt{\pi}L_x l_B}} e^{-\frac{1}{2l_B^2}(y-y_0)^2}. \tag{1.55}$$

It is also useful to know the degeneracy of each LL as we have a largely degenerate system. To do this effect, we restrict ourselves to a finite region of the xy-plane. The rectangle have dimensions L_x and L_y in the x and y direction. The quantum system can be described by a particle in a box with allowed momentum values $k_x = 2\pi n/L_x$. The number of degenerate states in each LL for a system of size $L_x \times L_y$ is given by

$$N = \frac{L_x}{2\pi}\int_{-L_y/l_B^2}^{0} dk_x = \frac{L_x L_y}{2\pi l_B^2} \tag{1.56}$$

It is common to relate the degeneracy and more importantly the flux. The quantum of flux is defined as

$$\Phi_0 = \frac{2\pi\hbar}{e} = \frac{h}{e}, \tag{1.57}$$

so the degeneracy can be expressed as

$$N = \frac{L_x L_y B}{\Phi_0} = \frac{\Phi}{\Phi_0}. \tag{1.58}$$

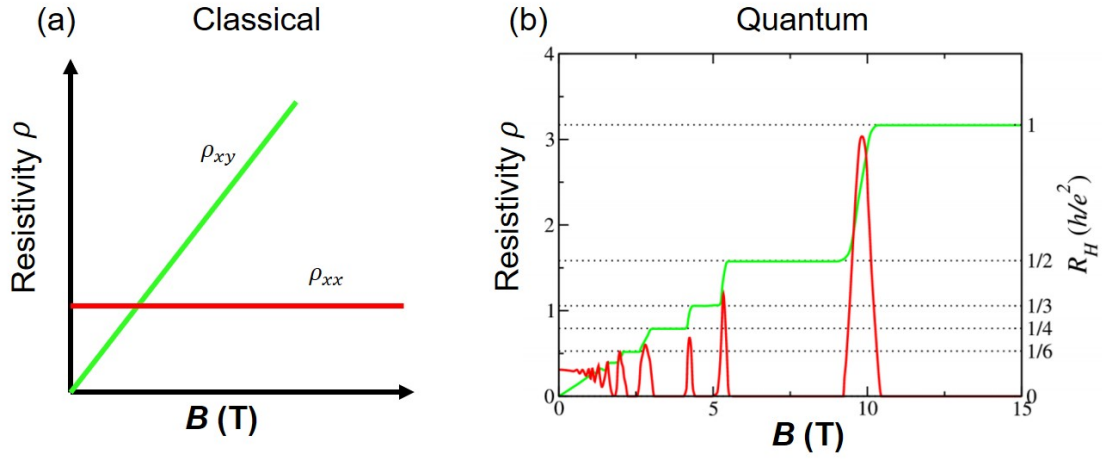

Figure 1.9: (a) Illustration of longitudinal and transverse resistivities as functions of the magnetic field. (a) Classical Hall effect behavior and (b) the IQHE. The red color. shows the ρ_{xx} while the green line denotes the Hall resistivity ρ_{xy}, which exhibits plateaus quantized in exact multiples of h/e^2.

Similarly, the filling factor is defined by

$$\nu = \frac{\Phi_0 n}{B}, \tag{1.59}$$

which is an important consideration in the IQHE and describes how many of the lowest LLs are filled. Note that $n = N/L_x L_y$. After discussing the classical and semiclassical Hall effect in 2DEG, we are now capable to derive the famous IQHE for relativistic fermions.

1.0.8 The Integer quantum Hall effect and chiral edge states

In this section, we discuss the integer quantum Hall effect. The IQHE was discovered in 1980 by Klaus von Klitzing for which he received a Nobel prize in 1985. Klitzing found that the diagonal or longitudinal resistivity ρ_{xx} became very small for certain values of the applied magnetic field for which the Hall resistivity ρ_{xy} sits on a plateau before jumping suddenly to the next plateau. Furthermore, on

each of these plateaus, the Hall resistivity ρ_{xy} takes the value

$$\rho_{xy} = \frac{h}{e^2}\frac{1}{\nu}, \tag{1.60}$$

where the prefactor the filling factor is an integer $\nu = 1, 2, ..,$ known as the filling factor [13]. This equation presents the quantization of the Hall resistivity. The experimental results of the longitudinal ρ_{xx} and Hall resistivity ρ_{xy} are shown in Fig. 1.9.

By looking again at the classical picture in Fig. 1.7, we notice that charges perform circular motion in the presence of a magnetic field. Some of the particles move in circular closed orbits known as cyclotron orbits. On the other hand, some of the charge carriers closer to the edge make open electron trajectories that hit repeatedly the sample edge, because the electrons cannot exit the sample. These are known as skipping orbits. The skipping orbits exhibit the formation of propagating edge states in a magnetic field. The classical picture is thus incomplete and unable to give us quantitative predictions. The picture needs quantum mechanical consideration to explain the quantized Hall effect.

In order to determine the Hall conductivity in the quantum picture, we consider a 2DEG confined in the xy plane. The system is subjected to a static magnetic field B and an electric field E in the z and y direction, respectively. The perturbation potential for the electric field is given by

$$\hat{H}_p = -eEy. \tag{1.61}$$

In the standard way, the perturbed eigenstates are given by [48, 54]

$$|n\rangle_E = |n\rangle + \sum_{n\neq m} \frac{\langle m|\hat{H}_p|n\rangle}{E_n - E_m}|m\rangle + \cdots = |n\rangle + \sum_{n\neq m} \frac{\langle m|(-eEy)|n\rangle}{E_n - E_m}|m\rangle + \cdots , \tag{1.62}$$

where E_n is the n^{th} LL energy. The corresponding expectation value of the longitudinal current density along the x direction due to the perturbation is

$$\langle j_x\rangle_E = \frac{e\,\langle v_x\rangle}{L^2}, \tag{1.63}$$

where v_x is the velocity of the electron in the x direction. The above equation can be expressed as,

$$\langle j_x \rangle_E = \sum_n f\left(E_n\right) \left\langle n|_E \left(\frac{ev_x}{L^2}\right) \mid n \right\rangle_E, \tag{1.64}$$

where $f_n = 1/(1 + e^{(E_n - \mu_F)/k_B T})$ is the Fermi Dirac distribution function at temperature T and chemical potential μ_F. To first order in E, the current density is given by

$$\langle j_x \rangle_E = \frac{1}{L^2} \sum_{\substack{m \\ m \neq n}} f\left(E_n\right) \left(\frac{\langle n \left| ev_x \right| m \rangle \langle m|(-eEy)|n\rangle + \langle n|(-eEy)|m\rangle \langle m \left| ev_x \right| n \rangle}{E_n - E_m} \right), \tag{1.65}$$

where have used the facts that $\langle n \left| j_x \right| n \rangle_{E=0} = 0$, because the current is zero without the perturbation field. From the Heisenberg equation of motion we can write

$$v_y = \frac{dy}{dt} = \frac{1}{i\hbar}[y, \hat{H}], \tag{1.66}$$

by taking the expectation value of the v_y, we obtain

$$\langle m \left| v_y \right| n \rangle = \frac{1}{i\hbar} \left(E_n - E_m\right) \langle m|y|n\rangle. \tag{1.67}$$

Therefore, the current density can be expressed as

$$\langle j_x \rangle_E = \frac{-i\hbar e^2 E}{L^2} \sum_{m \neq n} f\left(E_n\right) \left(\frac{\langle n \left| v_x \right| m \rangle \langle m \left| v_y \right| n \rangle - \langle n \left| v_y \right| m \rangle \langle m \left| v_x \right| n \rangle}{\left(E_n - E_m\right)^2} \right). \tag{1.68}$$

Now consider that the system potential is periodic in the absence of the electric field E, then according to Bloch theorem the eigenstates can be expressed as the Bloch states $|u_{nk}\rangle$. The expectation value of the velocity can be expressed in terms of the Bloch states as

$$\langle u_{nk} \left| v_\mu \right| u_{mk'} \rangle = \frac{1}{\hbar} \langle u_{nk}| \frac{\partial \hat{H}}{\partial k_\mu} |u_{mk'}\rangle. \tag{1.69}$$

Employing the product rule, the term on the right hand side can be expressed as

$$\langle u_{nk} \left| v_\mu \right| u_{mk'} \rangle \;\; = \;\; \frac{1}{\hbar} \langle u_{nk}| \frac{\partial}{\partial k_\mu} \left(\hat{H} \left| u_{mk'} \right\rangle \right) + \frac{1}{\hbar} \langle u_{nk}| \hat{H} \frac{\partial}{\partial k_\mu} |u_{mk'}\rangle. \tag{1.70}$$

Therefore, from Eq. (1.70), the product rule lead us to the identity

$$\langle u_{nk}\left|v_{\mu}\right|u_{mk'}\rangle=\frac{1}{\hbar}\left(E_{mk'}-E_{nk}\right)\langle u_{nk}|\frac{\partial}{\partial k_{\mu}}|u_{mk'}\rangle, \tag{1.71}$$

which allows us to re-write Eq. (1.68) in the form

$$\begin{aligned}\sigma_{xy} &= \frac{ie^2}{\hbar L^2}\sum_{n,k,k'} f\left(E_{nk}\right)\langle u_{nk}|\frac{\partial}{\partial k_x}|u_{mk'}\rangle\langle u_{mk'}|\frac{\partial}{\partial k_y}|u_{nk}\rangle \\ &- \frac{ie^2}{\hbar L^2}\sum_{n,k,k'} f\left(E_{nk}\right)\langle u_{nk}|\frac{\partial}{\partial k_y}|u_{mk'}\rangle\langle u_{mk'}|\frac{\partial}{\partial k_x}|u_{nk}\rangle.\end{aligned} \tag{1.72}$$

Expanding the first term in the above equation we obtain

$$\begin{aligned}&\sum_{m,k'}\langle u_{nk}|\frac{\partial}{\partial k_x}|u_{mk'}\rangle\langle u_{mk'}|\frac{\partial}{\partial k_y}|u_{nk}\rangle \\ &\qquad=\sum_{m,k'}\left[\frac{\partial}{\partial k_x}\left\langle u_{nk}\mid u_{mk'}\right\rangle-\left(\frac{\partial}{\partial k_x}\left\langle u_{nk}\right|\right)\left|u_{mk'}\right\rangle\right]\langle u_{mk'}|\frac{\partial}{\partial k_y}|u_{nk}\rangle.\end{aligned} \tag{1.73}$$

The first term on the right hand side is zero as the sum is restricted to $m \neq n$. Performing the sums over m and k', we obtain

$$\begin{aligned}&-\left(\frac{\partial}{\partial k_x}\left\langle u_{nk}\right|\right)\frac{\partial}{\partial k_y}\left|u_{nk}\right\rangle= \\ &\qquad -\frac{\partial}{\partial k_x}\left\langle u_{nk}\left|\frac{\partial}{\partial k_y}\right|u_{nk}\right\rangle+\left\langle u_{nk}\left|\frac{\partial^2}{\partial k_x\partial k_y}\right|u_{nk}\right\rangle.\end{aligned} \tag{1.74}$$

By interchanging k_x and k_y in the above expression, the second term in Eq. (1.72) can be obtained. We can express the Hall conductivity in terms of Bloch states as

$$\sigma_{xy}=\frac{ie^2}{\hbar L^2}\sum_{n,k} f\left(E_{nk}\right)\left[-\frac{\partial}{\partial k_x}\left\langle u_{nk}\left|\frac{\partial}{\partial k_y}\right|u_{nk}\right\rangle+\frac{\partial}{\partial k_y}\left\langle u_{nk}\left|\frac{\partial}{\partial k_x}\right|u_{nk}\right\rangle\right]. \tag{1.75}$$

The Hall conductivity can be easily reduces to

$$\sigma_{xy}=\nu\frac{e^2}{\hbar}, \tag{1.76}$$

where $\nu \in \mathcal{Z}$ which is the Landau levels (LL) filling fraction. Which is in agreement with Klitzing *et. al* well known formula of conductivity [13].

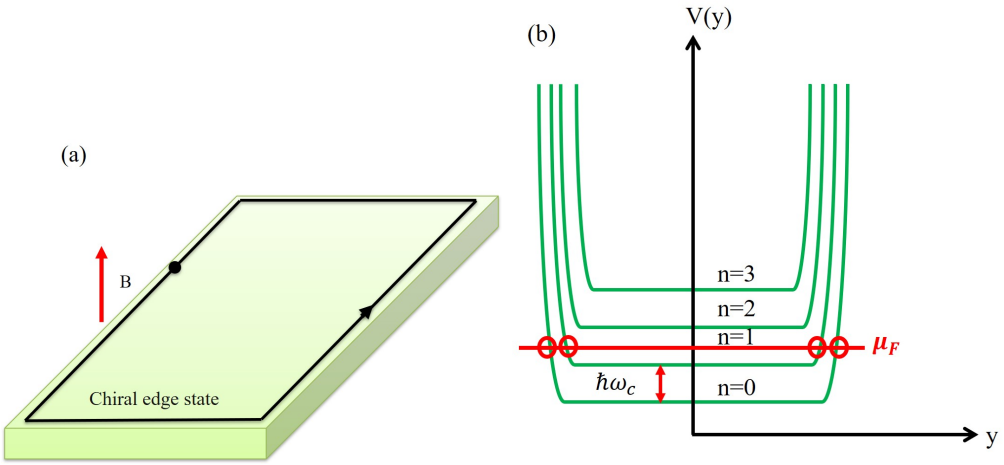

Figure 1.10: (a) The formation of a chiral extended edge state. (b) Representation of the Landau levels.

It must be noted that σ_{xy} and ρ_{xy} is independent of sample parameters. Now the question is how does the confining potential $V(y)$ affect the energy eigenvalues of the system? In the bulk of the sample, away from the edges, the confining potential is flat, i.e. $V(y) = 0$ as shown in Fig. 1.10 (a). In the bulk region of the sample, we get flat LLs, which are equally spaced by $\hbar\omega_c$. In the classical regime, we have shown these bulk states corresponding to the cyclotron orbits in Fig. 1.7. From Eq. (1.76), it is crystal clear that the periodic charge carrier motion is quantized. The skipping orbits transform into a one-dimensional edge channel encircling the interior of the sample as a result of the strong magnetic field as illustrated in Fig. 1.10 (a). The topological edge states give rise to an edge current that characterizes the IQHE. The topological edge states are very sensitive to the confining potential, so their LLs dispersion will be affected. The original LLs energies increase by an amount proportional to the confining potential.

If we place the chemical potential μ_F in between two LLs in the bulk gap as shown in Fig. 1.10 (b), there are states crossing it at the edges and cutting where the number is equal to the number of occupied levels. As a result, the number

of occupied LLs is exactly equal to the integer quantization of the Hall effect. It must be noted that for each edge, there are as many topological edge states as there are filled LLs in the bulk of the system.

In the quantum regime, we applied the electric field E is in the y-direction, so the directions of the current flow and electric field are perpendicular to each other, and thus the electric current produces no resistive heating. The chiral edge states are therefore responsible for dissipationless quantum Hall transport and the current is flowing without scattering. In any realistic system disorder created by randomly distributed ionized impurities is inevitably present that tends to induce elastic momentum scattering with resulting in $\vec{p} \mapsto -\vec{p}$. Due to the topological edge states, such backscattering is rigorously not allowed as there is no counter-propagating state available. The robust directiveness of the topological edge states is called chirality. In the next section, we will develop a relationship between the IQHE and topology.

1.0.9 Topological invariants and the quantum Hall effect

Our next goal is to introduce the notion of a topological invariant. An example of one such invariant is the Chern number. The Chern number allows us to classify topological phases of matter, which are preserved under continuous deformations of the band structure. In 1982, Thouless, Kohmoto, Nightingale, and den Nijs (TKNN) for the first time proposed that the quantized Hall conductivity is related to a topological invariant [45]. Following Eq. (1.75), the Hall conductivity can be written in terms of the Berry curvature as

$$\sigma_{xy} = \frac{e^2}{\hbar} \sum_n \int_{BZ} \frac{d^2k}{(2\pi)^2} \nabla_{\boldsymbol{k}} \times \boldsymbol{A}_n(\boldsymbol{k}), \tag{1.77}$$

where the Berry connection is given by Eq. (1.11) when $|n(\boldsymbol{R})\rangle$ represents the Bloch states $|u_{n\boldsymbol{k}}\rangle$:

$$\boldsymbol{A}_n(\boldsymbol{k}) = -i \langle u_{n\boldsymbol{k}} | \nabla_{\boldsymbol{k}} | u_{n\boldsymbol{k}} \rangle . \tag{1.78}$$

The Chern number can be defined in term of Berry connection as

$$\begin{aligned} \nu_n &= \int_{BZ} \frac{d^2k}{(2\pi)^2} \nabla_{\boldsymbol{k}} \times \boldsymbol{A}_n(\boldsymbol{k}) && (1.79) \\ &= \oint_{\partial BZ} \frac{dk}{(2\pi)} \cdot \boldsymbol{A}_n(\boldsymbol{k}) && (1.80) \\ &= \frac{1}{2\pi} \gamma_n. && (1.81) \end{aligned}$$

The Chern number ν_n is determined solely by the electronic band structure. The Hall conductivity can be linked with propagating edge states by the following equation

$$\sigma_{xy} = \frac{e^2}{\hbar} \sum_{n \in \text{occ}} \nu_n. \tag{1.82}$$

This formula is the statement that σ_{xy} is a topological invariant of the quantum system and the Hall conductivity is topological. The system wave-function is single valued in nature, therefore the change in Berry's phase can only be an integer multiple of 2π after encircling the BZ. Thus, ν_n must be an integer and known as the TKNN invariant.

1.1 Topological insulators

This thesis also deals with topological insulators (TIs). This section highlights some of the most important characteristics of TIs.

1.1.1 Time-reversal symmetry and Kramers's theorem

Before we discuss time-reversal symmetric topological insulators, we first need to understand what we actually mean by time reversal symmetry, and how it leads to Kramers' degeneracy. Symmetries play a crucial role in condensed matter physics. Commonly, the fundamental microscopic laws of nature are said to be invariant under time reversal transformations. In quantum mechanics, time reversal is a transformation that reverses the arrow of time, and mathematically, we can define

it as [40]

$$t \mapsto -t. \tag{1.83}$$

Consider a particle having momentum p and spin s placed at position r, then time reversal (TR) implies

$$r \mapsto r, \qquad p \mapsto -p, \qquad s \mapsto -s. \tag{1.84}$$

Under TR the position operator r is unchanged as TR commutes with any spatial symmetry. However, it flips the sign of the momentum operator p and spin operator s. The Hamiltonian of a physical system is said to be TR invariant if under TR transformations it is also preserved. Now consider an interesting example of the TRS Hamiltonian for non-relativistic particle

$$\hat{H} = v\sigma \cdot p = \frac{2v}{\hbar} s \cdot p, \tag{1.85}$$

where $s = \hbar\sigma/2$ and $\sigma = (\sigma_x, \sigma_y, \sigma_z)$ consists of 2×2 Pauli matrices. Here v is the velocity of the moving particle. The massles spin-1/2 particle Hamiltonian is odd in both momentum and spin. We would like to find the representation of the TR operator irrespective of the details of the physical system. Now TRS can be formally defined through the time reversal operator $\mathcal{T}$ as

$$\mathcal{T}\hat{H}\mathcal{T}^{-1} = \hat{H}, \tag{1.86}$$

$$\mathcal{T}\hat{H} = \hat{H}\mathcal{T}, \tag{1.87}$$

under the following constraints

$$\mathcal{T}r\mathcal{T}^{-1} = r, \tag{1.88}$$

$$\mathcal{T}p\mathcal{T}^{-1} = -p, \tag{1.89}$$

$$\mathcal{T}s\mathcal{T}^{-1} = -s. \tag{1.90}$$

From the preceding equations with $p = -i\hbar\nabla$, we notice that the TRS operator $\mathcal{T}$ involves complex conjugation, C, which can be written as

$$\mathcal{T} = UC, \tag{1.91}$$

where $U = \pm i\sigma_y$. To preserve the norm of the quantum state U must be a unitary matrix. The anti-unitary operator that represents TRS can be written as

$$\mathcal{T} = i\sigma_y C, \tag{1.92}$$

where the TRS operator has the property (for a spin 1/2 system)

$$\mathcal{T}^2 = -1 \qquad \Longleftrightarrow \qquad \mathcal{T}^{-1} = -\mathcal{T}. \tag{1.93}$$

After discussing TRS, we are now in a position to prove the Kramers' theorem which has important implications for TR-invariant quantum systems. Kramers theorem was constructed by the Hendrick Anton Kramers in 1930. The Kramers degeneracy theorem states that each energy level of a time-reversal symmetric system with non-integer spin is at least doubly degenerate [48]. Lets spell it out further. Consider an electric charge flowing in opposite directions, e.g. charge currents admissible on the edge of a 2D Hall sample. The quantum system has right and left-moving states $|+\rangle$ and $|-\rangle$. These states are related to each other by the following TR operation:

$$|+\rangle = \mathcal{T}|-\rangle \tag{1.94}$$

The states $|+\rangle$ and $|-\rangle$ must have the same energy, if $\mathcal{T}$ is an invariant symmetry of the Hamiltonian. Our goal is to prove that $|+\rangle$ and $|-\rangle$ are two independent orthogonal states, i.e,

$$\langle +|-\rangle = 0. \tag{1.95}$$

Using above equations, we can re-write the product $\langle +|-\rangle$ as

$$\langle +|-\rangle = \langle -|\mathcal{T}^\dagger \mathcal{T}^{-1}|+\rangle = -\langle -|\mathcal{T}^\dagger \mathcal{T}|+\rangle = -\langle -|+\rangle^* = -\langle +|-\rangle. \tag{1.96}$$

From this one can conclude that the product $\langle +|-\rangle$ vanishes identically, which proves the Kramers' theorem.

Before introducing two and three-dimensional topological insulators, we will discuss the spin-orbit coupling which is a fundamental concept in spin transport properties of 2D materials and topological insulators.

1.1.2 Spin-orbit coupling

Before we discuss the role of spin-orbit coupling in 3D and 2D topological insulators in details, it is helpful to recapitulate, the derivation of the spin-orbit coupling (SOC) term through the Dirac equation which is the defining equation in relativistic quantum mechanics [55]. The SOC is a relativistic effect between electrons and a local internal or external electric fields. Mobile electrons sense an effective magnetic field B_{eff} in their rest frame even when they are exposed to electric fields. We will start the derivation of the SOC from Dirac equation. In the presence of EM couplings, the relativistic Dirac equation can be written as

$$\left(\frac{\partial}{\partial x_\mu} - \frac{ie}{hc}A_\mu\right)\gamma_\mu\psi + \frac{mc}{\hbar}\psi = 0, \tag{1.97}$$

where $-i\hbar\left(\partial/\partial x_\mu\right) = -i\hbar\left(\partial/\partial x_\mu\right) - eA_\mu/c$. It must be noted that A_μ is time independent. The wave function ψ is known as a bispinor or Dirac spinor and is given by

$$\psi = \begin{pmatrix} \psi_\uparrow \\ \psi_\downarrow \end{pmatrix} = \psi(x,t)|_{t=0}\, e^{-iEt/\hbar}, \tag{1.98}$$

yielding the two coupled equations

$$\left[\boldsymbol{\sigma}\cdot\left(\mathbf{p} - \frac{e\mathbf{A}}{c}\right)\right]\psi_B = \frac{1}{c}\left(E - eA_0 - mc^2\right)\psi_A, \tag{1.99}$$

$$-\left[\boldsymbol{\sigma}\cdot\left(\mathbf{p} - \frac{e\mathbf{A}}{c}\right)\right]\psi_A = -\frac{1}{c}\left(E - eA_0 + mc^2\right)\psi_B. \tag{1.100}$$

From Eq. (1.100), we can eliminate ψ_A to obtain

$$\psi_B = \frac{1}{(E - eA_0 + mc^2)}\left[\boldsymbol{\sigma}\cdot\left(\mathbf{p} - \frac{e\mathbf{A}}{c}\right)\right]\psi_A, \tag{1.101}$$

which can be substituted back into Eq. (1.99) to yield

$$\left[\boldsymbol{\sigma}\cdot\left(\mathbf{p}-\frac{e\mathbf{A}}{c}\right)\right]\left[\frac{c^2}{E-eA_0+mc^2}\right]\left[\boldsymbol{\sigma}\cdot\left(\mathbf{p}-\frac{e\mathbf{A}}{c}\right)\right]\psi_A=\left(E-eA_0-mc^2\right)\psi_A. \tag{1.102}$$

We now assume that

$$E\approx mc^2,\quad |eA_0|\ll mc^2, \tag{1.103}$$

and define the energy difference measured from mc^2 by introducing the variables,

$$\tilde{E}=E-mc^2. \tag{1.104}$$

With this rescaling the denominator on the left-hand side of Eq. (1.102) can be expanded as

$$\frac{c^2}{E-eA_0+mc^2}=\frac{1}{2m}\left[\frac{2mc^2}{2mc^2+\tilde{E}-eA_0}\right]=\frac{1}{2m}\left[1-\frac{\tilde{E}-eA_0}{2mc^2}+\cdots\right], \tag{1.105}$$

and considering only the leading term in Eq. (1.105), we can write Eq. (1.102) as

$$\frac{1}{2m}\left[\boldsymbol{\sigma}\cdot\left(\mathbf{p}-\frac{e\mathbf{A}}{c}\right)\right]\left[\boldsymbol{\sigma}\cdot\left(\mathbf{p}-\frac{e\mathbf{A}}{c}\right)\right]\psi_A=\left(\tilde{E}-eA_0\right)\psi_A \tag{1.106}$$

The term on the left-hand side can be further simplified as

$$\begin{aligned}\frac{1}{2m}\boldsymbol{\sigma}\cdot\left(\mathbf{p}-\frac{e\mathbf{A}}{c}\right)&\boldsymbol{\sigma}\cdot\left(\mathbf{p}-\frac{e\mathbf{A}}{c}\right)\\&=\frac{1}{2m}\left(\mathbf{p}-\frac{e\mathbf{A}}{c}\right)^2+\frac{i}{2m}\boldsymbol{\sigma}\cdot\left[\left(\mathbf{p}-\frac{e\mathbf{A}}{c}\right)\times\left(\mathbf{p}-\frac{e\mathbf{A}}{c}\right)\right]\\&=\frac{1}{2m}\left(\mathbf{p}-\frac{e\mathbf{A}}{c}\right)^2-\frac{e\hbar}{2mc}\boldsymbol{\sigma}\cdot\mathbf{B},\end{aligned}$$

where we have used the identity

$$\mathbf{p}\times\mathbf{A}=-i\hbar(\boldsymbol{\nabla}\times\mathbf{A})-\mathbf{A}\times\mathbf{p}, \tag{1.107}$$

recalling the formula $(\sigma\cdot\mathbf{A})(\sigma\cdot\mathbf{B})=\mathbf{A}\cdot\mathbf{B}+i\boldsymbol{\sigma}\cdot(\mathbf{A}\times\mathbf{B})$. Eq. (1.106) eventually transforms to

$$\left(\frac{1}{2m}\boldsymbol{\sigma}\cdot\left(\mathbf{p}-\frac{e\mathbf{A}}{c}\right)-\frac{e\hbar}{2mc}\boldsymbol{\sigma}\cdot\mathbf{B}+eA_0\right)\psi_A=\tilde{E}\psi_A. \tag{1.108}$$

From Eq. (1.100), we noted that ψ_B is smaller than ψ_A by approximately $|\mathbf{p} - e\mathbf{A}/c| \approx v/2c$ based on the condition that Eq. (1.103) is valid. For this reason ψ_A and ψ_B are known as the large and small components of the Dirac spinor wave function, respectively.

Now we consider the second term in Eq. (1.105) and set $\mathbf{A} = 0$ for simplicity. The Schrodinger equation for the non-relativistic case is given by

$$\tilde{H}_A \psi_A = \tilde{E} \psi_A, \tag{1.109}$$

where

$$\tilde{H}_A = (\boldsymbol{\sigma} \cdot \mathbf{p}) \frac{1}{2m} \left(1 - \frac{\tilde{E} - eA_0}{2\mathrm{mc}^2} \right) (\boldsymbol{\sigma} \cdot \mathbf{p}) + eA_0. \tag{1.110}$$

The probabilistic interpretation of the Dirac theory implies that

$$\int \left(\psi_A^\dagger \psi_A + \psi_B^\dagger \psi_B \right) d^3x = 1 \tag{1.111}$$

where ψ_B is already of the order of v/c. We cannot identify ψ_A with the full wave function ψ anymore even if we consider the first and second term in Eq. (1.105), because a fraction of the probability density

$$\int \psi_A^\dagger \left(1 + \frac{\mathbf{p}^2}{4m^2c^2} \right) \psi_A d^3x \propto (v/c)^2, \tag{1.112}$$

has flowed into $\psi_B^\dagger \psi_B$. According to Eq. (1.100),

$$\psi_B \approx \frac{\sigma \cdot \mathbf{p}}{2mc} \psi_A \tag{1.113}$$

This suggests that we should replace ψ_A by a new two-component wave function define by

$$\Psi = \Omega \psi_A, \tag{1.114}$$

where

$$\Omega = 1 + \left(\mathbf{p}^2 / 8m^2c^2 \right), \tag{1.115}$$

which is correctly normalized to order $(v/c)^2$ since

$$\int \Psi^\dagger \Psi d^3x \approx \int \psi_A^+ \left[1 + \left(\mathbf{p}^2/4m^2c^2\right)\right] \psi_A d^3x. \tag{1.116}$$

Multiplying Eq. (1.109) from the left by $\Omega^{-1} = 1 - \left(\mathbf{p}^2/8m^2c^2\right)$, we obtain

$$\Omega^{-1}\tilde{H}_A\Omega^{-1}\Psi = \tilde{E}\Omega^{-2}\Psi. \tag{1.117}$$

We obtain from Eq. (1.117), up to order $(v/c)^2$

$$\left[\frac{\mathbf{p}^2}{2m} + eA_0 - \left\{\frac{\mathbf{p}^2}{8m^2c^2}, \left(\frac{\mathbf{p}^2}{2m} + eA_0\right)\right\} \frac{(\sigma\cdot\mathbf{p})}{2m}\left(\frac{\tilde{E} - eA_0}{2mc^3}\right)(\boldsymbol{\sigma}\cdot\mathbf{p})\right]\Psi = \tilde{E}\left(1 - \frac{\mathbf{p}^2}{4m^2c^2}\right)\Psi. \tag{1.118}$$

Now we can write, $\tilde{E}\mathbf{p}^2$ as $\frac{1}{2}\left\{\tilde{E}, \mathbf{p}^2\right\}$, we obtain

$$\left[\frac{\mathbf{p}^2}{2m} + eA_0 - \frac{\mathbf{p}^4}{8m^3c^2} - \frac{1}{8m^2c^2}\left(\left\{\mathbf{p}^2, \left(\tilde{E} - eA_0\right)\right\} - 2(\boldsymbol{\sigma}\cdot\mathbf{p})\left(\tilde{E} - eA_0\right)(\boldsymbol{\sigma}\cdot\mathbf{p})\right)\right]\Psi = \tilde{E}\Psi. \tag{1.119}$$

Generally, for operators A and B, we have the commutation

$$\left\{A^2, B\right\} - 2ABA = [A, [A, B]]. \tag{1.120}$$

Setting $\boldsymbol{\sigma}\cdot\mathbf{p} = A$ and $\tilde{E} - eA_0 = B$, we can define

$$\left[\boldsymbol{\sigma}\cdot\mathbf{p}, \left(\tilde{E} - eA_0\right)\right] = -ie\hbar\boldsymbol{\sigma}\cdot\mathbf{E} \tag{1.121}$$

and

$$[\boldsymbol{\sigma}\cdot\mathbf{p}, -ie\hbar\boldsymbol{\sigma}\cdot\mathbf{E}] = -e\hbar^2\boldsymbol{\nabla}\cdot E - 2e\hbar\boldsymbol{\sigma}\cdot(\mathbf{E}\times\mathbf{p}), \tag{1.122}$$

which are valid as $\nabla\cdot\mathbf{A_0} = -\mathbf{E}$ and $\nabla\times\mathbf{E} = 0$. Using Eqs. (1.120)–(1.122), we finally obtain

$$\left[\frac{\mathbf{p}^2}{2m} + eA_0 - \frac{\mathbf{p}^4}{8m^3c^2} - \frac{e\hbar\sigma\cdot(\mathbf{E}\times\mathbf{p})}{4m^2c^2} - \frac{e\hbar^2}{8m^2c^2}\nabla\cdot\mathbf{E}\right]\Psi = \tilde{E}\Psi, \tag{1.123}$$

where the first and second terms represent the usual parts of the non-relativistic Hamiltonian. The third term captures the relativistic correction to the kinctic energy, the fourth term represents the SOC, and the final part is a potential-induced energy shift. In following sections, we will be more concerned with the SOC term.

1.1.3 Quantum spin Hall effect

There exist different states of matter in the quantum world, for example, crystalline solids, ferromagnets, and superconductors. As we already discussed in Sec. 1.0.8, that a new topological state of quantum matter in condensed matter systems was discovered in the 1980s called the integer and fractional QHE. Both of these effects exist only in the presence of large magnetic fields. The search for topological states of matter that do not require magnetic fields has become a central goal for condensed matter physics. Most recently, a new class of topological states has emerged, called quantum spin Hall (QSH) states. The quantum spin Hall effect (QSHE) is topologically distinct from all other known states of quantum matter and in contrast to the QHE, the QSHE can exist without any external magnetic field and TR invariant. The QSH originates from the coupling of the charge and spin currents due to spin-orbit interaction. More details about the QSHE are coming in the following section.

1.1.4 Topological insulators in two dimensions

Topological insulators (TIs) are quantum materials that behave like bulk insulators (BIs) in their bulk but there exist topologically protected metallic surfaces with massless Dirac-type band structures that are responsible for the most unique and exotic electronic and optical properties [21, 28, 48]. The existence of the topological robust edge states in the IQHE is one of the most dominant points of view in condensed matter physics. The topological classifications of matter

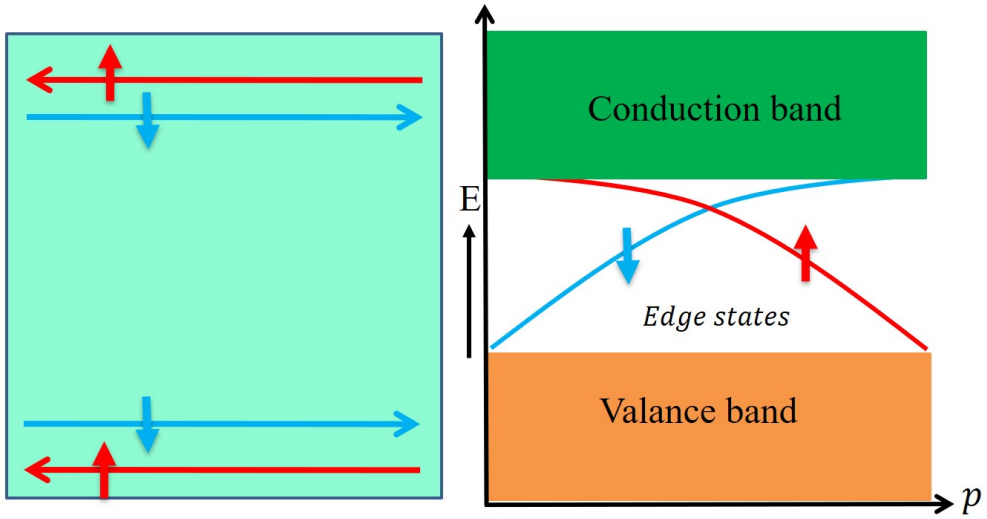

Figure 1.11: Representation of helical edge states in a two-dimensional topological insulator.

triggered physicists to search for other theoretical models which could give rise to exotic topological edge states. For the first time in 1988 Haldane proposed a model, which states that, unlike the quantum Hall systems, there may also exist topological edge states even in a zero magnetic field, that is without breaking the TRS. This effect is known as the quantum anomalous Hall effect (QAHE). It is anomalous because no external magnetic field is required for the existence of edge states. Such a system is an example of a topological insulator.

In 2005, Kane and Mele proposed in a model [15] originally meant for graphene that the existence of topological edge states in a zero magnetic field is due to the intrinsic spin-orbit coupling (SOC) in TI materials, and the SOC in the system can be viewed as an intrinsic effective magnetic field B_{eff} that points in the opposite directions for the spin up and spin down species, as illustrated in Fig. 1.11. Furthermore, the SOC opens up an energy gap Δ at the Dirac points in the band structure. Another perspective is that the QAHE is a consequence of non-zero Berry curvature in momentum space and having non-zero Chern numbers. In

other words, the quantum system behaves like bulk insulators (BIs) in their bulk but there exists a topologically gapless spectrum of chiral edge states with massless Dirac-type band structure.

The two spin subsystems can be viewed as two copies of the Haldane Hamiltonian with a gapless edge mode and having different signs of the mass term for the two spin species as shown in Fig. 1.12. The two counter-propagating edge states of an opposite spin result in zero Chern number and preservation of TRS. As depicted in Fig. 1.12, the locking between the spin and momentum directions is referred as helicity. The pair of helical edge modes gives rise to a spin current at the boundary and form a Kramers doublet with the energy-momentum dispersions crossing in the bulk band gap for different topological systems. Such type of a system is called quantum spin Hall insulator (QSHI) and represents a 2D topological insulator (TI).

In 2D TIs, the helical edge modes are available in both directions that is a spin-up fermion cannot backscatter into the counter-propagating channel without a spin-flip. In other words, the scattering between them is forbidden for any single-particle scattering and these edge modes are robust against TRS preserving impurities. The backscattering is only permissible in the presence of a magnetic impurity. This helical protection leads to robustness against deformations, which is a hallmark of topological states. The topological Chern number of the bulk 2D topological material tells us how many such 1D, chiral spin currents there have to be at the surface of the quantum spin Hall system. A remarkable property of a TI is that the total Chern number must be zero for the system.

Now to distinguish the TI (non-trivial) from an ordinary band insulator (trivial) another topological index can be used. The topological index is a $\mathcal{Z}_2$ classification, which is non-zero for the non-trivial and vanishes for trivial. If there is an even

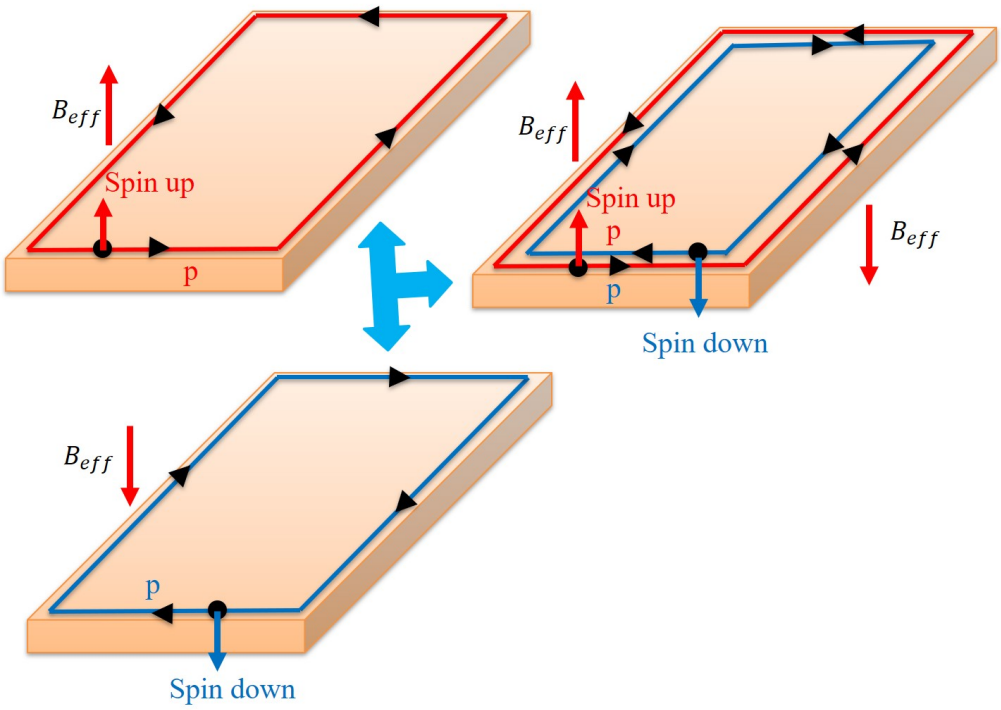

Figure 1.12: Representation of helical edge states in quantum spin Hall system.

(odd) number of band crossings at the edge then the system is trivial (non-trivial). In other words, the topological index ν takes the values 0 and 1 for the trivial and non-trivial phases, respectively.

1.1.5 From two to three dimensions

Topological protected helical edge states are one of the hottest topics in condensed matter physics right now. Even though we have introduced a 2D QSHI as an example of a TI. The term topological insulator was first introduced with reference to the 3D systems [56]. After the discovery of 2D TIs, theorists realized that the formalism for 2D topological phases with broken TRS could be extended to 3D systems as well [15, 57]. Three-dimensional topological insulators (TIs) are quantum materials that behave like band insulators (BIs) in their bulk but there exist

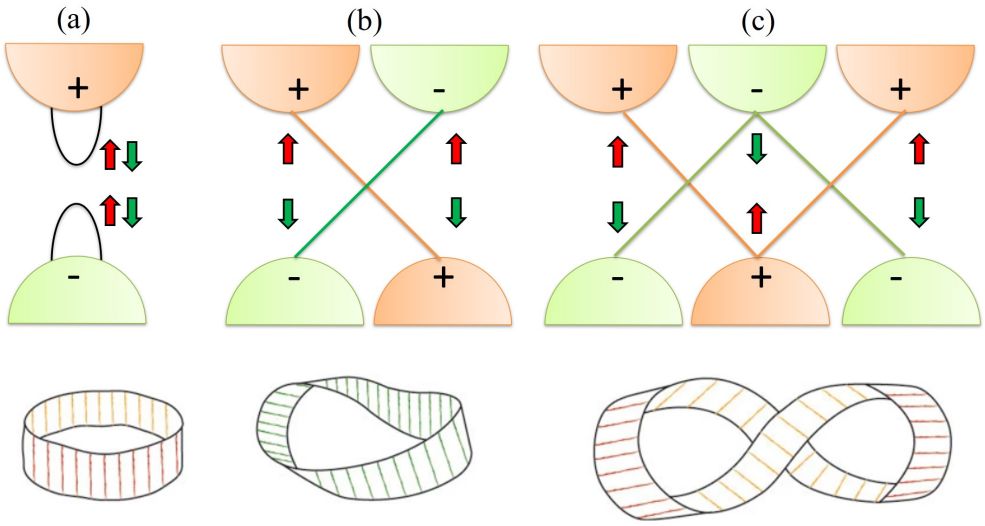

Figure 1.13: (a) The conduction and valence bands of a 3D solid. The shaded regions represent the bands in the bulk while the black lines are the bands at the surface of the 3D solid. The conduction (valence) band is symmetric (antisymmetric). (b) The degeneracy of the electron spins is lifted due to the SOC. The conduction band becomes antisymmetric and the valence band becomes symmetric (+). The red and blue lines are the edge states at the boundary of the bands. Here backscattering is not possible. (c) Further increasing the SOC leads to more changes and the electrons at the edges can be backscattered. The purpose of the Möbius strips indicates the number of topological twists in the band structure.

topologically protected metallic surfaces with massless Dirac-type band structures that are responsible for most unique and exotic electronic and optical properties [21, 48].

In Fig. 1.13(a), we depict the conduction and valence bands of a typical 3D solid. The red and green shaded regions represent the bands in the bulk and the black lines are the bands at the surface of the solid. The conduction band is symmetric while the valence band is anti-symmetric. As already mentioned, the SOC opens up a gap and lifts the degeneracy of the electron spins as illustrated in Fig. 1.13(b). The conduction band becomes antisymmetric (−) and the valence band becomes symmetric (+) for positive momenta. At boundaries, the changes

produced by SOC can be even more dramatic and as a result, the conduction and valence bands cross over once (or an odd number of times). The flow of charge is dissipationless as it is not possible for electrons to be backscattered, which is a distinguishing characteristic of the odd states.

To characterize 3D TI, we require four topological $\mathcal{Z}_2$ invariants namely $(\nu_0; \nu_1; \nu_2; \nu_3)$. A TI can be classified on the bases of ν_0, if $\nu_0 = 1$ ($\nu_0 = 0$), then the 3D TI is strong (weak). On the other hand, $\nu_2 = 1$ corresponds to a TI, whereas $\nu_2 = 0$ corresponds to a trivial insulator. Further, increasing the strength of the SOC result in more changes. If we look at Fig. 1.13(c), it is clear that electrons can be backscattered without flipping their spin in this system as the conduction and valence bands cross over twice or there may exist an even number of twists.

1.1.6 Three dimensional hybridized topological insulator

Three-dimensional hybridized topological insulators support protected electronic states characterized by an integer topological $\mathcal{Z}_2$ invariant for the topological electronic structure in momentum space on the surface of bulk material as shown in Fig. 1.14. The Dirac-like band structure of the surface states is robust against perturbations of the system parameters, as they are protected by topological properties of the bulk quantum mechanical wave functions. Time-reversal symmetry (TRS) in these 3D TI materials guarantees the pairing of top and bottom Dirac surface states (SSs) [21, 57]. These characteristic SSs have a topological origin and are potentially useful for the design of nano-scale devices in spintronics and practical applications in quantum computations [58, 59]. The topologically protected SSs of a TI thin film has a finite decay length (also called the penetration depth of the SSs) over which the SSs decay into the bulk region. As the thickness L of the TI thin film becomes comparable to, or smaller than, the penetration depth, quantum tunneling between SSs occurs due to which the top and bottom SSs hybridize to open up an energy gap Δ_H at the Dirac points [60, 61]. This

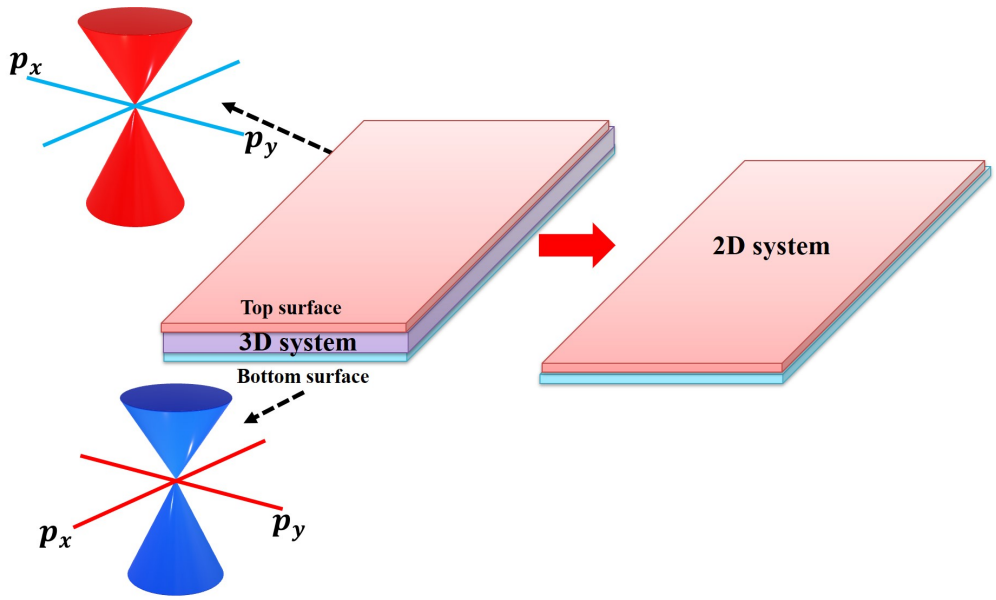

Figure 1.14: Schematic of a 3D TI with the top (Red) and bottom (Blue) surface states Dirac systems and of its quasi-2D counterpart (right).

can happen for 1 to 5 quintuple layers with a thickness of the order of L =5 nm [62, 63]. In Chapter 3, we will introduce the model Hamiltonian for the hybridized topological insulator thin films in the presence of a magnetic field to explore the magneto-optic response.

1.1.7 Concluding remarks

In this chapter, we briefly discussed quantum materials which is a broad term in condensed matter physics. To set the stage for the 2D quantum materials which is the main theme of this thesis, we started with the band topology. We found that the key role players in topological band theory are the Berry phase and topological invariant. We started from the classical Hall effect and finally derived the quantized Hall resistivity ρ_{xy} and connected it to the topological invariant. In the next chapter, we will discuss the tight-binding Hamiltonian of the graphene

family and will derive the energy dispersion relation of these materials. We will use the low energy Hamiltonian and will find out the quantization of Landau levels in the presence of a magnetic field in graphene, silicene, and three-dimensional hybridized topological insulator thin films.

Chapter 2

Electronic properties of 2D quantum materials

With the brief introduction to some basic concepts in condensed matter physics presented in the preceding chapter, we are ready to explore the interesting physics of several low-dimensional systems. In this chapter, we will discuss the electronic properties of the graphene family. We will describe how the topological phase transitions can be modulated by external electric or irradiating circularly polarized light. We will also derive the energy dispersion relations and eigenstates, which are useful for the determination of optical conductivity. Finally, we show how the magnetic field modifies the dispersion relations.

2.1 Introduction

Carbon is the most important and second-most abundant element on earth. Three-dimensional structures of carbon consist of diamond and graphite while the lower dimensional allotropes of carbon are fullerenes, nanotubes, and graphene. In a remarkable experimental feat back in 2004, Novoselov *et.al* successfully isolated a monolayer of graphite [33] which further catalyzed an ever-expanding research field.

The discovery of 2D materials has also stimulated growing interest in silicene [64], the silicon analog of graphene. Stable silicene can be experimentally synthesized [24]. There are many electronic and physical similarities between graphene and silicene as both are found in the same group of the periodic table. The major difference is that silicene has a large SOI with an electrically tunable bandgap. Just like silicene, germanene and tinene also possess stable honeycomb lattice structures [24, 25]. Due to the relatively large SOI, these materials have buckled structures, providing a mass to the otherwise massless Dirac fermions. In silicene [65], germanene [66] and tinene [67], the values of Δ_{so} have been predicted to lie in the range 1.55–7.9 meV, 24–93 meV, and 100 meV respectively. Subsequently, the interaction of an external electric field with silicene, germanene, and the tinene-substrate system renders the Dirac mass controllable at the K and K' points, which leads to various topological phase transitions [68].

Throughout this chapter, our primary interest will be on low-energy Dirac physics of 2D quantum material systems based on the graphene Hamiltonian. We start from the tight-binding Hamiltonian and derive the low energy dispersion relation of graphene and silicene. We also will explore the Landau levels quantization inside these materials. This Chapter will serve as a prelude to our theoretical studies and magneto-optic simulations in subsequent chapters.

2.2 Electronic properties graphene

Graphene is a single layer atomic sheet of carbon atoms that are periodically arranged in a honeycomb lattice structure. In graphene carbon atoms are connected in a hexagonal structure with sp^2 hybridized C-C covalent bonding, as shown in Fig. 2.1. There are six electrons in each carbon atom in which the two electrons in the s shell are inert for electronic interactions. From the four outer-shell electrons, three electrons occupy sp^2 orbitals forming three σ bonds as shown in the diagram.

The σ bonds are strong covalent bonds that impart to the material's structural rigidity and energetic stability. The remaining outer-shell electron of each carbon atom which occupies a p_z orbital forms a π bond.

We investigate the low energy dynamics of graphene by assuming the tight-binding approximation and taking into account the nearest-neighbor hopping. The Hamiltonian in the second quantized form is then given by,

$$H_{TB} = -|t| \sum_{j} \sum_{\delta=1}^{3} \left(a^{\dagger}_{j+\delta} b_j + b^{\dagger}_{j} a_{j+\delta} \right), \tag{2.1}$$

where $a^{\dagger}_{j}$ and a_j denote the fermion creation and annihilation operators for the electron, respectively in the sublattice A whose position is demonstrated by δ_j, where $j = 1, 2, 3$. Similarly $b^{\dagger}_{j}$ and b_j are the fermion creation and annihilation

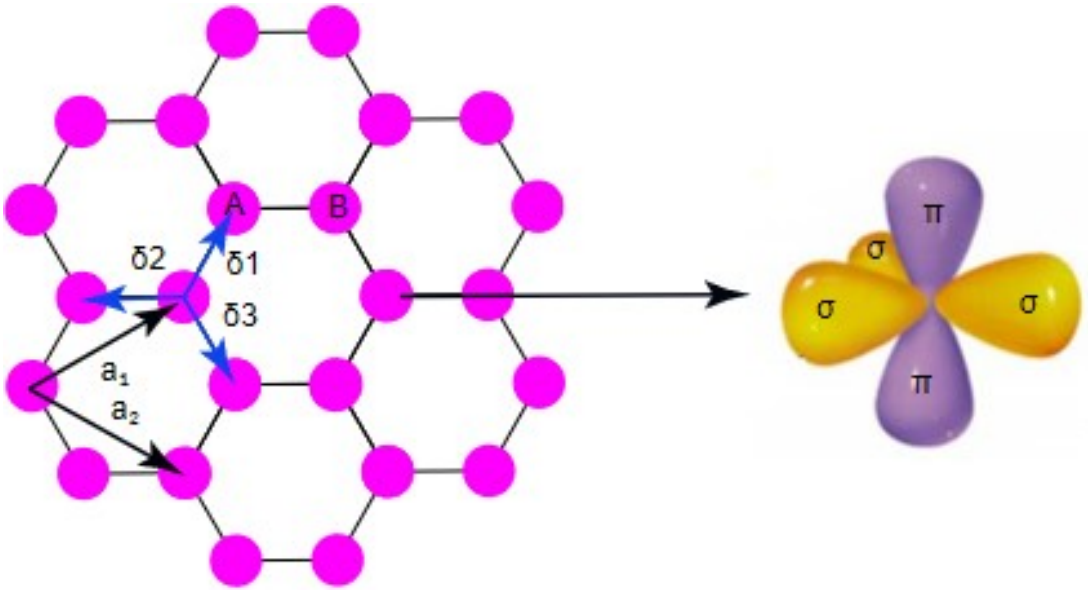

Figure 2.1: The basis vectors in the hexagonal lattice of graphene with primitive vectors a_1 and a_2 ($a = 1.42$ A) and the position vectors δ_1, δ_2 and δ_3 are position vectors. On the right, we also show the three sp^2 orbitals forming σ bonds and a p_z orbital forming a π bond across neighbours.

operators in the sublattice B located at the site δ_j. Fourier expanding the creation and annihilation operators to the reciprocal space, we obtain

$$a_j = \frac{1}{\sqrt{N}} \sum_k e^{i\mathbf{k}\cdot\mathbf{j}} a_{\mathbf{k}}, \qquad b_j = \frac{1}{\sqrt{N}} \sum_k e^{i\mathbf{k}\cdot\mathbf{j}} b_{\mathbf{k}}, \tag{2.2}$$

where N denotes the number of unit cells. Let's consider the first term,

$$\begin{aligned} -|t| \sum_j \sum_{\delta=1}^{3} \left(a_{j+\delta}^{\dagger} b_j \right) &= -|t| \sum_{jkk'} \sum_{\delta=1}^{3} \left(e^{i\mathbf{k}\cdot(\mathbf{j}+\delta)} e^{-i\mathbf{k}'\cdot\mathbf{j}} a_k^{\dagger} b_{k'} \right) \\ &= -|t| \sum_{jkk'} \sum_{\delta=1}^{3} \left(e^{i(\mathbf{k}-\mathbf{k}')\cdot\mathbf{j}} e^{i\mathbf{k}\cdot\delta} a_k^{\dagger} b_{k'} \right). \end{aligned} \tag{2.3}$$

Similarly, the second term of the Hamiltonian after Fourier transormation assumes the form

$$\begin{aligned} -|t| \sum_j \sum_{\delta=1}^{3} \left(b_j^{\dagger} a_{j+\delta} \right) &= -|t| \sum_{jkk'} \sum_{\delta=1}^{3} \left(e^{i\mathbf{k}\cdot\mathbf{j}} e^{-i\mathbf{k}'\cdot(\mathbf{j}+\delta)} b_k^{\dagger} a_{k'} \right) \\ &= -|t| \sum_{jkk'} \sum_{\delta=1}^{3} \left(e^{i(\mathbf{k}-\mathbf{k}')\cdot\mathbf{j}} e^{-i\mathbf{k}'\cdot\delta} b_k^{\dagger} a_{k'} \right). \end{aligned} \tag{2.4}$$

Substituting Eqs. (2.3) and (2.4) into Eq. (2.1), we obtain

$$H_{TB} = -|t| \sum_{\mathbf{jkk'}} \sum_{\delta=1}^{3} \left(e^{i(\mathbf{k}-\mathbf{k}')\cdot\mathbf{j}} e^{i\mathbf{k}\cdot\delta} a_k^{\dagger} b_{k'} + e^{i(\mathbf{k}-\mathbf{k}')\cdot\mathbf{j}} e^{-i\mathbf{k}'\cdot\delta} b_k^{\dagger} a_{k'} \right). \tag{2.5}$$

By making use of following useful identity

$$\sum_j e^{i(\mathbf{k}-\mathbf{k}')\cdot\mathbf{j}} = \delta_{kk'}, \tag{2.6}$$

the Hamiltonian can be rewritten as

$$\begin{aligned} H_{TB} &= -|t| \sum_{\mathbf{k}} \sum_{\delta=1}^{3} \left(\alpha a_k^{\dagger} b_k + \alpha^* b_k^{\dagger} a_k \right) \\ &= -|t| \sum_{\mathbf{k}} \sum_{\delta=1}^{3} \left(\alpha a_k^{\dagger} b_k \right) + -|t| \sum_{\mathbf{k}} \sum_{\delta=1}^{3} \left(\alpha^* b_k^{\dagger} a_k \right) \\ &= \sum_{\mathbf{k}} \begin{pmatrix} a_k^{\dagger} & b_k^{\dagger} \end{pmatrix} \begin{pmatrix} 0 & -|t|\alpha \\ -|t|\alpha^* & 0 \end{pmatrix} \begin{pmatrix} a_k \\ b_k \end{pmatrix}, \end{aligned} \tag{2.7}$$

where we have suppressed the $\vec{k}$ dependence of α, i.e.,

$$\alpha = \alpha(\vec{k}) = \sum_{\delta=1}^{3} e^{i\mathbf{k}\cdot\delta} = \left(e^{i\mathbf{k}\cdot\boldsymbol{\delta_1}} + e^{i\mathbf{k}\cdot\boldsymbol{\delta_2}} + e^{i\mathbf{k}\cdot\boldsymbol{\delta_3}}\right). \tag{2.8}$$

The eigenvalues of the matrix given in Eq. (2.7) are

$$E^{\pm}(\mathbf{k}) = \pm|t|\sqrt{\alpha^2}, \tag{2.9}$$

which provides the dispersion relation of the Dirac fermions in graphene, where $+$ and $-$ signs denote the conduction and valence band, respectively. The position vectors are

$$\vec{\delta}_1 = \frac{a}{2}\left(1, \sqrt{3}\right) \tag{2.10}$$

$$\vec{\delta}_2 = \frac{a}{2}\left(1, -\sqrt{3}\right) \tag{2.11}$$

$$\vec{\delta}_3 = -a\,(1, 0)\,, \tag{2.12}$$

where a is lattice constant. Based on the unit cell translations $\vec{a}_1$ and $\vec{a}_2$, the reciprocal lattice vectors are given by

$$b_1 = \frac{2\pi}{3a}\left(\sqrt{3}, 1\right) \quad \text{and} \quad b_2 = \frac{2\pi}{3a}\left(\sqrt{3}, -1\right). \tag{2.13}$$

Eq. (2.8) can therefore be written as

$$\begin{aligned}
\alpha\,(k) &= \left(e^{i\mathbf{k}\cdot\boldsymbol{\delta_1}} + e^{i\mathbf{k}\cdot\boldsymbol{\delta_2}} + e^{i\mathbf{k}\cdot\boldsymbol{\delta_3}}\right) \\
&= \left(e^{i(k_x/2+\sqrt{3}k_y/2)a} + e^{i(k_x/2-\sqrt{3}k_y/2)a} + e^{-ik_x a}\right) \\
&= e^{-ik_x a}\left(e^{i3k_x a/2}e^{i\sqrt{3}k_y a/2} + e^{i3k_x a/2}e^{-i\sqrt{3}k_y a/2} + 1\right) \\
&= e^{-ik_x a}\left(1 + 2e^{i3k_x a/2}\cos(\sqrt{3}k_y a/2)\right),
\end{aligned} \tag{2.14}$$

from which we can obtain the modulus square

$$\begin{aligned}
|\alpha\,(k)|^2 &= \left(1 + 2e^{\frac{i3k_x a}{2}}\cos\frac{\sqrt{3}k_y a}{2}\right)\left(1 + 2e^{\frac{-i3k_x a}{2}}\cos\frac{\sqrt{3}k_y a}{2}\right) \\
&= \left(1 + 4\cos\left(\frac{3k_x a}{2}\right)\cos\left(\frac{\sqrt{3}k_y a}{2}\right) + 4\cos^2\left(\frac{\sqrt{3}k_y a}{2}\right)\right).
\end{aligned} \tag{2.15}$$

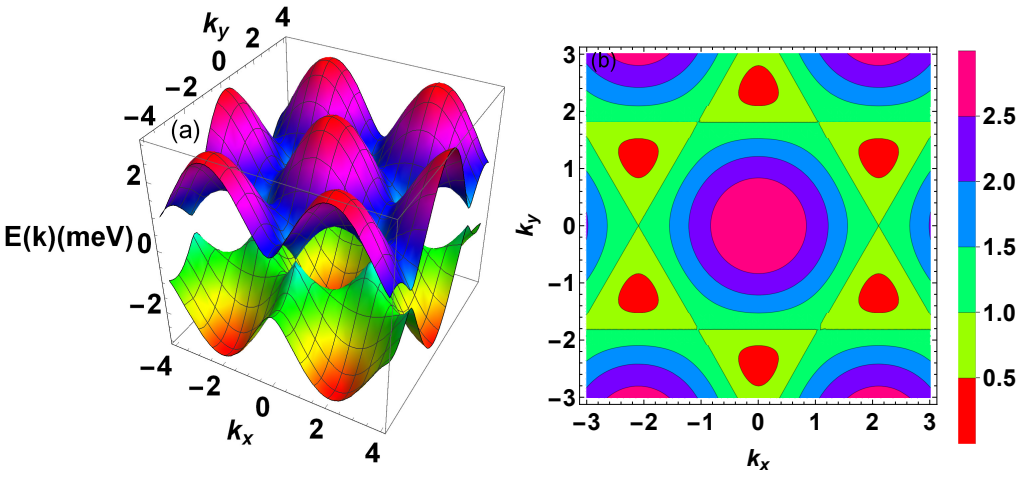

Figure 2.2: Linear dispersion relation of graphene.: (a) Band structure of monolayer graphene. (b) Contour plot of band structure in (a).

The energy bands are therefore given by

$$E_{\pm}(k) = \pm|t|\sqrt{1 + 4\cos\left(\frac{3k_x a}{2}\right)\cos\left(\frac{\sqrt{3}k_y a}{2}\right) + 4\cos^2\left(\frac{\sqrt{3}k_y a}{2}\right)}. \tag{2.16}$$

A plot of the low-energy band structure of the graphene around the first Brillouin zone is shown in Figs. 2.2(a) and (b) showing three-dimensional (3D) and contour plots respectively.

2.2.1 Momentum space description

The coordinates of the so-called K and K' Dirac points in the first Brillouin zone (BZ) are given by

$$K = \frac{2\pi}{3a}\left(1, 1/\sqrt{3}\right), \quad K' = \frac{2\pi}{3a}\left(1, -1/\sqrt{3}\right). \tag{2.17}$$

At the Dirac points the energy bands cross and the gap closes as illustrated in Fig. 2.3. These points in k-space refer to as the valleys. We will expand as this concept in due course. To extract the low energy physics, we will expand the Hamiltonian around K and K' points. Let's look at the behavior of $\alpha(k)$ in the

vicinity of the Dirac point K. Defining the relative momentum $\mathbf{q} = \mathbf{k} - \mathbf{K}$, we can write α_k in terms of $\mathbf{q}$ as

$$\begin{aligned} \alpha(\mathbf{K}+\mathbf{q}) &= e^{-iK_x a} e^{-iq_x a}\left[1 + 2e^{i3(K_x+q_x)a/2}\cos\left(\frac{\sqrt{3}\,(K_y+q_y)\,a}{2}\right)\right] \\ &= e^{-iK_x a} e^{-iq_x a}\left[1 - 2e^{3iaq_x/2}\cos\left(\frac{\pi}{3} + \frac{\sqrt{3}a}{2}q_y\right)\right]. \end{aligned} \tag{2.18}$$

Expanding the above equation to first order about $\mathbf{q} = \mathbf{0}$, we obtain

$$\alpha(\mathbf{K}+\mathbf{q}) = -ie^{-iK_x a}\frac{3a}{2}(\xi q_x + iq_y). \tag{2.19}$$

For convenience, we ignore the phase $ie^{-iK_x a}$, as it carries no physical significance. We thus have

$$\alpha(\mathbf{K}+\mathbf{q}) = -\frac{3a}{2}(\xi q_x + iq_y). \tag{2.20}$$

About the Dirac point $\mathbf{K}$, the Hamiltonian can be approximated as

$$\mathbf{H}(\mathbf{K}+\mathbf{q}) = v_F\begin{pmatrix} 0 & \xi q_x + iq_y \\ \xi q_x - iq_y & 0 \end{pmatrix}. \tag{2.21}$$

Similarly, for the K' point the relative momentum is $\mathbf{q} = \mathbf{k} - \mathbf{K}'$. Expanding α_k about the K', we find

$$\alpha(\mathbf{K}+\mathbf{q}) = -\frac{3a}{2}(\xi q_x - iq_y), \tag{2.22}$$

so for the K' point we can write the Hamiltonian as

$$\mathbf{H}(\mathbf{K}'+\mathbf{q}) = v_F\begin{pmatrix} 0 & \xi q_x - iq_y \\ \xi q_x + iq_y & 0 \end{pmatrix}. \tag{2.23}$$

The famous 2D massles Dirac Hamiltonian of graphene is given by

$$\hat{H}_\xi = v_F\hat{\tau}\cdot q = v_F(\xi\hat{\tau}_x q_x + \hat{\tau}_y q_y) = \hbar v_F(\xi\hat{\tau}_x k_x + \hat{\tau}_y k_y), \tag{2.24}$$

where $\vec{\tau}_x$ and $\vec{\tau}_y$ are the Pauli matrices associated with the pseudospin of the system and $\xi = \pm 1$ corresponds to the valleys (K and K') in momentum space.

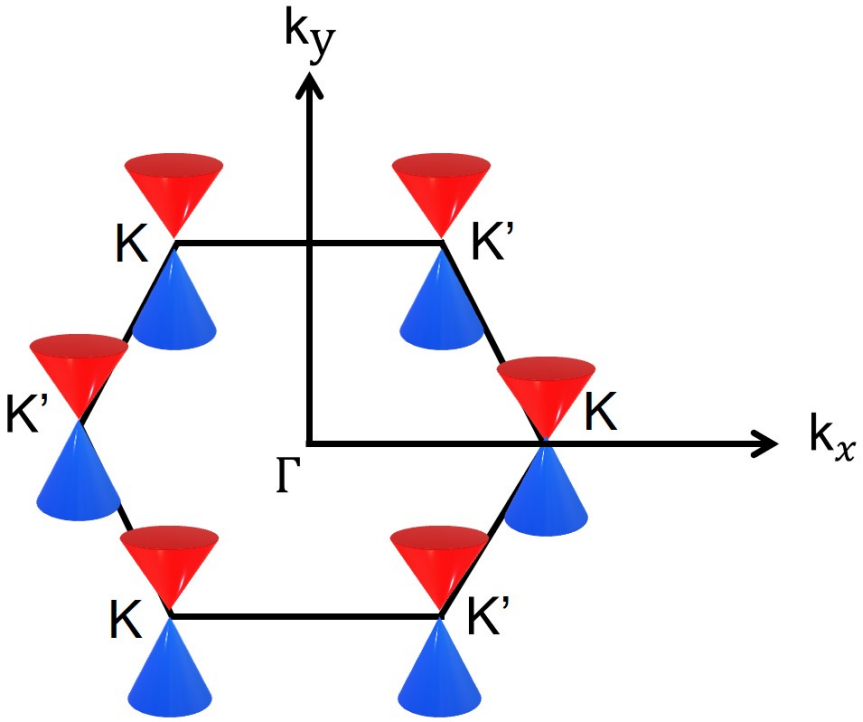

Figure 2.3: The first Brillouin zone of graphene. The cones indicate the K and K' valleys.

The notion of the valley represents the energy minima and extrema in the electronic band structure of graphene and is regarded as a new degree of freedom for electrons, additional to charge and spin. In the band structure of graphene, there are two valleys in the first Brillouin zone as shown in Fig. 2.2. These are known as the K and K' valleys. We can suppose the K valley as being "pseudospin up" and the K' valley as being "pseudospin down". The valley, just like the real spin, can also be used to encode and process information, this is now the burgeoning field of valleytronics [37]. In general for both valleys the Hamiltonian becomes

$$\hat{H}_\xi(\mathbf{k}) = \begin{pmatrix} 0 & \hbar v_F(\xi k_x - i k_y) \\ \hbar v_F(\xi k_x + i k_y) & 0 \end{pmatrix}. \tag{2.25}$$

The energy eigenvalues can be easily computed and are given by

$$E_\xi(k) = \pm \xi \hbar v_F |\mathbf{k}|, \tag{2.26}$$

where $+/-$ denotes the conduction/valence band.

2.2.2 Eigenfunctions of the graphene Hamiltonian

In order to obtain the eigen-states of the graphene Hamiltonian $\hat{H}_\xi(k)$, we can write

$$\xi k_x \pm i k_y = |k| e^{\pm i\xi\phi_k}, \quad k_x = |k|\cos\phi, \quad k_y = |k|\sin\phi \tag{2.27}$$

The 2D spinor wave function is given as

$$\Psi_{t\mathbf{k}}(\mathbf{r}) = \begin{pmatrix} \Psi_A \\ \Psi_B \end{pmatrix} \exp(\mathrm{i}\mathbf{k}\cdot\mathbf{r}). \tag{2.28}$$

Utilizing the eigenvalue equation for the K valley ($\xi = 1$), we arrive at

$$\hbar v_F \begin{pmatrix} 0 & k_x - ik_y \\ k_x + ik_y & 0 \end{pmatrix} \begin{pmatrix} \Psi_A \\ \Psi_B \end{pmatrix} = E \begin{pmatrix} \Psi_A \\ \Psi_B \end{pmatrix}, \tag{2.29}$$

which yields two coupled equations

$$(k_x - ik_y)\Psi_B = E\Psi_A \tag{2.30}$$

and

$$(k_x + ik_y)\Psi_A = E\Psi_B. \tag{2.31}$$

By developing the above equations we reach at

$$\Psi_B = \frac{(k_x + ik_y)}{E} = \frac{\hbar v_F (k_x + ik_y)}{\hbar v_F |\mathbf{k}|}\Psi_A. \tag{2.32}$$

$$\Psi_B = t\mathrm{e}^{i\phi_k}\Psi_A. \tag{2.33}$$

The corresponding momentum space pseudospinor eigenfunction becomes

$$\Psi_{t,k} = \begin{pmatrix} \Psi_A \\ \Psi_B \end{pmatrix} = \begin{pmatrix} 1 \\ t\mathrm{e}^{\mathrm{i}\phi_k} \end{pmatrix} \Psi_A$$

and the wave function is

$$\Psi(x,y) = \begin{pmatrix} \Psi_A(x,y) \\ \Psi_B(x,y) \end{pmatrix} = \begin{pmatrix} 1 \\ te^{i\phi_k} \end{pmatrix} \Psi_A e^{ik_x x + ik_y y}. \tag{2.34}$$

Normalizing the wave function, we finally obtain $\Psi_A = \frac{1}{\sqrt{2}L}$, wherc L^2 is the area of system: The wave function can be written as

$$\Psi(x,y) = \frac{1}{\sqrt{2}L} \begin{pmatrix} 1 \\ te^{i\phi_k} \end{pmatrix} \mathrm{e}^{ik_x x + ik_y y} \tag{2.35}$$

which in momentum space can be written as:

$$|\Psi_{\xi,t}(k)\rangle = \frac{1}{\sqrt{2}} \begin{pmatrix} 1 \\ te^{+i\xi\phi_k} \end{pmatrix}. \tag{2.36}$$

The index $t = \pm$ is the band index ($t = +1$ for the conduction band and $t = -1$ for the valence band). The preceding discussion describes the low-energy physics of graphene using a simple nearest-neighbor tight-binding Hamiltonian. In the following section, we will discuss the formation of Landau levels in the presence of a magnetic field.

2.2.3 Magnetic field effects in graphene

In this section we look at the dispersion relation of graphene in a perpendicular magnetic field in a similar fashion to Section 1.0.7, but here we are dealing with relativistic fermions. We apply a static uniform magnetic field B perpendicular to the graphene sheet along the z-direction and utilize the earlier description to determine the eigenstructure of this problem and derive the Landau levels (LLs). Introducing the Landau gauge for the magnetic vector potential $A = (-yB, 0, 0)$ and utilizing Peierl's substitution we can write,

$$\hbar k \to \hbar k + \frac{e}{c} A, \tag{2.37}$$

where e is the electronic charge of the electron, $c = 1$ is the speed of light and $\hbar k$ is the momentum of the Dirac fermions in the absence of B. Therefore for a single valley the Hamiltonian can be written as

$$\hat{H}_\xi = \begin{pmatrix} 0 & \hbar v_F \left(\xi \left(k_x - i\frac{eBy}{\hbar}\right) - ik_y\right) \\ \hbar v_F \left(\xi \left(k_x - i\frac{eBy}{\hbar}\right) + ik_y\right) & 0 \end{pmatrix}. \tag{2.38}$$

In terms of the spinors, we can define our wave function as

$$\Psi = \begin{pmatrix} \psi_A \\ \psi_B \end{pmatrix}. \tag{2.39}$$

Employing the Schrodinger equation $\hat{H}\Psi = E\Psi$, we obtain

$$\begin{pmatrix} 0 & \hbar v_F \left(\xi \left(k_x - i\frac{eBy}{\hbar}\right) - ik_y\right) \\ \hbar v_F \left(\xi \left(k_x - i\frac{eBy}{\hbar}\right) + ik_y\right) & 0 \end{pmatrix} \begin{pmatrix} \psi_A \\ \psi_B \end{pmatrix} = E \begin{pmatrix} \psi_A \\ \psi_B \end{pmatrix}. \tag{2.40}$$

It is convenient to define the two ladder operators as following

$$-i\frac{\sqrt{2}\hbar v_F}{l_B}\hat{a} = \hbar v_F \left(\left[k_x - \frac{eB}{\hbar}y\right] - ik_y\right) \tag{2.41}$$

and

$$i\frac{\sqrt{2}\hbar v_F}{l_B}\hat{a}^\dagger = \hbar v_F \left(\left[k_x - \frac{eB}{\hbar}y\right] + ik_y\right), \tag{2.42}$$

where $l_B = \sqrt{\hbar/(eB)}$ is the magnetic length. The Fock state of the harmonic oscillator is denoted by $|n\rangle$, where $n = 0, 1, 2.....$ These ladder operators satisfy the commutation relation $\left[\hat{a}, \hat{a}^\dagger\right] = 1$. Recalling, $\hat{a}|n\rangle = \sqrt{n}|n-1\rangle$ and $\hat{a}^\dagger|n\rangle = \sqrt{n+1}|n+1\rangle$. Our eigenvalue equation at the K point becomes

$$\begin{pmatrix} 0 & -i\frac{\sqrt{2}\hbar v_F}{l_B}\hat{a} \\ i\frac{\sqrt{2}\hbar v_F}{l_B}\hat{a}^\dagger & 0 \end{pmatrix} \begin{pmatrix} \psi_A \\ \psi_B \end{pmatrix} = E \begin{pmatrix} \psi_A \\ \psi_B \end{pmatrix}, \tag{2.43}$$

which yields the two equations

$$-i\frac{\sqrt{2}\hbar v_F}{l_B}\hat{a}\psi_B = E\psi_A \tag{2.44}$$

and

$$i\frac{\sqrt{2}\hbar v_F}{l_B}\hat{a}^\dagger\psi_A = E\psi_B. \tag{2.45}$$

Substituting Eq. (2.44) in Eq. (2.45), we obtain

$$i\frac{\sqrt{2}\hbar v_F}{l_B}\hat{a}^\dagger \frac{-i\frac{\sqrt{2}\hbar v_F}{l_B}\hat{a}\psi_A}{E} = E\psi_A \tag{2.46}$$

$$\frac{2\hbar^2 v_F^2}{l_B^2}\hat{a}^\dagger\hat{a}\psi_A = E\psi_A. \tag{2.47}$$

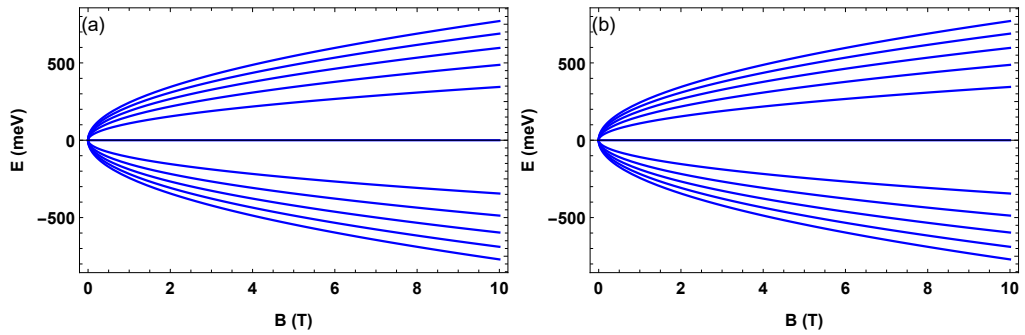

Figure 2.4: Landau levels evolution of graphene as a function of magnetic field B for $|n| \leq 5$, (a) for the K valley and (b) K' valley.

We can define $\hat{a}^\dagger \hat{a} = n$, so that $n|n\rangle = E|n\rangle$. Therefore for either of the two valleys, we obtain the low-energy LL dispersion of graphene

$$E_{n,t} = t\sqrt{2\hbar e v_F^2 |n|B}, \tag{2.48}$$

where $t = \text{sgn(n)}$ denotes the conduction/valence band.

Looking at Eq. (2.48), we noted that there are some striking differences and characteristics between the graphene relativistic LLs and those of the conventional (non-relativistic) LLs discussed in Section 1.0.7. A plot of the LL evolution with magnetic field B is shown in Figs. 2.4(a) and (b) for the K and K' valleys, respectively. The results are identical for both valleys. One of the remarkable differences is that unlike 2DEG the LLs in graphene are no longer equally spaced. Here, $E_{n,t} \propto \sqrt{n}$ and the level spacing decreases as n increases. The second difference is that the $n \neq 0$ LL scale as $\sqrt{B}$ while the $n = 0$ level is pinned at zero energy. The conduction and valence bands are mirror-symmetric with respect to the $E = 0$ axis.

2.2.4 The associated eigenfunctions of graphene in the presence of magnetic field

The wave function of the system in term of the two spinors is given as

$$\Psi = \begin{pmatrix} \psi_A \\ \psi_B \end{pmatrix}. \tag{2.49}$$

We can define the $A-B$ sublattice basis as: $\psi_B = \beta|n\rangle$, and $\psi_A = \alpha|m\rangle$. Applying the system Hamiltonian to ψ, we obtain

$$-i\frac{\sqrt{2}\hbar v_F}{l_B}\hat{a}\beta|n\rangle = E_{n,t}\alpha|m\rangle \tag{2.50}$$

and

$$i\frac{\sqrt{2}\hbar v_F}{l_B}\hat{a}^\dagger\alpha|m\rangle = E_{n,t}\beta|n\rangle. \tag{2.51}$$

From the above equation it is clear that $m = n-1$, and

$$\beta = it\alpha. \tag{2.52}$$

The wave function at the K point is given by

$$\Psi_K = |\bar{n}\rangle_K = \begin{pmatrix} \alpha|m\rangle \\ \beta|n\rangle \end{pmatrix}, \tag{2.53}$$

which upon normalization becomes

$$|\bar{n}\rangle_K = \frac{1}{\sqrt{2}}\begin{pmatrix} -it|n-1\rangle \\ |n\rangle \end{pmatrix}. \tag{2.54}$$

The zero-energy LL with $n = 0$ deserves special attention and to be treated separately. Indeed, for $n = 0$, the first component in Eq. (2.54) is zero. We find that the zero energy states at the K valley is entirely due to electrons from the B sublattice. In this case the solution of the eigenvalue equation yields an eigenvector

$$|0\rangle_K = \begin{pmatrix} 0 \\ |0\rangle \end{pmatrix}. \tag{2.55}$$

Similarly, for the K' valley, we obtain the associated wave functions as

$$|\bar{n}\rangle_{K'} = \frac{1}{\sqrt{2}}\begin{pmatrix} -it|n\rangle \\ |n-1\rangle \end{pmatrix}. \tag{2.56}$$

In summary, for the K and K' valleys, the eigen wave functions can be written as

$$|\bar{n}\rangle_{\xi=+1} = \begin{pmatrix} -i\alpha_{n,t}|n-1\rangle \\ \beta_{n,t}|n\rangle \end{pmatrix} \tag{2.57}$$

and

$$|\bar{n}\rangle_{\xi=-1} = \begin{pmatrix} -i\alpha_{n,t}|n\rangle \\ \beta_{n,t}|n-1\rangle \end{pmatrix}, \tag{2.58}$$

where $|n\rangle$ is an orthonormal Fock state of the harmonic oscillator, and $\alpha_{n,t}$ and $\beta_{n,t}$ are given by,

$$\alpha_{n,t} = \begin{cases} \frac{t}{\sqrt{2}}, & \text{if } n \neq 0 \\ \frac{1-\xi}{2}, & \text{if } n = 0 \end{cases} \tag{2.59}$$

and

$$\beta_{n,t} = \begin{cases} \frac{1}{\sqrt{2}}, & \text{if } n \neq 0 \\ \frac{1+\xi}{2}, & \text{if } n = 0. \end{cases} \tag{2.60}$$

We noted that the zero-energy states at the K valley are restricted to the sublattice B, whereas those at the K' valley have a non-vanishing value only on the sublattice A. For the K and K' valleys, the index ξ has been defined such that $\xi = +1$ and $\xi = -1$, respectively. In the next section, we will explore the electronic properties of other members of the graphene family staggered 2D semiconductor materials, especially as we switch on the spin-orbit interaction.

2.3 The electronic properties of staggered 2D semiconductor materials

Graphene shares analogous properties with staggered 2D semiconductor monolayer. In staggered two-dimensional semiconductor atomic crystals (monolayer of silicon, germanium, and tin), atoms are still arranged in a honeycomb lattice. These monolayer structures hold great promise in the field of valleytronics, spintronics and optoelectronics due to their exceptional electronic and optical properties [69, 70]. We set up the discussion with the introduction of SOC in these 2D

quantum materials. The presence of SOC provides a mass to the Dirac fermions that result in the opening of a gap in their electronic band structure in each of the K and K' valleys. The lattice of these materials is shown in Fig. 2.5. The ionic size of the silicon atom is larger as compared to the carbon atom, which causing buckling due to an sp_3-like hybridization [66, 71, 72]. As a result of the buckled lattice, the inversion symmetry generates an in-plane electric field which in turn creates an on-site staggered potential difference between the A and B sublattices.

We introduce the concept of SOC in staggered 2D materials. The coupling is a relativistic interaction between electrons and a local (internal or external) electric potential gradient because the moving electrons experience an effective magnetic

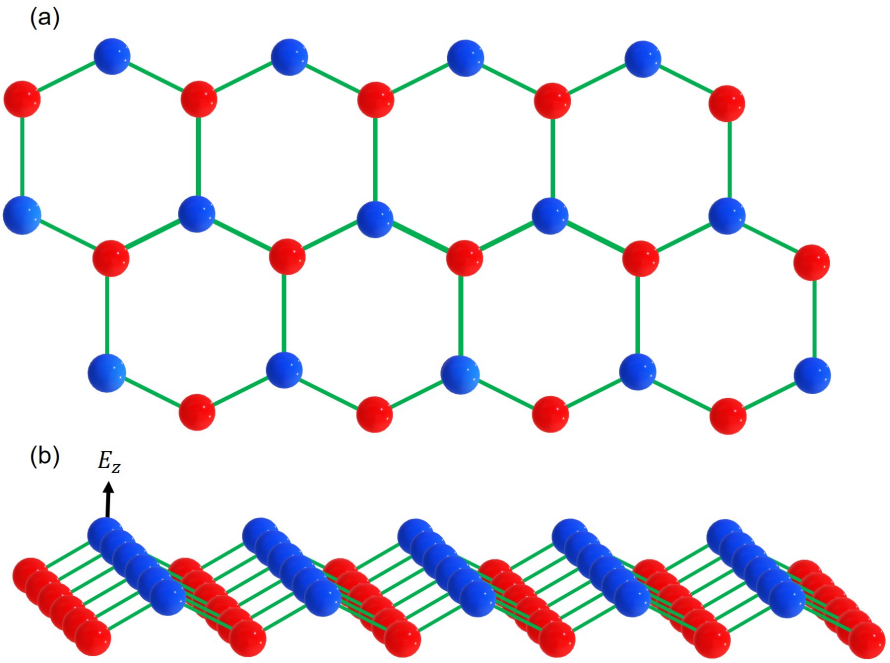

Figure 2.5: (a) The un-buckled structure of the staggered 2D semiconductor monolayer. (b) Illustration of the buckled honeycomb lattice of of the staggered 2D semiconductors which is distorted due to large ionic radius of a silicon atom and generates a staggered sublattice potential E_z.

field in their rest frame. We have already discussed it in Section 1.1.2, from where we also know the generic form of the intrinsic spin-orbit Hamiltonian and can be expressed as through the fourth term in L.H.S of Eq. (1.123)

$$H_{so} = \frac{\hbar}{4m^2c^2}\left(\vec{\nabla}V \times \vec{p}\right)\cdot\vec{\sigma} = -\frac{\hbar}{4m^2c^2}\left(\vec{F}\times\vec{p}\right)\cdot\vec{\sigma}, \tag{2.61}$$

where V is the potenial energy and $\vec{F}$ is the force parallel to the surface due to the potential gradient, $\vec{p}$ is momentum and $\vec{\sigma}$ is a Pauli matrix, representing the spin of the electron. The nearest-neighbor SOC is zero for staggered materials due to the presence of a structure's mirror symmetry, while the next-nearest-neighbor SOC is nonzero as shown in Fig. 2.6(a). The next-nearest-neighbor SOC can be divided into two types, one is parallel and the other is perpendicular to the plane, respectively. As illustrated in Fig. 2.6(b), the perpendicular components of the coloumbic force of sublattices A and B are non-coplanar. The Hamiltonian for the force parallel to the plane has the following form

$$H_{so1} = i\gamma_2(\vec{F_{\parallel}}\times\vec{d_{ij}})\cdot\vec{\sigma} \equiv it_2 v_{ij}\sigma_z, \tag{2.62}$$

where $t_2 = \Delta_{so}/(3\sqrt{3})$, $v_{ij} = (\vec{d_i}\times\vec{d_j})/|\vec{d_i}\times\vec{d_j}|$, $\vec{d_i}$ and $\vec{d_j}$ are the two unit vectors connecting atom j to its next-nearest-neighbors i [71]. The intrinsic SOC Hamiltonian of the staggered 2D materials in first quantization form is given by

$$H_{so1} = \frac{i\Delta_{so}}{3\sqrt{3}}v_{ij}\sigma_z. \tag{2.63}$$

The staggered 2D materials band structure can be altered in the presence of a perpendicular electric field as shown in Fig. 2.6(b). The origin of this field can be gate voltage or charge impurities in the substrate. Due to the application of the electric field, the spatial inversion symmetry breaks down and as a result, it induces a nearest-neighbor (extrinsic) SOC called Rashba SOC [71]. For the force perpendicular to the plane, the Hamiltonian has the generic form as

$$H_{so2} = i\gamma_1(\vec{\sigma}\times\vec{d}^{0}_{ij})\cdot\vec{F}^{A}_{\perp}\vec{e}_z = it_1\mu_{ij}(\vec{\sigma}\times\vec{d}^{0}_{ij})_z, \tag{2.64}$$

where, γ_1 and t_1 are undetermined material and interface-dependent parameters, j is the nearest neighbor of i, $\vec{d}^{0}_{ij} = \vec{d_{ij}}/|\vec{d_{ij}}|$ and $\mu_{ij} = \pm 1$ for the lattice A and B,

respectively. However, the Rashba coupling is typically neglected, since $\Delta_R \ll \Delta_{so}$ being roughly 10 times smaller in magnitude than Δ_{so}.

The so-called Kane-Mele Hamiltonian with SOC in these 2D materials in the vicinity of Dirac point K in second quantization form is given by the following equation [15, 71],

$$\begin{aligned} H = &-|t| \sum_{\langle ij \rangle \mu} (a^{\dagger}_{i\mu} b_{j\mu} + b^{\dagger}_{i\mu} a_{j\mu}) \\ &+ i \frac{\Delta_{so}}{6\sqrt{3}} \sum_{\langle\langle ij \rangle\rangle \mu\nu} v_{ij} a^{\dagger}_{i\mu} \sigma^{z}_{\mu\nu} a_{j\nu} \\ &- i \frac{\Delta_{so}}{6\sqrt{3}} \sum_{\langle\langle ij \rangle\rangle \mu\nu} v_{ij} b^{\dagger}_{i\mu} \sigma^{z}_{\mu\nu} b_{j\nu}, \end{aligned} \tag{2.65}$$

where $a^{\dagger}_{i\mu/\nu}(a_{i\mu/\nu})$ is the creation (annihilation) operator written in second quantization notation, which creates an electron (hole) in the sublattice A at site R_i with spin μ/ν. Similarly, $b^{\dagger}_{i\mu/\nu}(b_{i\mu/\nu})$ is the fermionic creation (annihilation) operator that creates (annihilates) an electron in the sublattice B at the site R_i with spin

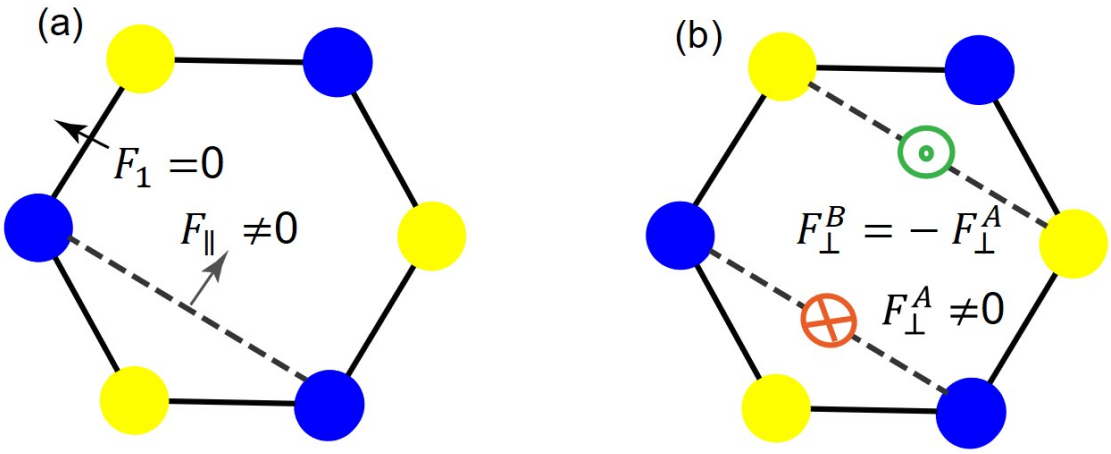

Figure 2.6: SOC in the staggered 2D materials. (a) The nearest-neighbor force F_1 vanishes, while the next-nearest-neighbor force $\vec{F}_{\parallel}$ is non-zero in the horizontal plane. (b) The next-nearest-neighbor non-zero force $F_{\perp}^{A}$ equals negative $F_{\perp}^{B}$ in the perpendicular direction. The dark and light atoms correspond to atoms in the two staggered planes respectively.

μ/ν.

The first term in Eq. (2.65) is the usual low-energy graphene-like which describes nearest-neighbor hopping with hopping integral t and $\langle ij\rangle$ denotes the summation over the nearest neighbor. The second and third terms account for a complex hopping amplitude between next-nearest neighbors $\langle\langle ij\rangle\rangle$, here Δ_{so} is the strength of SOC. The parameter $v_{ij} = \pm 1$ corresponds to counter-clockwise or clockwise hopping, respectively and $\sigma^z_{\mu\nu}$ is the Pauli spin matrix. It is noticeable that the SOC of sublattice B denoted in the fourth term has a negative sign, as the direction of the force is opposite to that of sublattice A. According to Fig. 2.7(a), there are three nearest neighbor atoms and six next-nearest neighbors of the silicon atoms.

Now transforming the creation and annihilation operators in the momentum space using Fourier transformation, we have

$$a_i = \frac{1}{\sqrt{N}} \sum_k e^{i\mathbf{k}\cdot\mathbf{R_i}} a_k, \qquad b_i = \frac{1}{\sqrt{N}} \sum_k e^{i\mathbf{k}\cdot\mathbf{R_i}} b_k, \tag{2.66}$$

The first part of Eq. (2.65) is the usual graphene-like Hamiltonian. From Eq. (2.7), we can write

$$-|t| \sum_{\langle ij\rangle\mu} (a^\dagger_{i\mu} b_{j\mu} + b^\dagger_{i\mu} a_{j\mu}) \;=\; \sum_k \left(-|t|\alpha(k) a^\dagger_{k\uparrow} b_{k\uparrow} - |t|\alpha^*(k) b^\dagger_{k\uparrow} a_{k\uparrow} \right). \tag{2.67}$$

By using the Fourier transormed operators defined in Eq. 2.66, the second and third terms of Eq. 2.65 can be written in momentum space, respectively as

$$\begin{aligned} i\frac{\Delta_{\rm so}}{6\sqrt{3}} \sum_{\langle\langle ij\rangle\rangle\mu\nu} v_{ij} a^\dagger_{i\mu} \sigma^z_{\mu\nu} a_{j\nu} &= i\frac{\Delta_{\rm so}}{6\sqrt{3}} \sum_{i\mu\nu} \sum_{j=1}^{6} v_{ij} a^\dagger_{i\mu} \sigma^z_{\mu\nu} a_{j\nu} \\ &= i\frac{\Delta_{\rm so}}{6\sqrt{3}} \sum_k \sum_{\mu\nu} \sum_{j=1}^{6} a^\dagger_{k\mu} \sigma^z_{\mu\nu} a_{k\nu} v_j e^{i\mathbf{k}\cdot\mathbf{R}'_{\mathbf{j}}} \\ &= i\frac{\Delta_{\rm so}}{6\sqrt{3}} \sum_k \sum_{\mu\nu} a^\dagger_{k\mu} \sigma^z_{\mu\nu} a_{k\nu} v(\mathbf{k}). \end{aligned} \tag{2.68}$$

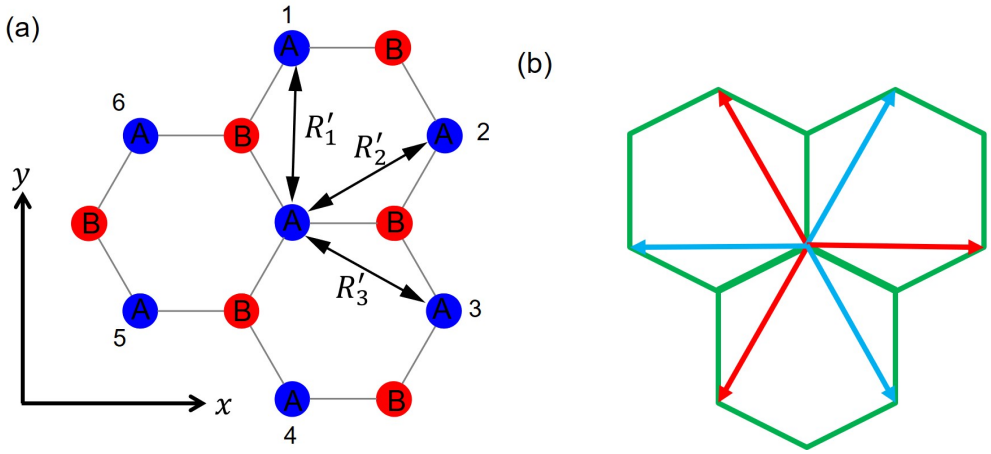

Figure 2.7: The staggered 2D semiconductor honeycomb lattice. (a) The six next-nearest neighbor atoms of sublattice A at site i ($i = 1, ..., 6$) are shown with number. The $R_j^{'}$ is the vector connecting the sublattice A at site i with its six next-nearest neighbors. (b) Next-nearest-neighbour hopping on the honeycomb lattice with $v_{ij} = \pm$.

Exapanding the $\sigma_{\mu\nu}^z$, this term becomes,

$$i\frac{\Delta_{\rm so}}{6\sqrt{3}}\sum_{i\mu\nu}\sum_{j=1}^{6} v_{ij}a_{i\mu}^{\dagger}\sigma_{\mu\nu}^{z}a_{j\nu} \;=\; i\frac{\Delta_{\rm so}}{6\sqrt{3}}\sum_{k}\Big(a_{k\uparrow}^{\dagger}a_{k\uparrow}-a_{k\downarrow}^{\dagger}a_{k\downarrow}\Big)v(\mathbf{k}). \qquad (2.69)$$

Similarly, for the third terms in Eq. 2.65, we obtain

$$i\frac{\Delta_{\rm so}}{6\sqrt{3}}\sum_{\langle\langle ij\rangle\rangle\mu\nu} v_{ij}b_{i\mu}^{\dagger}\sigma_{\mu\nu}^{z}b_{j\nu} \;=\; i\frac{\Delta_{\rm so}}{6\sqrt{3}}\sum_{k}\Big(b_{k\uparrow}^{\dagger}b_{k\uparrow}-b_{k\downarrow}^{\dagger}b_{k\downarrow}\Big)v(\mathbf{k}).$$

where $v(\mathbf{k})$ is given by,

$$\begin{aligned} v(\mathbf{k}) &= \sum_{j=1}^{6} v_j e^{i\mathbf{k}\cdot\mathbf{R}_{\mathbf{j}}'} \\ &= -e^{i\mathbf{k}\cdot\mathbf{v_1}} - e^{i\mathbf{k}\cdot\mathbf{v_2}} - e^{i\mathbf{k}\cdot\mathbf{v_3}} + e^{-i\mathbf{k}\cdot\mathbf{v_1}} + e^{-i\mathbf{k}\cdot\mathbf{v_2}} + e^{-i\mathbf{k}\cdot\mathbf{v_3}} \\ &= -2i\big(\sin(\mathbf{k}\cdot\mathbf{v_1}) + \sin(\mathbf{k}\cdot\mathbf{v_2}) + \sin(\mathbf{k}\cdot\mathbf{v_3})\big), \end{aligned} \qquad (2.70)$$

where $\mathbf{v_1}$, $\mathbf{v_2}$ and $\mathbf{v_3}$ are the values of next-nearest neighbor atoms vectors of sublattice A as shown in Fig. 2.7(a). $R_j^{'}$ is the vector of the j-th next-nearest

neighbor atoms. We note that,

$$\mathbf{R'_1} = -\mathbf{R'_4} = \mathbf{v_1} = (0, a) \tag{2.71}$$

$$\mathbf{R'_2} = -\mathbf{R'_4} = \mathbf{v_2} = \left(\frac{\sqrt{3}a}{2}, \frac{a}{2}\right) \tag{2.72}$$

$$\mathbf{R'_3} = -\mathbf{R'_4} = \mathbf{v_3} = \left(\frac{\sqrt{3}a}{2}, -\frac{a}{2}\right). \tag{2.73}$$

The Hamiltonian of the staggered 2D materials in momentum space can be obtained by substituting Eqs. (2.67–2.73) into Eq. (2.65). Therefore, for each of the two spin projections, the Hamiltonian becomes

$$\begin{aligned} H_\uparrow &= \sum_k \left(- |t|\alpha(k) a^\dagger_{k\uparrow} b_{k\uparrow} - |t|\alpha^*(k) b^\dagger_{k\uparrow} a_{k\uparrow} + i\frac{\Delta_{\rm so} v(\mathbf{k})}{6\sqrt{3}} \sum_k \left(a^\dagger_{k\uparrow} a_{k\uparrow} - b^\dagger_{k\downarrow} b_{k\downarrow} \right) \right) \\ &= \sum_k \begin{pmatrix} a^\dagger_{k\uparrow} & b^\dagger_{k\uparrow} \end{pmatrix} \begin{pmatrix} i\frac{\Delta_{\rm so} v(\mathbf{k})}{6\sqrt{3}} & -|t|\alpha(k) \\ -|t|\alpha^*(k) & -i\frac{\Delta_{\rm so} v(\mathbf{k})}{6\sqrt{3}} \end{pmatrix} \begin{pmatrix} a_{k\uparrow} \\ b_{k\uparrow} \end{pmatrix}. \end{aligned} \tag{2.74}$$

$$\begin{aligned} H_\downarrow &= \sum_k \left(- |t|\alpha(k) a^\dagger_{k\downarrow} b_{k\downarrow} - |t|\alpha^*(k) b^\dagger_{k\downarrow} a_{k\downarrow} - i\frac{\Delta_{\rm so} v(\mathbf{k})}{6\sqrt{3}} \sum_k \left(a^\dagger_{k\downarrow} a_{k\uparrow} - b^\dagger_{k\downarrow} b_{k\downarrow} \right) \right) \\ &= \sum_k \begin{pmatrix} a^\dagger_{k\downarrow} & b^\dagger_{k\downarrow} \end{pmatrix} \begin{pmatrix} -i\frac{\Delta_{\rm so} v(\mathbf{k})}{6\sqrt{3}} & -|t|\alpha(k) \\ -|t|\alpha^*(k) & i\frac{\Delta_{\rm so} v(\mathbf{k})}{6\sqrt{3}} \end{pmatrix} \begin{pmatrix} a_{k\downarrow} \\ b_{k\downarrow} \end{pmatrix}. \end{aligned} \tag{2.75}$$

Quite similar to graphene, for the staggered 2D materials, we obatin a 2×2 Hamiltonian matrix for each spin in the first quantization form. From Eqs. (2.74) and (2.75) we seek to find energy dispersion relation in the low energy limit. The coordinates for the staggered 2D material are given by $4\pi(0,-1)/3a$ and $4\pi(0,1)/3a$, respectively. Following Ref. [71], the diagonal terms can be approximated to the first order as

$$\frac{i\Delta_{so} v(\mathbf{K}+\mathbf{k})}{6\sqrt{3}} \approx -\frac{\Delta_{so}}{2}, \tag{2.76}$$

$$\frac{i\Delta_{so} v(\mathbf{K'}+\mathbf{k})}{6\sqrt{3}} \approx \frac{\Delta_{so}}{2}. \tag{2.77}$$

Finally, a general low-energy Hamiltonian for silicene, germanene, and tinene can be written as

$$H_{\xi\sigma} = \begin{pmatrix} -\xi\sigma_z\frac{\Delta_{so}}{2} & \hbar v_F(\xi k_x - i k_y) \\ \hbar v_F(\xi k_x + i\xi k_y) & \sigma_z\frac{\Delta_{so}}{2} \end{pmatrix}, \tag{2.78}$$

where σ_z represents the real spin degrees of freedom, $\xi = \pm 1$ for the K and K' valleys and v_F is the Fermi velocity. The precceeding discussion describes the evalution of Hamiltonian in the presence of SOC. In the next sextion, we will explore how this Hamiltonian may be modified by the application of electric field.

2.3.1 Impact of an electric field

When an electric field is applied perpendicular to the silicene sheet, then there is an on-site potential difference between sublattices A and B, due to the buckled structure. The Hamiltonian given by Eq. (2.65) picks up the additional term and can be rewritten as

$$H = -|t| \sum_{\langle ij \rangle \mu} (a^{\dagger}_{i\mu} b_{j\mu} + b^{\dagger}_{i\mu} a_{j\mu}) + i \frac{\Delta_{so}}{6\sqrt{3}} \sum_{\langle\langle ij \rangle\rangle \mu\nu} v_{ij} a^{\dagger}_{i\mu} \sigma^{z}_{\mu\nu} a_{j\nu} - i \frac{\Delta_{so}}{6\sqrt{3}} \sum_{\langle\langle ij \rangle\rangle \mu\nu} v_{ij} b^{\dagger}_{i\mu} \sigma^{z}_{\mu\nu} b_{j\nu} + \frac{\Delta_z}{2} \sum_{i} a^{\dagger}_{i\mu} a_{i\mu}. \tag{2.79}$$

The fourth term represents the electric field contribution, The staggered potential difference is $\Delta_z = eE_z l$, E_z being an electric field and l being the lattice constant. The low-energy effective Dirac Hamiltonian for the staggered graphene system in the presence of an electric field is now expressed as

$$\hat{H}_{\xi\sigma} = \begin{pmatrix} -\xi\sigma_z \frac{\Delta_{so}}{2} + \frac{1}{2}\Delta_z & \hbar v_F(\xi k_x - i k_y) \\ \hbar v_F(\xi k_x + i k_y) & \xi\sigma_z \frac{\Delta_{so}}{2} - \frac{1}{2}\Delta_z \end{pmatrix}. \tag{2.80}$$

In terms of Pauli matrices the above Hamiltonian can be written as

$$\hat{H}_{\xi\sigma} = \hbar v_F(\xi k_x \hat{\tau}_x + k_y \hat{\tau}_y) - \frac{1}{2}\xi \Delta_{so} \hat{\sigma}_z \hat{\tau}_z + \frac{1}{2}\Delta_z \hat{\tau}_z. \tag{2.81}$$

The first term in Eq. (2.81) is the usual low-energy graphene-like Hamiltonian for describing massless Dirac fermions. The parameter $\xi = \pm 1$ corresponds to the valleys (K and $K^{'}$) in momentum space and the vector operators $\vec{\tau} = (\hat{\tau}_x, \hat{\tau}_y, \hat{\tau}_z)$ and $\vec{\sigma} = (\hat{\sigma}_x, \hat{\sigma}_y, \hat{\sigma}_z)$ respectively represent Pauli matrices of the lattice pseudo spin and real spin degrees of freedom. The second term in the Hamiltonian captures

intrinsic spin-orbit coupling with a band gap of Δ_{so}. The energy dispersion relation of the Dirac electron in staggered 2D quantum materials is given by

$$E(\xi, \sigma, t, k) = t\sqrt{(\hbar v_F k)^2 + \Delta_{\xi\sigma}^2}, \tag{2.82}$$

Here, $t = \text{sgn(n)}$ denotes the conduction/valence band and $\Delta_{\xi\sigma} = -\frac{1}{2}\xi\sigma\Delta_{so} + \frac{1}{2}\Delta_z$ is general Dirac mass. The aforementioned discussion concludes the Hamiltonian's evalution in the presence of electric field. In the forthcoming section, we will investigate how this electric field drives a quantum material through different topological phases. In litrature, these transitions are often deemed as topological quantum phase transition in 2D quantum materials.

2.3.2 Topological qunatum phase transition in 2D quantum materials

The discovery of topological phases and topological quantum phase transitions (TQPTs) in a wide range of new quantum materials, such as graphene, staggered 2D semiconductors (i.e. silicene, germanene, stanene), 2D transition metal dichalcogenides (TMDCs), Dirac-Weyl semimetals, and their artificial analogs have provided a new frame of mind to the understanding of the origin of quantum states of matter. In section 1.0.9, we derived the expression for the Berry connection. We now recapitulate. For any insulating state $|\psi(\boldsymbol{k})\rangle$ in the momentum space, the Berry coneection is given as [73, 74]

$$\boldsymbol{A}_i(\boldsymbol{k}) = -i\left\langle \psi(\boldsymbol{k})|\frac{\partial}{\partial k_i}|\psi(\boldsymbol{k})\right\rangle. \tag{2.83}$$

We may now define the Berry curvature (BC), which acts as a fictitious magnetic field in the momentum space and is given by

$$\Omega(\boldsymbol{k}) = \frac{\partial}{\partial k_x}A_y(\boldsymbol{k}) - \frac{\partial}{\partial k_y}A_x(\boldsymbol{k}). \tag{2.84}$$

If we integrate the the Berry curvature over the first Brillouin zone, we get the Chern-number (CN) or topological charge as

$$\mathcal{C} = \frac{1}{2\pi}\int_{FBZ} d^2kF(\boldsymbol{k}). \tag{2.85}$$

Now the Hamiltonian in Eq. (2.81), can be written as

$$\hat{H}_{\xi\sigma} = \vec{d}\cdot\vec{\tau}, \tag{2.86}$$

where $d_x = \xi\hbar v_F k_x$, $d_y = \hbar v_F k_y$ and $d_z = \Delta_{\xi\sigma}$. The Berry curvature in Eq. (1.28) can be modified for this system as

$$\Omega_{\xi\sigma}(k) = \frac{1}{2}\hat{d}\cdot\left(\frac{\partial\hat{d}}{\partial k_x}\times\frac{\partial\hat{d}}{\partial k_y}\right), \tag{2.87}$$

where the vector $\mathbf{d}$ in component notation can be expressed as

$$\hat{\mathbf{d}}(\mathbf{k}) = \frac{\mathbf{d}(k)}{|\mathbf{d}|} = \frac{\left(\xi\hbar v_F k_x, \hbar v_F k_y, \Delta_{\xi\sigma}\right)}{\sqrt{(\hbar v_F k_x)^2 + (\hbar v_F k_y)^2 + \Delta_{\xi\sigma}^2}}. \tag{2.88}$$

We finally determined the BC for each valley as

$$\Omega_{\xi\sigma}(k) = -\xi\frac{\Delta_{\xi\sigma}}{2\left((\hbar v_F k)^2 + \Delta_{\xi\sigma}^2\right)^{3/2}}. \tag{2.89}$$

For any 2×2 Hamiltonian as in (2.80), the CN is equivalent to the Pontryagin number [74] and is given by

$$\mathcal{C}_\sigma^\xi = \frac{1}{4\pi}\int \Omega_{\xi\sigma}(k)d^2k. \tag{2.90}$$

The Pontryagin number is certain topological invariant or topological number which counts how many times $\hat{\boldsymbol{d}}$ wraps a sphere. The CN is determined by the Dirac mass and is given by

$$\mathcal{C}_\sigma^\xi = \frac{\xi\mathbf{sgn}(\Delta_{\xi\sigma})}{2}, \tag{2.91}$$

where we already have defined the the Dirac mass $\Delta_{\xi\sigma}$. The CN is quantized as $\mathcal{C}_\sigma^\xi = \pm 1/2$. In particular, these topological spin numbers take the form

$$\mathcal{C}_\sigma = \frac{1}{2}\sum_{\xi=\pm 1}\left(\mathcal{C}_+^\xi + \mathcal{C}_-^\xi\right). \tag{2.92}$$

Similarly, the corresponding valley CN is given by

$$\mathcal{C}^{\xi} = \frac{1}{2}\sum_{\sigma=\pm 1}\left(\mathcal{C}_{\sigma}^{+} + \mathcal{C}_{\sigma}^{-}\right). \tag{2.93}$$

It must be remembered that the CN numbers are insensitive to a smooth deformation of the band structure provided the bandgap is open as we have shown in Section 1.0.2 in Fig. 1.5. On the other hand, the CN number changes its sign when the Dirac mass $\Delta_{\xi\sigma}$ changes its sign. It is noteworthy that a topological quantum phase transition (TQPT) occurs when the sign of the $\Delta_{\xi\sigma}$ changes.
For an insulator phase, we define four independent CNs as

$$\begin{aligned}
\mathcal{C} &= \mathcal{C}_{\uparrow}^{K} + \mathcal{C}_{\uparrow}^{K'} + \mathcal{C}_{\downarrow}^{K} + \mathcal{C}_{\downarrow}^{K'} && (2.94)\\
\mathcal{C}_{\sigma} &= \frac{1}{2}\left(\mathcal{C}_{\uparrow}^{K} + \mathcal{C}_{\uparrow}^{K'} - C_{\downarrow}^{K} - \mathcal{C}_{\downarrow}^{K'}\right) && (2.95)\\
\mathcal{C}^{\xi} &= \mathcal{C}_{\uparrow}^{K} - \mathcal{C}_{\uparrow}^{K'} + \mathcal{C}_{\downarrow}^{K} - \mathcal{C}_{\downarrow}^{K'} && (2.96)\\
\mathcal{C}_{\sigma}^{\xi} &= \frac{1}{2}\left(\mathcal{C}_{\uparrow}^{K} - \mathcal{C}_{\uparrow}^{K'} - \mathcal{C}_{\downarrow}^{K} + \mathcal{C}_{\downarrow}^{K'}\right), && (2.97)
\end{aligned}$$

where $\mathcal{C}$ is the total CN, $\mathcal{C}_{\sigma}$ is the spin CN, $\mathcal{C}^{\xi}$ is the valley CN and $\mathcal{C}_{\sigma}^{\xi}$ is the spin-valley CN [74]. The energy gap is tunable through the application of the staggered electric potential Δ_z or impingence of circularly polarized light. The electronic energy dispersion evolution with Δ_z is shown in Fig. 2.8. As illustrated in Fig. 2.8(a), for $\Delta_z = 0$, the spin degeneracy is witnessed with energy bands separated by an insulating gap of $2\Delta_{so}$ and the system is in the TI regime. For the particular case where staggered electric potential is finite ($\Delta_z = 0.5\Delta_{so}$), the possible CN and spin-Chern number is $(0, 1)$ and we identify this state as the quantum spin Hall insulator (QSHI) [75]. The QSHI state is also called the topological insulator (TI) regime or non-trivial state. Each spin state in this regime splits into two new features and gives rise to two Dirac energy gaps as shown in Fig. 2.8 (b).

When Δ_z is increased to $\Delta_z = \Delta_{so}$, then the lower bandgap of the Dirac fermions closes and the system transforms to the valley-spin polarized metal (VSPM) state.

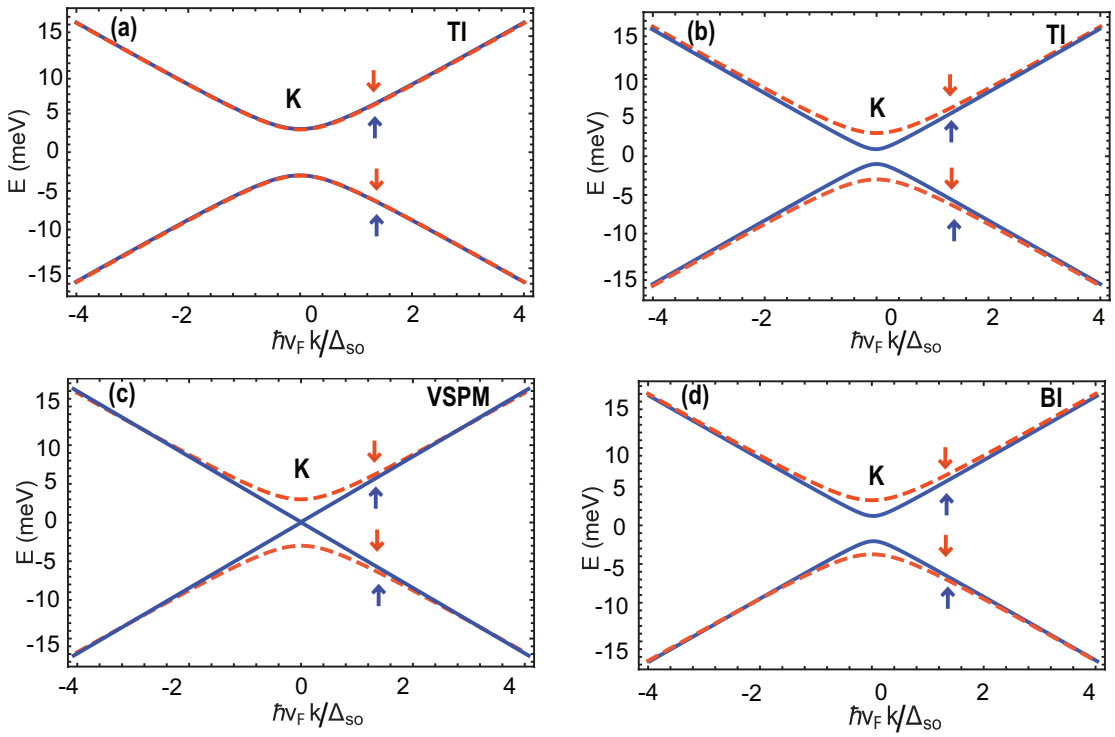

Figure 2.8: The electronic energy dispersion of the staggered 2D monolayer for the K valley corresponding to three different topological regimes: (a) TI ($\Delta_z = 0$), (b) TI ($\Delta_z = 0.5\Delta_{so}$), (c) VSPM ($\Delta_z = \Delta_{so}$) and (d) BI ($\Delta_z = 2\Delta_{so}$) respectively. The solid blue (dashed red) curves are for spin up (down).

In this phase, the CN is $(1, 1/2)$ and is shown in Fig. 2.8 (c). For an even higher staggered electric potential $\Delta_z > \Delta_{so}$, the system reaches to the band insulator (BI) state $(0, 0)$ and the lowest energy gap reopens, although a band inversion has occurred as shown in Fig. 2.8(d). In the forthcoming chapters, we will explicitly discuss the TQPTs in the presence of a magnetic field for the determination of the magnet-optical effects in the graphene family.

2.3.3 Two-component spinor wave functions of 2D quantum materials

In order to obtain the eigenstates of $\hat{H}_{\xi\sigma}$ in Eq. (2.81), we can write

$$\xi k_x \pm i k_y = |k| e^{\pm i\xi\phi_k}, \tag{2.98}$$

where, $|k| = k = \sqrt{k_x^2 + k_y^2}$, $\cos\theta = \frac{\Delta_{\xi\sigma}}{E(\xi,\sigma,t,k)}$ and $\sin\theta = \frac{\xi\hbar v_F k}{E(\xi,\sigma,t,k)}$. Eq. (2.80) becomes $H_{\xi\sigma}(k) = E(\xi,\sigma,t,k)h_\xi(k)$, where $h_\xi(k)$ is given by

$$h_\xi(k) = \begin{pmatrix} \cos\theta & \sin\theta e^{-i\xi\phi_k} \\ \sin\theta e^{i\xi\phi_k} & -\cos\theta \end{pmatrix} \tag{2.99}$$

The above matrix is Hermitian and exhibits real eigenenergies. The corrosponding eigenfunctions for the K and K' points of $H_{\xi\sigma}(k)$ are two-component spinors given as follows

$$\Psi = \frac{1}{\sqrt{S}} \begin{pmatrix} \psi_A \\ \psi_B \end{pmatrix} e^{i\mathbf{k}\cdot\mathbf{r}}, \tag{2.100}$$

where $S = L_x L_y$ is the area of the sample and $|\psi_A|^2 + |\psi_B|^2 = 1$. Using standard diagonalization procedure, we have eigenvalue equation $H_{\xi\sigma}(k)\Psi = E_{\xi\sigma}(k)\Psi$, resulting in

$$\begin{pmatrix} \cos\theta - t & \sin\theta e^{-i\xi\phi_k} \\ \sin\theta e^{i\xi\phi_k} & -\cos\theta - t \end{pmatrix} \begin{pmatrix} \psi_A \\ \psi_B \end{pmatrix} = 0, \tag{2.101}$$

which leads to

$$(\cos\theta - t)\,\psi_A + \sin\theta e^{-i\xi\phi_k}\psi_B = 0, \tag{2.102}$$

$$\sin\theta e^{i\xi\phi_k}\psi_A - (\cos\theta + t)\,\psi_B = 0. \tag{2.103}$$

By multiplying Eq. (2.102) by ψ_A and taking the conjugate of Eq. (2.103) and then multiplying with ψ_B, we have

$$(\cos\theta - t)\,|\psi_A|^2 + \sin\theta e^{-i\xi\phi_k}\psi_B\psi_A^* = 0, \tag{2.104}$$

$$\sin\theta e^{-i\xi\phi_k}\psi_A^*\psi_B - (\cos\theta + t)\,|\psi_B|^2 = 0. \tag{2.105}$$

Subtracting thes equations, we have

$$(\cos\theta - t)|\psi_A|^2 + (\cos\theta + t)|\psi_B|^2 = 0, \tag{2.106}$$

$$(\cos\theta - t)|\psi_A|^2 + (\cos\theta + t)|1 - \psi_A|^2 = 0, \tag{2.107}$$

$$|\psi_A|^2 = \frac{1}{2t}\left(1 + t\cos\theta\right). \tag{2.108}$$

As we know that $t^2 = 1$, therefore we can therefore rewrite the above equation as

$$\psi_A = \frac{1}{\sqrt{2}}\sqrt{(1 + t\cos\theta)}. \tag{2.109}$$

From Eq. (2.104) , we have

$$\psi_B = \frac{(t - \cos\theta)}{\sin\theta}\psi_A e^{i\xi\phi_k}, \tag{2.110}$$

Substituting the value of ψ_A into Eq. (2.110), we obtain

$$\begin{aligned}\psi_B &= \frac{t}{\sqrt{2}}\frac{(1 - t\cos\theta)\sqrt{1 + t\cos\theta}}{\sqrt{1 - t^2\cos^2\theta}}e^{i\xi\phi_k}, \\ &= \frac{t}{\sqrt{2}}\sqrt{1 + t\cos\theta}e^{i\xi\phi_k}.\end{aligned} \tag{2.111}$$

The full normalized eigenstates follow

$$\Psi_{(K,t,\sigma,\mathbf{k})} = \begin{pmatrix}\psi_A \\ \psi_B\end{pmatrix} = \frac{1}{\sqrt{2S}}\begin{pmatrix}\sqrt{1 + t\cos\theta} \\ t\sqrt{1 - t\cos\theta}\end{pmatrix}e^{i\mathbf{k}\cdot\mathbf{r}}, \tag{2.112}$$

where $t = \mathrm{sgn(n)}$ denotes the conduction/valence band. Following the same procedure, the corresponding wave functions at the K' point can be obtain as

$$\Psi_{(K',t,\sigma,\mathbf{k})} = \begin{pmatrix}\psi_A \\ \psi_B\end{pmatrix} = \frac{1}{\sqrt{2S}}\begin{pmatrix}t\sqrt{1 - t\cos\theta} \\ \sqrt{1 + t\cos\theta}\end{pmatrix}e^{i\mathbf{k}\cdot\mathbf{r}}. \tag{2.113}$$

Now we are fully prepare to introduce the magnetic field effect in these staggered 2D quantum materials.

2.3.4 Landau level quantization

The low-energy Hamiltonian of silicene, germanene and tinene is given by Eq. (2.81)

$$\hat{H}_{\xi\sigma} = \hbar v_F(\xi k_x\hat{\tau}_x + k_y\hat{\tau}_y) - \frac{1}{2}\xi\Delta_{so}\hat{\sigma}_z\hat{\tau}_z + \frac{1}{2}\Delta_z\hat{\tau}_z. \tag{2.114}$$

In order to achieve Landau level (LL) quantization, we apply a static uniform magnetic field B perpendicular to this plane. Introducing the Landau gauge for the magnetic vector potential $A = (-yB, 0, 0)$ [76, 77]. In the presence of a magnetic field, for a single spin and valley the low-energy physics of the silicenic materials is well described in matrix form using Pauli matrices as

$$\hat{H}_{\xi\sigma} = \begin{pmatrix} \Delta_{\xi\sigma} & \hbar v_F \left[\xi \left(k_x - i\frac{eBy}{\hbar}\right) - ik_y\right] \\ \hbar v_F \left[\xi \left(k_x - i\frac{eBy}{\hbar}\right) + ik_y\right] & -\Delta_{\xi\sigma} \end{pmatrix}, \tag{2.115}$$

where $\Delta_{\xi\sigma} = -\frac{1}{2}\xi\sigma\Delta_{so} + \frac{1}{2}\Delta_z$. The Hamiltonian $\hat{H}_{\xi\sigma}$ is expressed in the A and B sublattices basis $(\psi_A, \psi_B)^T$. The two ladder operators can be defined as

$$-i\frac{\sqrt{2}\hbar v_F}{l_B}a = \hbar v_F \left(\left[k_x - \frac{eB}{\hbar}y\right] - ik_y\right) \tag{2.116}$$

and

$$i\frac{\sqrt{2}\hbar v_F}{l_B}a^\dagger = \hbar v_F \left(\left[k_x - \frac{eB}{\hbar}y\right] + ik_y\right), \tag{2.117}$$

where $l_B = \sqrt{\hbar/(eB)}$. The Fock state of the harmonic oscillator is denoted by $|n\rangle$, where $n = 0, 1, 2.....$ These ladder operators satisfy the commutation relation $\left[a, a^\dagger\right] = 1$. Recalling, $a|n\rangle = \sqrt{n}|n-1\rangle$ and $a^\dagger|n\rangle = \sqrt{n+1}|n+1\rangle$. Our eigenvalue equation at the K point yields

$$\begin{pmatrix} \Delta_{K\sigma} & -i\frac{\sqrt{2}\hbar v_F}{l_B}a \\ i\frac{\sqrt{2}\hbar v_F}{l_B}a^\dagger & -\Delta_{K\sigma} \end{pmatrix} \begin{pmatrix} \psi_A \\ \psi_B \end{pmatrix} = E \begin{pmatrix} \psi_A \\ \psi_B \end{pmatrix}. \tag{2.118}$$

By applying the Hamiltonian on Ψ, we obtain

$$\Delta_{K\sigma}\psi_A - i\frac{\sqrt{2}\hbar v_F}{l_B}a\psi_B = E\psi_A \tag{2.119}$$

and

$$i\frac{\sqrt{2}\hbar v_F}{l_B}a^\dagger\psi_A - \Delta_{K\sigma}\psi_B = E\psi_B. \tag{2.120}$$

Eliminating ψ_A from Eq. (2.119), we obtain

$$\psi_A = \frac{-i\sqrt{2}\hbar v_F/l_B}{E - \Delta_{K\sigma}}a\psi_B, \tag{2.121}$$

and upon substituting Eq. (2.121) in Eq. (2.120), we arrive at

$$\frac{2\hbar^2 v_F^2/l_B^2}{E-\Delta_{K\sigma}} a^\dagger a\psi_B - \Delta_{K\sigma}\psi_B = E\psi_B, \tag{2.122}$$

which can be further simplified to

$$\frac{2\hbar^2 v_F^2/l_B^2}{E-\Delta_{K\sigma}} n\psi_B = (\Delta_{K\sigma}+E)\,\psi_B. \tag{2.123}$$

For $n \neq 0$, the dispersion relation of the silicenic materials in the K valley are given by

$$E(K,\sigma,n,t) = t\sqrt{2v_F^2\hbar eB|n| + \Delta_{K\sigma}^2}. \tag{2.124}$$

For $n = 0$, LL in the K valley, Eq. (2.120) can be written as

$$-\Delta_{K\sigma}\psi_B = E\psi_B. \tag{2.125}$$

The $n = 0$ LL energy is given by

$$E(\xi,\sigma,0) = -\Delta_{K\sigma}. \tag{2.126}$$

Similarly, for the K' valley, we can solve the simple eigenvalue equation

$$\begin{pmatrix} \Delta_{K'\sigma} & -i\frac{\sqrt{2}\hbar v_F}{l_B}a^\dagger \\ i\frac{\sqrt{2}\hbar v_F}{l_B}a & -\Delta_{K'\sigma} \end{pmatrix} \begin{pmatrix} \psi_A \\ \psi_B \end{pmatrix} = E \begin{pmatrix} \psi_A \\ \psi_B \end{pmatrix}, \tag{2.127}$$

which yields

$$\Delta_{K'\sigma}\psi_A - i\frac{\sqrt{2}\hbar v_F}{l_B}a^\dagger\psi_B = E\psi_A \tag{2.128}$$

and

$$-\Delta_{K'\sigma}\psi_B + i\frac{\sqrt{2}\hbar v_F}{l_B}a\psi_A = E\psi_B, \tag{2.129}$$

and upon eliminating ψ_B from Eq. (2.129), we obtain

$$\psi_B = \frac{i\sqrt{2}\hbar v_F/l_B}{\mathcal{E}+\Delta_{K'\sigma}}a\psi_A. \tag{2.130}$$

Finally, substituting Eq. (2.130) into Eq. (2.128), we obatain

$$\frac{2\hbar^2 v_F^2/l_B^2}{E+\Delta_{K'\sigma}} a^\dagger a\psi_A = (E-\Delta_{K'\sigma})\,\psi_B, \tag{2.131}$$

where $a^\dagger a\psi_A = n\psi_A$, the low-energy LL dispersion of the graphene family for the K' valley is given by

$$E(K', \sigma, n, t) = t\sqrt{2v_F^2 \hbar eB|n| + \Delta_{K'\sigma}^2}. \tag{2.132}$$

For $n = 0$ minifold in the K' valley, Eq. (2.128) can be recast as

$$\Delta_{K'\sigma}\psi_B = E\psi_B. \tag{2.133}$$

The zeroth LLs energy in the K' valley is given by

$$E(K', \sigma, 0) = \Delta_{K\sigma}. \tag{2.134}$$

The low-energy LL dispersion of the system for the K and K' valleys are therefore described as

$$E(\xi, \sigma, n, t) = \begin{cases} t\sqrt{2v_F^2 \hbar eB|n| + \Delta_{\xi\sigma}^2}, & \text{if } n \neq 0 \\ -\xi\Delta_{\xi\sigma}, & \text{if } n = 0. \end{cases} \tag{2.135}$$

Here, $t = \text{sgn(n)}$ denotes the conduction/valence band, n is an integer, the quantum number denoting the Landau quantization and $\sigma = \pm 1$ for spin up ($\uparrow$) and down ($\downarrow$), respectively.

In graphene, the $n = 0$ energy levels are pinned at zero energy as previously shown in Fig. 2.4 (a) and (b) for the K and K' valleys respectively. But in staggered 2D materials, the four-fold spin and valley split n=0 manifold is located at different locations in the conduction and valance bands in different regimes. One of the main differences between graphene and these staggered materials is that the $n = 0$ LL energies in silicenic materials are independent of the magnetic field and can be linearly manipulated by the electric field only, whereas both the electric and magnetic fields play a role in setting the position of the $n\neq 0$ levels. The locations of these four $n = 0$ LLs can be controlled by the applied electric field. Similar to graphene, non-zero LLs energies scale as $\sqrt{B}$.

In Figs. 2.9(a)–(d), we have illustrated how the $n = 0$ LL undergoes TQPTs

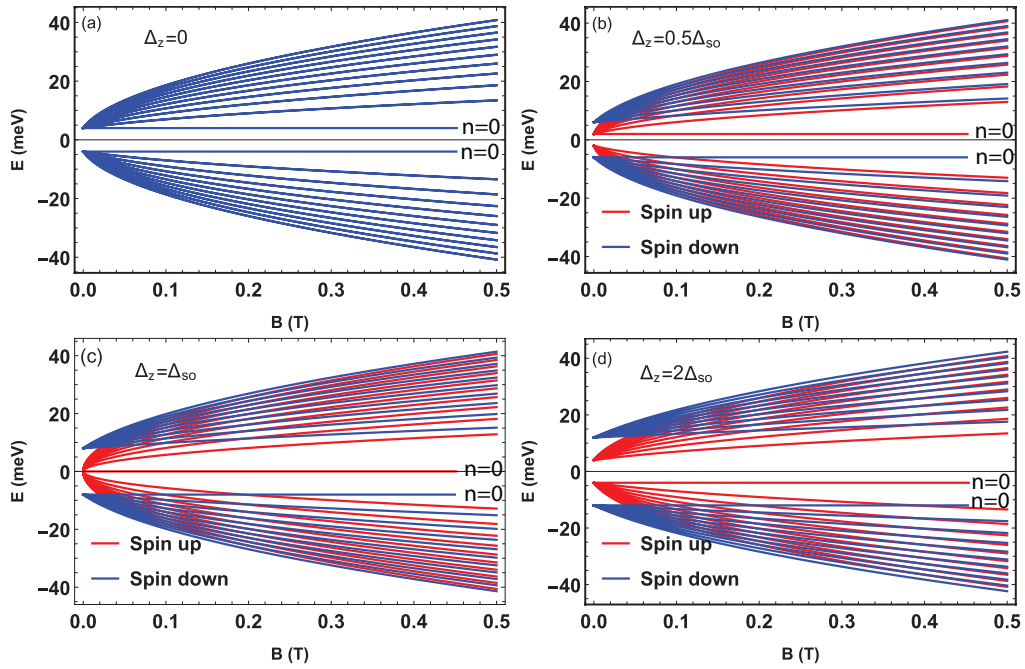

Figure 2.9: The staggered 2D semiconductor Landau level energies as a function of the external magnetic field B for three distinct topological regimes, TI, VSPM and BI for both spin up and down ($\sigma_z = \pm 1$). (a) For $\Delta_z = 0$ the energy spectrum is gapped due to SOC energy, and we have a TI phase. (b) For $\Delta_z \neq 0$ but $\Delta_z < \Delta_{so}$, the degeneracy is lefted but the spctrum is still gapped and we have a TI phase. (c) When $\Delta_z = \Delta_{so}$, the energy spectrum becomes gappless giving rise to a the valley-spin polarized metal (VSPM) regime. (d) For $\Delta_z > \Delta_{so}$, the energy gap re-opens giving rise to a phase transition from VSPM to a BI phase.

from the non-trivial to trivial states. In the absence of electric field $\Delta_z = 0$, the $n = 0$ energy levels are degenerate and set at Δ_{so} in the conduction and valance bands as shown in Fig. 2.9 (a). When Δ_z is turned on, the spin degeneracy is lifted and the bands become spin-split representing two energy gaps. In the TI regime, the spin-up LL is residing at positive energy while the spin-down level is at negative energy as depicted in Fig. 2.9 (b).

In the valley-spin polarized metal (VSPM) instance [65], the gap of one of the spin-split bands closes giving rise to a Dirac point. In the VSPM phase, the $n = 0$ spin-up LL at the K valley sits at zero energy, which exhibits graphene-like be-

havior. This is shown in Fig. 2.9 (c). On the other hand, the $n = 0$ spin-down LL is at negative energy. For an even higher electric field, the system transitions from the TI to BI state, and the lowest bandgap is opened again. In this regime, both of the $n = 0$ spin-up and spin-down LLs living in the valance band are shown in Fig. 2.9 (d).

2.3.5 Wave functions

The next goal is to calculate the wave function of the system in the presence of a magnetic field. In order to determine the eigenfunctions for the staggered 2D materials, we already know that for the K valley $\psi_A \propto |n-1\rangle$ and $\psi_B \propto |n\rangle$. The proposed eigenfunction for the K valley is given

$$\Psi_K = \begin{pmatrix} A|n-1\rangle \\ B|n\rangle \end{pmatrix}, \tag{2.136}$$

with determinable constants A and B. The eigenvalue equation yields

$$\begin{pmatrix} \Delta_{K\sigma} & -i\frac{\sqrt{2}\hbar v_F}{l_B} \\ i\frac{\sqrt{2}\hbar v_F}{l_B}a^\dagger & -\Delta_{K\sigma} \end{pmatrix} \begin{pmatrix} A|n-1\rangle \\ B|n\rangle \end{pmatrix} = E \begin{pmatrix} A|n-1\rangle \\ B|n\rangle \end{pmatrix}, \tag{2.137}$$

which can be cast into components forms

$$\Delta_{K\sigma} A|n-1\rangle - i\frac{\sqrt{2}\hbar v_F}{l_B} aB|n\rangle = EA|n-1\rangle \tag{2.138}$$

and

$$i\frac{\sqrt{2}\hbar v_F}{l_B} a^\dagger A|n-1\rangle - \Delta_{K\sigma} B|n\rangle = EB|n\rangle. \tag{2.139}$$

Now using $a^\dagger|n\rangle = \sqrt{n+1}|n+1\rangle$ and $a|n\rangle = \sqrt{n}|n-1\rangle$, Eqs. (2.138) and (2.139), can be rewritten as, respectively,

$$\Delta_{K\sigma} A|n-1\rangle - i\frac{\sqrt{2}\hbar v_F}{l_B} B\sqrt{n}|n-1\rangle = EA|n-1\rangle \tag{2.140}$$

and

$$i\frac{\sqrt{2}\hbar v_F}{l_B} A\sqrt{n}|n-1\rangle - \Delta_{K\sigma} B|n\rangle = EB|n\rangle. \tag{2.141}$$

From Eq. (2.141), we can attempt to eliminate A arriving at the relationship

$$A = \frac{(E + \Delta_{K\sigma})}{i\sqrt{2n\hbar e\overline{B}}v_F}B. \tag{2.142}$$

Now the eigenfunction for the K valley becomes

$$\Psi_K = \begin{pmatrix} \frac{(E+\Delta_{K\sigma})}{\sqrt{2n\hbar e\overline{B}}v_F}B|n-1\rangle \\ B|n\rangle \end{pmatrix}. \tag{2.143}$$

Utilizing the normalization condition $\Psi_K^*\Psi_K = 1$, we obtain

$$\Psi_K = |\bar{n}\rangle\Big|_{\xi=1} = \begin{pmatrix} -iA_n|n-1\rangle \\ B_n|n\rangle \end{pmatrix}, \tag{2.144}$$

where $|n\rangle$ is an orthonormal Fock state of the harmonic oscillator, and A_n and B_n are given by,

$$A_n = \begin{cases} \frac{\sqrt{|E(\xi,\sigma,n,t)|+t\Delta_{\xi\sigma}}}{\sqrt{2|E(\xi,\sigma,n,t)|}}, & \text{if } n \neq 0. \\ \frac{1-\xi}{2}, & \text{if } n = 0. \end{cases} \tag{2.145}$$

and

$$B_n = \begin{cases} \frac{\sqrt{|E(\xi,\sigma,n,t)|-t\Delta_{\xi\sigma}}}{\sqrt{2|E(\xi,\sigma,n,t)|}}, & \text{if } n \neq 0. \\ \frac{1+\xi}{2}, & \text{if } n = 0. \end{cases} \tag{2.146}$$

Similarly, for the K' valley, the wave function is given by

$$\Psi_{K'} = \begin{pmatrix} A|n\rangle \\ B|n-1\rangle \end{pmatrix}. \tag{2.147}$$

The eigenvalue equation for the K' valley is $\hat{H}\Psi_{K'} = E\Psi_{K'}$

$$\begin{pmatrix} \Delta_{K'\sigma} & -i\frac{\sqrt{2}\hbar v_F}{l_B}a^\dagger \\ i\frac{\sqrt{2}\hbar v_F}{l_B}a & -\Delta_{K'\sigma} \end{pmatrix} \begin{pmatrix} A|n\rangle \\ B|n-1\rangle \end{pmatrix} = E \begin{pmatrix} A|n\rangle \\ B|n-1\rangle \end{pmatrix}. \tag{2.148}$$

Once again applying the Hamiltonian on Ψ_K yields

$$\Delta_{K'\sigma}A|n\rangle - i\frac{\sqrt{2}\hbar v_F}{l_B}B\sqrt{n}|n\rangle = EA|n\rangle \tag{2.149}$$

and

$$i\frac{\sqrt{2}\hbar v_F}{l_B}A\sqrt{n}|n-1\rangle - \Delta_{K'\sigma}B|n-1\rangle = EB|n-1\rangle. \tag{2.150}$$

From Eq. (2.150), we can write

$$A = \frac{(E+\Delta_{K'\sigma})}{i\sqrt{2n\hbar eB}v_F}B. \tag{2.151}$$

Substituting Eq. (2.151) into Eq. (2.147) and normalizing the wave function in similar manner as before we obatin

$$\Psi_{K'} = |\bar{n}\rangle\Big|_{\xi=-1} = \begin{pmatrix} -iA_n|n\rangle \\ B_n|n-1\rangle \end{pmatrix} \tag{2.152}$$

$$|\bar{n}\rangle\Big|_{\xi=-1} = \begin{pmatrix} -iA_n|n\rangle \\ B_n|n-1\rangle \end{pmatrix}, \tag{2.153}$$

where A_n and B_n are given by,

$$A_n = \begin{cases} \frac{\sqrt{|E(\xi,\sigma,n,t)|+t\Delta_{\xi\sigma}}}{\sqrt{2|E(\xi,\sigma,n,t)|}}, & \text{if } n \neq 0. \\ \frac{1-\xi}{2}, & \text{if } n = 0. \end{cases} \tag{2.154}$$

$$B_n = \begin{cases} \frac{\sqrt{|E(\xi,\sigma,n,t)|-t\Delta_{\xi\sigma}}}{\sqrt{2|E(\xi,\sigma,n,t)|}}, & \text{if } n \neq 0. \\ \frac{1+\xi}{2}, & \text{if } n = 0. \end{cases} \tag{2.155}$$

The corresponding solutions of eigenstates of the K and K' valleys will be extensively used for the calculation of magneto-optical conductivities in the following chapters and we will also form the basis of the subsequent work.

2.4 3D hybridized topological insulator ultra-thin films in a magnetic Field

In section 1.1.5, we discussed that a bulk system with Dirac-like surface states inside the bandgap is a 3D topological insulator (TI). To begin with, we discuss

how a 3D TI thin film is different from that of graphene and staggered 2D quantum materials. The Dirac fermions in TI thin films share analogous features with graphene, silicene, germanene, and tinene [78]. The top and bottom SSs of 3D TIs are analogous to the K and K' valleys in the graphene family, yet there are key differences between the graphene family and the surface states of a 3D TI. For example, unlike graphene which has four Dirac points, in 3D TI thin films there exists an odd number of not spin degenerate Dirac points at any surface. Additionally, due to SOC, TIs exhibit a distinct spin-momentum locking in SSs [79]. In 3D TI thin film there is only a spin degeneracy $g_s = 2$ for Dirac top and bottom SSs, while in the graphene family, there is also a valley as well as spin degeneracy for the Dirac states.

The hybridization gap in 3D TI thin film provides mass to the otherwise massless Dirac fermions on the top and bottom SSs. Subsequently, the Zeeman energy field with 3D TIs renders the Dirac mass controllable at the top and bottom SSs, which leads to various TQPTs. Unlike the staggered 2D materials, here, we employ a different stimulus to drive TQPTs between different phases from BI to quantum spin Hall (QSH) state in TIs through the application of the magnetic field. To elucidate the surface states dependent LL quantization, we consider the effective Hamiltonian for large group of materials that host topological surface states such as Bi_2Te_3, Bi_2Se_3, Sb_2Te_3 and $(BiSb)Te$ in the presence of an out-of-plane magnetic field in the z direction [78, 80, 81] and spell it out as

$$H_{\sigma\tau} = \hbar v_F(\pi_y\sigma_x - \tau_z\pi_x\sigma_y) + (\tau_z\Delta_z + \Delta_H)\sigma_z, \tag{2.156}$$

where $\pi_i = (k_i + A_i)$ are the gauge-invariant momenta, A_i is the i_{th} component of the magnetic vector potential, $\vec{\sigma} = (\hat{\sigma}_x, \hat{\sigma}_y, \hat{\sigma}_z)$ represent the Pauli matrices of the lattice spin degrees of freedom, τ_z correspond to whether the Dirac surface states are localized near the top ($\tau_z = +1$) or bottom ($\tau_z = -1$) surface and v_F is the Fermi velocity. The term in the Hamiltonian Δ_H represents effective energies induced by the hybridization between the top and bottom SSs of the TI, whereas

the third term captures the Zeeman energy with a band gap of Δ_z=$g\mu_B B/2$. Here g is the surface effective g-factor and μ_B is the Bohr magneton. To determine the eigenmodes of the quantum system, let us define the two ladder operators

$$-i\hbar\frac{\sqrt{2}v_F a}{l_B} = \hbar v_F(\pi_x - i\tau_z(\pi_y - eBx/\hbar)) \tag{2.157}$$

and

$$i\hbar\frac{\sqrt{2}v_F a^\dagger}{l_B} = \hbar v_F(\pi_x + i\tau_z(\pi_y - eBx/\hbar)). \tag{2.158}$$

For $\tau_z = +1$, the Hamiltonian in Eq. (2.156) can be written in matrix form as

$$H_{\tau=+1} = \begin{pmatrix} (\Delta_z + \Delta_H) & -i\hbar\frac{\sqrt{2}v_f a}{l_B} \\ i\hbar\frac{\sqrt{2}v_f a^\dagger}{l_B} & -(\Delta_z + \Delta_H) \end{pmatrix}, \tag{2.159}$$

whereas for $\tau_z = -1$,

$$H_{\tau=-1} = \begin{pmatrix} -(\Delta_z - \Delta_H) & -i\hbar\frac{\sqrt{2}v_f a^\dagger}{l_B} \\ i\hbar\frac{\sqrt{2}v_f a}{l_B} & (\Delta_z - \Delta_H) \end{pmatrix}, \tag{2.160}$$

In terms of two-component spinors, we can define our wave function as

$$|\psi\rangle = \begin{pmatrix} \psi_\uparrow \\ \psi_\downarrow \end{pmatrix}. \tag{2.161}$$

Applying the eigenvalue equation ($\hat{H}\Psi = E\Psi$) to the top surface yields

$$\begin{pmatrix} (\Delta_z + \Delta_H) & -i\hbar\frac{\sqrt{2}v_F a}{l_B} \\ i\hbar\frac{\sqrt{2}v_F a^\dagger}{l_B} & -(\Delta_z + \Delta_H) \end{pmatrix} \begin{pmatrix} \psi_\uparrow \\ \psi_\downarrow \end{pmatrix} = E \begin{pmatrix} \psi_\uparrow \\ \psi_\downarrow \end{pmatrix}, \tag{2.162}$$

which results in

$$(\Delta_z + \Delta_H)\psi_\uparrow - i\frac{\sqrt{2}\hbar v_F}{l_B} a\psi_\downarrow = E\psi_\uparrow \tag{2.163}$$

and

$$i\frac{\sqrt{2}\hbar v_F}{l_B} a^\dagger\psi_\uparrow - (\Delta_z + \Delta_H)\psi_\downarrow = E\psi_\downarrow. \tag{2.164}$$

Eliminating $\psi_\uparrow$ from Eq. (2.163), we obtain

$$\psi_\uparrow = \frac{-i\sqrt{2}\hbar v_F/l_B}{E - (\Delta_z + \Delta_H)} a\psi_\downarrow, \tag{2.165}$$

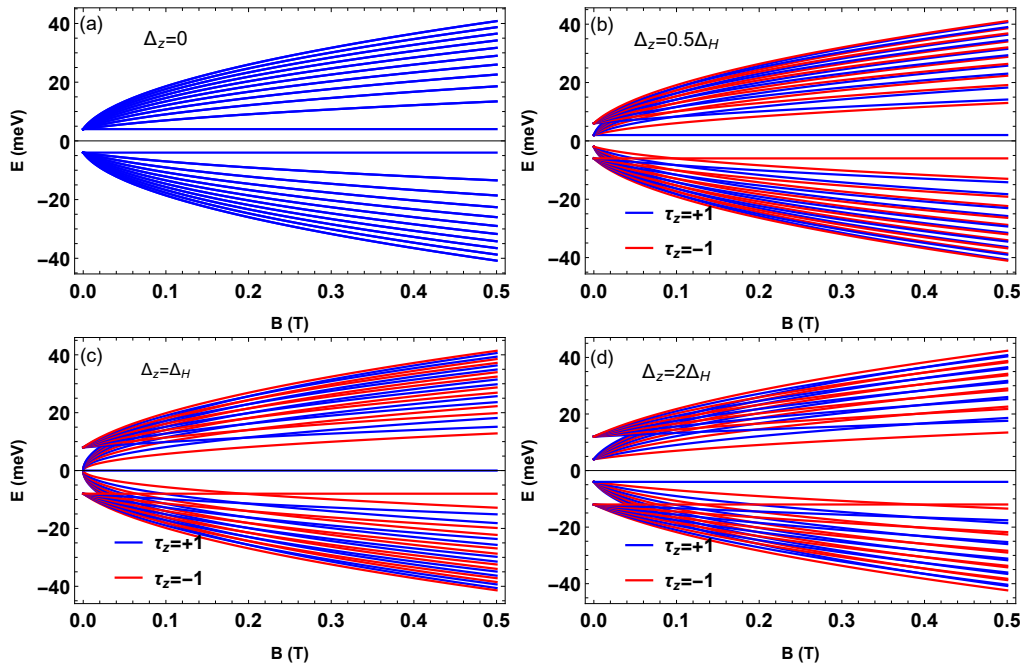

Figure 2.10: Landau level energies as a function of the external magnetic field B for three distinct topological regimes, TI, CNP and NI for top and bottom SSs ($\tau_z = \pm 1$). (a) For $\Delta_z = 0$ the energy spectrum is gapped due to Hybridization energy, and we have a TI phase. (b) For $\Delta_z \neq 0$ but $\Delta_z < \Delta_H$, the degeneracy is lefted but the spctrum is still gapped and we have a TI phase. (c) When $\Delta_z = \Delta_H$, the energy spectrum becomes gappless giving rise to a Dirac point called charge Neutrality point (CNP). (d) For $\Delta_z > \Delta_H$, the energy gap re-opens giving rise to a phase transition from CNP to a NI phase.

and putting Eq. (2.165) into Eq. (2.164), we obtain

$$\frac{2\hbar^2 v_F^2/l_B^2}{E-(\Delta_z+\Delta_H)} a^\dagger a\psi_\downarrow - (\Delta_z+\Delta_H)\psi_\downarrow = E\psi_\downarrow. \tag{2.166}$$

It is clear that $\psi_\uparrow \propto |n-1\rangle$ and $\psi_\downarrow \propto |n\rangle$, then $a^\dagger a\psi_\downarrow = n|n\rangle$, so

$$\frac{2\hbar^2 v_F^2/l_B^2}{E-(\Delta_z+\Delta_H)} n\psi_\downarrow = ((\Delta_z+\Delta_H)+E)\,\psi_\downarrow. \tag{2.167}$$

For $n \neq 0$, the LL dispersion relation of the TI thin film for the top surface state is given by

$$E(\tau_z, n, t) = t\sqrt{E_B^2|n| + \Delta_{\tau_z}^2}, \tag{2.168}$$

For $n = 0$, and for the top surface state, Eq. (2.85) can be written as

$$-(\Delta_z + \Delta_H)\psi_B = E\psi_B. \tag{2.169}$$

The zeroth LLs energy is given by

$$E(\tau_z, 0) = -(\Delta_z + \Delta_H). \tag{2.170}$$

The general dispersion relation for the top and bottom SSs of TIs thin film is given as below

$$E(\tau_z, n, t) = \begin{cases} t\sqrt{E_B^2|n| + \Delta_{\tau_z}^2}, & \text{if } n \neq 0. \\ -\Delta_{\tau_z}, & \text{if } n = 0. \end{cases} \tag{2.171}$$

Here, $t = \text{sgn(n)}$ denotes the electron/hole band, $E_B = v_F\sqrt{2e\hbar B}$ and n is an integer representing Landau quantization.

The CN for the 3D TI thin film can be determined by the Dirac mass and is given by

$$\Delta_{\tau_z} = (\Delta_z + \tau_z\Delta_H). \tag{2.172}$$

In particular, these topological quantum numbers for the TI take the form,

$$\mathcal{C}_\tau = \frac{\tau \mathtt{sgn}(\Delta_{\tau_z})}{2}. \tag{2.173}$$

We note that the energy gap Δ_H can be controlled through the Zeeman interaction energy Δ_z. Here we demonstrate that 3D TI thin films pass through a phase transition from Band insulator (BI) to quantum spin Hall (QSH) states.

In Fig. 2.10(a)–(d) we have shown the LL evolution with respect to the magnetic field. Just like the staggered materials, the zeroth LL is quantum anomalous in the TI thin film. When Δ_z is turned on, the bands become spin-split representing two energy gaps determined by $2\Delta_{min}$ and $2\Delta_{max}$. In the regime $\Delta_z < \Delta_H$, the energy spectrum remains gapped and represents a topological phase, i.e., the QSHI phase as shown in Fig. 2.10(b). The corresponding CN and SS-Chern number $(\mathcal{C}, \mathcal{C}_\tau)$ in this regime are (0, 1). When Δ_z is increased to $\Delta_z = \Delta_H$, the lower

bandgap closes and the system transforms to the charge neutrality point (CNP) state as depicted in Fig. 2.10(c) and the corresponding topological numbers are (1,1/2). Furthermore, increasing Δ_z beyond Δ_H, the bandgap opens up again and the system transforms to the BI phase where the topological numbers are (0,0) as illustrated in Fig. 2.10(d).

2.4.1 Wave functions

The corresponding solutions of eigenstates of the top and bottom surface states are

$$|\bar{n}\rangle\Big|_{\tau_z=1} = \begin{pmatrix} -\alpha_n|n-1\rangle \\ \beta_n|n\rangle \end{pmatrix} \tag{2.174}$$

and

$$|\bar{n}\rangle\Big|_{\tau_z=-1} = \begin{pmatrix} -\alpha_n|n\rangle \\ \beta_n|n-1\rangle \end{pmatrix}, \tag{2.175}$$

where $|n\rangle$ is an orthonormal Fock state of the harmonic oscillator, and $alpha_n$ and $beta_n$ are given by,

$$\alpha_n = \begin{cases} \frac{\sqrt{|E(\tau_z,n,t)|+t\Delta_{\tau_z}}}{\sqrt{2|E(\tau_z,n,t)|}}, & \text{if } n \neq 0. \\ \frac{1-\tau_z}{2}, & \text{if } n = 0. \end{cases} \tag{2.176}$$

and

$$\beta_n = \begin{cases} \frac{\sqrt{|E(\tau_z,n,t)|-t\Delta_{\tau_z}}}{\sqrt{2|E(\tau_z,n,t)|}}, & \text{if } n \neq 0. \\ \frac{1+\tau_z}{2}, & \text{if } n = 0. \end{cases} \tag{2.177}$$

In this section, we explored the LLs quantization of 3D TI thin films in the presence of the magnetic field. In the next chapter, we will derive analytical expressions for the MO longitudinal and Hall conductivities of the TI thin film based on these eigenmodes. With these eigenstructures in hand we will be finally able to evaluate the Faraday and the Kerr rotations and ellipticities, as well as Goos-Hänchen shifts and will be able to describe the photonic spin Hall effect in these materials.

Chapter 3

Quantized magneto-transport in 2D quantum materials

In this chapter, we will describe the basic formalisms that are useful for the main calculations in the forthcoming chapters. We will briefly introduce Green's functions which are the main ingredients for the linear response theory. In the precceding chapter, we discussed the electronic structure of the graphene family and topological insulator in the presence of magnetic field, which is used in the linear response theory for obtaining the magneto-optical conductivity. Finally we show how to determine the magneto-optical spectra of the graphene family, which are useful for discussion of the magneto-optical effects. A fuller background description of linear response theory and Kubo formalism can be found in the references [82, 83].

3.0.1 Introduction

Consider a monolayer graphene system which is exposed to an optical field of frequency Ω. A photon of frequency Ω can be absorbed by exciting an electron from the valance band to the conduction band in the graphene sample. The associated electric field with this photon is given by

$$E(\Omega) = E_0 e^{i\Omega t}. \tag{3.1}$$

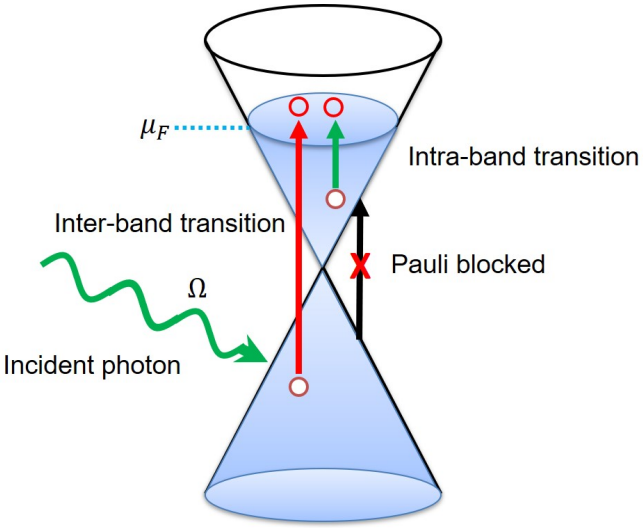

Figure 3.1: Schematic representation of the graphene family conductivity in terms of inter-band and intra-band transitions between energy bands.

The induced current by this electric field is given by Ohm's law

$$J(\Omega) = \sigma(\Omega)E(\Omega), \tag{3.2}$$

where $\sigma(\Omega)$ is the conductivity of the material which measures the response of the material to the applied electric field. It is pertinent to mention here, that the total current density J_{tot} in an optical medium is normally due to two sources. The first source is an optical field that may induce current and the other source is an external current source which generate external current. Thus the total current density is $J_{tot} = J_{ind} + J_{ext}$. As the optical properties of a material is entirely governed by the response of the material to an external optical field, here we suppose that $J_{ext} = 0$ and $J_{tot} = J_{ind}$.

In the graphene family this can be understood in terms of inter-band and intra-band transitions between energy bands. Fig. 3.1 shows the low energy graphene family dispersion for the K valley. The point where the two Dirac cones meet is called the charge neutrality or Dirac point. For a finite chemical potential μ_F, we can see that all the electronic states below the chemical potential are occupied and those above are unoccupied. The inter-band transitions occur when an incident

photon with sufficient energy excite an electron in the lower cone from an occupied state to an unoccupied state in the upper cone thus leaving behind a hole. These transitions are only possible when the electron energies are greater than $2\mu_F$.

On the other hand, we can also have intra-band transitions in which an electron can be excited from a state just below the μ_F to a state just above as shown by green arrow in Fig. 3.1. These electronic transitions are heavily influenced by the chemical potential μ_F and result in the well-known Drude conductivity. By changing the frequency of the incident photon, we can probe the important energy scales and extract information about the band structure.

This process can be best demonstrated in terms of a Feynman diagram as illustrated in Fig. 3.2. We can see that an incident photon with energy $\hbar\omega$ hits the system and creates an electron-hole pair with energy $\hbar\omega + \hbar\Omega$ and $\hbar\omega$, respectively. The associated Green's function are shown in the Feynman bubble.

With the brief introduction to low-energy phenomena of Dirac fermions in graphene and buckled honeycomb lattices with intrinsic SOC presented in the preceding chapter, we are ready to explore the optical conductivity of 2DEG and other 2D systems. In this chapter, we will discuss the linear response theory for obtaining the optical conductivity. The Kubo formalism is useful for discussing inter-band and intraband transitions. It is well known that, in the presence of incident light and applied magnetic field, transitions may occur between Landau levels in these materials. Finally, we will derive analytic expressions for magneto-optical conductivity in the terahertz regime.

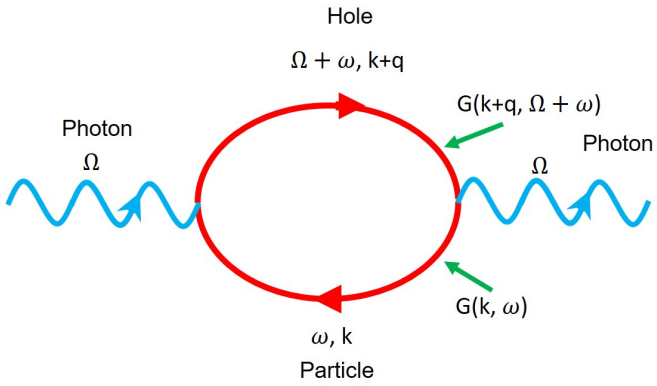

Figure 3.2: Feynman bubble for conductivity.

3.1 Linear response theory

Linear response theory is an extremely popular concept in condensed matter physics. The linear response theory (LRT) was formulated by Kubo in 1957 describing the electrical conductivity in solids and for constructing a statistical-mechanical theory for irreversible thermodynamic processes [84]. Consider an open quantum system say one comprising Dirac electrons, which is placed in an interacting environment. The system will attain an equilibrium state sooner or later depending upon the temperature of the environment and the external stimuli. If the temperature or the external perturbing fields change slowly, in other words, the field is weak, then the system can attain the new equilibrium state instantaneously, and this is called a reversible process. On the contrary, if the perturbing fields change rapidly or the fields are strong, the system will remain far away from the equilibrium and the process is irreversible. In the presence of a perturbing field, the properties of a system coupled to the field, change accordingly. For weak coupling, this change is proportional to the external field. The response (changing properties) to the stimulus (external field) is captured by the linear response function and *is described by retarded Green's functions*. There is also a close relationship between the time-dependent response functions and dynamical properties of the system at equilibrium, also expressed by LRT. The theory is however only

applicable in weak external fields.

In the following section we will derive a formal theory for the linear response of a quantum mechamical system immersed in an external field and discuss some application to the study of the transport properties of 2D systems.

3.1.1 Kubo's prescription for linear response theory

Consider a typical optical experiment, where a weak time dependent electromagnetic (EM) field is impinged on the surface of a metal. By invoking the linear approximation, the electric current density $\vec{J}$ can be related to the EM field $\vec{E}$ by Ohm's law as

$$\vec{J} = \sigma \vec{E}, \tag{3.3}$$

where the constant of proportionality σ is termed conductivity. Our system is quantum mechanical, in thermodynamic equilibrium and descibed by the Hamiltonian H_0. At some time $t = t_0$, an external agent interacts with the system, driving the system out of equilibrium. The perturbed Hamiltonian for this problem takes the form [82, 85]

$$H(t) = H_0 + H_t^{'}\theta(t - t_0), \tag{3.4}$$

where $H_t^{'}$ is the time dependent perturbed Hamiltonian and $\theta(t - t_0)$ is the step function, which ensures that the perturbation starts at $t = t_0$. Suppose that we are doing typical measurement by probing the system through an EM field to measuring an observable quantity A. The next task is to find out the expectation value of the observable A at $t > t_0$ where the expectation value of the observable quantity A as a function of time is given by

$$\langle A(t)\rangle = \frac{1}{Z_0}\sum_n \langle n(t)|A|n(t)\rangle e^{-\beta E_n}, \tag{3.5}$$

where Z_0 is the partitition function, $|n(t)\rangle$ is the time-dependent state and E_n is the eigenvalue of the system. The states $|n(t)\rangle$ of the quantum system evolve

according to the Schrödinger equation

$$i\hbar\frac{\partial}{\partial t}|n(t)\rangle = H(t)|n(t)\rangle, \tag{3.6}$$

It is often convenient to use the interaction reperesentation in which the time dependence of the state is given by

$$|\hat{n}(t)\rangle = \hat{U}(t-t_0)|\hat{n}(t_0)\rangle, \tag{3.7}$$

where ground state has the form

$$|\hat{n}(t_0)\rangle = e^{iH_0t_0/\hbar}|n(t_0)\rangle = |n\rangle \tag{3.8}$$

where $\hat{U}(t,t_0)$ is the unitary opertor which depends on the perturbing part of the Hamiltonian $H^{'}(t)$ and $|\hat{n}(t)\rangle$ is the state in the interaction picture reperesentation. As we are only intereseted in terms linear in the electric field, so we will only keep terms which are linear in $H^{'}(t)$ by expanding the unitary operator

$$\hat{U}(t,t_0) \approx 1 + \frac{i}{\hbar}\int_{t_0}^{t} dt^{'}\hat{H}^{'}(t^{'}). \tag{3.9}$$

Utlizing Eq. (3.7), the state in Schrödinger picture is related with the interaction picture state by the following equation,

$$\begin{aligned} |n(t)\rangle &= e^{iH_0t/\hbar}|\hat{n}(t)\rangle \\ &= e^{iH_0t/\hbar}\hat{U}(t,t_0)|\hat{n}(t_0)\rangle. \end{aligned} \tag{3.10}$$

Substituting Eqs. (3.9) and (3.10) into Eq. (3.5), the expectation value at a given time t up to linear order in perturbation is obtained in the following manner,

$$\begin{aligned} \langle A(t)\rangle = \frac{1}{Z_0}\sum_n \langle\hat{n}(t)|e^{iH_0t/\hbar}\left(1+\frac{i}{\hbar}\int_{t_0}^{t}dt^{'}\hat{H}^{'}(t^{'})\right) \\ \times Ae^{-iH_0t/\hbar}\left(1-\frac{i}{\hbar}\int_{t_0}^{t}dt^{'}\hat{H}^{'}(t^{'})\right)|\hat{n}(t)\rangle e^{-\beta E_n}, \end{aligned} \tag{3.11}$$

which can be further simplified as

$$\begin{aligned}\langle A(t)\rangle &= \langle A\rangle_0 - \frac{i}{\hbar}\int_{t_0}^{t} dt^{'}\frac{1}{Z_0}\sum_n e^{-\beta E_n}\left\langle \hat{n}(t)\right|\left[\hat{A}(t),\hat{H}^{'}(t^{'})\right]\left|\hat{n}(t)\right\rangle \\ &= \langle A\rangle_0 - \frac{i}{\hbar}\int_{t_0}^{t} dt^{'}\frac{1}{Z_0}\sum_n e^{-\beta E_n}\left\langle n(t_0)\right|\left[\hat{A}(t),\hat{H}^{'}(t^{'})\right]\left|n(t_0)\right\rangle \\ &= \langle A\rangle_0 - \frac{i}{\hbar}\int_{t_0}^{t} dt^{'}\sum_n\left\langle\left[\hat{A}(t),\hat{H}^{'}(t^{'})\right]\right\rangle_0, \end{aligned} \tag{3.12}$$

where all the averages $\langle....\rangle_0$ represents an equilibrium which are taken with respect to the H_0. Indeed it is a remakable result in which the non-equilibrium quantity $\langle A(t)\rangle$ can be written in terms of correlation functions of the system. The linear response represented by Eq. (3.12) can be rewritten in terms of retarded correlation function as

$$\delta\langle A(t)\rangle = \langle A(t)\rangle - \langle A(t)\rangle_0 = \int_{t_0}^{\infty} dt^{'} C^R_{AH'}(t,t')\, e^{\eta(t-t')}, \tag{3.13}$$

where

$$C^R_{AH'}(t,t') = -i\theta(t-t')\left\langle\left[\hat{A}(t),\hat{H}^{'}(t^{'})\right]\right\rangle_0. \tag{3.14}$$

Eq. (3.12) is the famous Kubo formula, which can be used for the linear response to an external perturbation. The average in Eq. (3.12) is known as the retarded correlation function, because the response A appears after the perturbation starts $(t > t_0)$.

3.1.2 Kubo formula for optical conductivity

The optical conductivity of a medium implies the induction of current in response to an incident optical field of frequency Ω which connects the current density to the electric field for general frequencies. To derive the optical conductivity from general Kubo formalism, we consider a quantum system for which the eigenstates of H_0 (unperturbed Hamiltonian) are denoted by $|n\rangle$, such that

$$H_0|n\rangle = E_n|n\rangle. \tag{3.15}$$

These states form a complete set, $\sum |n\rangle\langle n| = 1, \langle n \mid m\rangle = \delta_{nm}$. Now there is a weak external EM field H' that varies with time so that the total Hamiltonian is

$$H = H_0 + H'(t). \tag{3.16}$$

Suppose that $H'(t)$ is slowly turned on, *i.e.*, $H'(t \to -\infty) = 0$ and $|\Psi(t = -\infty)\rangle$ is $|n\rangle$. For the time being we set $\hbar = 1.$, and the evalution of state in the interaction picture can be written as

$$|\Psi(t)\rangle_I \equiv e^{iH_0 t}|\Psi(t)\rangle, \tag{3.17}$$

where $|\Psi(t)\rangle$ is the state at time. The ultimate goal is to find this state. Taking derviative of Eq. (3.17) with respect to time t and multiplying by i on both sides, we can write

$$\begin{aligned}
i\frac{d}{dt}|\Psi(t)\rangle_I &= \left(i\frac{d}{dt}e^{iH_o t}\right)|\Psi(t)\rangle + e^{iH_o t} i\frac{d}{dt}|\Psi(t)\rangle \\
&= -H_o e^{iH_o t}|\Psi(t)\rangle + e^{iH_o t}H|\Psi(t)\rangle \\
&= e^{iH_o t}\left(H - H_o\right)|\Psi(t)\rangle \\
&= e^{iH_o t}\left(H - H_o\right)e^{-iH_o t}e^{iH_o t}|\Psi(t)\rangle \\
&= e^{iH_o t}H'(t)e^{-iH_o t}|\Psi(t)\rangle_I \\
&= H'_I(t)|\Psi(t)\rangle_I
\end{aligned} \tag{3.18}$$

It must be noted that $[H'(t_1), H'(t_2)] \neq 0$. By integrating Eq. (3.18) with limits $-\infty$ to t, we obtain

$$\begin{aligned}
|\Psi(t)\rangle_I &= \exp\left[-i\int_{-\infty}^{t} dt' H'_I(t')\right]|n\rangle \\
&= 1 - i\int_{-\infty}^{t} dt' H'_I(t')\,|n\rangle + O\left(H'^2_I\right),
\end{aligned} \tag{3.19}$$

since the perturbation is weak, we are justified in ignoring the 2nd order term in $H'_I(t)$. Eq. (3.17) can be expressed as

$$\begin{aligned} |\Psi(t)\rangle &= e^{-iH_o t}|\Psi(t)\rangle_I \\ &= e^{-iH_o t}\left(1 - i\int_{-\infty}^{t} H'_I(t')\right)|n\rangle \\ &= \left\{e^{-iE_n t} - i\int_{-\infty}^{t} dt' e^{iH_o(t'-t)} H'_I(t) e^{-iH_o t'}\right\}|n\rangle \\ &= e^{-iE_n t}|n\rangle - i\sum_m \int_{-\infty}^{t} dt' e^{iE_m(t'-t)}|m\rangle \langle m|H'|n\rangle e^{-iE_n t'}. \end{aligned} \tag{3.20}$$

Here we introduce the completeness relation,

$$\sum |m\rangle\langle m| = 1, \tag{3.21}$$

allowing us to write

$$|\Psi(t)\rangle = e^{-iE_n t}|n\rangle - i\sum_m |m\rangle e^{-iE_m t}\int_{-\infty}^{t} dt' e^{i(E_m - E_n)t'} \langle m|H'(t')|n\rangle \tag{3.22}$$

In an EM field, the time dependent perturbation is harmonic, say with a fundamental frequency Ω allowing us to decompose the perturbation as

$$\hat{H}'(t) = \hat{h}e^{-i\Omega t} + \hat{h}^\dagger e^{i\Omega t}, \tag{3.23}$$

where

$$\begin{aligned} \langle m|H'(t')|n\rangle &= \langle m|\hat{h}|n\rangle e^{-i\Omega t} + c.c \\ &= V_{mn}e^{-i\Omega t} + c.c. \end{aligned} \tag{3.24}$$

Upon substituting Eq. (3.24) into Eq. (3.22), we obtain

$$|\Psi(t)\rangle = e^{-iE_n t}|n\rangle - i\sum_m e^{-iE_m t}|m\rangle V_{mn} \underbrace{\int_{-\infty}^{t} dt' e^{i(E_m - E_n - \Omega)t'}}_{I(t)} + c.c. \tag{3.25}$$

The integral I is no longer well-defined. Let's assume $\Omega \to \Omega + i\Gamma$.

$$I(t) = \int_{-\infty}^{t} dt' e^{i(E_m - E_n - \Omega - i\Gamma)t'} = \frac{e^{i(E_m - E_n - \Omega)t'}}{i(E_m - E_n - \Omega - i\Gamma)}, \tag{3.26}$$

so that Eq. (3.25) becomes

$$|\Psi(t)\rangle = \left\{ |n\rangle - \sum_m \frac{V_{mn} e^{-i\Omega t}}{(E_m - E_n) - \Omega - i\Gamma} |m\rangle + \sum_m \frac{V^*_{mn} e^{i\Omega t}}{(E_m - E_n) - \Omega + i\Gamma} |m\rangle \right\} e^{-iE_n t}. \tag{3.27}$$

Eq. (3.27) is the time evolved state for any general time dependent perturbation. In next section we will use this state to determine the optical conductivity of the two dimensional electron gas.

3.1.3 Optical conductivity of the two-dimensional electron gas

Consider a two dimensional electron gas (2DEG) which is described by the perturbed Hamiltonian as follows

$$H = \frac{p^2}{2m} + V. \tag{3.28}$$

Here, V is the external potential. In the presence of the EM field, the canonical momentum is modified and is given by Peierls substitution ($\vec{p} - e\vec{A}/c$), which in turn changes the Hamiltonian to

$$H = \frac{\left(\vec{p} - \frac{e}{c}\vec{A}\right)^2}{2m} + V, \tag{3.29}$$

where $\vec{A}$ is the magnetic vector potential, which can be expressed as

$$\vec{A} = \vec{A}_o e^{-i\Omega t} + c.c. \tag{3.30}$$

From elementary electrodynamics, the optical field is given by

$$\begin{aligned} \vec{E} &= -\nabla\phi - \frac{1}{c}\frac{\partial \vec{A}}{\partial t} \\ &= \frac{i\omega}{c}\vec{A}_o e^{-i\Omega t} + c.c \\ &= \vec{E}_o e^{-i\Omega t} + c.c. \end{aligned} \tag{3.31}$$

Now expanding Eq. (3.29) and ignoring higher order term in $\vec{A}$, we obtain

$$H = \frac{p^2}{2m} - \frac{e}{mc} p \cdot A, \tag{3.32}$$

where the first term is unperturbed Hamiltonian H_o and $H'(t)$ represents the perturbation which oscillates at frequency Ω.

$$H = H_o - \frac{e}{mc} p \cdot A_o e^{-i\Omega t}. \tag{3.33}$$

From Eq. (3.31), $A = cE/i\Omega$

$$H = H_o + ie\frac{p \cdot E}{m\Omega} e^{-i\Omega t}. \tag{3.34}$$

Utilizing the Heisenberg equation to calculate the velocity $\vec{\dot{x}}$

$$\begin{aligned} -i\hbar\vec{\dot{x}} &= [H, \vec{x}] = [H_o, \vec{x}] + [H', \vec{x}] \\ &= -2i\hbar\frac{\vec{p}}{2m} - i\hbar\frac{ie}{m\Omega}\vec{E}e^{-i\Omega t} \end{aligned} \tag{3.35}$$

Using the commutation relation for momentum and position operators, we obtain

$$\vec{v} = \frac{\vec{p}}{m} + \frac{ie}{m\Omega}\vec{E}e^{-i\Omega t} - \frac{ie}{m\Omega}\vec{E}e^{i\Omega t}. \tag{3.36}$$

For 2DEG we obtain the time dependent harmonic perturbation as

$$H'(t) = \frac{ie}{m\Omega}\vec{E}e^{-i\Omega t} - \frac{ie}{m\Omega}\vec{E}e^{i\Omega t}. \tag{3.37}$$

The current density is given by

$$\hat{j}_\alpha = \sigma_{\alpha\beta} E_\beta. \tag{3.38}$$

Multiplying both sides with $e^{-i\Omega t}$, we obtain

$$\hat{j}_\alpha e^{-i\Omega t} = \sigma_{\alpha\beta}(\Omega) E_\beta e^{-i\Omega t}. \tag{3.39}$$

Our primary task is to evaluate the expectation value of the current density using the perturbed state

$$\langle \hat{j}_\alpha \rangle = \left\langle \Psi(t) \left| \hat{j}_\alpha \right| \Psi(t) \right\rangle = \langle \Psi(t) \left| e\hat{v}_\alpha \right| \Psi(t) \rangle . \tag{3.40}$$

From Eq. (3.27), the zeroth order perturbed state is given by

$$|\Psi(t)\rangle = e^{-iE_n t}|n\rangle, \tag{3.41}$$

which is utilized to obtain the average current density or the expectation value of current as

$$\langle \hat{j}_\alpha \rangle_{(o)} = \langle \Psi(t) \left| e\hat{v}_\alpha \right| \Psi(t) \rangle = \frac{ie^2}{m\Omega} E_\beta \delta_{\alpha\beta}, \tag{3.42}$$

where E_β is the electric field. Similarly, we determine the first order current expectation value using the perturbed state in Eq. (3.27), as

$$\begin{aligned} \langle \hat{j}_\alpha \rangle_{(1)} &= \langle \Psi(t) \left| \hat{j}_\alpha \right| \Psi(t) \rangle \\ &= \langle n|\hat{j}_\alpha| - \sum_m \frac{V_{mn}}{(E_m - E_n) - \Omega - i\Gamma}|m\rangle \\ &- \langle m|\hat{j}_\alpha| \sum_m \frac{V^*_{mn}}{(E_m - E_n) - \Omega + i\Gamma}|n\rangle, \end{aligned} \tag{3.43}$$

where V_{mn} is given as

$$V_{mn} = \langle m| - \frac{e}{mc}\vec{p}\cdot\vec{A}|n\rangle = \frac{ie}{\Omega} \langle m \left| v_\alpha \right| n \rangle E_\beta. \tag{3.44}$$

Combining the zero'th and first order terms, we obtain

$$\hat{j}_\alpha = \frac{ie^2}{m\Omega} E_\beta \delta_{\alpha\beta} - i\frac{e^2}{\Omega} \sum_m \frac{\langle n \left| v_\alpha \right| m \rangle \langle m \left| v_\beta \right| n \rangle}{(E_m - E_n) - \Omega - i\Gamma} E_\beta + i\frac{e^2}{\omega} \sum_\beta \frac{\langle n \left| v_\beta \right| m \rangle \langle m \left| v_\alpha \right| n \rangle}{(E_m - E_n) + \Omega - i\Gamma} E_\beta. \tag{3.45}$$

Plugging Eq. (3.44) into Eq. (3.45) and using the definition of conductivity in Eq. (3.38), we obtain

$$\sigma_{\alpha\beta} = \frac{ie^2}{m\Omega} \left\{ \delta_{\alpha\beta} - \sum_m m \left\{ \frac{\langle n \left| v_\alpha \right| m \rangle \langle m \left| v_\beta \right| n \rangle}{(E_m - E_n) - \Omega - i\Gamma} - \frac{\langle n \left| v_\beta \right| m \rangle \langle m \left| v_\alpha \right| n \rangle}{(E_m - E_n) + \Omega - i\Gamma} \right\} \right\}. \tag{3.46}$$

The first term is zero because the equilibrium state does not carry any current, so we can write

$$\sigma_{\alpha\beta} = \frac{e^2}{i\Omega} \sum_m \left[\frac{\langle n \left| v_\alpha \right| m \rangle \langle m \left| v_\beta \right| n \rangle}{(E_m - E_n) - \Omega - i\Gamma} + \frac{\langle n \left| v_\beta \right| m \rangle \langle m \left| v_\alpha \right| n \rangle}{(E_m - E_n) + \Omega - i\Gamma} \right] \tag{3.47}$$

The expression in Eq. (3.47) is for a single occupied state. Consider an electron in state $|n\rangle$ which is excited into a state $|m\rangle$, where $|n\rangle \neq |m\rangle$. If there is a Fermi sea in which all levels below fermi energy μ_F are occupied and above μ_F, all are empty, then we can write

$$\sigma_{\alpha\beta}^{Tot} = \sum_{E_n<\mu_F} \sum_{E_m>\mu_F} \sigma_{\alpha\beta}, \tag{3.48}$$

which results in

$$\sigma_{\alpha\beta} = \frac{e^2}{i\Omega} \sum_{n\neq m} f_n \sum_m \frac{\langle n|v_\alpha|m\rangle \langle m|v_\beta|n\rangle}{(E_m - E_n) - \Omega - i\Gamma} + \frac{e^2}{i\Omega} \sum_{n\neq m} f_n \sum_m \frac{\langle n|v_\beta|m\rangle \langle m|v_\alpha|n\rangle}{(E_m - E_n) + \Omega - i\Gamma}, \tag{3.49}$$

where $f_n = 1/(1 + e^{(E_n-\mu_F)/k_BT})$ is the Fermi Dirac distribution function at temperature T and chemical potential μ_F. The above equation can be simplifyingly written as

$$\sigma_{\alpha\beta}(\Omega) = \frac{e^2}{i\Omega} \sum_{n\neq m} (f_n - f_m) \frac{\langle n|j_\alpha|m\rangle \langle m|j_\beta|n\rangle}{(E_m - E_n) + \Omega - i\Gamma}, \tag{3.50}$$

and reintroducing $\hbar$ in the above expression we obtain [86, 87]

$$\sigma_{\alpha\beta}(\Omega) = \frac{i\hbar e^2}{S} \sum_{n\neq m} \frac{f_n - f_m}{(E_n - E_m)} \frac{\langle n|j_\alpha|m\rangle \langle m|j_\beta|n\rangle}{E_m - E_n + \hbar\Omega - i\Gamma}. \tag{3.51}$$

Eq. (3.51) can be used to calculate the optical conductivity of the graphene, silicene, TMDCs, and other 2D materials. To derive the magneto-optical conductivity i.e. in the presence of a magnetic field, Eq. (3.51) can be slightly modified.

3.2 Magneto-optical conductivity of the graphene family

In the previous chapter, we discussed the energy dispersion of the Dirac electrons for the graphene family in the presence of a magnetic field. We have already discovered that unlike 2DEG, where the LLs energies are equally spaced by $\hbar\omega_c$, in

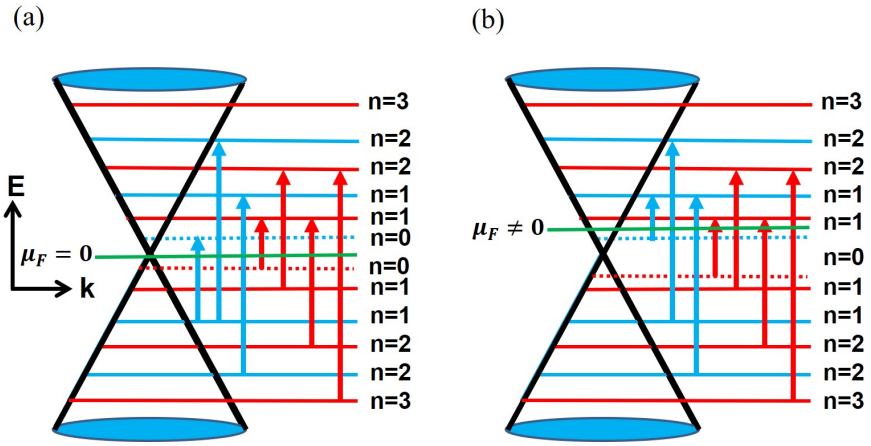

Figure 3.3: Schematic representation of the allowed transitions between LLs for two different chemical potentials in the K valley. (a) $\mu_F = 0$ and (b) $\mu_F \neq 0$.

the graphene family the non-zero LLs energies scale as $\sqrt{B}$.

We will start our derivation of the magneto-optical (MO) conductivity with a brief discussion of LL transitions from an energy band perspective. A schematic of the allowed and Pauli blocked transitions between lower and upper cones for finite chemical potential μ_F are shown in Figs. 3.3(a) and (b). Blue lines represent LLs for the spin up and red lines represent LLs for spin down. The same color scheme applies to the LLs transitions. The LLs are marked on the right and the two values of chemical potential are labeled by the green line. In Fig. 3.3(a), the chemical potential is placed at the charge neutrality point. All the electronic states up to the chemical potential are occupied. The inter-band transitions occur when an incident photon with sufficient energy excites an electron from an occupied state to an unoccupied state thus leaving behind a hole. The LL transitions are heavily influenced by the chemical potential μ_F. When the chemical potential lies in between the n=0 and n=1 LLs then in contrast to charge-neutral graphene, we have inter-band as well as intra-band transitions as illustrated in Fig. 3.3(b).

Our main interest in this chapter is to derive analytical expression of magneto-

optical conductivity for the graphene family. Kubo formula is used to derive the following general expressions for the optical conductivity tensor [83, 88, 89, 90],

$$\sigma_{\mu\nu}(\Omega) = \frac{i\hbar}{2\pi l_B^2} \sum_{\sigma,\xi=\pm 1} \sum_{mn} \frac{f_n - f_m}{E_n - E_m} \frac{\langle \bar{n}|\hat{j}_\mu|\bar{m}\rangle\langle \bar{m}|\hat{j}_\nu|\bar{n}\rangle}{\hbar\Omega - (E_n - E_m) + i\Gamma}, \tag{3.52}$$

where $\hat{j}_\mu = (e/\hbar)\left(\partial\hat{H}/\partial k_\alpha\right)$ is the current density operator, E_n is the energy of the n'th Landau level, Γ is the transport scattering rate responsible for the broadening of the energy levels and $l_B = \sqrt{\hbar/eB}$ is the magnetic length.
In section 2.3.4, we have already derived the energy dispersion and eigen-functions of the staggered 2D materials in the presence of an external magnetic field in section 2.3.4. We are now in a position to use the Kubo formalism to calculate the frequency dependent conductivity of silicene, germanene, stanene and plumbene etc. We start directly from the graphene family Hamiltonian given in Eq. (2.83),

$$\hat{H}_{\xi\sigma} = \hbar v_F(\xi k_x\hat{\tau}_x + k_y\hat{\tau}_y) - \frac{1}{2}\xi\Delta_{so}\hat{\sigma}_z\hat{\tau}_z + \frac{1}{2}\Delta_z\hat{\tau}_z. \tag{3.53}$$

The expectation value of the current density along the x-axis is given by

$$\langle\hat{j}_x\rangle = \frac{e}{\hbar}\frac{\partial\hat{H}_\xi}{\partial k_x} = ev_F\xi\left\langle \bar{n}t\left|\hat{\tau}_x\right|\bar{m}t'\right\rangle, \tag{3.54}$$

where $\hat{\tau}_x$ is the pseudospin Pauli matrix. The normalized eigenfunctions are

$$|\bar{n}\rangle\Big|_{\xi=1} = \begin{pmatrix} -iA_n|n-1\rangle \\ B_n|n\rangle \end{pmatrix} \tag{3.55}$$

and

$$|\bar{n}\rangle\Big|_{\xi=-1} = \begin{pmatrix} -iA_n|n\rangle \\ B_n|n-1\rangle \end{pmatrix}, \tag{3.56}$$

where $|n\rangle$ is an orthonormal Fock state of the harmonic oscillator, and A_n and B_n are given by (as outlined in Eqs (2.145) and (2.146)),

$$A_n = \begin{cases} \frac{\sqrt{|E(\xi,\sigma,n,t)|+t\Delta_{\xi\sigma}}}{\sqrt{2|E(\xi,\sigma,n,t)|}}, & \text{if } n \neq 0. \\ \frac{1-\xi}{2}, & \text{if } n = 0. \end{cases} \tag{3.57}$$

and

$$B_n = \begin{cases} \frac{\sqrt{|E(\xi,\sigma,n,t)|-t\Delta_{\xi\sigma}}}{\sqrt{2|E(\xi,\sigma,n,t)|}}, & \text{if } n \neq 0. \\ \frac{1+\xi}{2}, & \text{if } n = 0. \end{cases} \tag{3.58}$$

The current operator evaluates as

$$\begin{aligned} \langle \hat{j}_x \rangle = ev_F\xi \langle \bar{n}t \,|\hat{\tau}_x|\, \bar{m}t' \rangle &= ev_F\xi \begin{pmatrix} iA_{n,t}\langle n-1| & B_{n,t}\langle n| \end{pmatrix} \begin{pmatrix} 0 & 1 \\ 1 & 0 \end{pmatrix} \\ &\times \begin{pmatrix} -iA_{m,t'}|m-1\rangle \\ B_{m,t'}|m\rangle \end{pmatrix} \\ &= ev_F\xi(iA_{n,t}B_{m,t'}\delta_{n-1,m} - iB_{n,t}A_{m,t'}\delta_{n+1,m}). \end{aligned} \tag{3.59}$$

Similarly, we also have

$$\begin{aligned} \langle \hat{j}_x \rangle = ev_F\xi \langle \bar{m}t' \,|\hat{\tau}_x|\, \bar{n}t \rangle &= ev_F\xi \begin{pmatrix} iA_{m,t'}\langle m-1| & B_{m,t'}\langle n| \end{pmatrix} \begin{pmatrix} 0 & 1 \\ 1 & 0 \end{pmatrix} \\ &\times \begin{pmatrix} -iA_{n,t}|n-1\rangle \\ B_{n,t}|n\rangle \end{pmatrix} \\ &= ev_F\xi(iA_{m,t'}B_{n,t}\delta_{m-1,n} - iB_{m,t'}A_{n,t}\delta_{m+1,n}). \end{aligned} \tag{3.60}$$

The product of the previous two conductivity expressions can be calculated as

$$\begin{aligned} &e^2v_F^2\xi(iA_{n,t}B_{m,t'}\delta_{n-1,m} - iB_{n,t}A_{m,t'}\delta_{n+1,m})(iA_{m,t'}B_{n,t}\delta_{m-1,n} - iB_{m,t'}A_{n,t}\delta_{m+1,n}) \\ &= (A_{m,t'}B_{n,t})^2\delta_{m-1,n} + (B_{m,t'}A_{n,t})^2\delta_{m+1,n} - 2A_{m,t'}B_{n,t}B_{m,t'}A_{n,t}\delta_{m+1,n}\delta_{m-1,n}, \end{aligned} \tag{3.61}$$

where the last term involves two Kronecker δ-functions, so it is zero. Eq.(3.61), becomes

$$\langle \bar{n}s \,|\hat{\tau}_x|\, \bar{m}t' \rangle \langle \bar{m}t' \,|\hat{\tau}_x|\, \bar{n}t \rangle = (A_{m,t'}B_{n,t})^2\delta_{m-1,n} + (B_{m,t'}A_{n,t})^2\delta_{m+1,n}. \tag{3.62}$$

Substituting Eq.(3.62) into Eq.(3.52), we obtain

$$\sigma_{xx}(\Omega) = \frac{i\hbar e^2v_F^2}{2\pi l_B^2} \sum_{\sigma,\xi=\pm1} \sum_{mn} \frac{f_n - f_m}{E_n - E_m} \frac{(A_{m,t'}B_{n,t})^2\delta_{m-1,n} + (B_{m,t'}A_{n,t})^2\delta_{m+1,n}}{\hbar\Omega - (E_n - E_m) + i\Gamma}, \tag{3.63}$$

we can drop the band indices as $t = t' = \pm 1$. So the expression for the longitudinal conductivity take the form

$$\sigma_{xx}(\Omega) = \frac{i\hbar e^2 v_F^2}{2\pi l_B^2} \sum_{\sigma,\xi=\pm 1} \sum_{mn} \frac{\Theta(E_n - \mu_F) - \Theta(E_m - \mu_F)}{E_n - E_m} \frac{(A_m B_n)^2 \delta_{m-1,n} + (B_m A_n)^2 \delta_{m+1,n}}{\hbar\Omega - (E_n - E_m) + i\Gamma}. \tag{3.64}$$

To express the conductivity explicitly in real and imaginary parts, we multiply and divide Eq. (3.64) by $\hbar\Omega - (E_n - E_m) - i\Gamma$.

$$\begin{aligned}\sigma_{xx}(\Omega) = \frac{i\hbar e^2 v_F^2}{2\pi l_B^2} \sum_{\sigma,\xi=\pm 1} \sum_{mn} & \frac{\Theta(E_n - \mu_F) - \Theta(E_m - \mu_F)}{E_n - E_m} \\ & \times \frac{(A_m B_n)^2 \delta_{m-1,n} + (B_m A_{n,t})^2 \delta_{m+1,n}}{\hbar\Omega - (E_n - E_m) + i\Gamma} \times \frac{\hbar\Omega - (E_n - E_m) - i\Gamma}{\hbar\Omega - (E_n - E_m) - i\Gamma}. \end{aligned} \tag{3.65}$$

Finally, at $T = 0$ K we can compute the real and imaginary parts of the longitudinal conductivity as follows [76, 89]

$$\begin{aligned}\frac{\left.\begin{matrix}\mathrm{Re}\\ \mathrm{Im}\end{matrix}\right\}\big(\sigma_{xx}(\Omega)\big)}{\sigma_0} = \frac{2v^2\hbar eB}{\pi} \sum_{\xi,\sigma} \sum_{m,n} & \frac{\Theta(E_n - \mu_F) - \Theta(E_m - \mu_F)}{E_n - E_m} \\ & \times \Big[(A_m B_n)^2 \delta_{|m|-\xi,|n|} + (B_m A_n)^2 \delta_{|m|+\xi,|n|}\Big] \begin{cases} F_{nm} \\ G_{nm} \end{cases}, \end{aligned} \tag{3.66}$$

where

$$F_{nm} = \frac{\Gamma}{\Big((\hbar\Omega - (E_n - E_m))^2 + \Gamma^2\Big)} \tag{3.67}$$

and

$$G_{nm} = \frac{\hbar\Omega - (E_n - E_m)}{\Big((\hbar\Omega - (E_n - E_m))^2 + \Gamma^2\Big)}. \tag{3.68}$$

In these expressions, $\sigma_0 = e^2/4\hbar$ is the universal conductivity. The Kronecker deltas ensure the rules for electric dipole transitions between the LL's are satisfied. The Heaviside functions $\Theta(E_n - \mu_F)$ ensure that only transitions across the Fermi level are possible, hence they effectively account for the so-called Pauli blocking [91, 92]. There are certain specific selection rules for LL transitions [92].

Similarly, for transverse Hall conductivity the spatial index are $\alpha = x$ and $\beta = y$, Eq. (3.52) becomes

$$\sigma_{xy}(\Omega) = \frac{i\hbar}{2\pi l_B^2} \sum_{\sigma,\xi=\pm 1} \sum_{mn} \frac{f_n - f_m}{E_n - E_m} \frac{\langle \bar{n}|\hat{j}_x|\bar{m}\rangle\langle \bar{m}|\hat{j}_y|\bar{n}\rangle}{\hbar\Omega - (E_n - E_m) + i\Gamma}. \tag{3.69}$$

The current density matrix along the y direction can be determined as

$$\begin{aligned}\langle \hat{j}_y \rangle = ev_F \langle \bar{m}t' |\hat{\tau}_y| \bar{n}t\rangle &= ev_F \begin{pmatrix} iA_{m,t'}\langle m-1| & B_{m,t'}\langle n| \end{pmatrix} \begin{pmatrix} 0 & -i \\ i & 0 \end{pmatrix} \begin{pmatrix} -iA_{n,t}|n-1\rangle \\ B_{n,t}|n\rangle \end{pmatrix} \\ &= ev_F(A_{m,t'}B_{n,t}\delta_{m-1,n} + B_{m,t'}A_{n,t}\delta_{m+1,n}).\end{aligned}$$

The product of $\langle \hat{j}_x \rangle$ and $\langle \hat{j}_y \rangle$ is given by

$$\langle \bar{n}|\hat{\tau}_x|\bar{m}\rangle \langle \bar{m}|\hat{\tau}_y|\bar{n}t\rangle = (A_m B_n)^2 \delta_{m-1,n} - (B_m A_n)^2 \delta_{m+1,n}. \tag{3.70}$$

Here, the Eq. (3.69) can be recast as

$$\sigma_{xy}(\Omega) = \frac{i\hbar e^2 v_F^2}{2\pi l_B^2} \sum_{\sigma,\xi=\pm 1} \sum_{mn} \frac{\Theta(E_n - \mu_F) - \Theta(E_m - \mu_F)}{E_n - E_m} \frac{(A_m B_n)^2 \delta_{m-1,n} - (B_m A_n)^2 \delta_{m+1,n}}{\hbar\Omega - (E_n - E_m) + i\Gamma}. \tag{3.71}$$

In the same fashion, the real and imaginary parts of the transverse Hall conductivity are given [76, 89]

$$\begin{aligned}\frac{\left.\begin{matrix}\text{Re} \\ \text{Im}\end{matrix}\right\}\big(\sigma_{xy}(\Omega)\big)}{\sigma_0} &= \frac{2v^2\hbar eB}{\pi} \sum_{\xi,\sigma} \sum_{m,n} \xi \frac{\Theta(E_n - \mu_F) - \Theta(E_m - \mu_F)}{E_n - E_m} \\ &\quad \times \Big[(A_m B_n)^2 \delta_{|m|-\xi,|n|} - (B_m A_n)^2 \delta_{|m|+\xi,|n|}\Big] \begin{cases} -G_{nm} \\ F_{nm} \end{cases}. \end{aligned} \tag{3.72}$$

These are the analytical expressions for both longitudinal and transverse conductivities of the graphene family subjected to external electric and magnetic fields. These conductivities display interesting physics as functions of the incident light frequency Ω, the chemical potential μ_F, temperature T, and applied magnetic field B. We will be exploring these properties shortly. In the limit $\Delta_{so} = \Delta_z = 0$, we recover graphene's Hall conductivity [91]. For these expressions, the real (imaginary)

part of $\sigma_{xx}(\sigma_{xy})$ is a sum of absorptive Lorentzians, each of whose FWHM depends on the scattering rate Γ; a higher Γ resulting in broader and shorter peaks. Likewise, the real (imaginary) part of $\sigma_{xy}(\sigma_{xx})$ is a sum of dispersive Lorentzian. These peaks are positioned at $\hbar\Omega = (E_n - E_m)$, which we call the magneto-excitation energies. The transitions obey the appropriate selection rules namely $|n| - |m| = \pm 1$ and the conservation of real spin implying that transitions between $\sigma = +1$ and -1 levels are spin forbidden.

It is worth discussing the magneto-optical conductivities for different magnetic fields in the TI regime. The relevant parameters used are $\Delta_z = 0.5\Delta_{so}$ and chemical potential $\mu_F = 0$. We quickly recount the effect of the magnetic field on the energy level structure and subsequently the MO response. Schematic diagrams showing the allowed transitions between Landau levels (LL's) for three different magnetic field (B =1, 3 and 5 T) all in the topological insulator regime ($\Delta_z < \Delta_{so}$) and in the K valley are shown in Fig. 3.4(a)–(c). The transition energy is determined from the energy difference between LL's obeying certain selection rules namely $|n| - |m| = \pm 1$ and the conservation of real spin implying that transitions between $\sigma = +1$ and -1 levels are spin forbidden.

The excitation energies corresponding to the different transitions, $E_{m,K(K'),\uparrow(\downarrow)} \rightarrow E_{n,K(K'),\uparrow(\downarrow)}$ are labelled as $\Delta_{mn,K(K'),\uparrow(\downarrow)}$. Blue lines represent Landau levels for spin up ($\sigma =\uparrow$) and red lines represent Landau levels for spin down ($\sigma =\downarrow$) [76]. In each of the depicted transitions, one of the participating levels is an n=0 level.

For example for $B = 1$ T, the first and second magneto-excitation energies correspond to the $\Delta_{-10,K,\uparrow}$ and $\Delta_{01,K,\downarrow}$ for spin up and spin down respectively and are calculated at 20.3 meV (4.9 THz) and 25.1 meV (6.1 THz) respectively. Explicit values of these MO transitions are summarized in Table 3.1.

A static electric field E_z, controls the electronic band structure of the 2D staggered

Table 3.1: Table of allowed transitions in K valley in the $n = -1, 0, 1$ subspace, for different magnetic fields in the TI regime with $\Delta_{so} = 0.5\Delta_z$.

$\Delta_{mn,K(K'),\uparrow(\downarrow)}$	B (T)	Frequency (THz)
$\Delta_{-10,K,\uparrow}$	1	4.9
$\Delta_{01,K,\downarrow}$	1	6.1
$\Delta_{-10,K,\uparrow}$	3	8.1
$\Delta_{01,K,\downarrow}$	3	9.2
$\Delta_{-10,K,\uparrow}$	5	10.3
$\Delta_{01,K,\downarrow}$	5	11.4

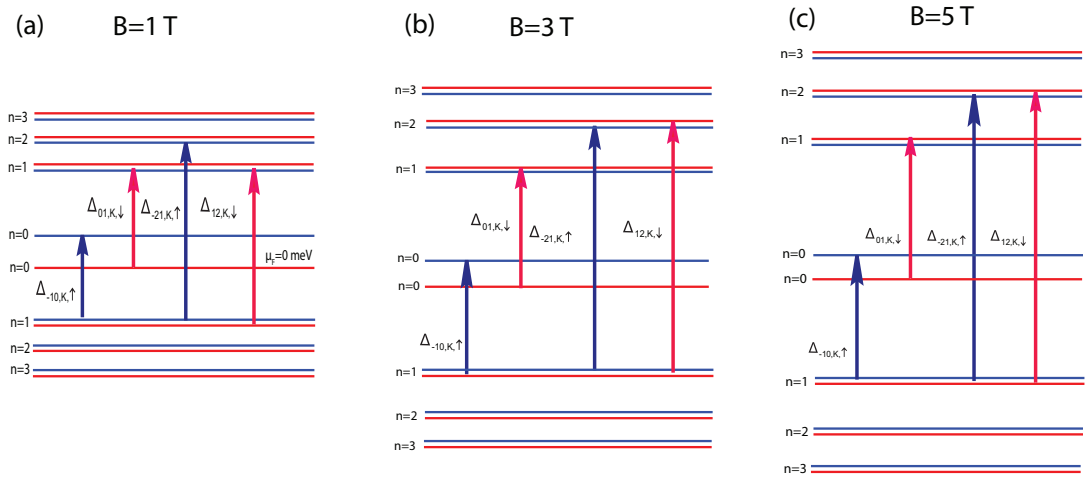

Figure 3.4: Schematic representation of the allowed transitions between LLs for three different magnetic fields in the K valley for magnetic field (a) 1 T (b) 3 T (c) 5 T. Blue lines represent Landau levels for spin up ($\sigma =\uparrow$) and red lines represent Landau level for spin down ($\sigma =\downarrow$). The same color scheme applies for the Landau levels transitions.

graphene family by generating a staggered sublattice potential Δ_z. An increase in the electric field triggers a well-known quantum phase transition that occurs from topological insulator to band insulator state [65]. Fig. 3.5(d) shows the longitudinal conductivity versus photon energy for various values of Δ_z. As we increase the applied electric field Δ_z, each interband peak splits into two spin-polarized peaks in the TI regime ($\Delta_z < \Delta_{so}$). Concomitantly, due to a redistribution of spectral weight, the intensity of the peaks is reduced for larger fields values. When $\Delta_z = \Delta_{so}$, the gap of one of the spin-split bands closes and a new type of metallic

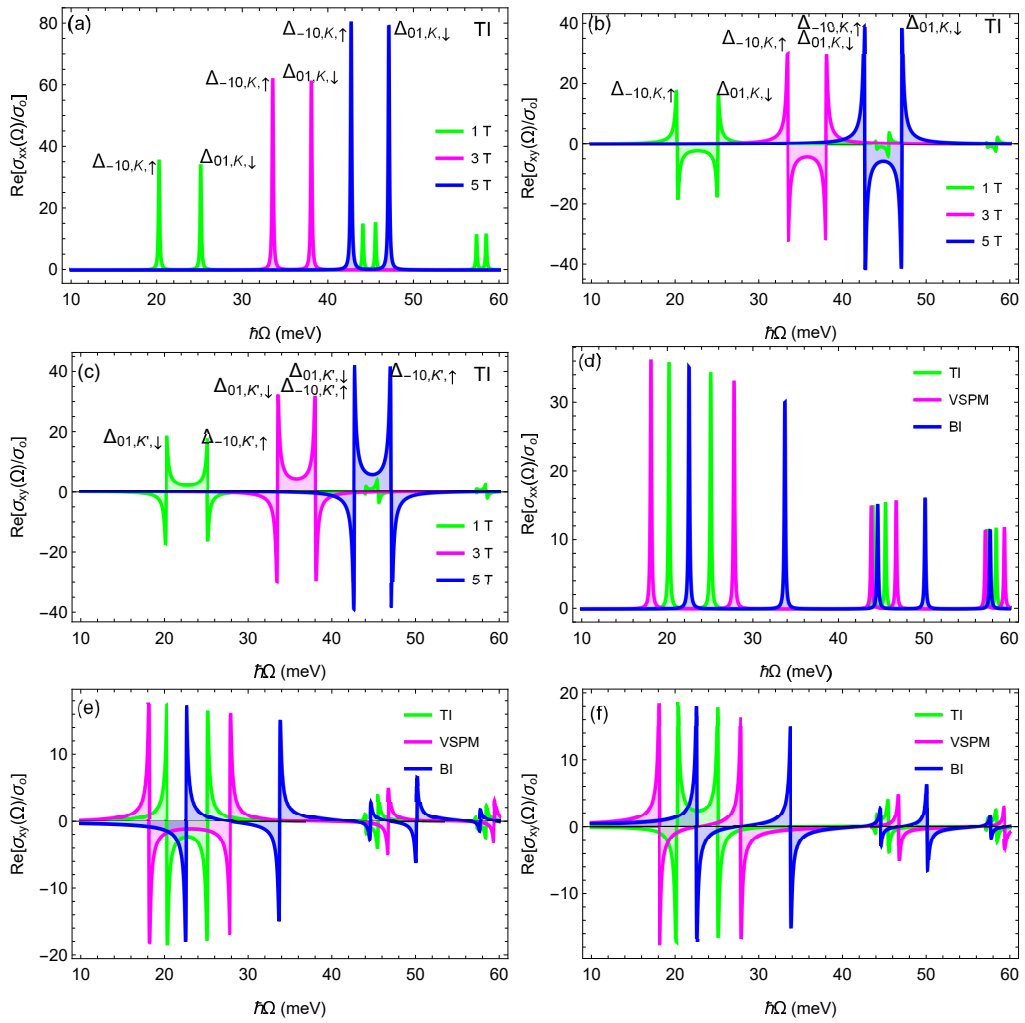

Figure 3.5: Longitudinal and transverse Hall conductivities as a function of photonic energy for different magnetic fields in the TI regime. (a) Longitudinal conductivities in the K and K' valleys, respectively. (b) and (c) Hall conductivities in the K valley and K' valleys, respectively. Longitudinal and transverse Hall conductivities as a function of photonic energy for magnetic field of 1 T in different topological regimes. (d) Longitudinal conductivities in the K and K' valleys, respectively. (e) and (f) Hall conductivities in the K valley and K' valleys, respectively. The parameters used are Δ_z=8 meV, $\Delta_z = 0.5\Delta_{so}$ and chemical potential $\mu_F = 0$.

phase emerges called the valley-spin polarized metal (VSPM) state.

At the VSPM point, the lowest frequency peaks, move apart: the $\Delta_{-10,K,\uparrow}$ peak

Table 3.2: Table of allowed transitions in K valley in the $n = -1, 0, 1$ subspace, for $B = 1$ T in three different topological regimes for $\Delta_{so} = 8$ meV.

$\Delta_{mn,K(K'),\uparrow(\downarrow)}$	Δ_z (meV)	Regime	Photonic energy (meV)
$\Delta_{-10,K,\uparrow}$	0	TI	22.6
$\Delta_{01,K,\downarrow}$	0	TI	22.6
$\Delta_{-10,K,\uparrow}$	4	TI	20.3
$\Delta_{01,K,\downarrow}$	4	TI	25.1
$\Delta_{-10,K,\uparrow}$	8	VSPM	18.2
$\Delta_{01,K,\downarrow}$	8	VSPM	27.8
$\Delta_{-10,K,\uparrow}$	16	BI	33.8
$\Delta_{01,K,\downarrow}$	16	BI	22.6

is red-shifted while the $\Delta_{01,K,\downarrow}$ peak is blue shifted. The excitation energies corresponding to the first two peaks at the VSPM point are now 18.2 meV (4.4 THz) and 27.8 meV (6.7 THz) for the spin up and down, respectively. Further increasing Δ_z results in re-opening of the gaps and the system transitions from the VSPM to the band insulator (BI) state. In the BI regime, all interband peaks move to higher energies. The magneto-excitations frequencies are presented in Table 3.2 for the first two transitions in three different regimes. The main role of the electric field is that it controls the band structure and is responsible for spin and valley polarized responses, and therefore, quite similar to magnetic fields, also controls the magneto-optic excitation energies [76].

The MO conductivity of the graphene family in the THz regime, besides its dependence on several other parameters (e.g, the polarization of incident beam, frequency ω, scattering rate Γ), is heavily influenced by chemical potential μ_F as expressed in Eqs. (3.70) and (3.71) [76]. In this chapter, we described the basic underlying physics for the optical conductivities of 2D materials. We started with the linear response theory, which is the main character. Using the Kubo formalism we derived the general optical conductivity expression for the 2DEG which is equally applicable to the 2D materials. Finally, we were able to derive and discuss

the longitudinal and Hall magneto-optical conductivities.

Chapter 4

Magneto-optic polarization re-orientation effects in 2D quantum materials

This chapter mainly addresses the magneto-optical effects in two different quantum materials, in particular the polarization re-orientation affected by these materials. In the first part of this chapter, we discuss the response of staggered 2D quantum materials. We will calculate the Fresnel coefficients of silicene by using the magneto-optic conductivity derived in Section 3.2. They are then used to determine unusually large Faraday and Kerr rotations and ellipticity. In the second part, we will study the response of the 3D hybridized topological insulator thin films in the presence of a perpendicular magnetic field. The mathematical formalism developed in the previous chapter will be heavily employed. Material in this chapter has been published in *Optics Express* [76] and *Optical Materials Express* [81].

4.1 Faraday and Kerr rotation for the Landau level manifold of 2D lattices with spin-orbit interaction

4.1.1 Background and motivation

Monolayer graphene has garnered immense interest from a large global community of researchers. This is primarily due to its unique electronic and optical properties [33] derived from its exotic electronic structure. For example, graphene possesses a gapless Dirac-type band structure [34], high carrier mobilities and universal broadband optical conductivities (due to interband transitions) [93]. Due to its fascinating optical properties, graphene is also considered to be a promising material for photonic and optoelectronic applications in the terahertz (THz) to mid-infrared ranges.

For example, Faraday and Kerr rotations are non-reciprocal magneto-optic (MO) effects, in which the polarization of a plane wave is rotated when linearly polarized light is respectively transmitted or reflected from a transparent medium in the presence of a static uniform perpendicular magnetic field B. Both of these effects originate from the breaking of time-reversal symmetry by an external applied magnetic field. Graphene exhibits an exceptionally large Faraday and Kerr rotation in the THz region and therefore is considered a futuristic candidate for non-reciprocal tunable devices [94, 95, 96]. The magnitude of FR is about 6° in a field of strength 7 T. Unfortunately, the FR and magneto-optic Kerr effects (MOKE) observed in a single layer graphene sheet exist only at low frequencies (< 3 THz) and that too in the presence of large magnetic fields.

Graphene shares analogous properties with a large range of 2D quantum materials [26]. For example, recently, transition metal dichalcogenides (TMDC) have attracted a lot of attention due to their novelty [26, 27]. TMDC's have the formula

MX_2, where M is a transition metal element (Mo, W, V, etc) and X is a chalcogen atom (S, Se, or Te). TMDC's are of particular interest because they possess a valley degree of freedom and exhibit large band gaps due to SOI [97]. These interesting spin-valley structures make TMDC's highly attractive candidates for spintronic, valleytronic [27, 97, 98, 99] and optoelectronic devices [100, 101].

The discovery of 2D materials has also stimulated growing interest in silicene [64], the silicon analog of graphene. Stable silicene can be experimentally synthesized [24]. There are many electronic and physical similarities between graphene and silicene as both are found in the same group of the periodic table. The major difference is that silicene has a large SOC with an electrically tunable bandgap. Just like silicene, germanene and tinene also possess stable honeycomb lattice structures [24, 25]. Due to the relatively large SOI, these materials have buckled structures, providing a mass to the otherwise massless Dirac fermions. In silicene [65], germanene [66] and tinene [67], the values of Δ_{so} have been predicted to lie in the range 1.55–7.9 meV, 24–93 meV, and 100 meV respectively. Subsequently, the interaction of an external electric field with silicene, germanene, and the tinene-substrate system renders the Dirac mass controllable at the K and K' points, which leads to various topological phase transitions [68].

In addition to charge and spin, which are intrinsic degrees of freedom, Dirac electrons have another degrees of freedom called the valley [37, 102, 103]. The valley can also be used to encode and process information, this is the now burgeoning field of valleytronics [37]. A promising platform for valleytronics is provided by silicene. Due to spin and valley polarized responses, silicene also offers the possibility to realize novel tuneable MO devices [102, 104]. The possibility of dynamic adaptability of silicene's electronic structure via electric and magnetic fields makes it favorable for tuneable THz applications. However, the two most important MO responses namely FR and MOKE of monolayer silicene and the wider class of Dirac

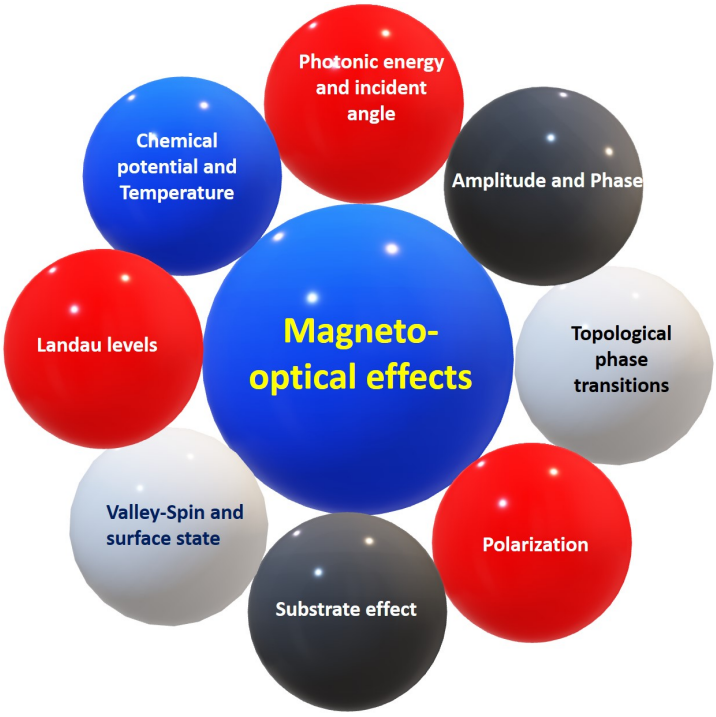

Figure 4.1: Overview of magneto-optic effects in 2D quantum material.

materials deserve a rigorous exploration.

The purpose of this work is to study FR and MOKE in these 2D lattices. Subsequently, the magnetic field-dependent MO effects can be directly utilized for magnetic field sensing and optical modulation [105, 106, 107]. Furthermore, we also investigate the dependence of these MO effects on the incident angle, polarization state, chemical potential, and temperature, an overview is shown in Fig. 4.1. The present part of this chapter is divided into the following sections. In Section 4.1.2, we will derive the Fresnel's coefficients. In Section 4.1.3, we discuss the theoretical background for the magneto-optic Kerr effect and Faraday rotation. Finally, we present the results for our simulative investigations followed by a discussion in Section 4.1.4.

4.1.2 Fresnel coefficients

We now present a general method to calculate the Faraday and Kerr rotation angles and the resulting ellipticities. Due to the rich LL structure, these MO effects are modulated by myriad stimuli such as electric and magnetic fields [94, 108, 109], chemical potential gating [108], modification through doping, optical pumping [110] as well as temperature [111] and the substrate effect [94].

Let us consider the situation depicted in Fig. 4.2. We consider a well-collimated, monochromatic, Gaussian beam of light with nontotal reflection impinging from one medium to the planar interface of the silicene-substrate system at an incidence angle θ_1. The beam of light of frequency Ω has polarization in an arbitrary direction, and is propagating through the incident and transmitted materials with *relative* permittivity and permeability ε_n and μ_n respectively, where n = (1,2). The beam make an angle θ_2 in the substrate which is assumed to be semi-infinite, obviating the need to consider finite substrate size effects and thin-film interference [112]. Consider that the substrate is a non-magnetic material, i. e. $\mu_1 = \mu_0$. The wave vectors are k_1 and k_2, $k_n = \Omega\sqrt{\mu_n\varepsilon_n}$, $Z_n = Z_0\sqrt{\mu_n/\varepsilon_n}$ and $Z_0 = \sqrt{\mu_0/\varepsilon_0}$, where μ_0 and ε_0 are the vacuum permeability and permittivity respectively.
The corresponding arbitrarily polarized impinging, reflected and transmitted electric and magnetic fields are given by [113]

$$\mathbf{E}_i = \left[E_i^s\epsilon_{s,1}^+ + E_i^p\epsilon_{p,1}^+\right] e^{-ik_{z,1}z}e^{i(\mathbf{k}\cdot\mathbf{x}-\omega t)}, \tag{4.1}$$

$$\mathbf{H}_i = \frac{1}{Z_1}\left[E_i^p\epsilon_{s,1}^+ - E_i^s\epsilon_{p,1}^+\right] e^{-ik_{z,1}z}e^{i(\mathbf{k}\cdot\mathbf{x}-\omega t)}, \tag{4.2}$$

$$\mathbf{E}_r = \left[E_r^s\epsilon_{s,1}^- + E_r^p\epsilon_{p,1}^-\right] e^{ik_{z,1}z}e^{i(\mathbf{k}\cdot\mathbf{x}-\omega t)}, \tag{4.3}$$

$$\mathbf{H}_r = \frac{1}{Z_1}\left[E_r^p\epsilon_{s,1}^- - E_r^s\epsilon_{p,1}^-\right] e^{ik_{z,1}z}e^{i(\mathbf{k}\cdot\mathbf{x}-\omega t)}, \tag{4.4}$$

and

$$\mathbf{E}_t = \left[E_t^s\epsilon_{s,2}^+ + E_t^p\epsilon_{p,2}^+\right] e^{-ik_{z,2}z}e^{i(\mathbf{k}\cdot\mathbf{x}-\omega t)}, \tag{4.5}$$

$$\mathbf{H}_r = \frac{1}{Z_2}\left[E_t^p\epsilon_{s,2}^+ - E_t^s\epsilon_{p,2}^+\right] e^{-ik_{z,2}z}e^{i(\mathbf{k}\cdot\mathbf{x}-\omega t)}. \tag{4.6}$$

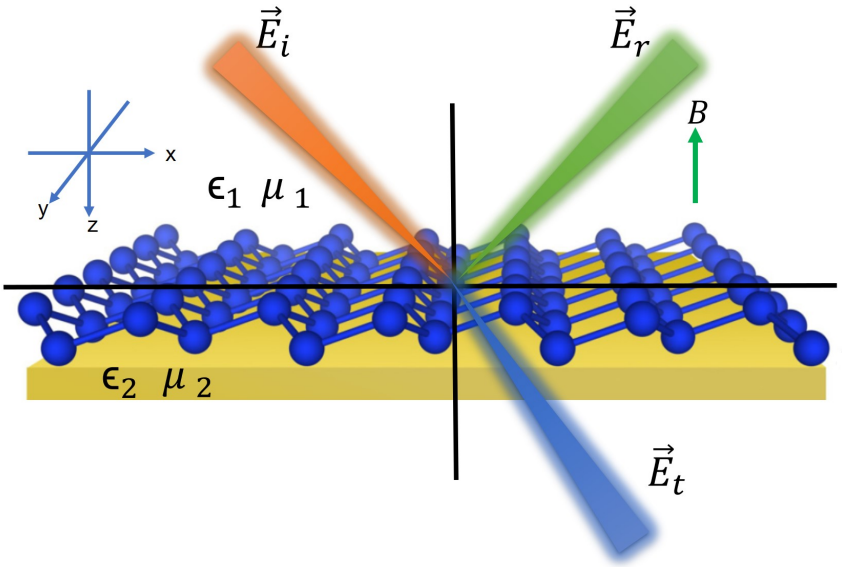

Figure 4.2: Schematic view of a monochromatic plane wave impinging on the surface of staggered 2D quantum material.

The polarization vectors are given by

$$\epsilon_s^{\pm} = \frac{k_y\hat{\mathbf{x}} - k_x\hat{\mathbf{y}}}{k}, \tag{4.7}$$

$$\epsilon_p^{\pm} = \frac{k\hat{\mathbf{z}}}{k_0} \pm \frac{k_z}{k_0}\frac{k_x\hat{\mathbf{x}} + k_y\hat{\mathbf{y}}}{k}, \tag{4.8}$$

where

$$k_z = \begin{cases} \sqrt{k_0^2 - k_x^2 - k_y^2} & = \sqrt{k_0^2 - k^2}, \quad k < k_0 \\ i\sqrt{k_x^2 + k_y^2 - k_0^2} & = i\sqrt{k^2 - k_0^2}, \quad k > k_0 \end{cases} \tag{4.9}$$

and the $+$ and $-$ signs correspond to $z > z'$ and $z < z'$, respectively. It must be noted these polarization vectors are orthogonal and normalized only for propagating modes ($k < k_0$). The relationship of the s and p polarized reflected and transmited coefficients are determined by the ratio of the reflected and incident amplitudes:

$$r_{\mathrm{i,j}} = \frac{\mathbf{E}_r^{\mathrm{i}}}{\mathbf{E}_i^{\mathrm{j}}} \quad \text{and} \quad t_{\mathrm{i,j}} = \frac{\mathbf{E}_t^{\mathrm{i}}}{\mathbf{E}_i^{\mathrm{j}}}, \tag{4.10}$$

where $(\mathrm{i},\mathrm{j}) = (s,p)$, The Fresnel reflection coefficients can be obtained by modeling the silicenic system as a surface current density $K = \sigma \cdot E|_{z=0}$ and applying

the electromagnetic (EM) boundary conditions at $z = 0$. The electric and magnetic fields of the 2D quantum material are connected at $z = 0$ by the Maxwell's boundary conditions:

$$\hat{z} \times \left[\mathbf{E}_t - \mathbf{E}_r - \mathbf{E}_i\right] = 0 \tag{4.11}$$

$$\hat{z} \times \left[\mathbf{H}_t - \mathbf{H}_r - \mathbf{H}_i\right] = \sigma \cdot \mathbf{E}_t, \tag{4.12}$$

For the 2D homogeneous anisotropic materials (e.g., graphene, silicene, etc) subjected to a perpendicular magnetic field, the MO conductivity tensor is given as

$$\sigma = \sigma_L \hat{\mathbf{e}}_\parallel \otimes \hat{\mathbf{e}}_\parallel + \sigma_T \hat{\mathbf{e}}_\perp \otimes \hat{\mathbf{e}}_\perp + \sigma_H \left(\hat{\mathbf{e}}_\perp \otimes \hat{\mathbf{e}}_\parallel - \hat{\mathbf{e}}_\parallel \otimes \hat{\mathbf{e}}_\perp\right)$$
$$+\sigma_{xy}^{\text{sym}} \left(\hat{\mathbf{e}}_\perp \otimes \hat{\mathbf{e}}_\parallel + \hat{\mathbf{e}}_\parallel \otimes \hat{\mathbf{e}}_\perp\right)$$

where $\hat{\mathbf{e}}_\parallel = k_x\hat{\mathbf{x}} + k_y\hat{\mathbf{y}}/|\mathbf{k}|$ and $\hat{\mathbf{e}}_\perp = k_y\hat{\mathbf{x}} - k_x\hat{\mathbf{y}}/|\mathbf{k}|$. Utilizing Eqs. (4.1)–(4.10) in Eqs. (4.11) and (4.12), we can write,

$$E_i^s + E_r^s = E_t^s, \tag{4.13}$$

$$\frac{k_{z,2}}{k_2}[E_i^p - E_r^p] = \frac{k_{z,1}}{k_1}E_t^p, \tag{4.14}$$

$$\frac{1}{Z_1}\frac{k_{z,1}}{k_1}\left[E_i^s - E_r^s\right] = \left(\sigma_T + \frac{1}{Z_2}\frac{k_{z,2}}{k_2}\right)E_t^s + \left(\sigma_H + \sigma_{xy}^{\text{sym}}\right)\frac{k_{z,2}}{k_2}E_t^p, \tag{4.15}$$

$$\frac{1}{Z_1}\left[E_i^p + E_r^p\right] = \left(\sigma_L\frac{k_{z,2}}{k_2} + \frac{1}{Z_2}\right)E_t^p + \left(\sigma_{xy}^{\text{sym}} - \sigma_H\right)E_t^s. \tag{4.16}$$

Now it is straightforward to obtain reflected and transmitted Fresnel coefficients in the presence of an external magnetic field [76, 113, 114]:

$$r_{pp} = \frac{\alpha_+^T\alpha_-^L + \beta}{\alpha_+^T\alpha_+^L + \beta}, \tag{4.17}$$

$$r_{ss} = -\left(\frac{\alpha_-^T\alpha_+^L + \beta}{\alpha_+^T\alpha_+^L + \beta}\right), \tag{4.18}$$

$$t_{pp} = 2\frac{Z_2\varepsilon_2}{Z_1}\frac{k_{1z}\alpha_+^T}{\alpha_+^T\alpha_+^L + \beta}, \tag{4.19}$$

$$t_{ss} = 2\mu_2\frac{k_{1z}\alpha_+^L}{\alpha_+^T\alpha_+^L + \beta}, \tag{4.20}$$

$$r_{sp} = t_{sp} = \frac{-2Z_0^2\mu_0\mu_1\mu_2k_{1z}k_{2z}(\sigma_H + \sigma_{xy}^{sym})}{Z_1(\alpha_+^T\alpha_+^L + \beta)}, \tag{4.21}$$

$$r_{ps} = -\frac{k_1 k_{2z}}{k_2 k_{1z}} t_{ps} = 2\frac{Z_0^2 \mu_1 \mu_2}{Z_1} \frac{k_{1z} k_{2z} (\sigma_{xy}^{sym} - \sigma_H)}{\alpha_+^T \alpha_+^L + \beta}, \tag{4.22}$$

where,

$$\alpha_\pm^L = (k_{1z}\varepsilon_2 \pm k_{2z}\varepsilon_1 + k_{1z}k_{2z}\sigma_L/(\varepsilon_0\Omega)), \tag{4.23}$$

$$\alpha_\pm^T = (k_{2z}\mu_1 \pm k_{1z}\mu_2 + \mu_0\mu_1\mu_2\sigma_T\Omega), \tag{4.24}$$

$$\beta = Z_0^2\mu_1\mu_2 k_{1z}k_{2z}[\sigma_H^2 - (\sigma_{xy}^{sym})^2]. \tag{4.25}$$

Here, $k_{1z} = k_1\cos(\theta_1)$ and $k_{2z} = k_2\cos(\theta_2)$. The conductivities $\sigma_L(\sigma_T)$ are the longitudinal (transverse) components. For homogeneous, isotropic media, $\sigma_L = \sigma_T = \sigma_{xx} = \sigma_{yy}$. The cross conductivity of a 2D system in the presence of magnetic field is antisymmetric [91, 115] $\sigma_{xy} = -\sigma_{yx}$. In fact, the cross conductivity σ_{xy} has symmetric σ_{xy}^{sym} and asymmetric $\sigma_{xy}^{antisym}$ parts. For anisotropic materials, such as phosphorene [116], σ_{xy}^{sym} is non-zero because the band structure of phosphorene is Dirac like (linear in k) in one direction and Schrodinger like (parabolic in k) in the other direction [116]. However, for isotropic materials such as graphene and other staggered materials (silicene, germanene, stanene, and plumbene etc.) σ_{xy}^{sym}=0. Therefore in Eqs. (4.21) and (4.22), we use $\sigma_H = \sigma_{xy}$ which comprises wholly of the anti-symmetric part.

The real and imaginary parts of the magneto-optical conductivity are already separately computed in Eqs. (3.66) and (3.72) in Section 3.2. In our case, medium 1 is vacuum (ε_1= 1, μ_1=1) and medium 2 is nonmagnetic μ_2=1. The Fresnel coefficients which are derived from the magneto-optical conductivities, subsequently determine the magneto-optic rotations and ellipticity.

4.1.3 Phenomenological description of the magneto-optic effects

For incident s and p polarization, the Faraday rotation and ellipticity are computed using the expressions

$$\Theta^{\mathrm{F,s(p)}} = \frac{1}{2}\tan^{-1}\left(2\frac{\mathrm{Re}\left(\chi^{\mathrm{F,s(p)}}\right)}{1-|\chi^{\mathrm{F,s(p)}}|^2}\right), \tag{4.26}$$

$$\text{and } \eta^{\mathrm{F,s(p)}} = \frac{1}{2}\sin^{-1}\left(2\frac{\mathrm{Im}\left(\chi^{\mathrm{F,s(p)}}\right)}{1-|\chi^{\mathrm{F,s(p)}}|^2}\right), \tag{4.27}$$

where,

$$\chi^{\mathrm{F,s}} = \frac{t_{ps}}{t_{ss}} = Z_0\sqrt{\frac{\varepsilon_1}{\mu_1}}\frac{k_1 cos(\theta_1)\sigma_H}{\alpha_+^L}, \tag{4.28}$$

$$\text{and } \chi^{\mathrm{F,p}} = \frac{t_{sp}}{t_{pp}} = -Z_0\sqrt{\frac{\mu_2}{\varepsilon_2}}\mu_0\mu_1\frac{k_2 cos(\theta_2)\sigma_H}{\alpha_+^T}. \tag{4.29}$$

Similarly, for MOKE, the rotations and ellipticities are

$$\Theta^{\mathrm{K,s(p)}} = \frac{1}{2}\tan^{-1}\left(2\frac{\mathrm{Re}\left(\chi^{\mathrm{K,s(p)}}\right)}{1-|\chi^{\mathrm{K,s(p)}}|^2}\right), \tag{4.30}$$

$$\text{and } \eta^{\mathrm{K,s(p)}} = \frac{1}{2}\sin^{-1}\left(2\frac{\mathrm{Im}\left(\chi^{\mathrm{K,s(p)}}\right)}{1-|\chi^{\mathrm{K,s(p)}}|^2}\right), \tag{4.31}$$

where,

$$\chi^{\mathrm{K,s}} = \frac{r_{ps}}{r_{ss}} = \frac{2Z_0\sqrt{\mu_1\varepsilon_1}\mu_2 k_{1z}k_{2z}\sigma_H}{\alpha_-^T\alpha_+^L+\beta}, \tag{4.32}$$

$$\text{and } \chi^{\mathrm{K,p}} = \frac{r_{sp}}{r_{pp}} = \frac{-2Z_0\sqrt{\mu_1\varepsilon_1}\mu_0\mu_2 k_{1z}k_{2z}\sigma_H}{\alpha_+^L\alpha_-^L+\beta}. \tag{4.33}$$

A note about the notation is in place here. The spin ($\uparrow$ or $\downarrow$) or valley (K or K') will be specified in the subscripts while the superscripts identify the Faraday (F) or Kerr rotation (K) as well as the polarization state (s) or (p). If the χ's are small, $\chi \ll 1$, Eqs. (4.26) and (4.27) reduce to $\Theta^{\mathrm{F,s(p)}} \approx \mathrm{Re}(\chi^{\mathrm{F,s(p)}})$ and $\eta^{\mathrm{F,s(p)}} \approx \mathrm{Im}(\chi^{\mathrm{F,s(p)}})$ and vis-a-vis for the Kerr effect. However, for Landau quantized systems, there is no reason to believe, at the ontset, that the MO effects are small.

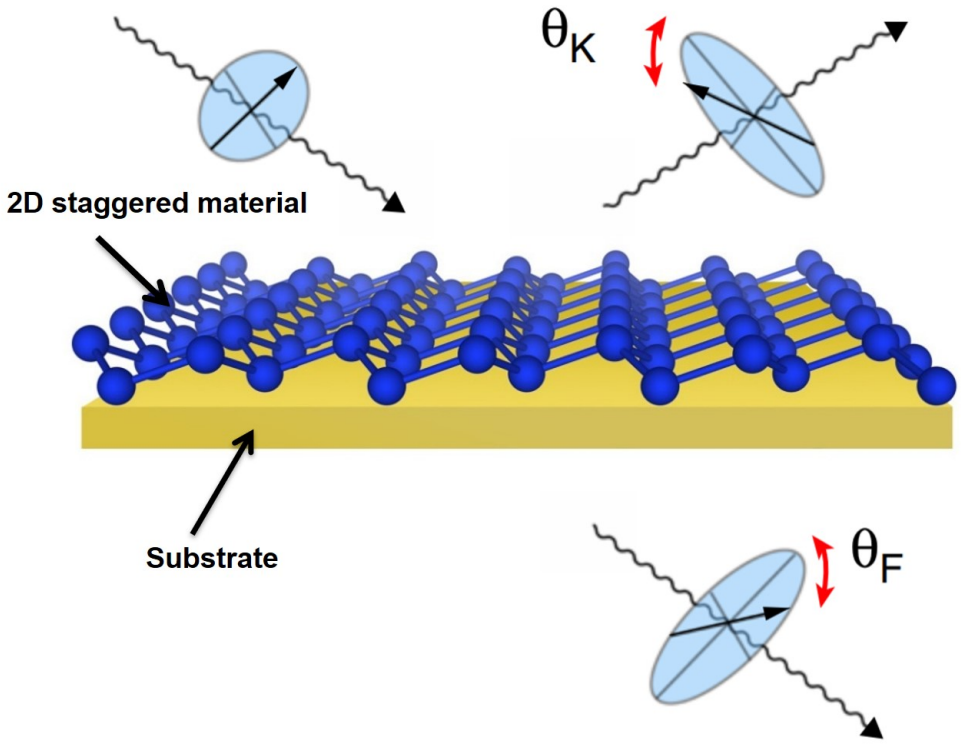

Figure 4.3: Schematic view of magneto-optic Kerr and Faraday effects on the surface of staggered 2D quantum material.

4.1.4 Results and discussion

4.1.4.1 Electric field modulated Faraday rotation and ellipticity

First, we discuss Faraday rotation (FR) for charge-neutral 2D silicene, where the inter-band transitions bridge across the valance and conduction bands. Hence $\mu_F = 0$. Fig. 4.4(a) shows the FR spectra as a function of incident photon frequency with modulation of the external electric field, landing the band structure into three distinct topological regimes [89]. The signal originating from a single spin orientation in only one of the valleys is dispersive Lorentzian, with a positive followed by a negative (or vice versa) signature. Let's call this an anti-phase peak. This terminology is borrowed from NMR literature [117]. The anti-phase peak is centred at the magneto-optic excitation frequency $E_n - E_m$ with positive and

negative maxima at $E_n - E_m \pm \Gamma$. For the opposite spin in the same valley and an identical LL transition, we still see an absorptive anti-phase peak whose sign may be reversed, the possibility of reversal depending on the exact topological regime.

The peaks corresponding to the different transitions, $E_{m,K(K'),\uparrow(\downarrow)} \rightarrow E_{n,K(K'),\uparrow(\downarrow)}$

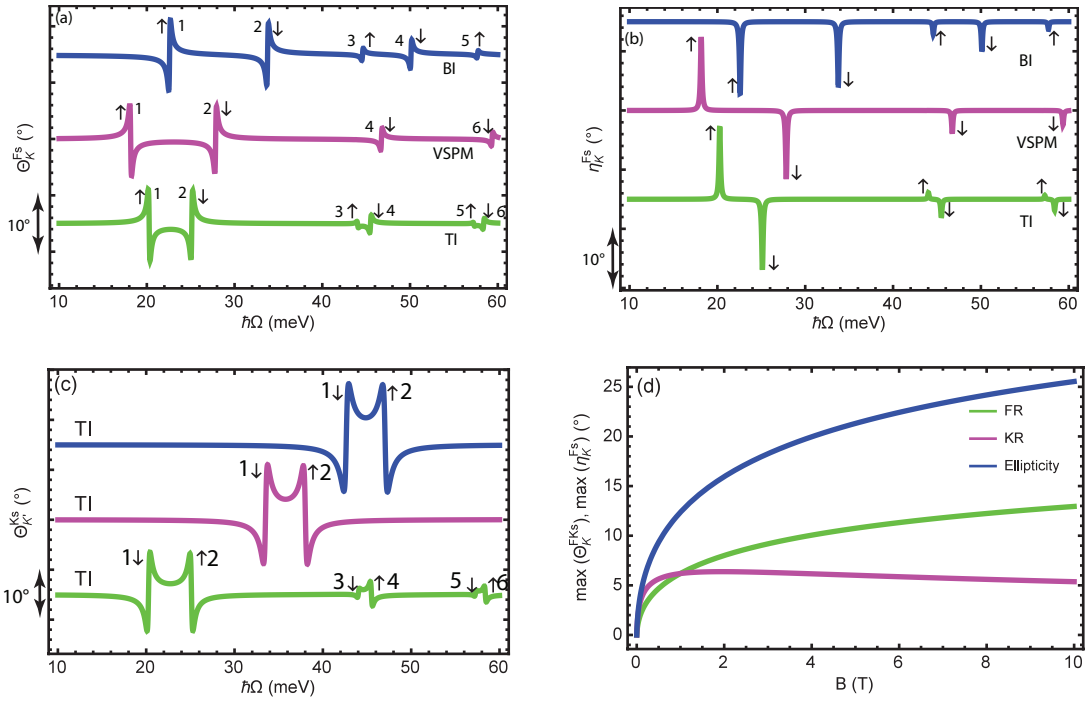

Figure 4.4: Faraday, Kerr rotation and ellipticity of silicene-substrate system as a function of photon energy electric and magnetic fields. (a) The s polarized Faraday rotation and (b) ellipticity as a function of incident photon energy in the K valley with modulation of the external electric field for the three distinct topological regimes, TI, VSPM, and BI for a magnetic field of 1 T. The spectral peaks are labeled 1 through 6 and their origin is identified in the main text. The spectrum are vertically shifted by 15° among themselves for clearer viewing. Furthermore, in this figure we use $\Delta_z = \Delta_{so}/2$ (TI) and $\Delta_z = 2\Delta_{so}$ (BI). (c) The s polarized Kerr rotation as a function of incident photon energy in the K' valley with modulation of the external magnetic field for the TI regime for three different values of B =1, 3 and 5 T. (d) The maximum Faraday, Kerr rotation and ellipticity as a function of the magnetic field in the K valley for the single transition $\Delta_{-10,K,\uparrow}$. The parameters used are Δ_z=8 meV, $\theta_1 = 30°$, $\Gamma = 0.01\Delta_{so}$, refractive index $n_2 = 1.84$ and chemical potential $\mu_F = 0$.

are labelled as $\Delta_{mn,K(K'),\uparrow(\downarrow)}$. For higher frequencies, the magnitude of the rotation is reduced in accordance with the factor of $1/(E_n - E_m)$ appearing in the denominator of Eqs. (3.66) and (3.72). We now explore the three distinct topological regimes. In the topological insulator (TI) regime ($\Delta_z < \Delta_{so}$), the first and second anti-phase peaks correspond to the $\Delta_{-10,K,\uparrow}$ and $\Delta_{01,K,\downarrow}$ transitions for spin up and spin down respectively. In each of these transitions, one of the participating levels is an n=0 level.

In a magnetic field of 1 T and $\Delta_z = \Delta_{so}/2$, these magneto-excitation energies are calculated as 20.3 meV (4.9 THz) and 25.1 meV (6.1 THz) respectively and are shown as 1 and 2 in the bottom spectrum of Fig. 4.4(a). The anti-phase peaks switch sign with spin within the same valley. The s polarized FR angles for the first two anti-phase peaks are $\sim \pm 6.5°$. The subsequent anti-phase peaks appearing at different resonant frequencies differ in magnitude for the spin-up and spin-down cases due to spin-dependent energies. The anti-phase peaks labeled 3 through 6 can also be assigned to the various transitions. For example the multiplet structure 3 originates from $\Delta_{-12,K,\uparrow}$, 4 is due to $\Delta_{-21,K,\downarrow}$, 5 is due to $\Delta_{-23,K,\uparrow}$ and 6 comes from $\Delta_{-32,K,\downarrow}$.

In the valley-spin polarized metal (VSPM) instance ($\Delta_z = \Delta_{so}$), the gap of one of the spin-split bands closes [89] giving rise to a Dirac point. As we increase the applied electric field and begin to approach the VSPM point, the lowest frequency peaks, labeled 1 and 2 in the middle spectrum of Fig. 4.4(a) move apart: the $\Delta_{-10,K,\uparrow}$ peak is red shifted and $\Delta_{01,K,\downarrow}$ peak is blue shifted. The excitation energies corresponding to the first two anti-phase peaks at the VSPM point are now 18.2 meV (4.4 THz) and 27.8 meV (6.7 THz). However, it is observed that at this precise electric field, the spectrum is cleaner and exhibiting fewer peaks. The peaks labeled 4 and 6 originate from the $\Delta_{-21,K,\downarrow}$ and $\Delta_{-32,K,\downarrow}$ transitions.

The peaks that were labeled 3 and 5 in the TI regime and came from the $\Delta_{-12,K,\uparrow}$ and $\Delta_{-23,K,\uparrow}$ transitions are now annihilated. Eq. (6.3) shows that at the Dirac point in the K valley ($\xi = 1$), the spin-up ($\sigma = 1$) transitions leads to $\Delta_{\xi\sigma} = 0$ which results in $A_n = B_n = 1/\sqrt{2}$ irrespective of the Landau quantum number n. For these spin up levels, therefore $(A_m B_n)^2 = (B_m A_n)^2$ and from Eq. (3.72), the minus sign between the terms in the square brackets results in annihilation of the spectral response at the Δ_{-12} and Δ_{-23} frequencies. So even though, these transitions are allowed by selection rules, destructive interference between their quantum amplitudes extinguishes the response. Conversely, in the K' valley (data not shown), the spin-down peaks will be annihilated at the Dirac points.

For an even higher electric field ($\Delta_z > \Delta_{so}$), the system transitions from the VSPM to the band insulator (BI) state, and the lowest bandgap is opened again, resulting in sign change of some of the anti-phase peaks with respect to the TI phase. Compare the peaks 1 through 5 between the TI and BI shown in Fig. 4.4(a). The full range of the allowed peaks also resurfaces once the VSPM point is crossed. The separation between the anti-phase pair keeps on growing in the BI state. Consequently, all the peaks gradually shift towards higher frequencies. The magnitude of the maximum spin-polarized FR angles for the first two peaks inside the anti-phase pair is $\sim \pm 8^\circ$.

If we change the polarization of the incident light, the sign of anti-phase peaks inverts with respect to the baseline. Alternatively, the same effect is achieved by switching from one valley to another. If we change the valley, the spin identity of the anti-phase also changes. The juxtaposition of identities between the spin-up and down polarized peaks after band inversion is also observed in the K' valley. Consequently, the s polarized FR in the K valley will have the same form as the p polarized FR response in the K' valley. The MOKE rotation spectra (data not shown) follow a similar trend. The MOKE response is also spin and valley polar-

ized and the magnitudes of the rotation angle range between 5–15° for both valleys and all three topological regimes, which are in general larger than the FR angle.

Fig. 4.4(b) shows the series of peaks in the ellipticity acquired by transmitted light from s polarized incident radiation originating from the K valley manifold. Faraday geometry is considered though analogous results are obtained for reflection as well. It is evident that extremely large ellipticities, of the order of 8–15°, appear for the lowest excitations. The spectrum for ellipticity comprises absorptive Lorentzians, which are spin and valley polarized. These maxima are at the excitation energies $E_n - E_m$. The rotation and ellipticity data when considered together, indicate that at the exact excitation energy $E_n - E_m$, the rotation is zero while the ellipticity is maximum. Furthermore, when the rotation is maximum ($\hbar\Omega = E_n - E_m \pm \Gamma$), the ellipticity drops to 50% of its maximum value. The intertwined effects, although both being ultra-large, limit the use of the silicene-substrate system for a *pure* MO rotator since significant ellipticity is also introduced.

4.1.4.2 Magnetic field modulated Faraday and Kerr rotation

We now demonstrate the effect of how the magnetic field modifies the magneto-optic response. The s polarized MOKE in the K' valley is only one possible illustration and is shown in Fig. 4.4(c). Here we plot the MO spectrum in the TI regime for three different values of B =1, 3, and 5 T, while keeping $\mu_F = 0$ and $\theta = 30°$. The impact on the MOKE signal in terms of shifting magneto-excitation frequency and the amount of Kerr rotation is clear. The silicene energy levels are strongly dependent on the magnetic field B, as given by Eq. (6.3), and this is also true for other 2D materials including graphene [89, 93].

As we increase the strength of the applied magnetic field, the MO excitations

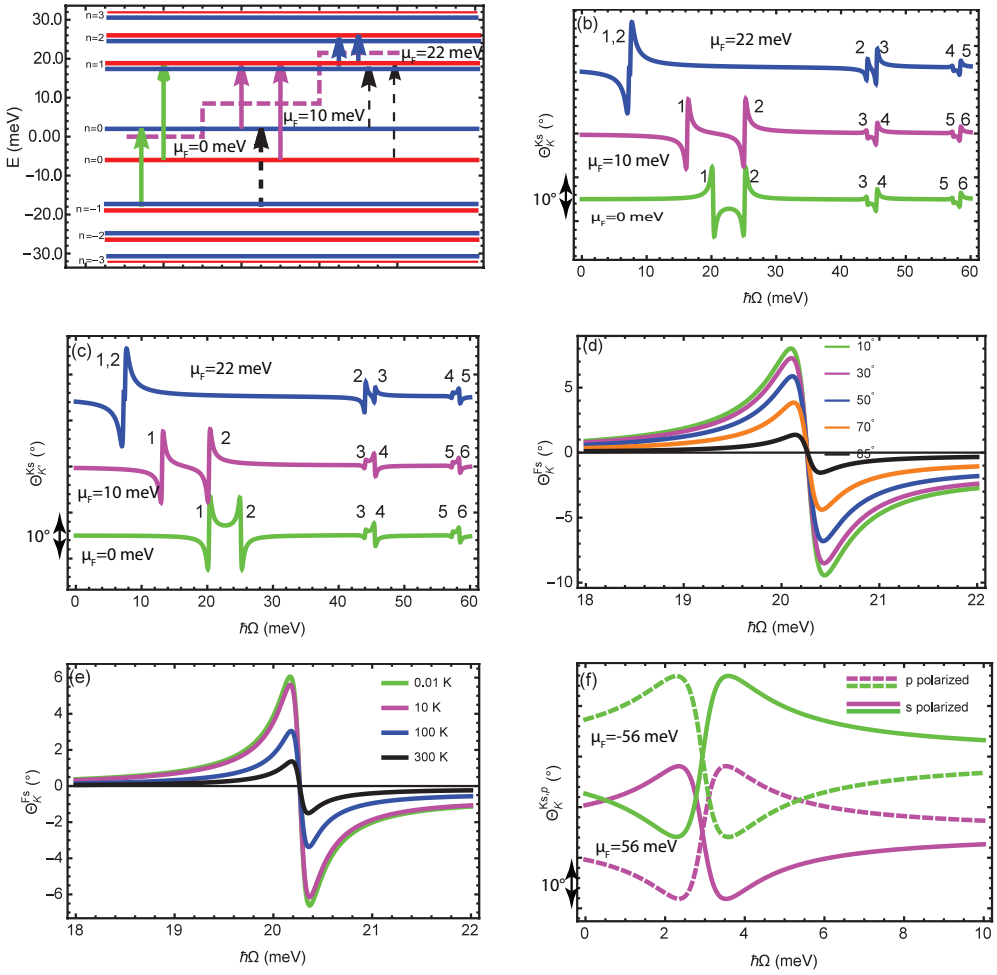

Figure 4.5: (a) Schematic representation of the allowed transitions between LL's for three different values of chemical potential μ_F =0, 10 and 22 meV; (b) and (c) the s polarized Kerr rotation as function of incident photon frequency in K and K' valleys with modulation of the chemical potential in the TI regime for a magnetic field of 1 T, respectively. (d) The s polarized Faraday rotation as function of incident photon energy in K valley for different incident angles for a single transition in the TI regime. (e) The s polarized Faraday rotation as function of incident photon energy in K for different temperatures for a single transition in the TI regime. (f) The s and p polarized Kerr rotation as function of incident photon frequency in the semiclassical limit for n-type and p-type silicene (μ_F = 56 and -56 meV), respectively. The solid line represents the s polarized and the dashed line p polarized. The parameters used are Δ_z=8 meV, $\theta = 30°$, $\Gamma = 0.01\Delta_{so}$ and refractive index $n_2 = 1.84$.

shift towards higher frequencies with a concomitant increase in the magnitude of the MOKE rotation angle. For example, the peaks labelled 1 and 2 have excitation energies 20.3 meV (4.9 THz) and 25.1 meV (6.1 THz) for $B = 1$ T, 33.5 meV (8.1 THz) and 38 meV (9.2 THz) for $B = 3$ T and finally, 42.7 meV (10.3 THz) and 47 meV (11.32 THz) for $B = 5$ T. The maximum value of the rotation $\Theta_{K'}^{Ks}$ exceeds $\sim \pm 13^{\circ}$ at a magnetic field of 5 T, which is an exceptionally large rotation for a monolayer silicene-substrate system. Similarly, the FR is also strongly field-dependent (data not shown).

The primary role of magnetic field tuning, therefore, is to shift the position of the magneto-optic excitation energies and also to modify the amount of rotation. However, unlike the electric field, the magnetic field does not switch the sign of the anti-phase doublets. Fig. 4.4(d) show the field dependence of Θ_K^{Fs} and Θ_K^{Ks} in the TI regime. Due to the dispersive MO spectrum, we chose to plot the maximum rotation. By increasing the magnetic field strength the amount of FR and Kerr rotations grows. However, for stronger fields, the Kerr signal slowly decreases. At a field of 10 T, we report $\Theta_K^{Fs} = 13^{\circ}$ and $\Theta_K^{Ks} = 5.5^{\circ}$. The ellipticity is also strongly field-dependent.

4.1.4.3 Effect of chemical potential

It is also instructive to discuss the effect of controlling the FR and MOKE spectra by varying the chemical potential of the silicene surface, e.g, by applying a bias voltage [108] or optical pumping [110]. For illustration purposes, we consider three different values of chemical potentials μ_F=0, 10 and 22 meV, while keeping the magnetic field 1 T, in the TI regime ($\Delta_z = 0.5\Delta_{so}$) and an angle of incidence of 30°.

In the first case the chemical potential is at zero and lies within the n=0 manifold, for μ_F=10 meV the chemical potential is in between the n=0 and n=1 LL's and for

μ_F=22 meV the chemical potential is in between the n=1 and n=2 LL's. These LLs are shown in Fig. 4.5(a). Only the K valley is depicted. For $\mu_F = 0$, the lowest energy excitations are also indicated on the same subfigure. They identify as $\Delta_{-10,K,\uparrow} = 20.3$ meV and $\Delta_{01,K,\downarrow} = 25.1$ meV. These result in the Kerr rotations shown by anti-phase peaks 1 and 2 in the bottom spectrum of Fig. 4.5(b). They are interband transitions since they occur across the zero energy datum. The combination of anti-phase peaks Δ_{-12} and Δ_{-21} in the K valley, for both spins yield the multiplet structure 3 and the transitions Δ_{-23}, Δ_{-32} yield the structure 4. These anti-phase are rather close in their excitation energies (e.g. $\Delta_{-12,K,\uparrow} = 44.0$ meV, $\Delta_{-21,K,\uparrow} = 44.0$ meV, $\Delta_{-12,K,\downarrow} = 45.5$ meV and $\Delta_{-21,K,\downarrow} = 45.5$ meV) and the ability to resolve this finer structure depends on the experimental capability.

As μ_F increases to 10 meV, certain transitions become Pauli blocked. For example the transition $\Delta_{-10,K,\uparrow}$ becomes forbidden and in its stead, the intra-band transition $\Delta_{01,K,\uparrow} = 16.0$ meV emerges. The Pauli blocked transition is shown by a dashed upward-pointing arrow in the middle part of Fig. 4.5(a) and the two lowest transitions, $\Delta_{-10,K,\uparrow} = 16.3$ meV and $\Delta_{01,K,\downarrow} = 25.1$ meV are shown by solid arrows. Once again, these yields the Kerr signatures 1 and 2 shown in Fig. 4.5(b). The higher frequency agglomerated multiplets 3 and 4 remain unchanged.

If μ_F is further increased to 22 meV, so that it lies between the n=1 and n=2 manifolds, both transitions starting from n=0, i.e, $\Delta_{-10,K,\uparrow}$ and $\Delta_{01,K,\downarrow}$ now become Pauli blocked. These are again indicated by the dashed arrows in the rightmost part of Fig. 4.5(a). In their place, however, the intra-band transitions $\Delta_{12,K,\uparrow} = 7.0$ meV and $\Delta_{12,K,\downarrow} = 7.2$ meV pop up. For higher n, the LL's are closely spaced. Hence the excitation energies also converge. These closely spaced transitions are separated by $\approx$ 200 μeV and are shown by the structure 1, 2 in top part of Fig. 4.5(b). The transitions involving the n=0 levels are completely missing from this magneto-optic spectrum. Furthermore, the transitions $\Delta_{-21,K,\uparrow}$ and $\Delta_{-21,K,\downarrow}$

become Pauli forbidden and hence are absent from the excitation structure labeled 3 which now comprises only $\Delta_{-12,K,\uparrow} = 44.0$ meV and $\Delta_{-12,k,\downarrow} = 45.5$ meV. Therefore peak 3 is a cleaner doublet of anti-phase structure when compared with the μ_F=0 and μ_F=10 meV cases. The structure 4 originates, as earlier, from rather closely spaced Δ_{-23} and Δ_{-32}.

The magneto-optic spectrum originating from the K' valley for the same values of μ_F is depicted in Fig. 4.5(c). For $\mu_F = 0$, the rotational peaks are coincident with the K valley as $\Delta_{mn,K,\uparrow} = \Delta_{nm,K',\downarrow}$ (when $m = 0$ and $n \neq 0$), $\Delta_{-10,K,\uparrow} = \Delta_{01,K',\downarrow}$ and $\Delta_{01,K,\downarrow} = \Delta_{-10,K',\uparrow}$. However, these valley-specific spectrums are sign inverted with respect to each other. For $\mu_F = 10$ meV, the lowest energy transitions 1 and 2 occur at different positions for the two valleys. For the K valley, 1 and 2 are $\Delta_{01,K,\uparrow} = 16$ meV and $\Delta_{01,K',\downarrow} = 25$ meV respectively whereas for the K' valley, the peaks 1 and 2 are $\Delta_{01,K',\uparrow} = 13.1$ meV and $\Delta_{01,K',\downarrow} = 20.3$ meV respectively.

4.1.5 Impact of angle of incidence

The FR and MOKE signatures are clearly sensitive to the incident angle θ_1. This is because the Fresnel coefficients are strongly dependent on the incidence angle. This dependence is shown in Fig. 4.5(d) for a single transition in the TI regime. An increasing incidence angle diminishes the amount of rotation until it disappears at complete grazing, $\theta_1 = \pi/2$. A similar trend can also be seen in the MO response of graphene [67, 106].

4.1.6 Role of temperature and scattering

All of the results presented so far are at 0 K but as the temperature goes up, the Fermi Dirac distribution function in Eqs. (3.66) and (3.72) starts becoming significant. We can explore the temperature dependence of the FR by introducing

Table 4.1: Table of allowed transitions in K valley in the $n = -1, 0, 1$ subspace, at a fixed Magnetic field and Chemical potential μ. Furthermore $x = \Delta_z/\Delta_{so}$, $y = \sqrt{\hbar v^2 eB/\Delta_{so}^2}$. and $\mu = \mu_F/\Delta_{so}$.

m	n	spin ($\uparrow\downarrow$)	Range of x	$\Delta_{mn,K(K'),\uparrow(\downarrow)}$
0	1	$\uparrow$	$x \geq 1 - 2\mu$	$-\frac{1}{2} + \frac{x}{2} + \sqrt{(\frac{x-1}{2})^2 + 2y^2}$
0	1	$\downarrow$	all x	$+\frac{1}{2} + \frac{x}{2} + \sqrt{(\frac{x+1}{2})^2 + 2y^2}$
-1	0	$\uparrow$	$x \leq 1 - 2\mu$	$+\frac{1}{2} - \frac{x}{2} + \sqrt{(\frac{x-1}{2})^2 + 2y^2}$
-1	0	$\downarrow$	not allowed	

these distributions in place of the Heaviside functions. Nevertheless, at 100 K, the FR angle is 3^o, while at 300 K, the FR angle is 1°. These results are shown in Fig. 4.5(e). The experimental value [111] of the FR angle for graphene at 1.5 K is 4 mrad which translates to 0.23°. This shows that silicene has a bigger Faraday rotation than graphene in the THz range.

In silicene, the electrons frequently interact with scatterers. There are many scattering mechanisms including Coulomb interaction, impurities, optical phonons, acoustic phonons, and radiative decay [115]. Due to these scattering channels, the peaks are additionally broadened [118]. However, in actuality, the temperature dependence of the scattering rate Γ must also be taken into account. This is ignored in the present work. The amount of MO rotation is strongly influenced by the presence of a substrate [94].

4.1.7 Response in the semiclassical limit

In studies on 2D materials placed inside magnetic fields, the semiclassical limit is valid when the LL spacing becomes unimportant [89]. This happens as $|n|$ goes up and when the chemical potential is high up in the conduction band or deep down

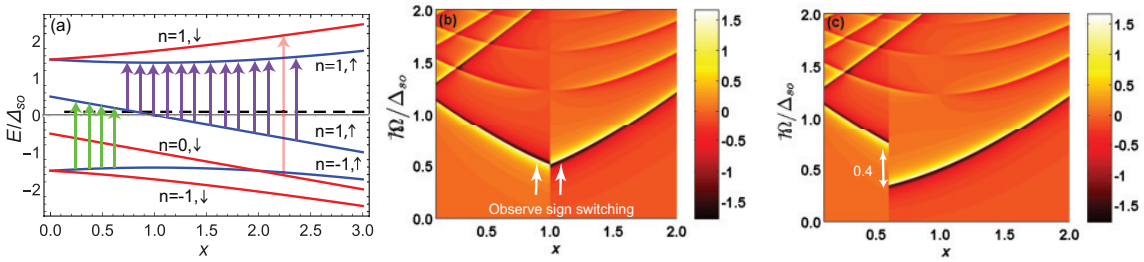

Figure 4.6: (a) Schematic representation of the allowed transitions between LL's for chemical potential $\mu = 0.2$. (b) and (c) the s polarized Faraday rotation contour plots as function of x in K valley for $\mu = 0$ and 1.25, repectively, where $x = \Delta_z/\Delta_{so}$ and $\mu = \mu_F/\Delta_{so}$. The parameters used are $\theta = 30°$, $\Gamma = 0.01\Delta_{so}$ and refractive index $n_2 = 1.84$.

in the valance band, $|\mu_F| \gg |E_0|$. In this case, the intra-band transitions between closely spaced levels are allowed. Suppose that μ_F lies between the $n-1$ and n LL's. Since the gap is minuscule, $\mu_F \approx E_n$. In this limit we have

$$E_{n+1} - E_n \approx \frac{\hbar v^2 eB}{\sqrt{\Delta_{\xi\sigma}^2 + 2n\hbar v^2 eB}} = \hbar\Omega_c, \tag{4.34}$$

where, $\Omega_c = \hbar v^2 eB/\mu_F$ is called the classical cyclotron frequency. In this regime the Faraday and Kerr rotations can also be derived from a purely classical point of view [119]. For finite μ_F and n, the allowed transitions are $\Delta_{(n-1)n}$, $\Delta_{-(n-1)n}$ and $\Delta_{-(n+1)n}$, however the latter two are large energies with diminished contributions to the magneto-optical conductivities, Eqs. (3.66) and (3.72). Hence, the allowed transition is the one that immediately across the chemical potential and results in a *single* large peak in all magneto-optic signatures. Furthermore in the semiclassical limit $A_n \approx A_{n-1} \approx B_n \approx B_{n-1} = 1/\sqrt{2}$, and we can straightforwardly derive, using Eqs. (4.37) and (4.38), the following conductivities summed over both valleys and both spins,

$$\frac{\mathrm{Re}\big(\sigma_{xx}(\Omega)\big)}{\sigma_0} = -\frac{\mathrm{Im}\big(\sigma_{xy}(\Omega)\big)}{\sigma_0} = \frac{\hbar\mu_F}{\pi}\frac{\Gamma}{(\hbar(\Omega-\Omega_c))^2+\Gamma^2}, \tag{4.35}$$

$$\frac{\mathrm{Im}\big(\sigma_{xx}(\Omega)\big)}{\sigma_0} = \frac{\mathrm{Re}\big(\sigma_{xy}(\Omega)\big)}{\sigma_0} = \frac{\hbar\mu_F}{\pi}\frac{\hbar(\Omega-\Omega_c)}{(\hbar(\Omega-\Omega_c))^2+\Gamma^2}. \tag{4.36}$$

These conductivities are shaped as absorptive and dispersive Lorentzians and are directly used to compute the Fresnel coefficients Eqs. (4.17)–(4.22) and subsequently the rotations. The conductivities, therefore, are modeled by classical Drude-like behavior [94, 120]. For example, in Fig. 4.5(f) we plot the s and p polarized Kerr rotation angles as a function of the incident photon frequency in the K valley. For n-type doping, we set μ_F=56 meV, which places chemical potential between the n=9 and 10 LL's. The transitions from n=0 to higher LL's are Pauli blocked, the selection rules dictate that only three transitions $\Delta_{-9\ 10}$, $\Delta_{-11\ 10}$ and $\Delta_{9\ 10}$ are allowed. The former two have negligible contributions, whereas the last mentioned transition results in a strong Drude peak, at 2.94 meV (0.71 THz).

Similarly, we plotted the s and p polarized Kerr rotation angles as a function of the incident photon frequency for p-type silicene, with $\mu_F = -56$ meV. The Kerr rotation angle switches between n-type and p-type silicene indicating modulation of the rotation angle by switching the chemical potential, e.g, by switching gate bias voltage. Also note that the spin and valley information is lost in the semiclassical limit. The value of electric field Δ_z also becomes inconsequential at higher doping and the silicene behaves as graphene, because not only that the resonant frequency approaches that of graphene in this limit [89], but also the role of SOI becomes inconsequential.

4.1.7.1 Probing topological quantum phase transitions via Faraday rotation

An alternative approach to understanding the magneto-optic response is by contour plotting the rotations as a function of two variables. This method also allows one to identify topologically distinct regions and topological phase transitions [89] and may reveal discontinuations that may otherwise go unnoticed. For example, we consider transitions in the K valley within the $n = -1, 0, 1$ subspace. We

use dimensionless variables to simplify the analysis. We can define $x = \Delta_z/\Delta_{so}$, $y = \sqrt{\hbar v^2 eB/\Delta_{so}^2}$ as measures of the electric and magnetic fields respectively, $\hbar\Omega/\Delta_{so}$ and $\mu = \mu_F/\Delta_{so}$ as variables for photon frequency and chemical potential.

In Fig. 4.6(a), we first plot the LL spectrum for the transitions under consideration. Table 4.1 summarizes the allowed transitions across the chemical potential. The excitation energies are also computed in the last column. It is evident that at the critical point $x = 1 - 2\mu$, the $\Delta_{-10,K,\uparrow}$ transition gives way to the $\Delta_{01,K,\uparrow}$ transition, we say that the former becomes Pauli blocked. For example for a precise value of $\mu = 0.2$, this is shown by the sequence of green-colored arrows that are only drawn for $x \leq 1-2\mu$ and the purple-colored arrows drawn only for $x \geq 1-2\mu$. For $\mu = 0$, this transition point is $x = 1.0$.

The contour plot in Fig. 4.6(b) aptly captures the scenario. For $x \leq 1.0$, the $\Delta_{-01,K,\uparrow}$ transitions causes the Faraday rotation while for $x \geq 1.0$, the $\Delta_{01,K,\uparrow}$ transition kicks in yielding the Faraday rotation. Upon this transition point, the sign of the anti-phase peaks also switches. For $\mu = 0.2$, this switching now occurs at a smaller value of $x_c = 1 - 2\mu = 0.6$ as depicted in Fig. 4.6(c). Furthermore at this switching point, $x_c = 1 - 2\mu$, one observes a discontinuous jump in the excitation energy. This can be computed by inserting x_c into the energies $\Delta_{01,K,\uparrow}|_{x_c} = -\mu + \sqrt{\mu^2 + 2y^2}$ and $\Delta_{-10,K,\downarrow}|_{x_c} = \mu + \sqrt{\mu^2 + 2y^2}$ which yields a discontinuity of magnitude 2μ in the contour plot. The uninterrupted rotation which continues upward to the top right is due to $\Delta_{01,K,\downarrow}$ transition which is always switched on and is shown by thick red-colored arrows in Fig. 4.6(a). The x_c point also indicates a topological phase transition from the TI to the BI regime.

4.1.7.2 Dependence on the silicene-substrate system

For realistic applications, the substrate effect cannot be ignored in Faraday and Kerr rotations. It is understood that the substrate does not introduce any magneto-

optic rotation itself. Compared to free-standing silicene, the substrate reduces the total rotation angle in silicene, just like in graphene [94]. If the refractive indices are small, in general, the magneto-optic rotation will be large. To get a higher value of the Faraday and Kerr rotations, it is recommended to use substrates with smaller refractive indices [120].

Fig. 4.7 shows the s and p polarized Faraday and Kerr rotation spectra as a function of incident photon energy in the K valley with modulation of relative permittivities in the TI regime for a magnetic field of 1 T. By increasing the relative permittivity strength the amount of FR and Kerr rotations reduces. In Fig. 4.8 we have shown

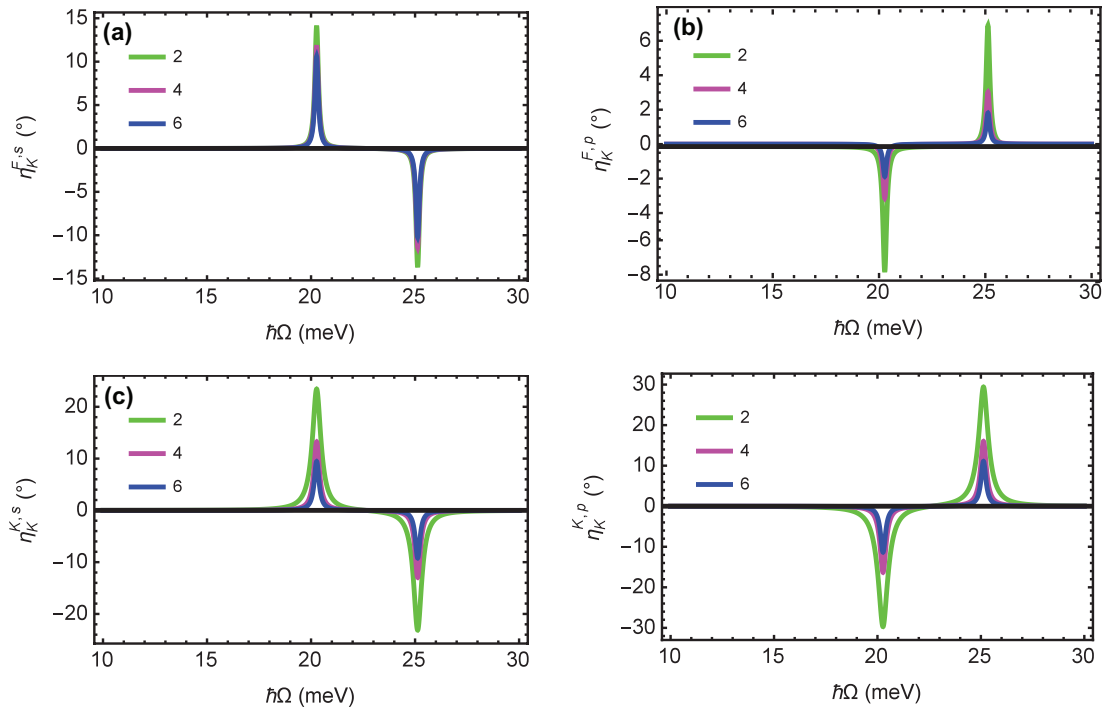

Figure 4.7: Faraday and Kerr rotation of silicene-substrate system as a function of photon energy for three different relative permittivities. (a) The s polarized and (b) p polarized Faraday rotation as a function of incident photon energy in the K valley with modulation of relative permittivities in the TI regime for a magnetic field of 1 T. (c) The s polarized and (d) p polarized Kerr rotation as a function of incident photon energy in the K valley with modulation of relative permittivities in the TI regime for a magnetic field of 1 T, for the two transitions. The parameters used are $\theta_1 = 30°$, $\Gamma = 0.01\Delta_{so}$ and chemical potential $\mu_F = 0$.

the s and p polarized Faraday and Kerr rotation spectra as a function of incident photon energy in the K valley with modulation of relative permeabilities in the TI regime for a magnetic field of 1 T. Here the magneto-optic effects show a different behavior, i.e. by increasing the relative permeability, the magnitude of Faraday and Kerr rotations grows. Fig. 4.9 shows the s and p polarized ellipticity peaks for two transitions acquired by reflected and transmitted light of the silicene-substrate system as a function of photon energy for three different relative permittivities.

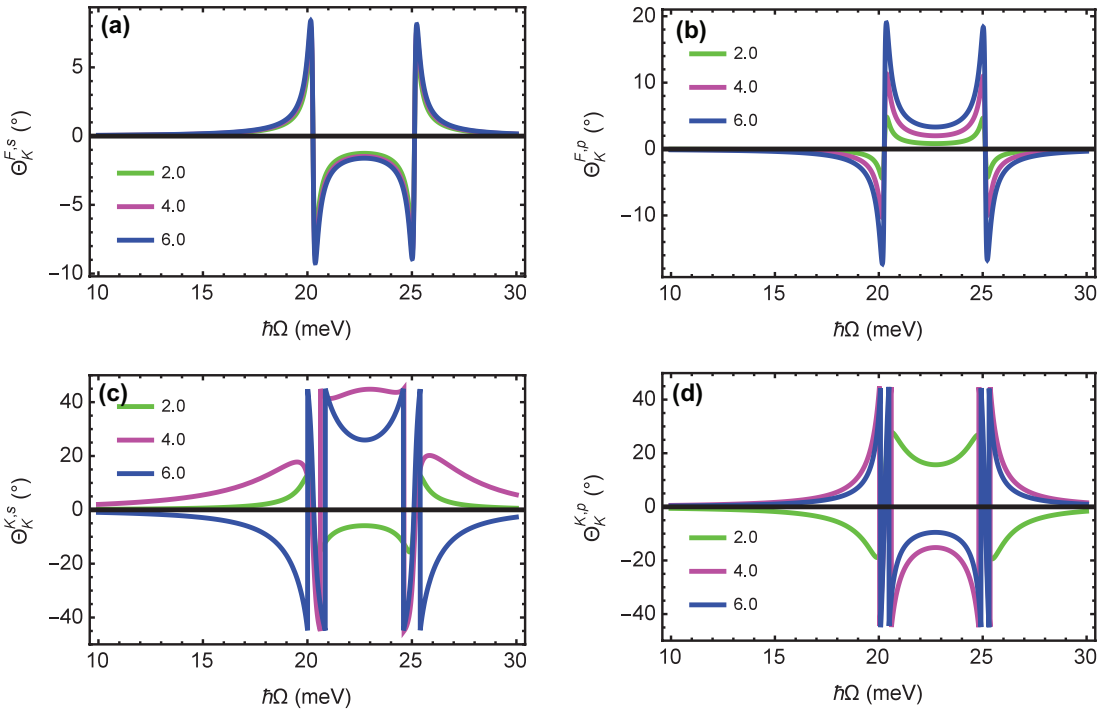

Figure 4.8: Faraday and Kerr rotation of silicene-substrate system as a function of photon energy for three different relative permeabilitis. (a) The s polarized and (b) p polarized Faraday rotation as a function of incident photon energy in the K valley with modulation of relative permeabilitis in the TI regime for a magnetic field of 1 T. (c) The s polarized and (d) p polarized Kerr rotation as a function of incident photon energy in the K valley with modulation of relative permeabilities in the TI regime for a magnetic field of 1 T, for the two transitions.

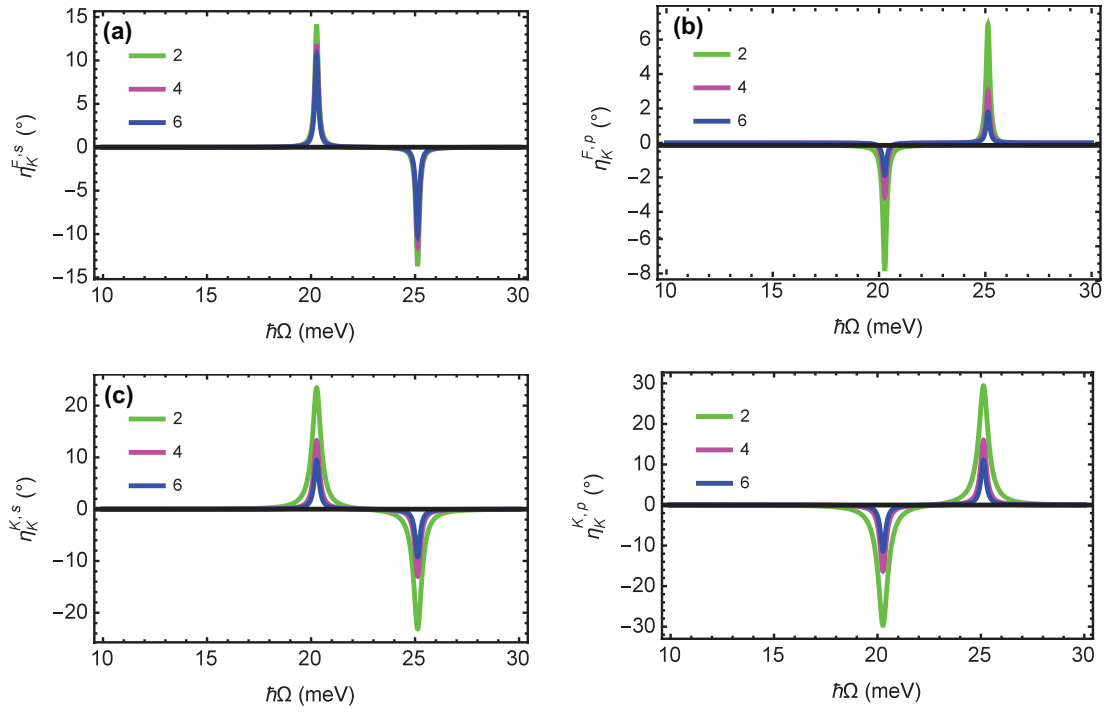

Figure 4.9: Faraday and Kerr ellipticities as a function of incident photon energy for three different relative permittivities. (a) The s polarized and (b) p polarized Faraday ellipticities as function of incident photon energy in the K valley with modulation of relative permittivities in the TI regime for a magnetic field of 1 T. (c) The s polarized and (d) p polarized Kerr ellipticities as a function of incident photon energy in the K valley with relative permittivities in the TI regime for a magnetic field of 1 T, for the two transitions. The parameters used are $\theta_1 = 30°$, $\Gamma = 0.01\Delta_{so}$ and chemical potential $\mu_F = 0$.

4.2 Polarization manipulation with hybridized topological insulator thin films

4.2.1 Background and motivation

The discovery of topological phases and topological phase transitions (TQPTs) in a wide range of new quantum materials, such as graphene, staggered 2D semiconductors (i.e. silicene, germanene, stanene), 2D transition metal dichalcogenides (TMDCs), Dirac-Weyl semimetals, and their artificial analogs have provided a new frame of mind to the understanding of the origin of quantum states of matter. Besides finding new quantum materials, searching the ways to tune a normal insulating (NI) phase into a topological one is of both theoretical and experimental importance. In 3D topological insulators thin films, one way to drive such TQPTs is to tune the thickness L of the film. The topologically protected SSs of a TI thin film has a finite decay length (also called the penetration depth of the SSs) over which the SSs decay into the bulk region.

As the thickness L of the TI thin film becomes comparable to, or smaller than, the penetration depth, quantum tunneling between SSs occurs due to which the top and bottom SSs hybridize to open up an energy gap Δ_H at the Dirac points [60, 61]. This can happen for 1 to 5 quintuple layers with a thickness of the order of L =5 nm [62, 63]. In the small L limit, the hybridization gap can be approximated by the relation $\Delta_H = 2B_1\pi^2/L^2$, where B_1 is a system parameter. For the band structure in the Bi_2Se_3 the parameter B_1 is equal to 10 eVA^2, which is obtained by first-principles calculations [61, 121].

However, tuning the thickness of the TI in real space is not a suitable way to drive TQPTs. There are other efficient ways in which TQPTs can be extrinsically induced in TIs, such as through band distortions in momentum space by in-plane or out-of-plane magnetic fields [122, 123], pressure and temperature [124, 125],

and an external electric field [126, 127]. There are studies that the response of TI thin films in an external magnetic field is highly nontrivial [128, 129]. Recently, successful TQPTs from NI to quantum spin Hall (QSH) state in TIs through the application of electric and magnetic fields have been experimentally reported [130].

In addition to having interesting topological features, TI thin films exhibit Faraday and Kerr rotations in the THz regime. Faraday and Kerr rotations are non-reciprocal magneto-optic (MO) effects that describe the rotation of linearly polarized light when it is respectively transmitted or reflected from a magnetic medium. At the surface of a TI, both of these effects originate from the breaking of TRS either by an external applied magnetic field or by doping the system with magnetic impurities [17].

In the THz range, W. K. Tse *et. al* theoretically studied the MO Faraday and Kerr effects of TIs thin films and found that MOKE exhibits a giant $\pi/2$ rotation [88, 131]. Experimentally, Colossal MOKE and FR in the presence of a strong magnetic field in Bi_2Se_3 thin films [132, 133] have been investigated. It has been demonstrated that THz FR in pure or magnetic TI films is equal to the fine structure constant [134]. Recently, FR and cyclotron resonances magneto-transmission spectroscopy of $(Bi_{1-x}Sb_x)_2Te_3$ and THz Faraday and Kerr rotation spectroscopy measurements on $Bi_{1-x}Sb_x$ thin films have been experimentally reported [135, 136]. Nedoliuk *et. al* observed colossal FR on Landau levels in high-mobility encapsulated graphene in the mid-infrared and THz ranges [137]. A. Stroppa *et. al* computationally determined the MO properties of (Ga,Mn)As within density functional theory [138]. Using first-principles calculations K. Yang *et. al* explored the MOKE for different spin configurations of the $(CrI_3)_2$ bilayer and in a hybrid organic-inorganic perovskite [139, 140].

In this part, we employ a different mechanism to drive TQPTs between different

phases and study FR and MOKE in a TI thin film. We make use of the Zeeman energy as a control knob to close and reopen the bandgap in order to drive the phase transition between a band insulator state and a topological insulator state in a hybridized TI thin film. Hybridization provides mass to the Dirac fermions on the top and bottom SSs. In the absence of Zeeman energy ($\Delta_z = 0$), the energy spectrum of the 3D TI is gapped (because of the hybridization energy) and electron-hole symmetry which leads to Shubnokov–de Haas oscillations. When Δ_z is less than Δ_H, the system is in the quantum spin Hall insulator (QSHI) regime. However, by tuning $\Delta_z = \Delta_H$ we enforce a TQPT at the charge neutrality point (CNP) where the energy of one of the $n = 0$ LLs becomes zero.

In this part of the chapter, we also study the FR and MOKE in the 2D SSs of a TI thin film, and the effects of a magnetic field and chemical potential. We believe that the magnetic field-dependent MO effects provide a convenient scheme that can be directly utilized for optical measurement of different quantum topological features, magnetic field sensing, Faraday rotators, isolators, current sensors, optical modulation, and communication [105, 106, 141]. This part of the chapter is organized as follows: in Section 4.2.2 we present the basic formalism for the FR and MOKE in the 2D SSs of a TI thin film. In Section 4.2.3.1 we use the formulation of the previous section to discuss the FR and MOKE simulations for the TI thin film.

4.2.2 Geometry of the the magneto-optic effects and conductivities

In order to calculate the MO effects, we consider an ultrathin film of a TI having thickness L such that $L \to 0$. In these conditions, the TI thin film SSs can be treated as 2D surfaces. We consider an arbitrarily polarized, well-collimated, monochromatic, Gaussian beam of light propagating in vacuum impinging from one medium to the planar interface of the TI-substrate system at an incidence angle θ_ψ. The interface of air and TI thin film is located at the $z = 0$ plane. The beam of

light of frequency Ω has polarization in an arbitrary direction and is propagating through the incident and transmitted materials with *relative* permittivity and permeability ε_n and μ_n respectively, where $n = (1,2)$. The beam makes an angle θ_χ in the substrate. Fresnel reflection and transmission coefficients are given in Section 4.1.2. For homogeneous, isotropic media, $\sigma_L = \sigma_{xx} = \sigma_{yy}$ and $\sigma_T = \sigma_{xy} = \sigma_H$. Following Section 3.2 calculation, at $T = 0$ K the expressions for the real and imaginary parts of the longitudinal conductivity of the 3D hybridized topological insulator thin films are given by [81]

$$\frac{\left.\begin{matrix}\text{Re}\\ \text{Im}\end{matrix}\right\}\big(\sigma_{xx}(\Omega)\big)}{\sigma_0} = \frac{E_B^2}{\pi}\sum_{\tau_z}\sum_{m,n}\frac{\Theta(E_n-\mu_F)-\Theta(E_m-\mu_F)}{E_n-E_m} \times\left[(\alpha_m\beta_n)^2\delta_{|m|-\tau_z,|n|}+(\beta_m\alpha_n)^2\delta_{|m|+\tau_z,|n|}\right]\left\{\begin{matrix}W_{mn}\\ W'_{mn}\end{matrix}\right., \quad (4.37)$$

where $\sigma_0 = e^2/4\hbar$, $W_{mn} = \eta/\big((\hbar\Omega-(E_n-E_m))^2+\eta^2\big)$ and $W'_{mn} = \big(\hbar\Omega-(E_n-E_m)\big)/\big((\hbar\Omega-(E_n-E_m))^2+\eta^2\big)$. Similarly, the real and imaginary parts of the transverse (Hall) conductivity are

$$\frac{\left.\begin{matrix}\text{Re}\\ \text{Im}\end{matrix}\right\}\big(\sigma_{xy}(\Omega)\big)}{\sigma_0} = \frac{E_B^2}{\pi}\sum_{\tau_z}\sum_{m,n}\tau_z\frac{\Theta(E_n-\mu_F)-\Theta(E_m-\mu_F)}{E_n-E_m} \times\left[(\alpha_m\beta_n)^2\delta_{|m|-\tau_z,|n|}-(\beta_m\alpha_n)^2\delta_{|m|+\tau_z,|n|}\right]\left\{\begin{matrix}W_{mn}\\ W'_{mn}\end{matrix}\right.. \quad (4.38)$$

In the limit $\Delta_z = \Delta_H = 0$, the above conductivity expressions reduce to the result for graphene for a single valley [91].

4.2.3 Results and discussion

4.2.3.1 Magnetic field effect on Faraday and Kerr rotations

To fully understand the FR and Kerr rotation in a TI thin film-substrate, we plot the real part of the longitudinal and Hall conductivities as a function of the photonic energy for three different values of magnetic field strengths, i.e. for 1, 3 and 5

T as shown in Figs. 4.10(a) and (b). The parameters for simulation are mentioned in the caption of the figure. Notably the angle of incidence θ_ψ is taken to be 30° for all simulations. The magnitudes of the MO effects depend on θ_ψ. For example, an increase in the incidence angle diminishes the amount of rotation. A similar trend can be seen in the MO response of graphene [106]. In the QSHI phase, the absorption peaks can be seen for interband transitions. Each transition is represented by a Lorentzian peak with a full width at half maximum η. Following the terminology mentioned in [142], the peaks corresponding to different transitions $E_m^{\tau_z=\pm1} \rightarrow E_n^{\tau_z=\pm1}$ are labeled as $T_{mn}^{\tau_z=\pm1}$.

Utilizing the expressions of Fresnel's coefficients and the s and p polarized Faraday and Kerr rotations in Sections 4.1.3 and 4.1.2, we performed these simulations. In this section, while investigating the FR and Kerr rotation in TI thin film-substrate system, we restrict ourselves to the lowest magneto-excitation transition frequencies (originating only from the T_{01}^{+1} and T_{-10}^{-1} transitions), unless specifically mentioned otherwise. We can see resonant peaks when the incident photon hits the magneto-excitation energy gap.

As we increase the strength of the applied magnetic field, the MO excitations shift towards higher frequencies. In Fig. 4.10(a), the first two absorption peaks correspond to T_{01}^{+1} (top surface) and T_{-10}^{-1} (bottom surface) transitions in which

Table 4.2: Allowed transitions for $\tau_z = \pm1$ in the $n = -1, 0, 1$ subspace, for B =1, 3 and 5 T in the QSHI phase $\Delta_z = 2$ meV.

$T_{mn}^{\tau_z=\pm1}$	Δ_z (meV)	B (T)	Photonic energy (meV)
T_{01}^{+1}	2	1	25.1
T_{-10}^{-1}	2	1	20.3
T_{01}^{+1}	2	3	38.0
T_{-10}^{-1}	2	3	33.5
T_{01}^{+1}	2	5	47.0
T_{-10}^{-1}	2	5	42.7

Table 4.3: Allowed transitions in the $n = -1, 0, 1$ subspace, for $B = 1$ T in three different topological regimes for $\Delta_H = 4$ meV.

$T_{mn}^{\tau_z=\pm1}$	Δ_z (meV)	Regime	Photonic energy (meV)
T_{01}^{+1}	2	QSHI	20.3
T_{-10}^{-1}	2	QSHI	25.1
T_{01}^{+1}	4	CNP	18.2
T_{-10}^{-1}	4	CNP	27.7
T_{01}^{+1}	8	NI	22.7
T_{-10}^{-1}	8	NI	33. 9

one of the participating level is zeroth LL. For higher magnetic fields we can see that the spectral weight increases with the increase in the strength of the applied magnetic field. The spectral weight decreases for higher magneto-excitation frequencies. To shed more light on MO excitations, we plot in Fig. 4.10(c)-(f) the s and p polarized magneto-transmission and reflection coefficients as a function of the incident photonic energy for different strengths of the magnetic field. We can see the normalized magneto-transmission and reflection peaks of the magneto-excitation energy for different transitions. Table 4.2 summarizes these results.

Next, we study the Kerr and Faraday rotation of the TI thin-films-substrate system by tuning the magnetic field for finite hybridization $\Delta_H = 4$ meV. The parameters used are $\theta_\psi = 30^\circ$, $\eta = 0.15\ \Delta_H$ (estimated from experimental findings [143]), refractive index $n_2 = 1.84$ and chemical potential $\mu_F = 0$, so that the inter-band transitions bridge across the valance and conduction bands. Fig. 4.11(a) shows the p polarized Kerr spectra as a function of the incident photonic energy for different values of the magnetic field strength. Borrowing ideas from [76], the signal originating from a single transition is dispersive Lorentzian, with a positive peak followed by a negative peak (or vice versa). We call this an anti-phase peak. We observed the first anti-phase peak of the Kerr rotations, which occurs when the incoming photon frequency resonates with a Landau level transition T_{01}^{+1}. Similarly, we can see a relatively small rotation anti-phase peak (with a negative followed

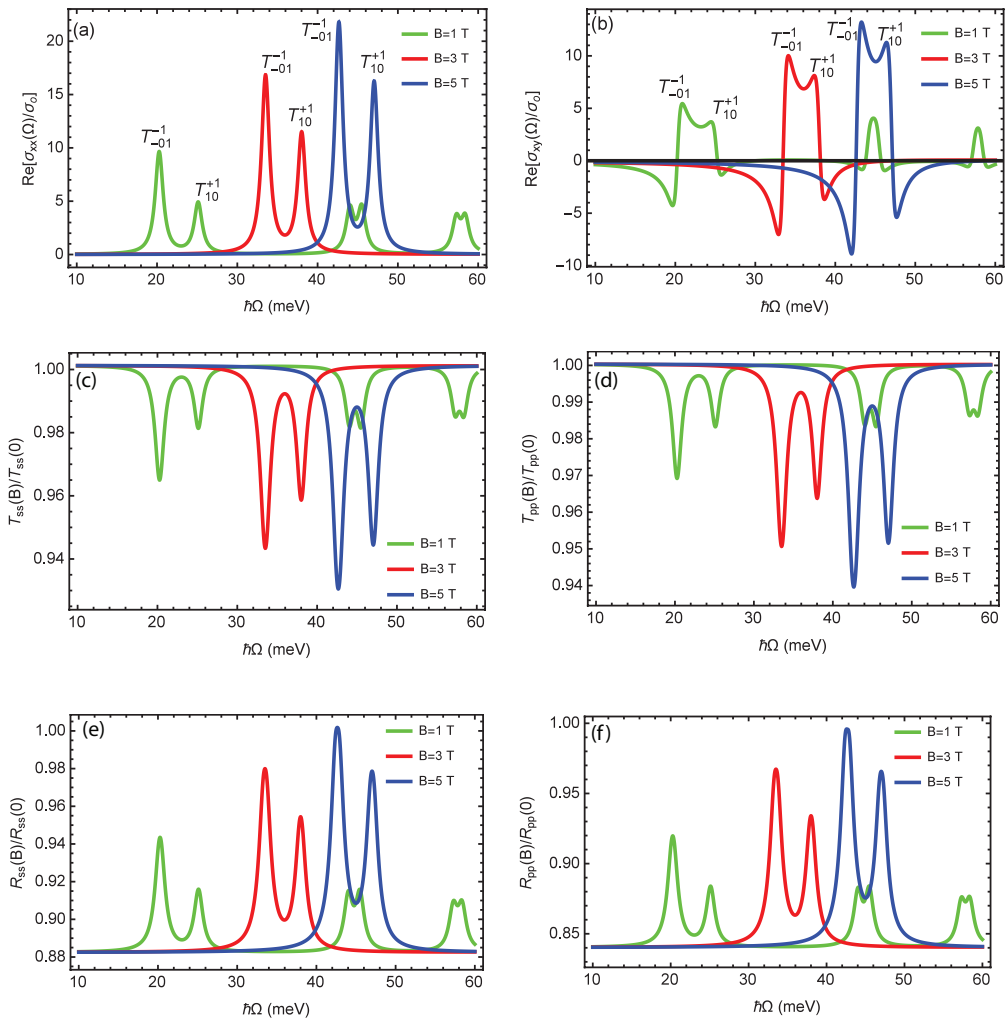

Figure 4.10: (a) and (b) Longitudinal and transverse Hall conductivities as a function of photonic energy for different magnetic fields in the QSHI regime for top and bottom SSs, respectively. (c)-(f) Modulus of the s and p polarized magneto-transmission and reflection coefficients for TI thin film-substrate system as a function of the incident photonic energy for different magnetic fields in the QSHI regime for top and bottom SSs, respectively. The parameters used for this simulation are Δ_H=4 meV, $\Delta_z = 0.5\Delta_H$, $\theta_\psi = 30°$, $\eta = 0.15\Delta_H$, refractive index $n_2 = 1.84$, and chemical potential $\mu_F = 0$.

by a positive) for the second magneto-excitation transition T^{-1}_{-10}. Like other 2D materials including graphene [93, 119] the TI energy levels are strongly dependent on the magnetic field B. As we increase the strength of the magnetic field, the

MO excitations shift towards higher frequencies.

Fig 4.11(b) shows the s polarized Kerr rotation spectra for different strengths of the magnetic field indicating that the anti-phase peaks switch signs. Furthermore, the sign of the MO rotation can be controlled by the polarization of the incident light. Fig. 4.11(c) shows that s polarized FR as a function of the incident photonic energy in the QSHI phase. The s polarized FR angles for the first two anti-phase peaks are $\approx \pm 6.5^{\circ}$. The main role of the modulated magnetic field is to shift the position of the MO excitation energies and also to change the magnitude of MO effects. Figures 4.11(d)-(f) represent the MO Kerr and FR rotations for different Zeeman interaction terms Δ_z in the THz regime. We display in Fig. 4.11(d) the p polarized Kerr rotation angle versus incident photonic energy for several values of the Zeeman field Δ_z. The first and second anti-phase peaks correspond to T_{01}^{+1} and T_{-10}^{-1} transitions in all three regimes. In the QSHI phase ($\Delta_z = 0.5\Delta_H$) with $B = 1$ T, these magneto-excitation energies are calculated as 20.3 meV (4.9 THz) and 25.1 meV (6.1 THz).

The magneto-excitations frequencies are presented in Table 4.3 for the first two transitions (T_{01}^{+1} and T_{-10}^{-1}) in the three distinct topological regimes. At the CNP ($\Delta_z = \Delta_H$), E_0^{-1} has exactly zero energy (see supplemental material). For QSHI phase E_0^{-1} is electron like and for NI phase it is hole like. The amount of Kerr rotation angles for both QSHI and CNP is $\approx \pm 6.0^{\circ}$ for $\tau_z = +1$. For higher MO excitation energies, we have T_{-10}^{-1} LLs transitions and the Kerr rotation angle $\geq \pm 2.0^{\circ}$. In the NI phase ($\Delta_z = 2\Delta_H$) the separation between the anti-phase pair keeps on growing and the peaks gradually shift towards higher frequencies (blue shifted). Here, the magnitude of the Kerr rotation angle is small as compared to the QSHI and CNP phases.

In Fig. 4.11(e) we plot the s polarized Kerr spectra as a function of photonic

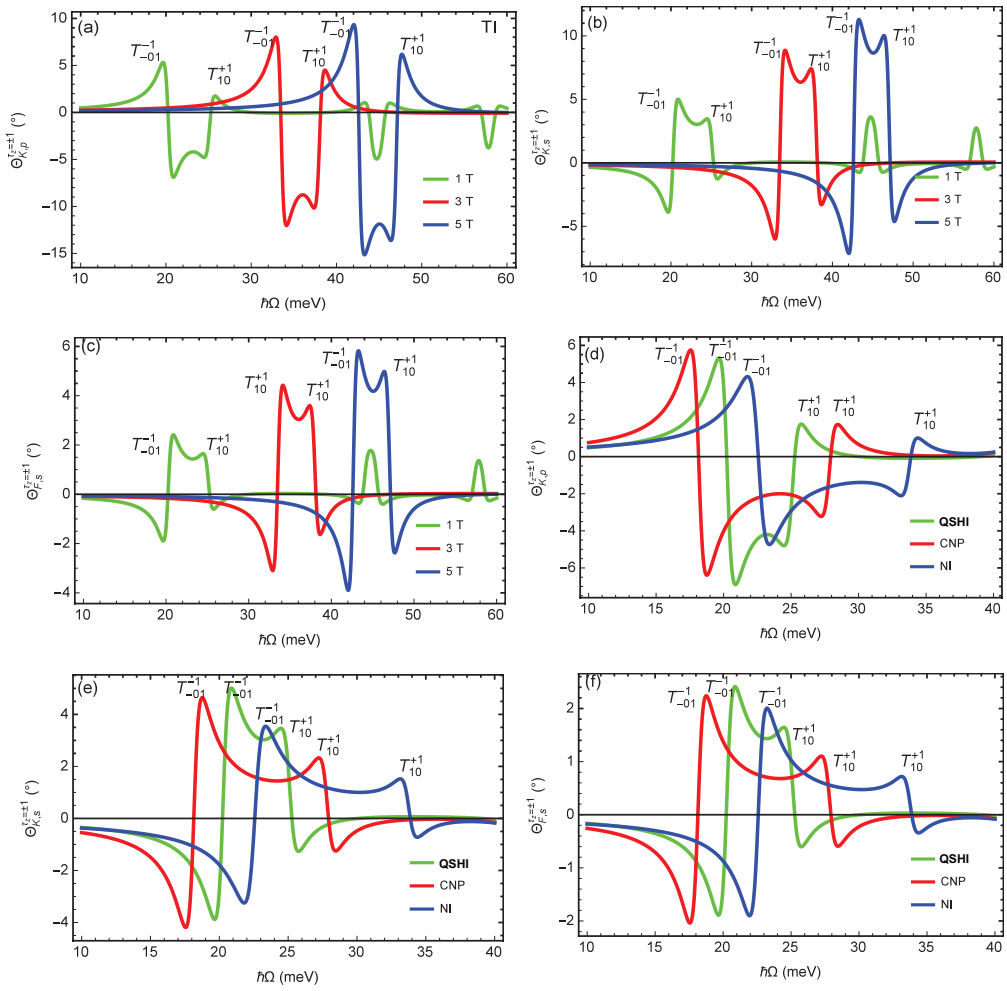

Figure 4.11: Kerr and Faraday rotation of TI thin film-substrate system as function of photonic energy for different values of magnetic field. (a) The p polarized and (b) s polarized Kerr rotation for magnetic field strength of 1, 3 and 5 T, in the QSHI regime. (c) The s polarized Faraday rotation for magnetic field strength of 1, 3 and 5 T, in the QSHI regime. (d) and (e) The s and p polarized Kerr rotation with modulation of the external Zeeman field interaction, for the QSHI ($\Delta_z = 0.5\Delta_H$), CNP ($\Delta_z = \Delta_H$) and BI ($\Delta_z = 2\Delta_H$) at a magnetic field of 1 T. (f) The s polarized Faraday rotation as function of the incident photonic energy with modulation of the external Zeeman field interaction, for the QSHI, CNP and BI at a magnetic field of 1 T. The parameters used for this simulation are Δ_H=4 meV, $\theta_\psi = 30°$, $\eta = 0.15\Delta_H$, refractive index $n_2 = 1.84$ and chemical potential $\mu_F = 0$.

energy for three distinct topological regimes, but only for two transitions. For s polarized incident light the polarity of the Kerr rotation angle is switched. The FR rotation spectra shown in Fig. 4.11(f) follow a similar trend. The magnitudes of the FR rotation angles range between $\approx \pm 2^{\circ}$ for all three topological regimes for top and bottom surfaces, which, in general, are smaller than the Kerr rotation angle.

4.2.3.2 Doping control of magneto-optic response

It is worth investigating the control of Kerr and FR spectra by varying the chemical potential μ_F. The LLs of the TIs top and bottom topological SSs can be tuned independently by employing top and back gate electrodes [144, 145]. Fine control of μ_F of the paired surface states in a dual-gated system has been recently reported [146]. In the subsequent analysis, the chemical potential is tuned near the Dirac point. For this purpose, we consider two different values of chemical potentials μ_F=10 and -10 meV while keeping the magnetic field 1 T in the QSHI regime ($\Delta_z = 0.5\Delta_H$), and an angle of incidence of 30°.

In the first case we assume n-type doping and μ_F=10 meV. The chemical potential lies in between the n=0 and $n = 1$ LLs as shown in Fig. 4.12(a). Blue lines represent LLs for top surfaces and red lines represent LLs for bottom surfaces. The same color scheme applies for the LL transitions with green line indicating the chemical potential μ_F. We identify these LL transitions as T^{+1}_{-01}, T^{-1}_{-10}, T^{-1}_{01}, T^{+1}_{-12} and T^{-1}_{-21} as shown in Fig. 4.12(a). The intra-band transition is shown by a dashed black upward pointing arrow. In the second case we consider p-type doping where $\mu_F = -10$ meV and the chemical potential is in between the n=0 and $n = -1$ LLs as displayed in Fig. 4.12 (b). For n-type doping, certain transitions become Pauli blocked. For example the transition $T^{-1}_{-10} = 20.3$ meV becomes forbidden and in their place the intra-band transition $T^{-1}_{01} = 16.3$ meV in the bot-

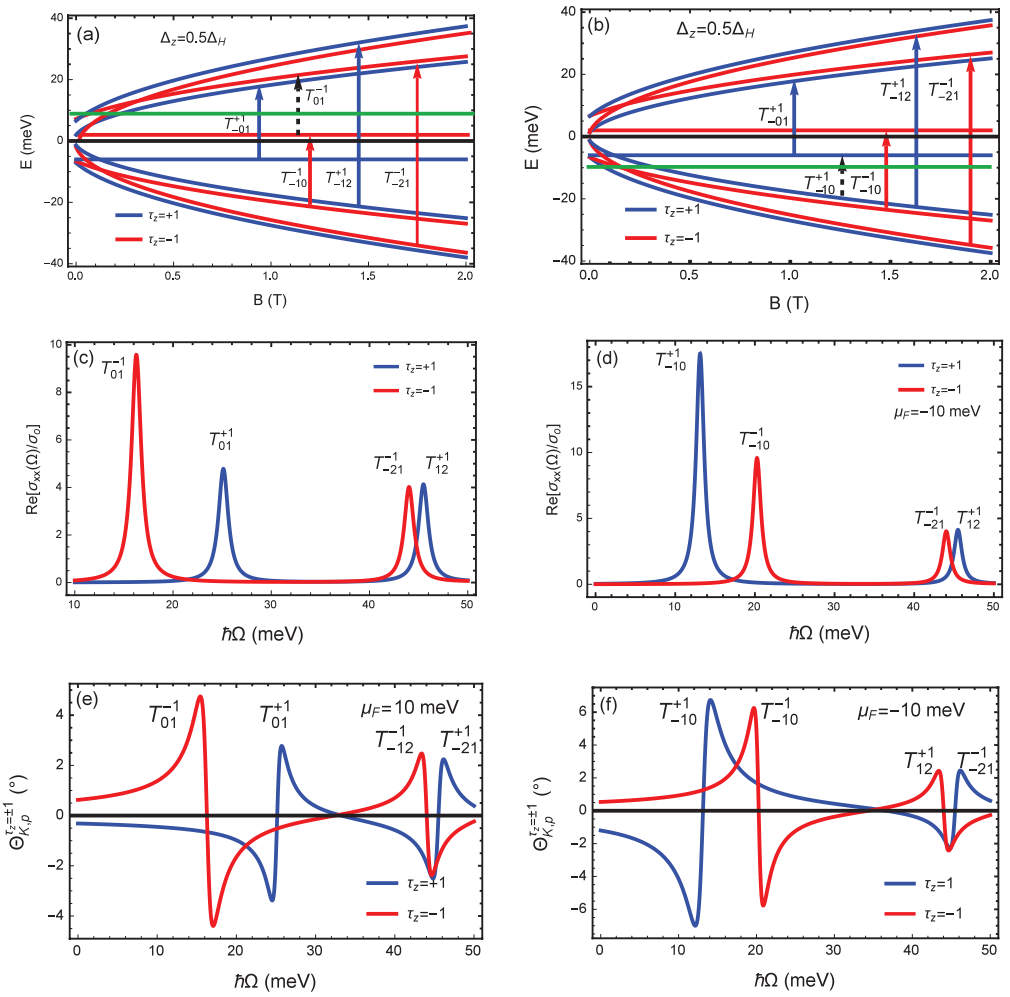

Figure 4.12: (a) and (b) Optically allowed inter-band and intra-band LL transitions satisfying the selection rule $\Delta n = \pm 1$ for top and bottom SSs in the QSHI regime. (c) and (d) Real parts of the optical conductivities for p-type and n-type TIs thin film-substrate system as a function of the incident photonic energy in the QSHI regime. (e) and (f) the p polarized Kerr rotation in the QSHI regime with n-type and p-type doping for a magnetic field of 1 T, respectively. (e) and (f) the p polarized Kerr rotation in the QSHI regime with n-type and p-type doping for a magnetic field of 1 T, respectively

tom surface appears. Similarly for p-type doping, when the chemical potential μ_F jumps between the n=0 and $n = -1$ LLs, owing to the Pauli blocking, transition $T_{01}^{+1} = 25.1$ meV disappears and $T_{-10}^{+1} = 13.1$ meV emerges.

The first and second magneto-excitation energies corresponding to T_{-01}^{+1} and

Table 4.4: Allowed LL transitions in the $n = -1, 0, 1$ subspace for different chemical potentials in the QSHI regime with $\Delta_H = 4$ meV.

$T_{mn}^{\tau_z=\pm1}$	μ_F (meV)	Inter/intraband	Photonic energy (meV)
T_{01}^{+1}	10	Inter	25.1
T_{01}^{-1}	10	Intra	16.3
T_{-10}^{+1}	-10	Intra	13.1
T_{-10}^{-1}	-10	Inter	20.3

T_{-01}^{+1} for top and bottom surfaces are calculated and summarized in Table 4.4. Higher-order inter-band transitions are weak where the LLs are closely spaced and the Kerr and FR originating from these transitions are very small hence we ignore them here. The longitudinal conductivities for n-type and p-type doped TIs are shown in Figs. 4.12(c) and (d). The intra-band and inter-band transitions are shown as pronounced dips at incident photonic energies in the QSHI regime for $B = 1$ T.

The spectral weights of these transitions are larger for p-type doping and smaller for n-type doping. The p polarized Kerr rotations anti-phase peaks are shown in Fig. 4.12(e) and (f) for μ_F=10 meV and -10 meV, respectively. For n-type doping, these anti-phase peaks originate from the two lowest transitions $T_{01}^{-1} = 16.3$ meV and $T_{01}^{+1} = 25.1$ meV as shown in Fig. 4.12(e). The maximum Kerr rotation is achieved at the bottom surface for n-type doping, while for the top surface the amount of rotation is small. On the other hand, for p-type doping, we have giant anti-phase peaks for the top surface and comparatively small peaks for the bottom surface as shown in Fig. 4.12 (f). For p-type doping, the Kerr rotation angles of $\approx \pm 10^\circ$ and $\approx \pm 9^\circ$ are observed (data not shown) for the two lowest transitions $T_{-10}^{+1} = 26.0$ meV and $T_{-10}^{-1} = 33.5$ meV for bottom and top surfaces respectively, for $B = 3$ T. This exceeds the maximum values reported in literature for graphene in the THz region [94, 109]. Please note that the asymmetric response from the

top and bottom surfaces arises due to the difference in their energies and not due to the permittivity of the medium.

4.2.3.3 Semiclassical approximation

In the semiclassical approximation, the LL spacing due to the applied magnetic field becomes negligible, which occurs when the chemical potential is very large $|\mu_F| \gg |E_1|$. This usage of the term 'semi-classical' is unique to these low dimensional quantum systems and different from other literature in atom-matter interactions, where the term describes quantized electronic systems interacting with light which is treated as a classical electromagnetic wave (though this is the assumption in the current work as well). In this case, the intra-band transitions between closely spaced LLs are allowed.

To compare the semi-classical results with the quantum mechanical ones, we study the real part of the longitudinal and transverse magneto-optical conductivities of the TIs thin film (see supplemental material for details). These conductivities are shaped as absorptive and dispersive Lorentzians which are directly used to compute the Fresnel coefficients Eqs. (4.17)–(4.22) and subsequently the rotations. We also investigate the dependence of Kerr and Faraday rotations on photonic energy in the semiclassical regime for n-type TIs thin film (see supplemental material for details). These rotation angles exceed the maximum values as discussed above in the quantum regime. At a field of 1 T, we report the p polarized Kerr rotation and s polarized Faraday rotations $\Theta_{K,p}^{\tau_z=+1} = 14^\circ$, $\Theta_{K,p}^{\tau_z=-1} = 10^\circ$, $\Theta_{F,s}^{\tau_z=+1} = 6^\circ$ and $\Theta_{F,s}^{\tau_z=+1} = 5^\circ$, respectively.

In the semiclassical approximation, the energy of intra-band transitions can be approximated as

$$E_{n+1} - E_n \approx \frac{\hbar v^2 eB}{\sqrt{E_B^2|n| + \Delta_{\tau_z}^2}} = \hbar\Omega_c, \tag{4.39}$$

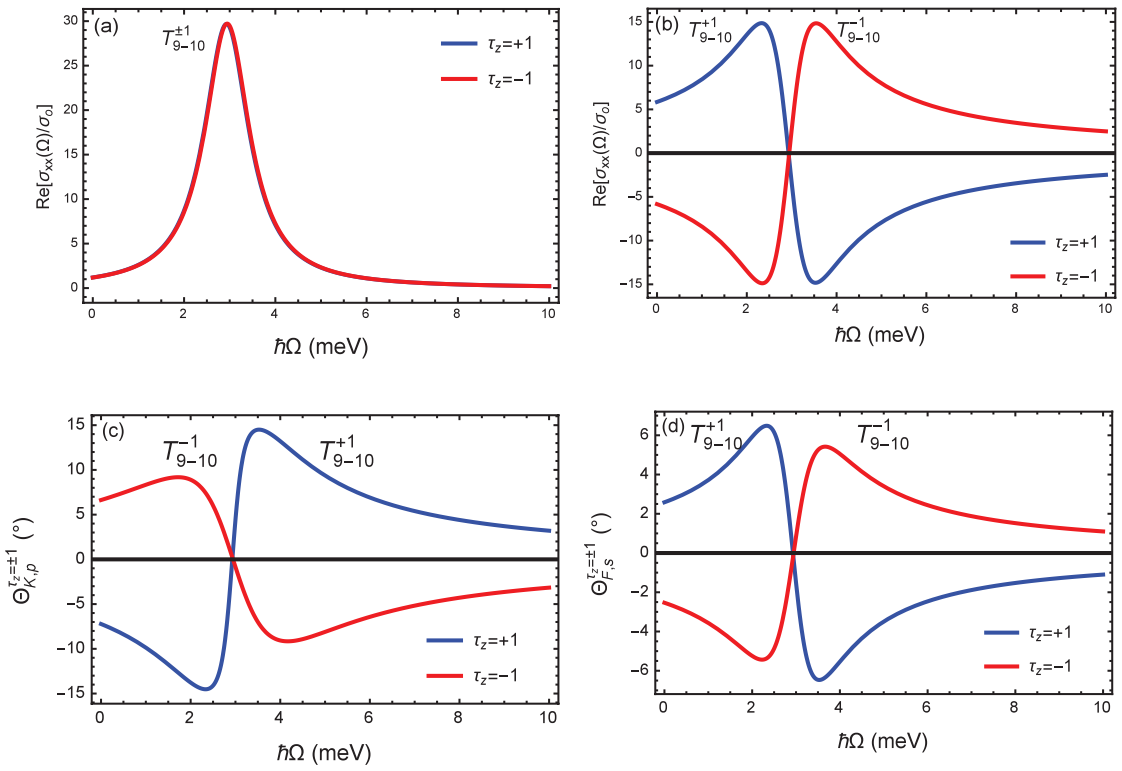

Figure 4.13: (a) The real part of the longitudinal and (b) transvers Hall conductivity as a function of incident photonic energy in the semiclassical limit for two transitions for n-type doping. (c) the p polarized Kerr rotation and (d) the s polarized Faraday rotation as a function of incident photonic energy in the semiclassical limit.

where, $\Omega_c = \hbar v^2 eB/\mu_F$ is called the classical cyclotron frequency. In the semiclassical limit the conductivities of the top and bottom surfaces can be modeled by classical Drude-like peaks and can be written as

$$\frac{\mathrm{Re}\big(\sigma_{xx}(\Omega)\big)}{\sigma_0} = -\frac{\mathrm{Im}\big(\sigma_{xy}(\Omega)\big)}{\sigma_0} = \frac{\hbar\mu_F}{\pi}\frac{\eta}{(\hbar(\Omega-\Omega_c))^2+\eta^2}, \tag{4.40}$$

$$\frac{\mathrm{Im}\big(\sigma_{xx}(\Omega)\big)}{\sigma_0} = \frac{\mathrm{Re}\big(\sigma_{xy}(\Omega)\big)}{\sigma_0} = \frac{\hbar\mu_F}{\pi}\frac{\hbar(\Omega-\Omega_c)}{(\hbar(\Omega-\Omega_c))^2+\eta^2}, \tag{4.41}$$

where $\alpha_n \approx \alpha_{n-1} \approx \beta_n \approx \beta_{n-1} = 1/\sqrt{2}$. In Figs. 4.13(a) and (b), we have plotted the real part of the longitudinal and transverse magneto-optical conductivities of the TIs thin film. For finite chemical potential μ_F and LL n, the allowed intraband transitions are $T^{\tau_z=+1}_{9-10}$ and $T^{\tau_z=-1}_{9-10}$. For large chemical potential the *strong*

intra-band absorption peak can be seen in Fig. 4.13(a). We also observe that the spectral weight increases with the chemical potential. These conductivities are shaped as absorptive and dispersive Lorentzians.

We plotted the Kerr and Faraday rotations verses photonic energy in Figs. 4.13(c) and (d) in semiclassical regime for n-type TIs thin film. We can see in Figs. 4.13(c) giant p polarized Kerr rotation anti-phase peaks for the incident beam exciting the $T_{9-10}^{\tau_z=+1}$ and $T_{9-10}^{\tau_z=-1}$ transitions respectively. These rotation angles exceeds the maximum values discussed in the quantum regime. Similarly, for s polarized Faraday rotation for $\mu_F = 55$ meV, the anti phase peak can be seen at classical cyclotron resonance frequencies. At a field of 1 T, the p polarized Kerr rotation and s polarized Faraday rotations are: $\Theta_{K,p}^{\tau_z=+1} = 14^\circ$, $\Theta_{K,p}^{\tau_z=-1} = 10^\circ$, $\Theta_{F,s}^{\tau_z=+1} = 6^\circ$ and $\Theta_{F,s}^{\tau_z=+1} = 5^\circ$.

Chapter 5

Mechanical beam shifts in 2D quantum materials

In this chapter, we will study the Goos-Hänchen shifts of a beam impinging on the surface of a 2D material-dielectric interface and we will show that the beam appears to undergo lateral as well as angular shifts as shown in Fig. 6.1. This mechanical displacement was first experimentally studied by Goos and Hänchen in 1947. Hence this effect is called the Goos-Hanchen effect. The effect is a direct consequence of the evanescent field produce in the rarer medium and hence cannot be explained from classical ray optics. In this chapter, by using the magneto-optical conductivities and Fresnel's coefficients of silicene and hybridized topological insulator thin films derived in Chapter 3, we calculate the lateral and angular shifts for these quantum materials, indicating the potential superiority of these materials relative to graphene.

The current chapter is structured into three major parts. In the first part, we will apply the GH shift formalism to investigate the electric and magnetic field modulated giant spatial and angular GH shifts in silicene. This part of the chapter has been published in *OSA Continuum* [142]. In the second part, we study the Goos-Hanchen (GH) shift from the surface of a hybridized topological insulator (TI) thin film in the presence of a static magnetic field. The second part has been

published in *Physica E: Low-dimensional Systems and Nanostructures* [147].

5.1 Magneto-optic modulation of lateral and angular shifts in spin-orbit coupled members of the graphene family

5.1.1 Background and motivation

The most common phenomena in classical optics are the reflection and refraction of light. To describe the interaction of a plane wave with an interface separating two dielectric media, the propagation of the reflected and transmitted waves is described by the well-known Fresnel and Snell laws. However, this traditional geometric optics picture is not applicable for a beam (the superposition of several plane wave components) of finite width in a subwavelength regime. On reflection, each plane wave suffers different amounts of spatial and angular phase shifts, resulting in longitudinal (parallel to the plane) and transverse (perpendicular to the plane) shifts, respectively called Goos-Hanchen (GH) and Imbert-Fedorov (IF) shifts [148, 149]. Such a striking optical phenomenon is attributed to the penetration of an evanescent field.

In order to understand the evanescent field description, Lotsch in 1968 presented an explicit calculation of the Poynting vector for the analysis of the energy redistribution, which gives the direction of energy flow [150]. He examined that a part of the incident beam enters the rarer medium and reappeared at another point to produce the observed shift. To understand the physics of the Goos-Hanchen shift, consider the pictorial representation of Schaefer and Pich [151] in Fig. 5.1. The incident beam is represented by $ABCD$. The beam is homogeneous in the central region BC and decays off to zero from B to A and C to D. The direction of the Poynting vector is toward the rarer medium, parallel to the surface, and

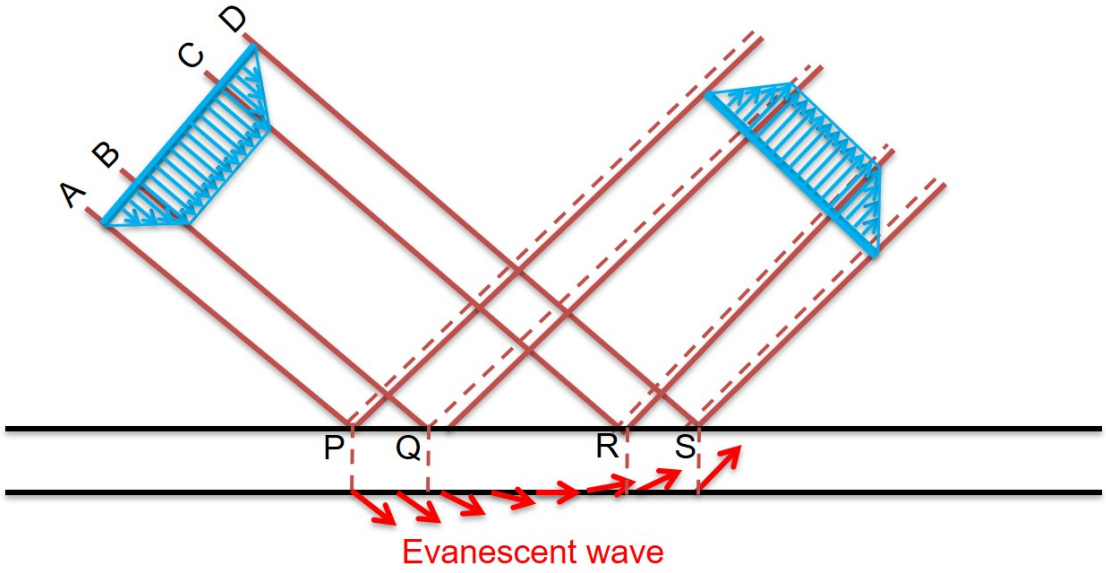

Figure 5.1: Schematic representation of the Poynting vector direction in different parts of a beam ABCD.

away from the rarer medium, in the regions PQ, QR, and RS respectively. The energy is entering into the rarer medium from the leading portion of the beam and returning from the rarer medium in the sweeping portion after reflection.

On imposing the boundary conditions it is evident that there should be an evanescent field in the rarer medium. This field decays exponentially away from the boundary. Initially, there is no evanescent field. However, when the leading portion of the beam is incident on the interface, it set up an evanescent field in a rarer medium. Because of this, the beam undergoes a spatial and angular deviation.

During the last decade, the GH shift has been extensively studied in many different systems, such as photonics [152, 153], plasmonics [154, 155], chiral materials [156], metamaterials [157] and quantum systems [158]. The potential applications of GH shift are in biosensors [155], optical measurement, and optical heterodyne sensors [159]. For example, controlling the Fermi energy in THz region, L. Jiang *et. al*

theoretically studied electrically tunable GH shifts of monolayer graphene [160]. The magnetic field and Fermi energy modulated giant quantized GH effect on the surface of graphene in the quantum Hall regime was recently predicted [161]. T. Tang *et. al* proposed an experimental scheme based on a prism-graphene coupling structure for MO tunable GH effect sensing [162, 163].

Recently the GH shift on the surface of silicene [75], TMDCs [164] and Weyl semimetals [165] has also been investigated. From an application perspective, Farmani *et. al* designed a bidirectional and tunable graphene plasmonic switch in a modified Kretschmann configuration in THz range [166]. In the THz to the mid-infrared range, the observation of GH effect in graphene may find significant new and interesting applications in extremely sensitive optical sensors [167, 168]. Many works are devoted to study the electronic analog of the valley and spin-polarized GH shift in silicene and gapped graphene structures [169, 170].

The novelty of this current work lies in obtaining large spin and valley resolved GH shifts simultaneously in staggered 2D materials in the presence of applied electric and magnetic fields, a scenario not comprehensively covered in previous works. The present study details the impact of the magnetic field, chemical potential, incident frequency, electric field, and incident angle modulation of the valley- and spin-polarized GH shifts in staggered 2D semiconductors materials.

Furthermore, the Brewster effect is a fundamental electromagnetic and optical phenomenon in which p polarized light experiences zero reflection [171, 172]. Controlling the Brewster angle is extremely important in broadband devices such as the solid-state modulator [173]. We also show that the Brewster effect in the silicenic atomic layer is strongly influenced by magnetic fields. Last, we find that angular and spatial GH shifts can be significantly enhanced by tuning the chemical potential, incident beam frequency, and the electric field which can render the sys-

tem in various regimes such as the topological insulator (TI), valley-spin polarized metal (VSPM) and band insulator (BI).

The MO-controlled Brewster angle can be used to develop a highly tunable solid-state modulator. More interestingly, the valleys and spins indices can be used for the switching of the GH shift from negative to positive and vice versa. The GH shift in staggered 2D materials paves the way for realizing spin and valley-dependent devices and systems that can be useful optical readout markers for experiments in quantum information processing, biosensing, spintronics, and valleytronics in the THz regime. Moreover, the electro-optic and MO tunable GH shifts can be used for the detection of electric field and magnetic field sensing and also for the determination of the doping level of these 2D staggered layers.

This part of the chapter is organized as follows: Section 5.1.2 will lay down the theoretical background for the lateral and angular shifts in spin-orbit coupled members of the graphene family. In Section 5.1.3, we will present the results and discussion. Finally, we will conclude our findings in Section **??**.

5.1.2 Model and theory

To illustrate GH shifts in a general beam propagation model, we consider an EM Gaussian beam of light of finite width, well collimated, monochromatic, with frequency ω, and is incident on a 2D material-substrate at an incident angle θ_ψ from the air. The refractive indices of the first and second media are n_1 and n_2, respectively. We consider the air-staggered 2D monolayer-substrate interface to be in the x, y plane of the laboratory Cartesian frame at $(z = 0)$. A static magnetic field is acting along the z axis which is perpendicular to a 2D material substrate. We use coordinates (x_i, y_i, z_i) and (x_r, y_r, z_r) to denote the incident and reflected

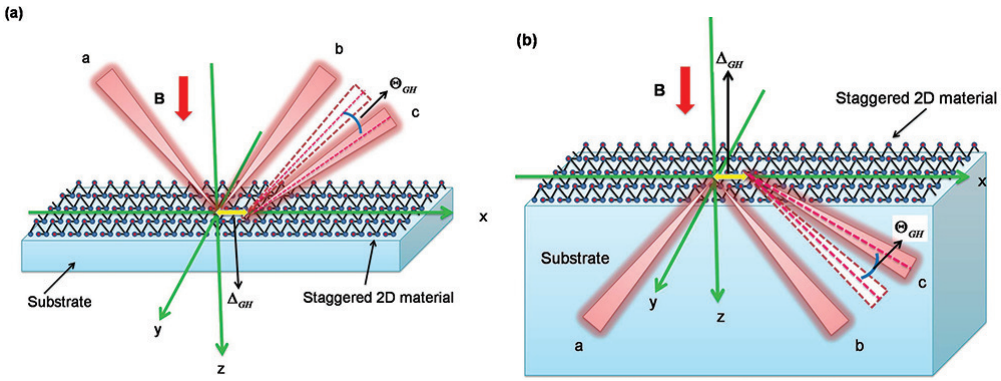

Figure 5.2: Schematic representation of the beam reflection at a 2D staggered material-substrate interface in the presence of external electric and magnetic fields are shown for partial reflection (PR) and total internal reflection (TIR) conditions. The spatial and angular GH shifts for (a) PR and (b) TIR. The incident, classically predicted and reflected beams are denoted by a, b and c respectively.

beams, respectively. The incident Gaussian beam can be expressed in the angular spectrum representation as

$$\tilde{E}_i(k_{ix}, k_{iy}) = \Phi_0 \hat{f}, \tag{5.1}$$

where $\Phi_0 = \exp[-\frac{w_0^2(k_{ix}^2+k_{iy}^2)}{4}]$ with the beam waist w_0. The unit complex vector $\hat{f} = (\hat{x}_i f_p + \hat{y}_i f_s)$ represents the polarization of the incident beam. The amplitudes of the incident and reflected angular spectrum are related as $\tilde{E}_r(k_{rx}, k_{ry}) = M_R \tilde{E}_i(k_{xi}, k_{ri})$ which can be expressed explicitly as

$$\begin{bmatrix} \tilde{E}_p^{(r)} \\ \tilde{E}_s^{(r)} \end{bmatrix} = \hat{R} \begin{bmatrix} \tilde{E}_p^{(i)} \\ \tilde{E}_s^{(i)} \end{bmatrix}, \text{with } \hat{R} = \begin{bmatrix} r_{pp} & r_{ps} \\ r_{sp} & r_{ss} \end{bmatrix}, \tag{5.2}$$

where r_{pp}, r_{ps}, r_{ss} and r_{sp} are the Fresnel reflection coefficients for parallel and perpendicular polarizations. Introducing the boundary condition $k_{rx} = -k_{ix}$ and $k_{ry} = k_{iy}$ and by making use of a Taylor series expansion the Fresnel reflection coefficients r_λ around the central wave vector can be written as

$$r_\lambda(k_{ix}) = r_\lambda(k_{ix}=0) + k_{ix}\left[\frac{\partial r_\lambda(k_{ix})}{\partial k_{ix}}\right]_{k_{ix}=0} + \sum_{j=2}^{N} \frac{k_{ix}^N}{j!}\left[\frac{\partial^j r_\lambda(k_{ix})}{\partial k_{ix}^j}\right]_{k_{ix}=0} \tag{5.3}$$

The angular spectrum of the reflected field can be written as

$$\tilde{E}_r(k_{rx},k_{ry}) = \Phi_0\hat{x}_r\left[f_p r_{pp}\left(1-\frac{k_{rx}}{k_0}\frac{\partial \ln r_{pp}}{\partial\theta_i}\right)+f_s r_{ps}\left(1-\frac{k_{rx}}{k_0}\frac{\partial \ln r_{ps}}{\partial\theta_i}\right)\right] + \Phi_0\hat{y}_r\left[f_s r_{ss}\left(1-\frac{k_{rx}}{k_0}\frac{\partial \ln r_{ss}}{\partial\theta_i}\right)+f_p r_{sp}\left(1-\frac{k_{rx}}{k_0}\frac{\partial \ln r_{sp}}{\partial\theta_i}\right)\right] \quad (5.4)$$

Upon reflection, the complex amplitude for the reflected beam using the Fourier transformations, can be expressed as

$$E_r(x_r,y_r,z_r) = \int\int dk_{rx}dk_{ry}\tilde{E}_R(k_{rx},k_{ry})\exp[i(k_{rx}x_r+k_{ry}y_r+k_{rz}z_r)] \quad (5.5)$$

For well collimated paraxial beams the transverse wavenumbers $k_x^2+k_y^2 \ll 1$, so using paraxial approximation, we can write $k_{rz}=\sqrt{k_r^2-(k_{rx}^2+k_{ry}^2)} = k_r-(k_{rx}^2+k_{ry}^2)/2k_r$. Using the above relation Eq. (5.5), can be written as

$$\mathbf{E}_r(x_r,y_r,z_r) = \int\int dk_{rx}dk_{ry}\tilde{E}_R(k_{rx},k_{ry})\exp[i(k_{rx}x_r+k_{ry}y_r+(k_r-\frac{(k_{rx}^2+k_{ry}^2)}{2k_r})z_r)] \quad (5.6)$$

In position space the general expression for the reflected angular spectrum is obtained as

$$\begin{aligned}\mathbf{E}_r \propto \exp&\left(ik_0z_r-\frac{k_0}{2}\frac{x_r^2+y_r^2}{\Lambda_R+iz_r}\right)\\ &\times\left\{\hat{\mathbf{x}}_r\left[f_p r_{pp}\left(1-\frac{ix_r}{\Lambda_R+iz_r}\frac{\partial \ln r_{pp}}{\partial\theta_i}\right)+f_s r_{ps}\left(1-\frac{ix_r}{\Lambda_R+iz_r}\frac{\partial \ln r_{ps}}{\partial\theta_i}\right)\right]\right.\\ &+\left.\left\{\hat{\mathbf{y}}_r\left[f_s r_{ss}\left(1-\frac{ix_r}{\Lambda_R+iz_r}\frac{\partial \ln r_{ss}}{\partial\theta_i}\right)+f_p r_{sp}\left(1-\frac{ix_r}{\Lambda_R+iz_r}\frac{\partial \ln r_{ps}}{\partial\theta_i}\right)\right]\right\}\end{aligned} \quad (5.7)$$

where, Λ_R is the Rayleigh range, $f_p = a_p \in \mathbf{R}$ and $f_s = a_s\exp(i\eta)$.

The next task is to find out the relationship for the Goos-Hanchen shift in staggered 2D monolayer materials. The intensity distribution of the reflected beam $I(x_r,y_r,z_r)$ is related to the longitudinal momentum current or another words to the Poynting vector. The time-averaged linear-momentum density can be written as [161]

$$\mathrm{S}_r = \frac{1}{c^2}\mathrm{Re}[\mathrm{E}_r\times\mathrm{H}_r^*] \quad (5.8)$$

Here the magnetic field is given by $\mathrm{H}_r = -ik_r^{-1}\nabla \times \mathrm{E}_r$. If one ignore the irrelevant proportionality factor, the intensity is directly proportional to the absolute square of the reflected angular spectrum $I(x_r, y_r, z_r) \propto |E_R|^2$. The longitudinal displacements of the field centroid at any given plane z_r=const, is given by

$$D_{GH} = \frac{\int\int x_r I(x_r, y_r, z_r) dx_r dy_r}{\int\int I(x_r, y_r, z_r) dx_r dy_r} \tag{5.9}$$

Considering only the horizontal polarization with $a_p = 1$, $a_s = 0$ and $\eta = 0$. Substituting Eqs. (5.7) into (5.9), the following expression is obtained

$$D_{GH} = \frac{2(^2_{pp}\varphi_{pp} + R^2_{ps}\varphi_{ps})\Lambda_R}{2k(R^2_{ps} + R^2_{pp})\Lambda_R + \chi_{pp} + \chi_{ps}} \tag{5.10}$$

$$- \; z_r \frac{2(R^2_{pp}\varphi_{pp} + R^2_{ps}\varphi_{ps})}{2k(R^2_{ps} + R^2_{pp})\Lambda_R + \chi_{pp} + \chi_{ps}} \tag{5.11}$$

where, $R_\lambda = R_\lambda \exp(i\phi_\lambda)$, $\rho_\lambda = \mathrm{Re}(\partial \ln R_\lambda / \partial\theta_i)$, $\varphi_\lambda = \mathrm{Im}(\partial \ln R_\lambda / \partial\theta_i)$ and $\chi_\lambda = R^2_\lambda(\varphi^2_\lambda + \rho^2_\lambda)$. Here R_λ is the amplitude and ϕ_λ is the phase of the reflection coefficients. The first term is the spatial GH shift and the second term the is the angular GH shift as a function of the beam propagation distance z_r. For p polarized incident light beam the GH shifts can be divided into spatial and angular shifts as [142]

$$\Theta^p_{\mathrm{GH}} = -\frac{2(R^2_{pp}\rho_{pp} + R^2_{ps}\rho_{ps})}{2k(R^2_{ps} + R^2_{pp})\Lambda_R + \chi_{pp} + \chi_{ps}}, \tag{5.12}$$

$$\Delta^p_{GH} = \frac{2(R^2_{pp}\varphi_{pp} + R^2_{ps}\varphi_{ps})\Lambda_R}{2k(R^2_{ps} + R^2_{pp})\Lambda_R + \chi_{pp} + \chi_{ps}}. \tag{5.13}$$

The superscripts identify the polarization state (p). By using Eqs. (3.66) and (3.72), we can calculate the Fresnel's reflection coefficients and subsequently the GH shifts.

5.1.3 Results and discussion

5.1.3.1 Magnetic field modulated Goos-Hanchen

We quickly recount the effect of the magnetic field on the energy level structure and subsequently the MO response. Schematic diagrams showing the allowed tran-

sitions between Landau levels (LL's) for three different magnetic field (B =1, 3 and 5 T) all in the topological insulator regime ($\Delta_z < \Delta_{so}$) and in the K valley are shown in Fig. 5.3(a)–(c). The transition energy is determined from the energy difference between LL's obeying certain selection rules namely $|n| - |m| = \pm 1$ and the conservation of real spin implying that transitions between $\sigma = +1$ and -1 levels are spin forbidden.

The excitation energies corresponding to the different transitions, $E_{m,K(K'),\uparrow(\downarrow)} \rightarrow E_{n,K(K'),\uparrow(\downarrow)}$ are labelled as $\Delta_{mn,K(K'),\uparrow(\downarrow)}$. Blue lines represent Landau levels for spin up ($\sigma =\uparrow$) and red lines represent Landau levels for spin down ($\sigma =\downarrow$). In each of the depicted transitions, one of the participating levels is an n=0 level. For example for $B = 1$ T, the first and second magneto-excitation energies correspond to the $\Delta_{-10,K,\uparrow}$ and $\Delta_{01,K,\downarrow}$ for spin up and spin down respectively and are calculated at 20.3 meV (4.9 THz) and 25.1 meV (6.1 THz) respectively. For higher n, the LL's are closely spaced, we ignore these transitions for the time being. Similarly for $B = 3$ and 5 T, the allowed transitions between LL's are shown in Fig. 5.3(b) and (c). In fact, Table 5.1 summarizes magneto-excitation frequencies within the $n = -1, 0, 1$ manifold for the magnetic fields considered.

In Fig. 5.3(d), we have shown the variation of the longitudinal conductivity as a function of photon frequency for three different magnetic fields also shown exclusively for the TI regime. We can see resonant peaks when the incident $\hbar\Omega$ hits the magneto-excitation energy. As we increase the strength of the applied magnetic field, the MO excitations shift towards higher frequencies. For practicality and simplicity, we will restrict ourselves to the lowest magneto-excitation transition frequency, originating only from the $\Delta_{-10,K,\uparrow}$ transition while investigating the GH shift in this article, unless otherwise specified.

With knowledge of the LL transitions and magneto-optical conductivities of the

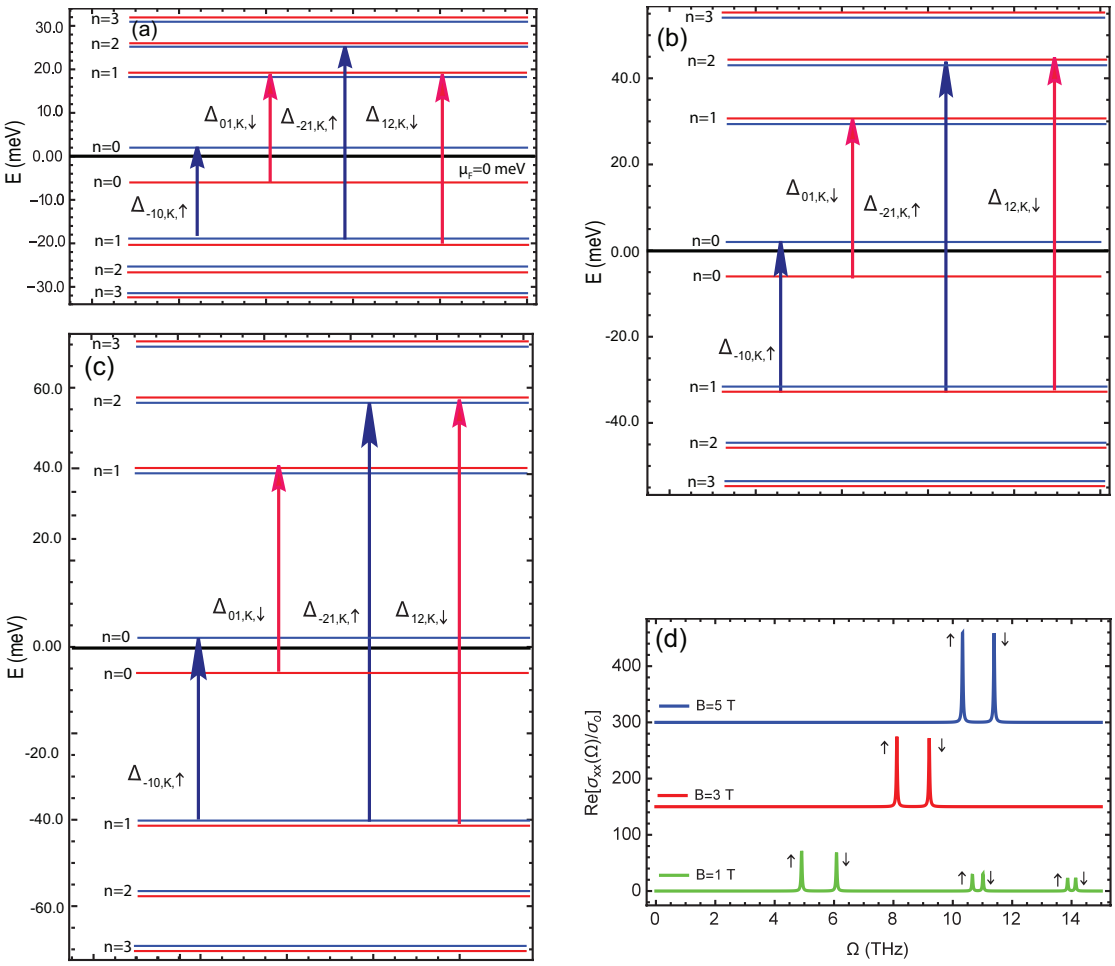

Figure 5.3: Schematic representation of the allowed transitions between LL's for three different magnetic fields in the K valley at (a) 1 T (b) 3 T (c) 5 T. Blue lines represent Landau levels for spin up ($\sigma =\uparrow$) and red lines represent Landau level for spin down ($\sigma =\downarrow$). The same color scheme applies for the Landau levels transitions. (d) Longitudinal conductivity as a function of photon frequency. The parameters used are Δ_{so}=8meV, $\Delta_z = 0.5\Delta_{so}$ and chemical potential $\mu_F = 0$.

2D materials for different magnetic fields at hand, we are now capable to study the spatial and angular GH shifts. We first discuss the reflectivity and phases of the reflected s and p polarized waves for incident light. Clearly, if the impinging Gaussian beam frequencies are smaller than all Dirac gaps, then no electrons can be excited from the valence to the conduction band. On the other hand, a resonant Gaussian wave will excite an electron-hole pair. As the resonance condition

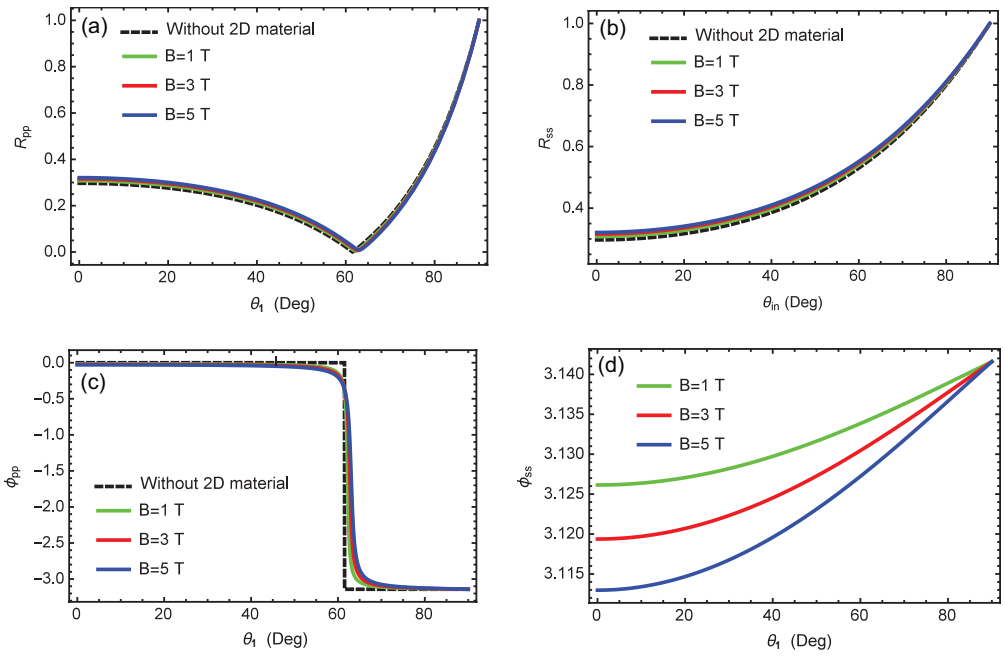

Figure 5.4: Modulus and phase of the s and p polarized reflection coefficients for 2D staggered graphene-substrate system as a function of incident angle for different magnetic fields in K valley for PR: (a) R_{ss}, (b)R_{pp}, (c) ϕ_{pp} and (d) ϕ_{ss}. The parameters used are Δ_{so}=8meV, $\Gamma = 0.2\Delta_{so}$, refractive index $n_2 = 1.84$ and chemical potential $\mu_F = 0$.

is spin-dependent, so spins of only one kind (say up spin) electrons will be excited. The resonant excitation energies (frequencies) for the $\Delta_{-10,K,\uparrow}$ transition are 20.3 meV (4.9 THz) at $B = 1$ T; 33.5 meV (8.1 THz) at $B = 3$ T and 42.6 meV (10.3 THz) at $B = 5$ T. Fig. 5.4 illustrates the magnetic field modulated reflectivity (R_{ss} and R_{pp}) and their phases (ϕ_{ss} and ϕ_{pp}) as a function of incident angle in the TI regime. In Fig. 5.4(a) and (b), the moduli of R_{pp} and R_{ss} are shown for various magnetic fields indicating that for p polarized incident light, R_{pp} achieves a minimum value at a certain θ_1 and rises again. This is called the pseudo-Brewster angle $\theta_B = \tan^{-1}(n_2/n_1)$, whereas R_{ss} increases smoothly as the angle of incidence is increased. At θ_B, the magnitude of reflection coefficient R_{pp} intensity for the uncoated surface (without 2D material) reaches zero, as shown in Fig. 5.4(a) by a dashed line. For the 2D staggered atomic layer, R_{pp} at the Brewster angle θ_B is

Table 5.1: Table of allowed transitions in K valley in the $n = -1, 0, 1$ subspace, for different magnetic fields in the TI regime with $\Delta_{so} = 0.5\Delta_z$.

$\Delta_{mn,K(K'),\uparrow(\downarrow)}$	B (T)	Frequency (THz)
$\Delta_{-10,K,\uparrow}$	1	4.9
$\Delta_{01,K,\downarrow}$	1	6.1
$\Delta_{-10,K,\uparrow}$	3	8.1
$\Delta_{01,K,\downarrow}$	3	9.2
$\Delta_{-10,K,\uparrow}$	5	10.3
$\Delta_{01,K,\downarrow}$	5	11.4

non-zero, because the MO conductivity of the graphene-family is complex.

The phase ϕ_{pp} shows the transition from 0 to $-\pi$ in the vicinity of θ_B for different magnetic fields. A similar variation has been reported in 2D-TMDC [164]. The phase ϕ_{ss} shows an increasing trend with θ_1 in the TI regime, as shown in Fig. 5.4(d). Note that we haven't shown results in the VSPM state and BI regime, for which R_{ss} and R_{pp} don't appreciably change for magnetic fields. In the remainder of this section, we will only discuss the magnetically induced spatial and angular s for the interesting case of p polarized light. The shifts for the charge-neutral graphene-family ($\mu_F = 0$ meV) are plotted as a function of incident angle for different magnetic fields in the TI regime in Fig. 5.11(a), whereas the angular GH shifts are represented in Fig. 5.11(b). Since $\partial\phi_p/\partial\theta_1 \neq 0$ and is accentuated in the vicinity of θ_B, the spatial shifts are dominant in the vicinity of the pseudo-Brewster angle.

To better visualize the dependence of the GH shifts with respect to the magnetic field consider the p polarized spatial GH shifts in Fig. 5.5(a), for the three different magnetic fields. We observe giant negative spatial beam shifts in the TI regime. If we look at the ϕ_{pp} spectra in Fig. 5.4(c) together with these shifts, we

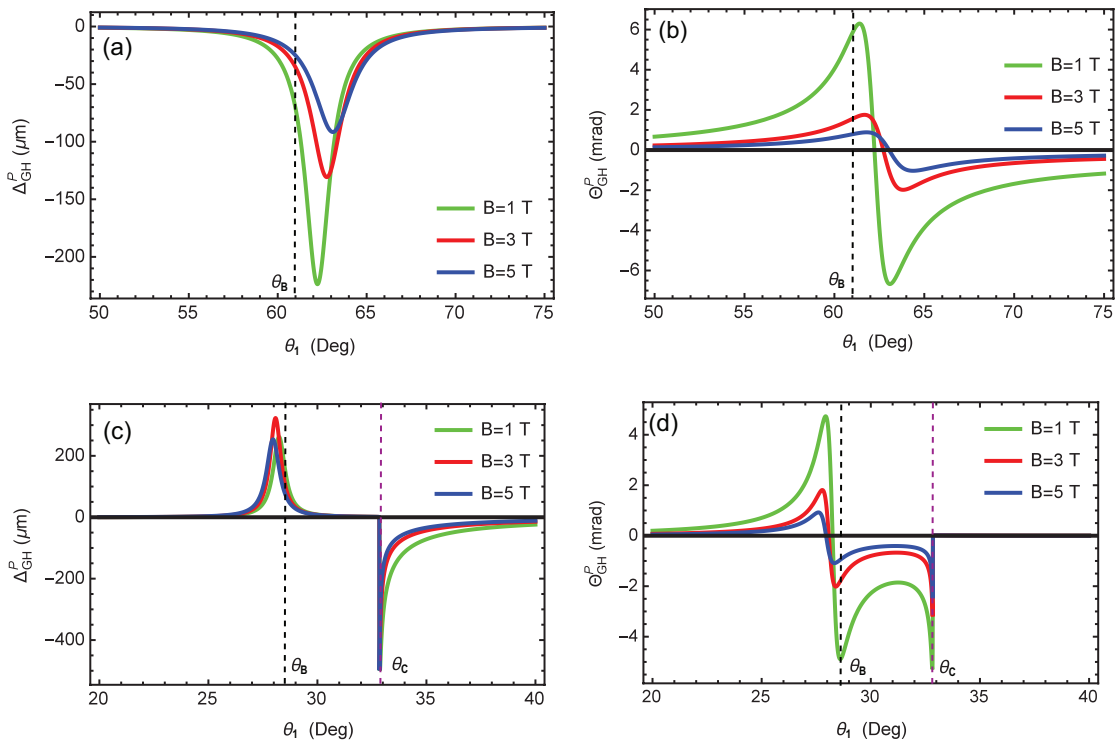

Figure 5.5: The p polarized spatial and angular GH shifts for charge neutral staggered graphene-substrate system as a function of incident angle for different magnetic fields in the K valley in the TI regime for PR and TIR. (a) The p polarized spatial GH shifts for PR, (b) the p polarized angular GH shifts for PR, (c) the p polarized spatial GH shifts for TIR and (d) the p polarized angular GH shifts for TIR. The dashed lines represents the values of θ_B and θ_C for the native dielectric substrate. The parameters used are identical across all figures, unless stated otherwise.

observe that ϕ_{pp} shows a change of $-\pi$ resulting in negative spatial GH shifts. The magnitude of spatial GH shifts are larger for smaller magnetic fields and smaller for large magnetic fields values; however, the extent of the spatial GH shifts for p polarization on a 2D staggered monolayer graphene-substrate system is larger compared to the case of the graphene-coated surface [174].

It is also worth noting that the Brewster angle is also sensitive to the applied magnetic field. From the results shown in Fig. 5.5(a), we observe that the Brew-

ster angle of the spatial GH shifts can be tuned from 62° to 63° by modulating the magnetic field for the three proposed magnetic fields.

Similarly, in Fig. 5.5(b), we also plot the angular GH shifts as a function of the incident angle. The angular GH shift Θ^p_{GH} is positive and gradually increases with incident angles, but as the incident angle reaches θ_B, Θ^p_{GH} decreases rapidly and results in a negative GH shift. By tuning the angle of incidence of the p polarized THz beam and the applied magnetic field, one can therefore control the polarity of the angular GH shift as well as its amplitude. Similar to the spatial counterpart, the amplitude of the angular GH decreases for increasing magnetic fields and this finding is in good agreement with purely graphene-coated surfaces [174]. Once again, the tuning of the Brewster angle θ_B with the magnetic field is also clearly observable.

Similarly, we plot the p polarized spatial and angular GH shifts under the total internally reflected (TIR) condition in Figs 5.5(c) and (d) respectively. Notable deviations from external reflection and certain additional features are vividly observable here. From Fig. 5.5(c) we observe that for magnetic fields of 1, 3, and 5 T, we have peaks in the vicinity of θ_B and sharply precipiced dips at the critical angle $\theta_C = \sin^{-1}(n_2/n_1)$, in the TI regime. Once again, the amplitude of the spatial GH shift is attenuated for larger magnetic fields. Similarly, the magnetic field modulated p polarized angular GH shifts for TIR geometry are depicted in Fig 5.5(d) wherein we expect unusual behavior of the GH shifts in the vicinity of both the Brewster and the critical angle. The angular GH shift Θ^p_{GH} is positive when the incidence angle is smaller than the Brewster angle and negative beyond. Similarly, just before the critical angle, the angular shift acquires a large negative spike and diminishes immediately after. Furthermore, near θ_B, the angular GH decreases in size with increasing magnetic field values.

5.1.3.2 Tuning the electric field

A static electric field E_z, controls the electronic band structure of the 2D staggered graphene family by generating a staggered sublattice potential Δ_z. An increase in the electric field triggers a well-known quantum phase transition that occurs from topological insulator to band insulator state [175]. Fig. 5.6(a) shows the longitudinal conductivity versus photon energy for various values of Δ_z. As we increase the applied electric field Δ_z, each interband peak splits into two spin-polarized peaks in the TI regime ($\Delta_z < \Delta_{so}$). Concomitantly, due to a redistribution of spectral weight, the intensity of the peaks is reduced for larger fields values.

When $\Delta_z = \Delta_{so}$, the gap of one of the spin-split bands closes and a new type of metallic phase emerges called the valley-spin polarized metal (VSPM) state. At the VSPM point, the lowest frequency peaks, move apart: the $\Delta_{-10,K,\uparrow}$ peak is red-shifted while the $\Delta_{01,K,\downarrow}$ peak is blue shifted. The excitation energies corresponding to the first two peaks at the VSPM point are now 18.2 meV (4.4 THz) and 27.8 meV (6.7 THz) for the spin up and down, respectively. Further increasing Δ_z results in re-opening of the gaps and the system transitions from the VSPM to the band insulator (BI) state. In the BI regime, all interband peaks move to higher energies. The magneto-excitations frequencies are presented in Table 5.2 for the first two transitions in the three different regimes. The main role of the electric field is that it controls the band structure and is responsible for spin and valley polarized responses, and therefore, similar to magnetic fields, also controls the magneto-optic excitation energies.

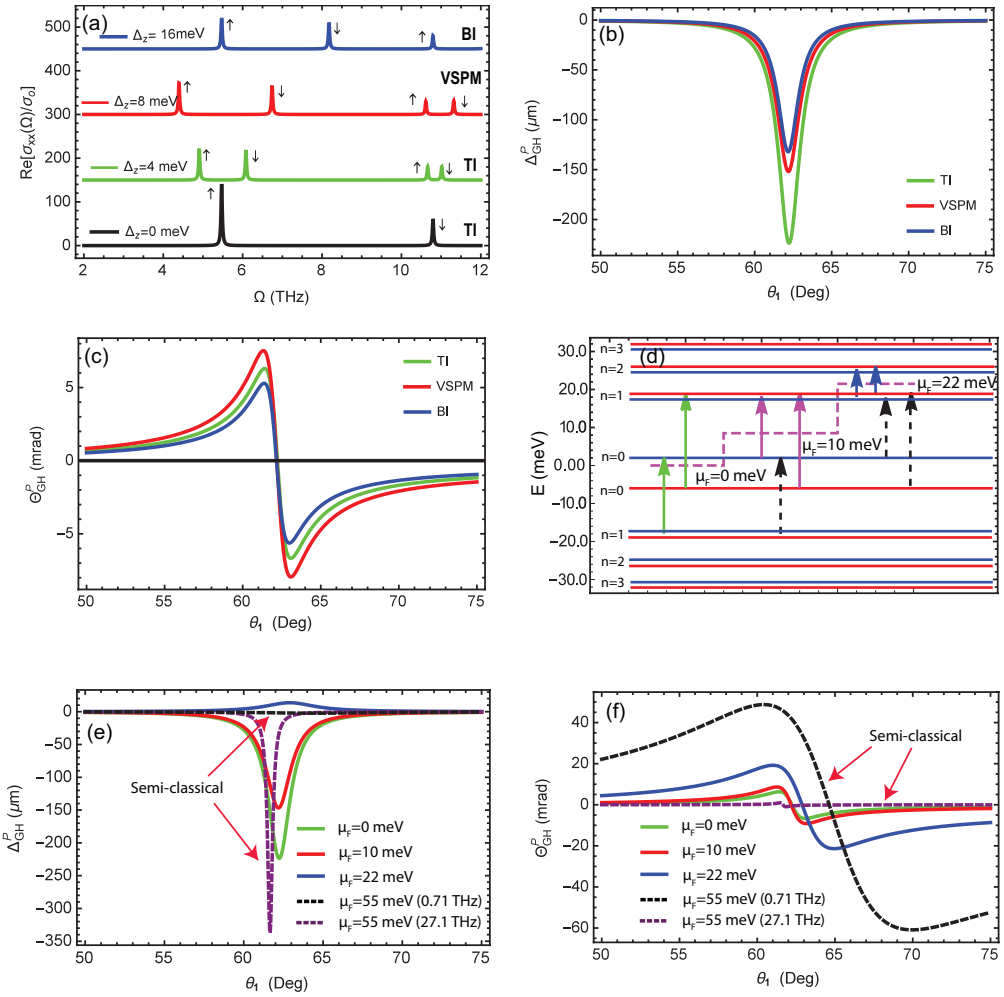

Figure 5.6: (a) Longitudinal conductivity as a function of incident photon frequency and the p polarized spatial and angular GH shifts for the staggered graphene-substrate system as a function of incident angle for magnetic field $B = 1$ T in the K valley in three distinct topological regimes and four different chemical potentials. The incidence is external PR, while (b) and (c) show the p polarized spatial and angular GH shifts with modulation of the external electric field, for the TI, VSPM, and the BI at a magnetic field of 1 T. (d) Schematic representation of the allowed transitions between LL's for three different values of chemical potential μ_F=0, 10 and 22 meV, and (e) and (f) are the p polarized spatial and angular GH shifts with modulation of the chemical potential in the TI and classical regimes for a magnetic field of 1 T.

Table 5.2: Table of allowed transitions in K valley in the $n = -1, 0, 1$ subspace, for $B = 1$ T in three different topological regimes for $\Delta_{so} = 8$ meV.

$\Delta_{mn,K(K'),\uparrow(\downarrow)}$	Δ_z (meV)	Regime	Frequency (THz)
$\Delta_{-10,K,\uparrow}$	0	TI	5.6
$\Delta_{01,K,\downarrow}$	0	TI	5.6
$\Delta_{-10,K,\uparrow}$	4	TI	4.9
$\Delta_{01,K,\downarrow}$	4	TI	6.1
$\Delta_{-10,K,\uparrow}$	8	VSPM	4.4
$\Delta_{01,K,\downarrow}$	8	VSPM	6.7
$\Delta_{-10,K,\uparrow}$	16	BI	5.5
$\Delta_{01,K,\downarrow}$	16	BI	8.2

In Figs. 5.6(b) and (c), we show the p polarized spatial and angular GH shifts as a function of the incident angle in the TI, VSPM and BI regimes, illustrating selective excitation of spin up carriers in the K valley. From Fig. 5.6(b), it is obvious that p polarized incident light produces giant negative spatial GH shifts. For example, in the TI regime when all Dirac gaps are open and at the magneto-excitation frequency of 4.9 THz, a maximum value of $\Delta^p_{GH} \approx 222$ μm is attained for a scattering rate of $\Gamma = 0.2\Delta_{so}$. Further increasing Δ_z results in reopening the lowest energy gaps and the system undergoes a topological phase transition from VSPM state to the BI regime. After band inversion, we observed smaller shifts, $\Delta^p_{GH} = 130$ μm. By increasing the electric field, the locations of the Brewster angle do not change but the spatial GH shifts diminish in size.

The p polarized angular GH shift as a function of the incident angle in the TI, VSPM, and the BI regimes can also be seen in Fig. 5.6(c), showing first, the sign inversion of the angular displacement across Brewster's angle and second, illustrating that the impact of the electric field is to suppress the size of the angular shifts.

5.1.3.3 Effect of chemical potential variation

The THz magneto-optical conductivity is heavily influenced by the chemical potential μ_F. We examine the p polarized beam shifts by modulating the chemical potential solely in the K valley. Results for the K' valley are analogous. We observe that the magnitude, sign, and position of Brewster's angle can all be controlled by this external stimulus. For this purpose, we choose three different values of the chemical potential of μ_F=0, 10, and 22 meV, while keeping the magnetic field 1 T positioning the system in the TI regime. In contrast to neutral staggered graphene (μ_F=0 meV), we now have interband as well as intraband transitions. For μ_F=10 meV the chemical potential lies in between the n=0 and n=1 LL's and for μ_F=22 meV the chemical potential is in between the n=1 and n=2 LL's.

A schematic diagram that helps us to understand the possible LL's transitions for this chemical potential adaptation is shown in Fig. 5.6(d). Moving from left to right, we can see the LL's interband transitions for $\mu_F = 0$ meV are energies $\Delta_{-10,K,\uparrow} = 20.3$ meV and $\Delta_{01,K,\downarrow} = 25.1$ meV. As μ_F increases to 10 meV, then according to selection rules, certain transitions become Pauli blocked. For instance, the interband transition $\Delta_{-10,K,\uparrow}$ becomes forbidden which is shown by the dashed upward-pointing arrow in the middle. In its lieu, the intra-band transition $\Delta_{01,K,\uparrow} = 16.0$ meV emerges whereas for the spin-down electron, we still have the allowed interband transition $\Delta_{01,K,\downarrow} = 25.1$ meV, shown by a solid arrow. If the chemical potential μ_F is further enhanced to 22 meV, so that it lies between the n=1 and n=2 manifolds, then both of the transitions $\Delta_{-10,K,\uparrow}$ and $\Delta_{01,K,\downarrow}$ become Pauli blocked, which are again indicated by the dashed arrows in the rightmost part of Fig. 5.6(d). In this case, the excitation energies (frequencies) corresponding to the first two intra-band transitions $\Delta_{12,K,\uparrow}$ and $\Delta_{12,K,\downarrow}$ are 7.5 meV (1.8 THz) and 7.2 meV (1.6 THz), respectively. Table 5.3 summarizes these results.

Table 5.3: Table of allowed transitions in K valley in the $n = -1, 0, 1$ subspace, for different chemical potentials in the TI regime with $\Delta_{so} = 8$ meV.

$\Delta_{mn,K(K'),\uparrow(\downarrow)}$	μ_F (meV)	Inter/intraband	Frequency (THz)
$\Delta_{-10,K,\uparrow}$	0	Inter	4.9
$\Delta_{01,K,\downarrow}$	0	Inter	6.1
$\Delta_{01,K,\uparrow}$	10	Intra	4.0
$\Delta_{01,K,\downarrow}$	10	Inter	6.1
$\Delta_{12,K,\uparrow}$	22	Intra	1.8
$\Delta_{12,K,\downarrow}$	22	Intra	1.6

Figs. 5.6(e) and (f) depicts the impact of altering the chemical potential (e.g. by chemical doping) on the GH shifts. Only the K valley is demonstrated for the sake of brevity. For these results, we selected the resonance frequency that excites only the first allowed LL transition for the spin-up electrons. The p polarized spatial GH shifts as a function of incident angle for different chemical potentials are shown in Fig. 5.6(e). For μ_F=0 meV, we have negative spatial GH shifts originating from the $\Delta_{-10,K,\uparrow}$ transition, which is purely interband. When the chemical potential μ_F=10 meV, we have the intra-band transition, and the magnitude of the p polarized spatial GH shift is larger.

As we further increase to μ_F=22 meV, we have purely intraband transitions. Here is the sign of GH shift switches which is a remarkable demonstration of chemical potential modulated angular GH shifts. Note that an intraband transition is responsible for the giant positive GH shift, precisely $\Delta_{12,K,\uparrow}$ and whose resonant frequency is 1.8 THz. With a further increase of chemical potential, the magnitude of the p polarized spatial GH shift decreases while its full width half maximum increases. Furthermore, we conclude that the pseudo-Brewster angles shifts to larger incidence angles due to the chemical modification. The inversion of signs of the GH shift from negative to positive has significant applications in optoelectronic devices and chemical potential measurement.

5.1.3.4 Semiclassical approximation, again!

In the semiclassical approximation, the LL spacing becomes unimportant, which occur when $|\mu_F| \gg |E_0|$, or another word when μ_F is high up in the conduction band or deep down in the valance band [76]. In this regime, the conductivities can be modeled by classical Drude-like peaks. For example, we suppose that μ_F=55 meV which places the chemical potential between the n=9 and 10 LL's. According to the selection rules, only two transitions $\Delta_{-9\ 10}$ and $\Delta_{9\ 10}$ are allowed [76]. The magneto excitation frequencies for $\Delta_{-9\ 10}$ and $\Delta_{9\ 10}$ are 27.1 and 0.71 THz respectively. We plot the spatial and angular GH shifts for this semi-classical scenario in Figs. 5.6(e) and (f). We can see in Figs. 5.6(e) a giant negative and minuscule spatial GH shift for the incident beam exciting the $\Delta_{-9\ 10}$ and $\Delta_{9\ 10}$ transitions respectively. We also observe that the Brewster angle is strongly influenced by the chemical potential and dramatically changes in the classical regime for the two different transitions. Similarly, we plot the p polarized angular GH shifts in Fig. 5.6(f) for the two mentioned transitions. Remarkably, we get a giant angular shift for $\Delta_{9\ 10}$ transition as compared to a small effect for the $\Delta_{-9\ 10}$ transition.

5.1.3.5 Valley and spin polarized beam shifts

In addition to charge and spin degree of freedom, the Dirac electrons in staggered 2D atomic layers possess a valley degree of freedom which acts like a fictitious spin 1/2 particle. The valley information for our system is actually embodied in the variable ξ, which is described in the system Hamiltonian in Eq. (2.81). Since the MO excitation energies are spin and valley dependent, one can selectively address the valley pseudospin in these materials to achieve full spin and valley-polarized GH shifts. For instance, by impinging right or left-handed circularly polarized light of the correct frequency, we can selectively excite spin up or spin down elec-

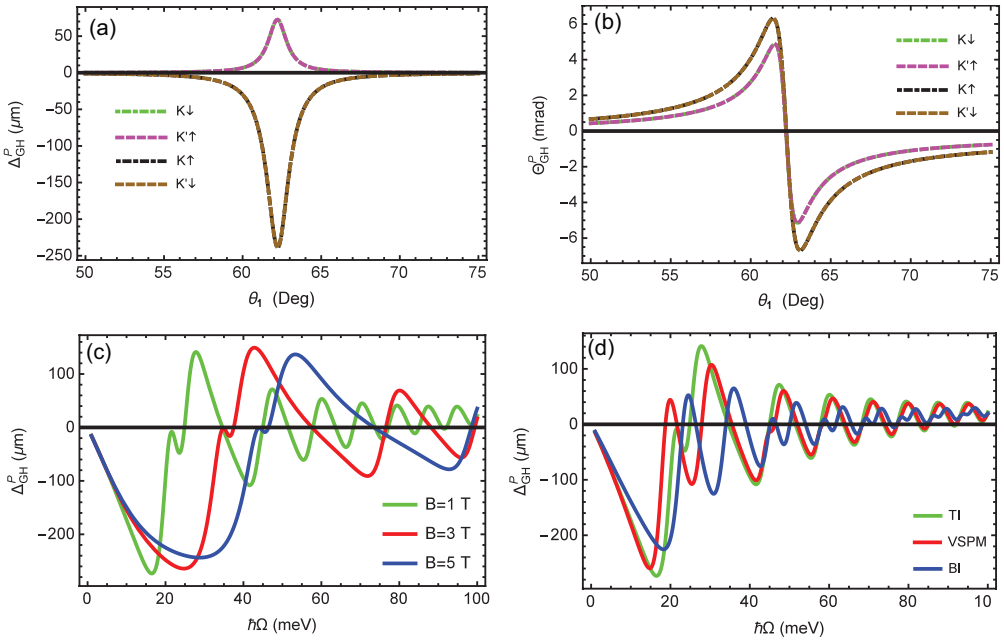

Figure 5.7: The valley and spin-polarized spatial and angular GH shifts for staggered 2D material-substrate system as a function of incident angle for K and K' valleys in the TI regime. (a) The spatial GH shifts for both spins and for both valleys, (b) the p polarized angular GH shifts for both spins and valleys. The spatial and angular GH shifts for staggered 2D material-substrate system as a function of photon energy in the K valley for different magnetic and electric fields. (c) the p polarized spatial and angular GH shifts for three different magnetic fields in the TI regime, (d) the spatial and angular GH shifts for $B = 1$ T in three distinct topological regimes. The p polarized response is shown only.

trons in either of the K or K' valleys. Hence we have full freedom to choose spin or valley by tuning the frequency and helicity of the impinging radiation.

In this vein, the valley and spin-dependence of the spatial GH shifts are depicted in Fig 5.7(a), indicating positive and negative GH shifts for both K and K' valleys. It is clear that this valley-dependent response is quite interesting. The sign of the lateral GH shift is inverted across the two valleys for the same spin identity. However, the angular shift does *not* undergo sign-inversion across the two valleys. Therefore for experimental verification, the direction of the lateral shift can allow

probing of the valley polarization tuning it into a prospective readout modality for the valley qubit in quantum information processing schemes.

5.1.3.6 Dependence on the incident photonic energy

As we vary the magnetic field imposed on the 2D atomic layer, the energy and hence the MO excitation energies manifold change. It is therefore instructive, to examine the dependence of the spatial and angular GH shifts on the frequency (energy) of the incident THz beam. In Fig. 5.7, we plot the beam shifts as a function of incident photon energy. In Fig. 5.7(c) we show the response for three different values of B =1, 3 and 5 T while keeping $\mu_F = 0$ and $\theta_1 = 61^\circ$ (near the Brewster angle) and keeping the electric field fixed to assign the system to the TI regime. Only the K valley spin-up polarized response is demonstrated. The beam shifts display an oscillating dependence moving gradually to higher frequencies as the magneto excitation energy is increased. This is shown in Fig. 5.7(c). Likewise for a fixed magnetic field ($B = 1$ T), as the electric field is changed, rendering the system into various topological regimes, the position, as well as the magnitudes of the beam shifts, change. From the TI→VSPM→BI progression, the GH shifts increase and then decreases. This is shown in Fig. 5.7(d).

5.2 Quantized Goos-Hänchen shifts on the surface of hybridized topological insulator thin films

5.2.1 Background and motivation

The emergence of topological insulators provides a new platform to reexamine the spatial and angular beam shifts at the unique optical interface by impinging a light beam on a topological insulator from an ordinary dielectric. Using the stationary-phase approach, it has been theoretically investigated that these lateral shifts on the surface of a topological insulator can be used to extract the surface characteristics of the TI slab, and to measure signatures of topological phase transitions [176, 177, 178].

Motivated by the advances in the study of GH shifts in TIs, in this part of the chapter, we theoretically investigate a large quantized GH shift on a surface of a TI thin film subjected to an external magnetic field by taking into account the hybridization between the SSs. This type of configuration has not been studied in detail in previous works. Our investigation can be demonstrated experimentally by impinging a beam of light on an air–TI interface in the presence of an external magnetic field, and then determining the direction of the optical beam after reflection. Techniques similar to those used for determining the angular deviations in the specular reflection of a light beam from an air-glass interface can be employed [179].

The present study covers the impact of a magnetic field, chemical potential, photonic energy, angle of incidence, and polarization of the incident beam on GH shifts in TI thin films. We further investigate GH shifts in different topological phases of the TI thin film by driving phase transitions through an external magnetic field. The study of GH shifts in different topological phases can provide a new way of

investigating the topological characteristics of TIs materials. The present part is divided into the following sections. Section 5.2.2 is based on the theoretical model for the lateral and angular Goos-Hänchen shifts in topological insulator thin films. Finally, we present the results for our simulative investigations followed by a discussion in Section 5.2.3.

5.2.2 Goos-Hänchen shifts

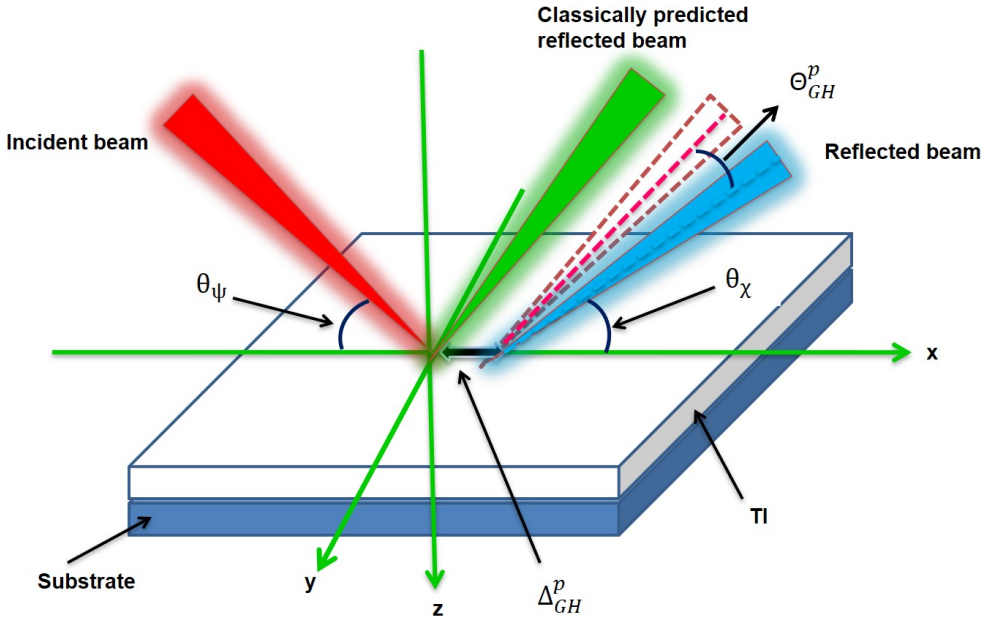

Figure 5.8: Schematic illustration of the GH shifts of a light beam reflected from a TI-substrate interface.

We consider a beam of light with Gaussian profile propagating in a vacuum and is incident on the planar interface of the TI-substrate system as shown schematically in Fig. 5.8. The beam makes an angle θ_ψ upon incidence, and θ_χ upon reflection with the simi-infinite substrate. The interface of air and TI thin film is assumed to be at the $z = 0$ plane. The Fresnel reflection coefficients can be obtained by considering the TI thin film as a surface current density $K = \sigma \cdot E|_{z=0}$

and applying the electromagnetic (EM) boundary conditions on the two sides of the thin film at $z = 0$. The electric and magnetic fields above and below the TI thin film are connected at $z = 0$ by Maxwell's boundary conditions:

$$\hat{z} \times \left[E_t - E_r - E_i\right] = 0 \tag{5.14}$$

$$\hat{z} \times \left[H_t - H_r - H_i\right] = \sigma \cdot E_t, \tag{5.15}$$

where E_i (H_i), E_r (H_r), and E_t (H_t) represent the incident, reflected, and transmitted electric (magnetic) fields, respectively. Here σ is the MO conductivity of the TI thin film. By decomposing the incoming field into its transverse-electric (TE) and transverse-magnetic (TM) components, the relationship of the TE, TE and TM, TM polarized reflected coefficients can be determined from the ratio of the reflected and incident amplitudes:

$$r_{i,j} = \frac{E_r^i}{E_i^j}. \tag{5.16}$$

The angular and spatial GH shifts are given by [142]

$$\Theta_{\mathrm{GH}}^{\mathrm{TM},\tau_z=\pm1} = -\frac{2(r_{\mathrm{TM,TM}}^2\rho_{pp} + r_{\mathrm{TM,TE}}^2\rho_{\mathrm{TM,TE}})}{2k(r_{\mathrm{TM,TE}}^2 + r_{\mathrm{TM,TM}}^2)\Lambda_R + \chi_{\mathrm{TM,TM}} + \chi_{\mathrm{TM,TE}}}, \tag{5.17}$$

$$\Delta_{\mathrm{GH}}^{\mathrm{TM},\tau_z=\pm1} = \frac{2(r_{\mathrm{TM,TM}}^2\varphi_{\mathrm{TM,TM}} + r_{\mathrm{TM,TE}}^2\varphi_{ps})\Lambda_R}{2k(r_{\mathrm{TM,TE}}^2 + r_{\mathrm{TM,TM}}^2)\Lambda_R + \chi_{\mathrm{TM,TM}} + \chi_{\mathrm{TM,TE}}}. \tag{5.18}$$

The superscripts identify the polarization state (TM) and the TI top and bottom SSs, while the subscripts specify the GH shift.

5.2.3 Results and Discussion

5.2.3.1 Effect of magnetic field on angular and spatial GH shifts

To investigate GH shifts in a TI thin film-substrate system, first, we plot the real part of the MO conductivities versus the photonic energy. We consider three different values of the magnetic field strength, i.e., for B =1, 3, and 5 T in the TI regime, as shown in Figs. 5.9(a) and (b). The absorption peaks occur at photon energies

for inter-band transitions (we ignore the contribution from intra-band transitions), and have Lorentzian shapes with a full width at half maximum at Γ. We label the Lorentzian peaks corresponding to different MO transitions $E_m^{\tau_z=\pm1} \rightarrow E_n^{\tau_z=\pm1}$ as $T_{mn}^{\tau_z=\pm1}$ following the nomenclature described in [142, 180]. For practicality, we consider only the lowest magneto-excitation transitions, i.e., T_{01}^{+1} and T_{-10}^{-1} to investigate the GH shifts.

When the frequency of the impinging Gaussian beam is equal to any of the Dirac gaps, an electron-hole pair will be excited. The Dirac electrons in the hybridized TI thin film have a degree of freedom related to the SS just like the valley degree of freedom in graphene, silicene, and other TMDCs. As a result, these electrons behave like pseudo spin 1/2 particles. We can selectively excite the Dirac electrons in either of the top or bottom SSs by impinging left-handed circularly (LHC) and right-handed circularly (RHC) polarized light beam, respectively.

Figures 5.9(a) and (b) show that the magneto-excitation energies of the Lorentzian peaks shift to the right with the increase in the strength of the magnetic field. The spectral weight (and absorption) increases with the strength of the magnetic field (at the peak magneto-excitation frequency). For higher magneto-excitation frequencies the spectral weight decreases. Figure 5.9(c) and (d) present variations of the TM and TE polarized magneto-reflection Fresnel coefficients with respect to the photonic energy for different strengths of B. The normalized magneto-reflection peaks are clearly observed at the magneto-excitation energies. We summarized these results in Table 5.4.

In Figs. 5.9 (e) and (f), we show the phases of the reflected TM and TE polarized EM beam with respect to the incident angle θ_ψ. The phase $\phi_{\rm TM}$ changes sharply from 0 to $-\pi$ in the proximity of Brewster angle θ_B. This transition smooths out

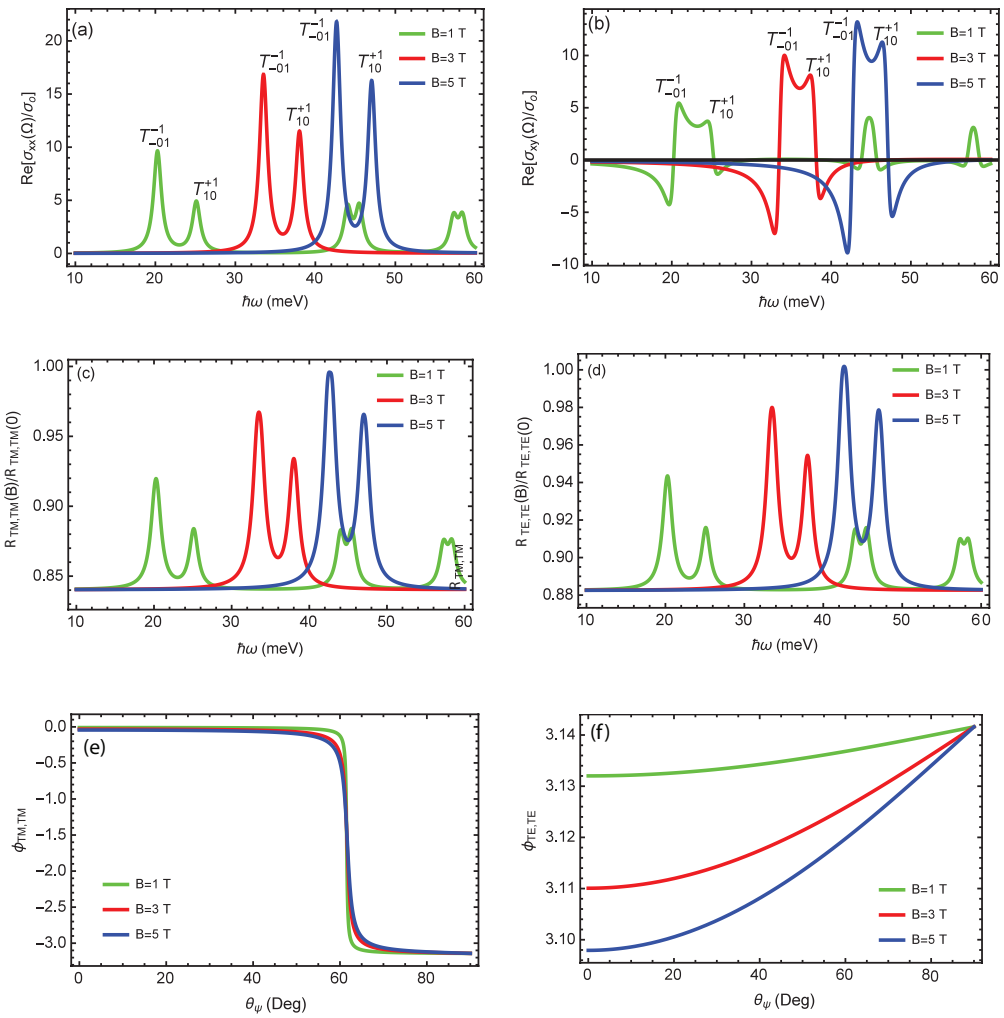

Figure 5.9: Real part of the (a) longitudinal and (b) transverse Hall conductivities as a function of the photonic energy for different strengths of the applied magnetic field in the TI regime for top and bottom SSs. Variations of the modulus of (c) the TE and (d) TM polarized normalized magneto-reflection coefficients for the TI thin film-substrate system with the incident photonic energy for different strengths of the magnetic field in the TI regime for top and bottom SSs. Variation of (e) the $\phi_{TM,TM}$ and (f) $\phi_{TE,TE}$ with the incident angle. Parameters used for TI SSs are Δ_H= 4 meV, $\Gamma = 0.15\Delta_z$, refractive index $n_2 = 1.84$, and chemical potential $\mu_F = 0$.

when the strength of B increases. The phase $\phi_{\rm TE}$ decreases (for a fixed value θ_ψ) with the increase in the strength of B in the TI regime (see Fig. 5.9(f)). However,

its behaviour as a function of θ_ψ is different for different strengths of B.

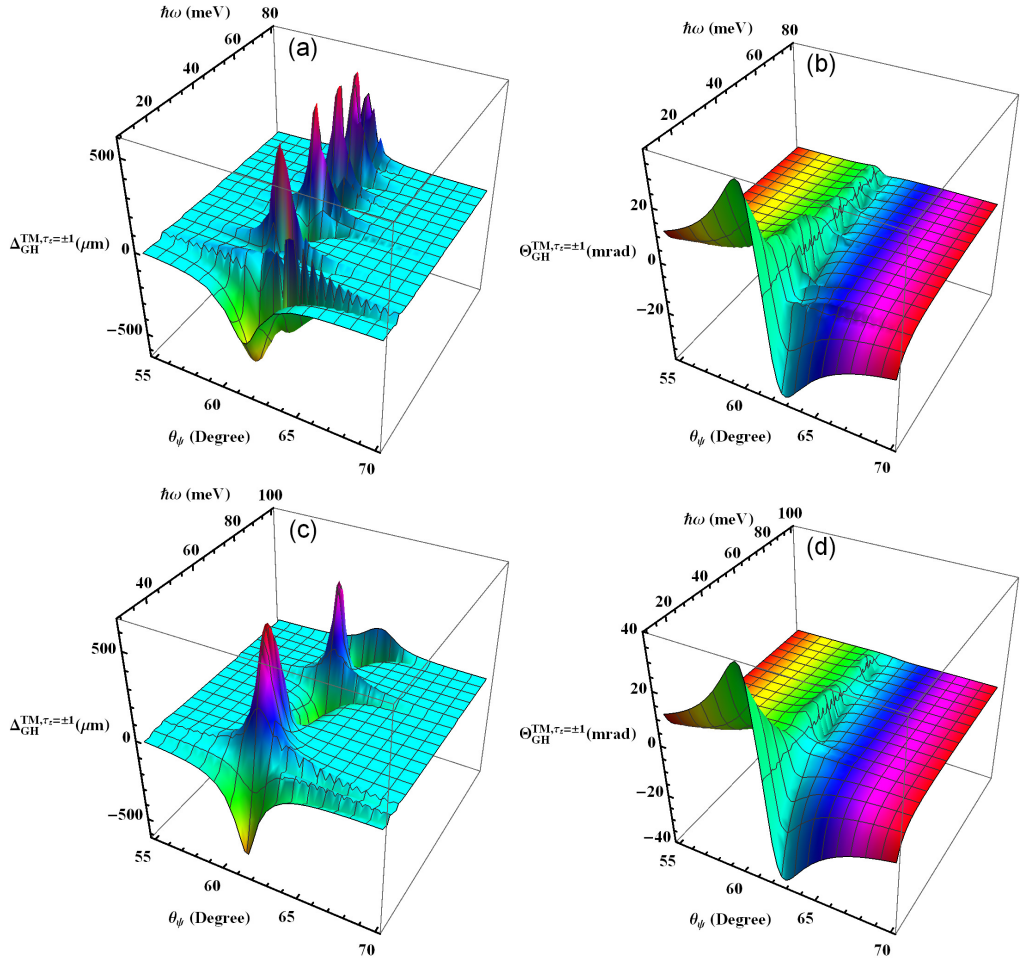

Figure 5.10: Magnetic field modulated TM polarized spatial and angular GH shifts on the surface of the TI thin film substrate-system versus photonic energy ($\hbar\omega$) and θ_ψ for two different values of B for top and bottom SSs. (a) The TM polarized spatial GH shifts and (b) the TM polarized angular GH shifts for $B = 1$ T. (c) The TM polarized spatial GH shifts and (d) the TM polarized angular GH shifts when $B = 3$ T.

In the remaining part of this chapter we investigate the lateral displacements of the beam under partial reflection conditions. We discuss only the magnetic field modulated spatial and angular shifts for the TM polarized light. In Fig. 5.10(a) we show the TM polarized spatial GH shift versus photonic energy and incident

Table 5.4: Allowed transitions for $\tau_z = \pm 1$ in the LLs subspace $n = -1,\ 0,\ 1$, for B =1 and 3 T in the TI phase $\Delta_z = 2$ meV.

$T_{mn}^{\tau_z=\pm 1}$	Δ_z (meV)	B (T)	Photonic energy (meV)
T_{01}^{+1}	2	1	25.1
T_{-10}^{-1}	2	1	20.3
T_{01}^{+1}	2	3	38.0
T_{-10}^{-1}	2	3	33.5

angle for $B = 1$ T in the TI regime (for both top and bottom SSs). The spatial shift in this case shows negative and positive giant peaks at the Brewster's angle ($\theta_B \approx 61.8°$), which is due to the fine transition of ϕ_{TM} from 0 to $-\pi$ at this angle. Due to the LL quantization of the MO conductivities and, consequentially, the Fresnel's coefficients of the TI SSs the GH shift shows quantized behavior. We summarize these transitions in Table 5.4. The SS polarized GH shift for T_{01}^{+1} and T_{-10}^{-1} transitions gives local minimum and maximum values around 20.3 meV and 25.1 meV, respectively. Thus in the hybridized TI thin film the GH shift is enhanced several times of the incident beam wavelength in the THz regime. The shift also switches sign on each transition as shown in Fig. 5.10(a). Similarly, in the proximity of θ_B we can see minima and maxima in the quantized GH spectra for higher photonic energies. Extreme values of the GH shift occur away from the resonant magneto-excitation energies in the proximity of the Brewster's angle. This agrees with the previous studies that the beam shifts give peak values around θ_B [142, 181].

In Fig. 5.10(b) we show the TM polarized angular GH shifts vs. $\hbar\omega$ and θ_ψ under PR condition. The shift is positive which grows slowly with θ_ψ, but as θ_ψ reaches θ_B, the angular shift starts decreasing and reaches a negative value. This shows that the amplitude and polarity of the angular GH shift can be controlled by modulating the incident angle of the TM polarized THz beam and the strength of the magnetic field. The magnitude of these shifts are larger for smaller values of the magneto-excitation energies and smaller for higher values. The imaginary part

of the MO conductivity of the TI SSs is responsible for ohmic loss [182], which is a reasonable justification of this behavior. At higher magnetic fields the magneto-resistance is large since the absorption is greater and the magnitude of angular GH shifts is smaller on higher photonic energies. For $B = 3$ T, Figs. 5.10(c) and (d) show that the spatial and transverse shifts are still quantized in the proximity of Brewster's angle. The local minima and maxima of the spatial shift occur at higher photonic energies.

5.2.3.2 Impact of Zeeman potential on angular and spatial beam shifts

The external magnetic field B alters the electronic band structure of the hybridized 3D TI by generating an exchange Zeeman potential Δ_z. By tuning Δ_z, one can control the Dirac mass of the SSs, which leads to a TQPT from TI to BI phase at $\Delta z = \Delta_H$. To manifest the role of topology in GH shifts, in Figs. 5.11(a) and (b) we show the variation of the TM polarized spatial and angular GH shifts with the photonic energy and the incident angle θ_ψ in the CNP and BI phases for $B = 2.3$ T. From Fig. 5.11(a) it is clear that the TM polarized beam generates large negative and positive spatial GH shifts. Due to the quantized Fresnel's coefficients, Brewster's angle is quantized. The local maxima and minima of the quantized spatial GH shift occur at off-resonant photonic energies. Similarly, the angular GH shifts in the CNP and TI regimes show similar behavior. In Table 5.5 we present the magneto-excitations energies of the TI thin film SSs for the first two transitions in the two distinct topological phases. The TM polarized spatial GH shift vs. $\hbar\omega$ and θ_ψ is depicted in Fig. 5.11(c). In the BI regime, the magneto-excitation energies move to the right and there are fewer minima and maxima of the spatial GH shift. From the angular GH shift spectra, we observe that the sign of the amplitude of the angular shifts is suppressed by increasing the Zeeman potential.

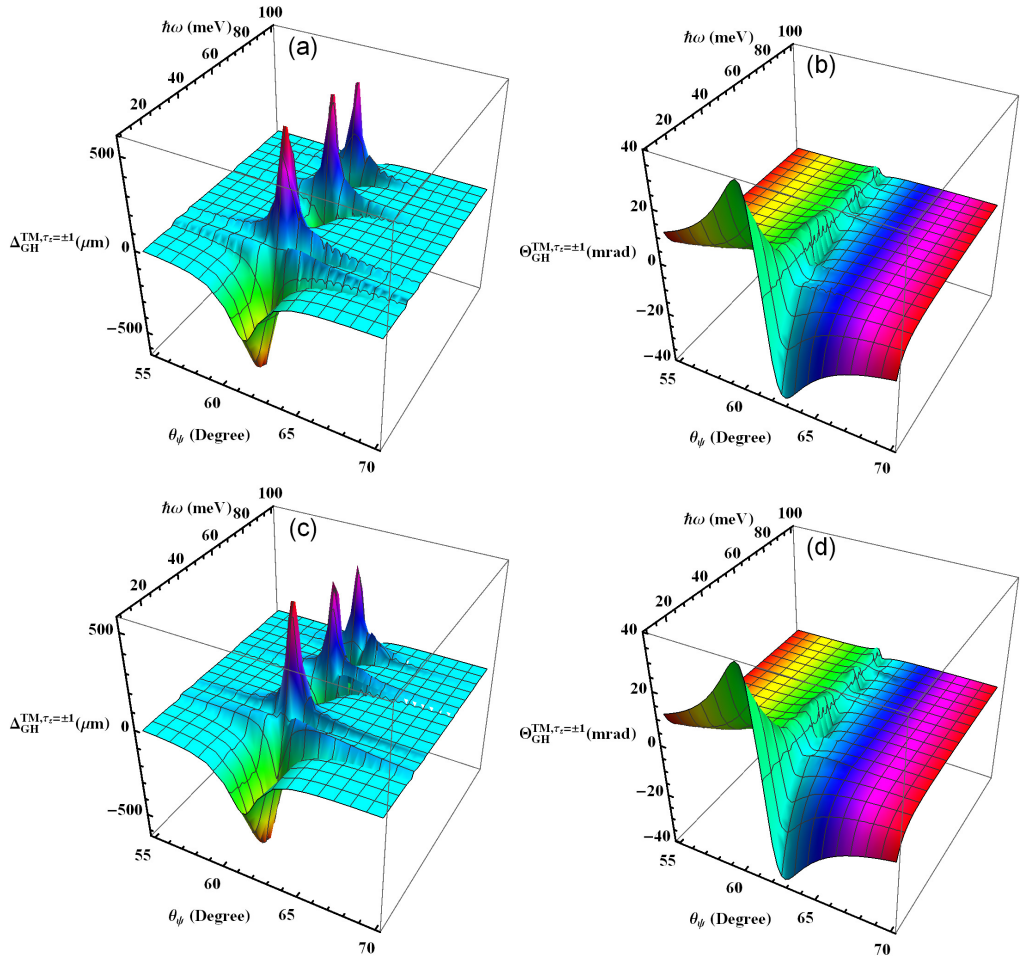

Figure 5.11: TM polarized spatial and angular lateral shifts on the surface of the TI thin film substrate-system as a function of the incident photonic energy and incident angle for two different topological regimes for top and bottom SSs. (a) The TM polarized spatial GH shifts and (b) the TM polarized angular GH shifts for $B = 2.3$ T in the CNP phase. (c) The TM polarized spatial GH shifts and (d) the TM polarized angular GH shifts for $B = 2.3$ T in the BI state.

5.2.3.3 Chemical potential modulated angular and spatial beam shifts

The MO conductivity of the hybridized TI thin film in THz regime, besides its dependence on several other parameters (e.g., the polarization of the incident beam, frequency ω, scattering rate Γ), is heavily influenced by the chemical potential μ_F

Table 5.5: Allowed transitions in the LLs subspace $n = -1,\ 0,\ 1$, for $B = 1$ T in three different topological regimes for $\Delta_H = 4$ meV.

$T_{mn}^{\tau_z=\pm1}$	Δ_z (meV)	Regime	Photonic energy (meV)
T_{01}^{+1}	4	CNP	18.2
T_{-10}^{-1}	4	CNP	27.7
T_{01}^{+1}	8	NI	22.7
T_{-10}^{-1}	8	NI	33. 9

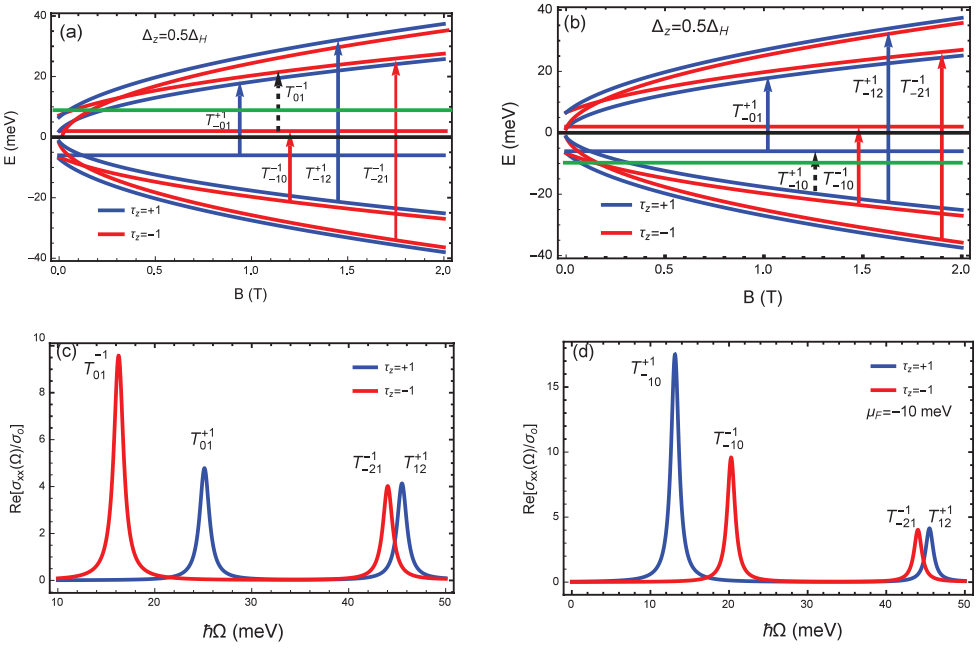

Figure 5.12: (a) and (b). MO allowed inter-band and intra-band LL transitions for top and bottom SSs in the TI regime and for $B = 1$ T. (c) and (d). Real parts of the MO conductivities for n-type and p-type TIs thin film-substrate system as a function of the incident photonic energy in the TI regime. (e) and (f). The TM polarized spatial and angular GH shifts with modulation of the chemical potential in the TI regime for $B = 1$ T.

as expressed in Eqs. (4.37) and (4.38). The quantized LLs of the TIs SSs can be independently controlled by employing top and back gate electrodes [144, 145]. Fine control of μ_F of the paired SSs in a dual-gated system has been recently reported [146]. To demonstrate the variation of the GH shift with the chemical potential, we consider two different values of the chemical potential, i.e., μ_F=10

meV and -10 meV while keeping $B = 1$ T in the TI regime. In the first case, we assume n-type doping and μ_F=10 meV. The chemical potential resides in between the n=0 and n=1 LLs as shown in Fig. 5.12(a). Blue lines represent LLs for the top surface and red lines represent LLs for the bottom surface. LL transitions are represented with the same color scheme with the green line indicating the chemical potential μ_F.

We represent these LL transitions by T^{+1}_{-01}, T^{-1}_{-10}, T^{-1}_{01}, T^{+1}_{-12}, and T^{-1}_{-21} as shown in Fig. 5.12(a). The first two magneto-excitation energies are presented in Table 5.5. The intra-band transition is represented by a dashed black arrow pointing upward. In the second case we consider p-type doping where μ_F=-10 meV and the chemical potential resides in between the n=0 and n=-1 LLs as shown in Fig. 5.12 (b). For n-type doping, there are certain transitions which become Pauli blocked. For example the transition $T^{-1}_{-10} = 20.3$ meV is not allowed and in their place the intra-band transition $T^{-1}_{01} = 16.3$ meV in the bottom surface appears. Similarly for p-type doping, when the chemical potential μ_F jumps between the n=0 and n=-1 LLs, owing to the Pauli blocking, transition $T^{+1}_{01} = 25.1$ meV disappears and $T^{+1}_{-10} = 13.1$ meV emerges. The longitudinal conductivity for n-type and p-type doped TIs are shown in Figs. 5.12(c) and (d). The intra-band and inter-band transitions are shown as pronounced dips at the incident photonic energies in the TI regime for $B = 1$ T.

Table 5.6: Allowed LL transitions in the $n = -1,\ 0,\ 1$ subspace for two different values of the chemical potential in the TI regime with $\Delta_H = 4$ meV.

$T^{\tau_z=\pm1}_{mn}$	μ_F (meV)	Inter/intraband	Photonic energy (meV)
T^{+1}_{01}	10	Inter	25.1
T^{-1}_{01}	10	Intra	16.3
T^{+1}_{-10}	-10	Intra	13.1
T^{-1}_{-10}	-10	Inter	20.3

In Figs. 5.13(a) and (b), we show the TM polarized spatial GH shifts vs. θ_ψ and

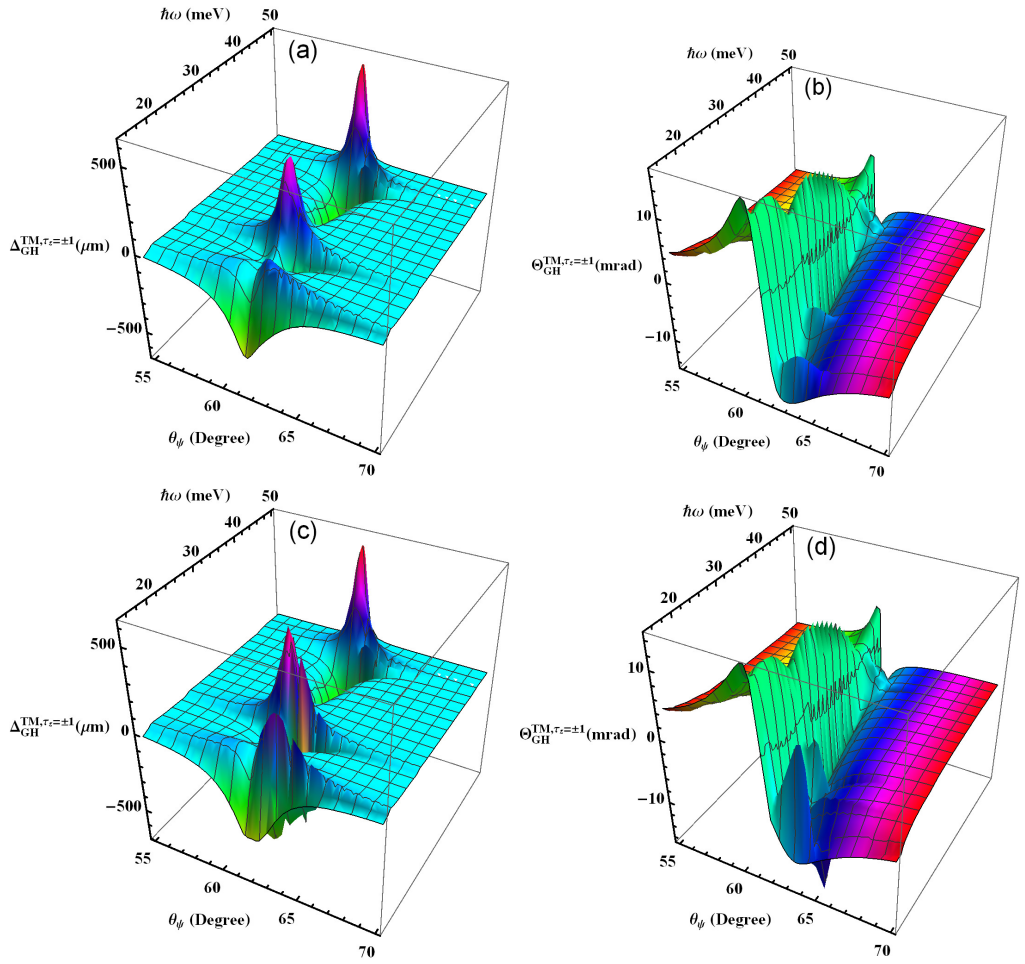

Figure 5.13: Chemical potential modulated TM polarized spatial and angular GH shifts on the surface of TI thin film substrate-system as a function of photonic energy and incident angle for two different chemical potential for both top and bottom SSs in the TI regime. (a) The TM polarized spatial and (b) angular GH shifts for n-type doping. (c) The TM polarized spatial and (d) angular GH shifts for p-type and magnetic of $B = 1$ T.

$\hbar\omega$ in the TI phase for n-type and p-type doping, respectively. For n-type doping, a negative giant spatial GH shift originates from a pure intra-band transition T_{01}^{-1}. The other minima and maxima of the quantized GH shift can be seen at higher inter-band transitions. Figure 5.13(b) shows that due to the LL quantization of MO conductivities, the angular GH shifts also exhibit quantized characteristic.

The minima and maxima due to the intra-band and inter-band transitions can be clearly seen, where the amplitude is smaller (as compared to the $\mu_F = 0$ case which is shown in Fig. 5.10(b)) due to n-type doping.

Figure 5.13(c) shows that maximum positive GH shifts arise for μ_F=-10 meV, for which the intra-band transition T^{+1}_{-10} is responsible. The sign switching of the GH shift is an interesting demonstration of chemical potential modulated spatial GH shifts. The magneto-excitation energies for the intra-band and inter-band transitions are shown in Table 5.6. Figure 5.13(d) illustrates the TM polarized angular GH shifts for p-type chemical potential. When $\theta_\psi < \theta_B$, the angular GH shift is positive and is negative in the opposite case, i.e., $\theta_\psi > \theta_B$.

Chapter 6

The photonic spin Hall effect in topological silicene

In this chapter, we discuss the valley and spin-polarized quantized photonic spin Hall effect in topological silicene. We explore the giant spin-dependent shifts of the graphene family-substrate system which can be tuned by an externally applied electric field *as well as* a magnetic field. Contents of this chapter have been published in *Physics Letters A* [183].

6.1 Background and motivation

A striking optical phenomenon generally arises due to spin-orbit interactions of light at the interface is the photonic spin Hall effect (PSHE), which demonstrates itself as spin-dependent splitting. The PSHE phenomenon occurs when a Gaussian beam of linearly polarized light (a linear combination of right-handed circularly polarized (RHCP) and left-handed circularly polarized (LHCP)) refracts or reflects at a planar dielectric interface where the light beam experiences a small spatial shift in both the transverse and in-plane directions [184, 185]. The PSHE is universal to any interface and has potential applications in precision metrology, biosensors [155], optical measurement and optical heterodyne sensors [159] including nanoprobing [186].

Recently, the PSHE has been theoretically studied in the graphene-substrate system in the quantum Hall regime in the presence of an external magnetic field [187]. The PSHE can be a new spin and valley sensitive topological tool to determine the physical and optical properties of nanostructures *i.e.*, metallic and magnetic thin films and 2D materials [188]. For example, W. Wu *et. al* show that weak-value measurement technique can be used to measure the minuscule optical signature of TQPTs [176]. L. Luo *et. al* and T. Tang *et. al* have examined that the giant PSHE appears when the Gaussian beam reflects or transmits through a graphene–substrate system and prism-graphene waveguide structure, respectively [163, 189]. In addition, the giant PSHE on the surface of other 2D anisotropic materials *e.g.*, black phosphorus has also been predicted [181, 190]. Finally, the spin-dependent shifts are sensitive to the refractive index variations of the sensing medium [191, 192].

To our knowledge, a complete semi-classical study of the PSHE reflected from the surface of the silicene in the presence of magnetic and electric fields hasn't been reported. Motivated by the spin and valley-coupled topological properties of the staggered 2D materials [22, 69, 70], we attempt to explore the giant spin-dependent shifts of the graphene family-substrate system which can be tuned by an externally applied electric field *as well as* the magnetic field. Our results depict that the in-plane and transverse spatial PSHE are quantized and show an oscillating behavior due to the valley and spin splitting of Landau levels (LLs). For larger magneto-excitation energies, the oscillation period of the PSHE gradually decreases with the increase of LL spacing. We observe that the resonant spectrum of the PSHE can be utilized to realize a multi-channel quantum switch. Further, we note that PSHE can be significantly enhanced by driving the system through several phase transitions involving topologically nontrivial and trivial states by tuning the staggered electric potential.

The chapter is organized as follows. In Section 6.2 we briefly present the basic formalism of the photonic spin Hall effect. Following this, in Section 6.3 we present our results for the valley and spin-polarized quantized spin-dependent photonic shifts in topological silicene.

6.2 General theoretical model

For the incident light, we consider a monochromatic Gaussian wave packet of frequency ω with a finite beam width illuminating from air to the surface of a staggered 2D semiconductors-substrate system at an incident angle θ_ψ. The refractive indices of the first and second media are n_1 and n_2 respectively. Consider the z axis of the laboratory Cartesian frame (x, y, z) is perpendicular to the 2D monolayer-substrate interface ($z = 0$). An external electric and magnetic field is applied perpendicularly to the system in the z direction. Furthermore, for the incident and the reflected beam, we use Cartesian coordinates (x_i, y_i, z_i) and (x_r, y_r, z_r), respectively. The wave vectors are k_1 and k_2, $k_n = \omega\sqrt{\mu_n\varepsilon_n}$, $Z_n = Z_0\sqrt{\mu_n/\varepsilon_n}$ and $Z_0 = \sqrt{\mu_0/\varepsilon_0}$, where μ_0 and ε_0 are the vacuum permeability and permittivity respectively. As a result the reflected Gaussian light beam can be split into LHCP and RHCP components, which experience the PSHE shift along the x and y-axis as shown in Figure 6.1(a) and (b). The amplitudes of the incoming horizontal $|H_i\rangle$ and vertical $|V_i\rangle$ polarization Gaussian states are related to the reflected horizontal $|H_r\rangle$ and vertical $|V_r\rangle$ polarization states by a transfer matrix, which can be written as [183, 187]

$$\begin{pmatrix} |H(k_r)\rangle \\ |V(k_r)\rangle \end{pmatrix} = \hat{R} \begin{pmatrix} |H(k_i)\rangle \\ |V(k_i)\rangle \end{pmatrix}, \tag{6.1}$$

where

$$\hat{R} = \begin{bmatrix} r_{pp} - \frac{k_{ry}\cot\theta_\psi(r_{ps}-r_{ps})}{k_0} & r_{ps} + \frac{k_{ry}\cot\theta_\psi(r_{pp}+r_{ss})}{k_0} \\ r_{ps} + \frac{k_{ry}\cot\theta_\psi(r_{pp}+r_{ss})}{k_0} & r_{ss} - \frac{k_{ry}\cot\theta_\psi(r_{ps}-r_{sp})}{k_0} \end{bmatrix}. \tag{6.2}$$

The Fresnel's coefficients r_{pp}, r_{ps}, r_{ss} and r_{sp} are already separately computed in Eqs. (4.17) and (4.22) in Section 4.1.2. Here we introduce the angular spectrum

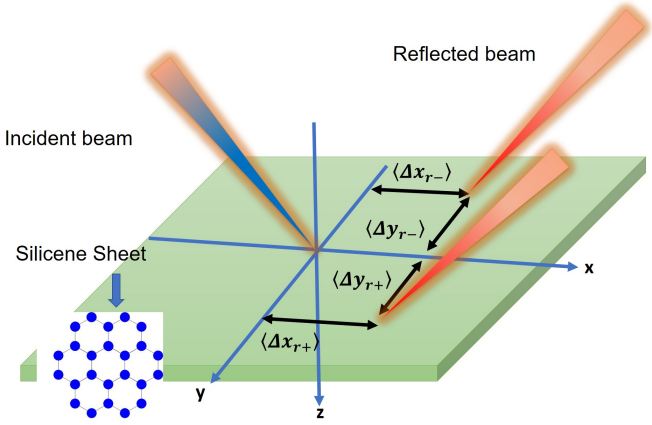

Figure 6.1: Schematic of the LHCP and RHCP spatial in-pane and transverse photonic spin Hall effect.

components of the incident and the reflected fields satisfying the boundary conditions $k_{rx} = -k_{ix}$ and $k_{ry} = k_{iy}$. The four Fresnel coefficients of the graphene family-substrate system in the presence of static magnetic field can are already given in Section 4.1.2. In the spin basis, linearly polarized states of the horizontal $|H\rangle$ and vertical $|V\rangle$ polarized Gaussian states can be broken down into two orthogonal spin components

$$|H\rangle = \frac{|+\rangle + |-\rangle}{2}, \tag{6.3}$$

$$|V\rangle = \frac{i(|-\rangle - |+\rangle)}{2}, \tag{6.4}$$

where the positive and negative states ($|+\rangle$ and $|-\rangle$) represent the LHCP and RHCP components, respectively. In the momentum space, the angular spectrum of the incident Gaussian beam can be represented by

$$|\Phi_0\rangle = \frac{w_0}{\sqrt{2\pi}} \exp\left(-\frac{w_0^2(k_{ix}^2 + k_{iy}^2)}{4}\right), \tag{6.5}$$

where w_0 is the beam waist. From Eqs. (6.1) and (6.5), the complex amplitudes for the reflected angular spectrum can be obtained as follows:

$$E_{r\pm}^{H/V} = \int\int dk_{rx} dk_{ry} \tilde{E}_{r\pm}^{H/V} \exp[i(k_{rx}x_r + k_{ry}y_r + k_{rz}z_r)]. \tag{6.6}$$

The LHCP and RHCP are the spin components of the reflected light beam undergoing in-plane and transverse displacements, which can be computed as

$$\langle \Delta x_{r\pm}^{H/V} \rangle = \frac{\int\int x_r |E_{r\pm}^{H/V}|^2 dx_r dy_r}{\int\int |E_{r\pm}^{H/V}|^2 dx_r dy_r} \tag{6.7}$$

$$\langle \Delta y_{r\pm}^{H/V} \rangle = \frac{\int\int y_r |E_{r\pm}^{H/V}|^2 dx_r dy_r}{\int\int |E_{r\pm}^{H/V}|^2 dx_r dy_r}, \tag{6.8}$$

where the integration is performed over the reflected electric fields coordinates x_r and x_r, respectively. In the following, we limit the discussion to the H polarized light beam only, although these results also hold for the V polarized beam. Compared to the geometrical-optics prediction the the displacements of field centroid at $z_r = const$ can be expressed as [183, 190]

$$\langle \Delta_{x_{r\pm}}^{K(K'),\uparrow,(\downarrow)} \rangle = \mp \frac{1}{k_0} \mathrm{Re}\left(\frac{r_{pp}}{\chi} \frac{\partial r_{sp}}{\partial \theta_\psi} - \frac{r_{sp}}{\chi} \frac{\partial r_{pp}}{\partial \theta_\psi} \right), \tag{6.9}$$

$$\langle \Delta_{y_{r\pm}}^{K(K'),\uparrow,(\downarrow)} \rangle = \mp \frac{\cot\theta_\psi}{k_0} \mathrm{Re}\left(\frac{\varphi r_{pp}}{\chi} - \frac{\rho r_{sp}}{\chi} \right), \tag{6.10}$$

where $\chi = (r_{pp}^2 + r_{sp}^2)$, $\varphi = (r_{pp} + r_{ss})$ and $\rho = (r_{ps} - r_{sp})$. The superscripts identify the valley (K, K') and spin $(\uparrow, \downarrow)$ information, while the subscripts specify the LHCP and RHCP spin dependent shifts.

6.3 Results and Discussion

6.3.1 Effect of magnetic field

Before analyzing the PSHE on the surface of staggered 2D silicenic mono-layer substrate system, we first quickly recount the effect of the applied magnetic field on the energy level structure. Details can be found in Ref. [142]. Schematic diagrams illustrate the allowed transitions between LLs satisfying the selection rule $\Delta n = \pm 1$ for different values of the magnetic field are shown in Fig. 6.2(a). Similarly, Fig. 6.2(b) presents the allowed LL transitions for three distinct topological

regimes for B =1 T in only the K valley. The transition energy is determined from the energy difference between LLs obeying the conservation of real spin which in turn implies that transitions between $\sigma = +1$ and -1 levels are spin forbidden.

Following the nomenclature described in [76, 142], the magneto-excitation energies corresponding to different transitions, $E_{m,K(K'),\uparrow(\downarrow)} \rightarrow E_{n,K(K'),\uparrow(\downarrow)}$ are labelled as $T_{mn,K(K'),\uparrow(\downarrow)}$. In each of the depicted transitions, one of the participating LL is n=0 level. The $n = 0$ sublevels is quantum anomalous and unlike graphene $n = 0$ LLs do not sit at zero energy. $E^{\xi}_{0,\sigma}$ is independent of the magnetic field, and only depends on the specific spin and valley indices. Tables 5.4 and 5.5 of Ref. [142] summarize the magneto-excitation energies within $n = -1, 0, 1$ subspace for different magnetic and electric fields.

The real part of the longitudinal MO conductivity is plotted as a function of the incident photon energy at 1, 2, and 3 T exclusively for the QSHI regime in Fig. 6.3(a). For simplicity, we only display here the two inter-band transitions $T_{-10,K,\uparrow}$ and $T_{01,K,\downarrow}$ within the $n = -1, 0, 1$ subspace where we have ignored the contribution from intra-band transitions. The inter-band absorption peaks can be clearly seen when the incident photon energy $\hbar\omega$ resonantly matches the magneto-excitation energy gap. Each inter-band transition is represented by a Lorentzian peak. As the strength of the applied magnetic field is increased, the MO photonic energies are blue shifted. Fig. 6.3(b) illustrates the MO longitudinal conductivity as a function of the incident photon energy for different topological regimes.

For $\Delta_z = 0$, only the spin-orbit coupling contributes to the strong absorptive responses related to inter-band transitions. For the particular case where staggered potential is finite ($\Delta_z = 0.5\Delta_{so}$), each spin state splits into two new features giving rise to *two* Dirac energy gaps. Due to the asymmetric distribution of the spectral weight between the spin-split features, the intensity of the inter-band tran-

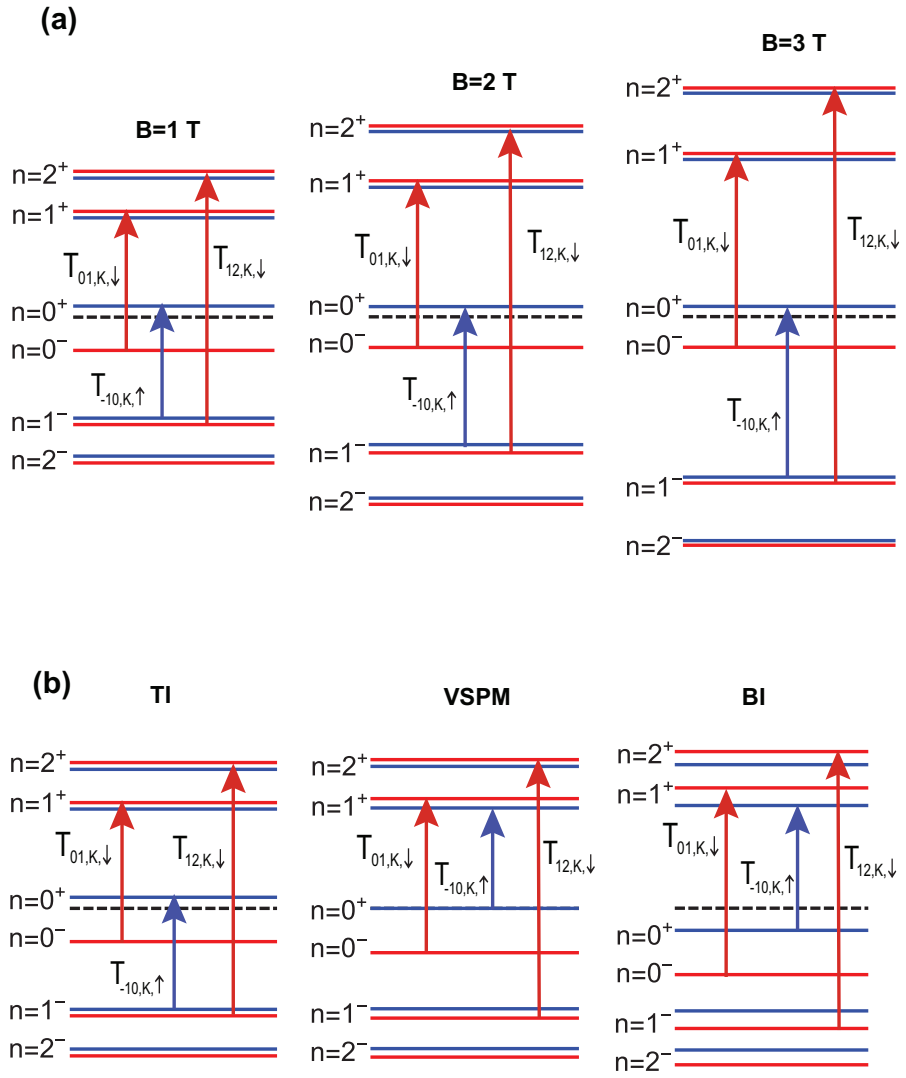

Figure 6.2: Schematic representation of the allowed transitions between LLs for (a) three different magnetic fields 1, 2 and 3 T for the QSHI regime in the K valley and (b) for three distinct topological regimes in the K valley for $B = 1$ T.

sition peaks is reduced. For $\Delta_z = \Delta_{so}$ *i.e.*, the valley-spin polarized metal (VSPM) regime, the spin-up absorption peaks are red-shifted which is an optical signature of the closing of the lowest bandgap of the Dirac fermions whereas the spin-down

absorptive peaks move higher in photonic energy due to the increase in the second bandgap as shown in Figure 6.3(b). For an even higher staggered electric potential $\Delta_z = 2\Delta_{so}$, the system reaches from the VSPM to the band insulator (BI) state. Finally, due to the reopening of the lowest gap, all inter-band features move to higher photonic energies as shown in Figure. 6.3(b) in the BI regime.

Fresnel's reflection coefficients are closely related to Landau quantization, which is induced by the MO response of the staggered silecenic monolayer. These quantized characteristics bleed into the PSHE as well. The effect of altering the magnetic field on LHCP in-plane and transverse PSHE is illustrated in Figures 6.3(c) and (d), respectively. We observe that the extreme values of PSHE appear away from conductivity peaks. For instance, for $B = 1$ T, the LHCP in-plane spatial shift $\langle \Delta_{x_{r+}}^{K,\uparrow,(\downarrow)} \rangle$ originated by $T_{01,K,\downarrow}$ transition gives maximum and minimum values in the vicinity of the first magneto-excitation energy. The oscillation period of $\langle \Delta_{x_{r+}}^{K,\uparrow,\downarrow} \rangle$ gradually decreases as the magneto-excitation energy increases. The amplitude of the $\langle \Delta_{x_{r+}}^{K,\uparrow,(\downarrow)} \rangle$ decreases by increasing the magnetic field and photonic energy as shown in Figs. 6.3(c). In Figure. 6.3(d), we have shown the spin and valley polarized transverse PSHE $\langle \Delta_{y_{r+}}^{K,\uparrow,(\downarrow)} \rangle$ as a function of the incident photon energy. Unlike the $\langle \Delta_{x_{r+}}^{K,\uparrow,(\downarrow)} \rangle$, the oscillation period of $\langle \Delta_{y_{r+}}^{K,\uparrow,(\downarrow)} \rangle$ is different. This is in agreement with results on Landau quantization of PSHE in monolayer black phosphorus [181]. Figs. 6.3(e) and (f) illustrate the LHCP in-plane and transverse spatial displacements as a function of the incident photon energy for the spin up and down in the K valley in three distinct topological regimes.

The oscillation period of the electric field modulated spin-dependent shifts gradually increases as the photonic energy increases. In Figures. 6.4(a) and (b), the valley and spin polarized $\langle \Delta_{x_{r+}}^{K,\uparrow,(\downarrow)} \rangle$ and $\langle \Delta_{y_{r+}}^{K,\uparrow,(\downarrow)} \rangle$ as a function of the incident pho-

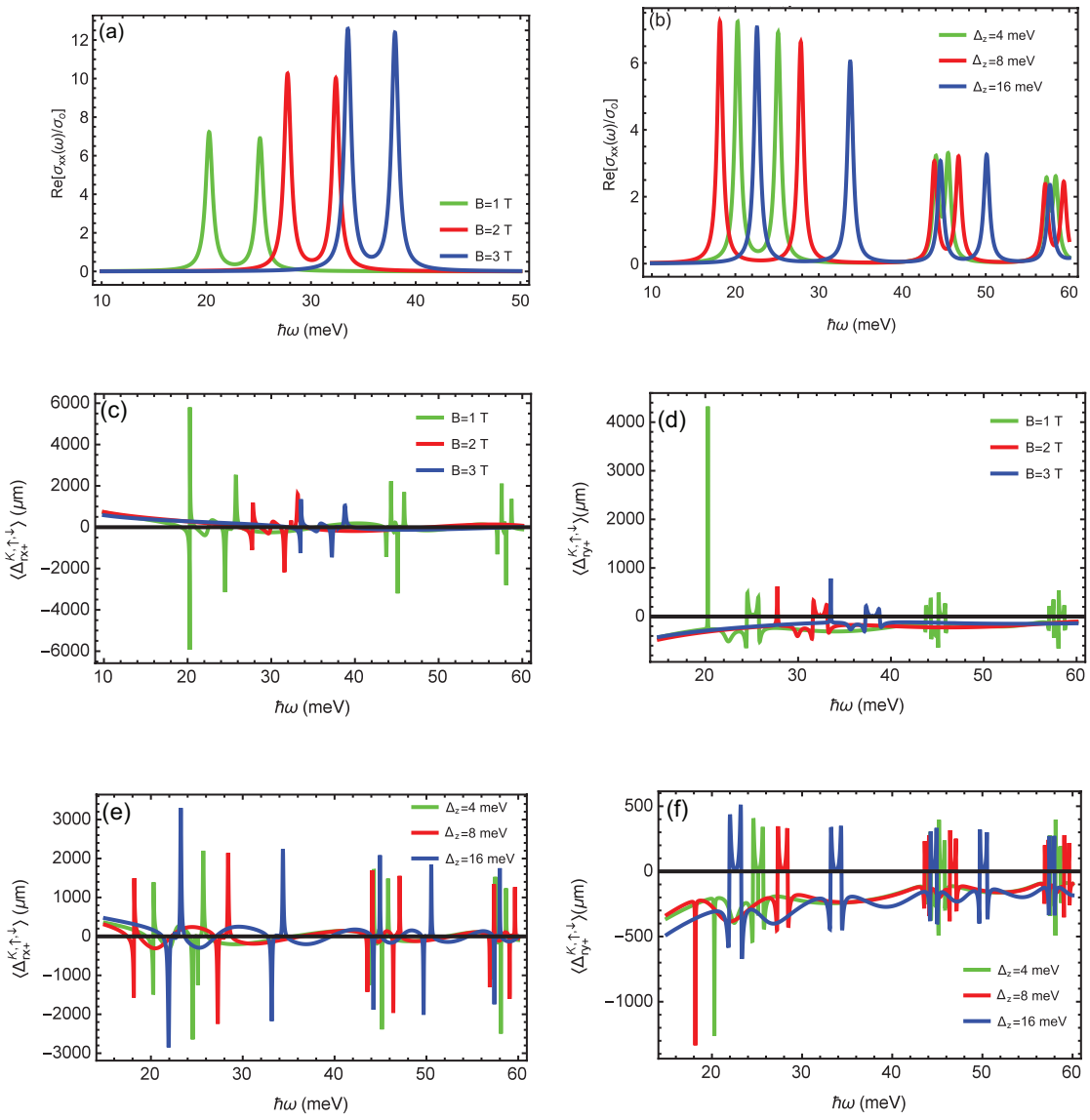

Figure 6.3: (a) Magnetic field modulated longitudinal conductivity as a function of the incident photon energy for different magnetic fields in the K valley for the QSHI regime. (b) Electric field modulated longitudinal conductivity as a function of the incident photon energy for three distinct topological regimes in the K valley for $B = 1$ T. (c) and (d) magnetic field modulated in-plane and transverse spatial shifts. (e) and (f) electric field modulated in-plane and transverse spatial shifts in distinct topological regimes. The parameters used are Δ_{so}=8 meV, $\Delta_z = 0.5\Delta_{so}$, $\theta_\psi = 61.9°$ and chemical potential $\mu_F = 0$.

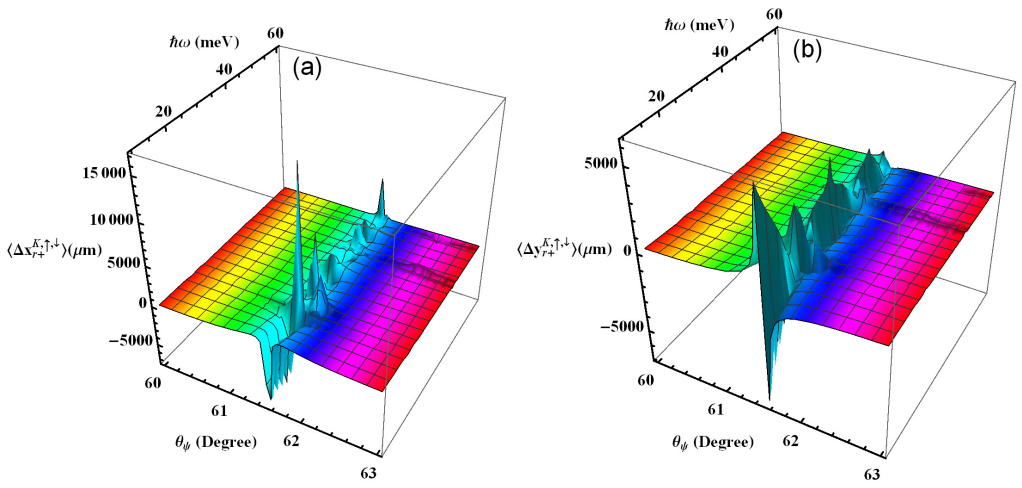

Figure 6.4: Magnetic field modulated LHCP (a) in-plane and (b) transverse PSHE as a function of the incident photon energy and the incident angle for both spins in the K valley. The applied magnetic field is 1 T.

ton energy and the incident angle for a magnetic field of 1 T in the QSHI regime are depicted. Due to the quantization of the MO conductivities and consequently Fresnel's coefficients, the PSHE is quantized and their values are enhanced by several orders of magnitude. It is observed that the spin dependent shifts exhibit extreme values near Brewster's angles, which in our case is 61.9° [181, 193]. We can see that at $T_{01,K,\downarrow}$ transition, the in-plane spatial shift $\langle\Delta_{x_{r+}}^{K,\uparrow,(\downarrow)}\rangle$ switch sign from negative to positive in the proximity of the Brewster's angle as shown in Figure. 6.4(a). For spin and valley polarized transverse shifts, when $\theta_\psi < \theta_B$, the quantized PSHE is positive whereas for the opposite case ($\theta_\psi > \theta_B$), the spatial shift is negative as presented in Figure. 6.4(b). These quantized steps in this system can be experimentally verified by a direct optical measurement [194].

6.3.2 Electric field modulated photonic spin Hall effect

In Figures 6.5(a) and (b), we have shown the spin dependent shifts for the VSPM ($\Delta_z = \Delta_{so}$) point. An increase in the electric potential Δ_z activates TQPTs and

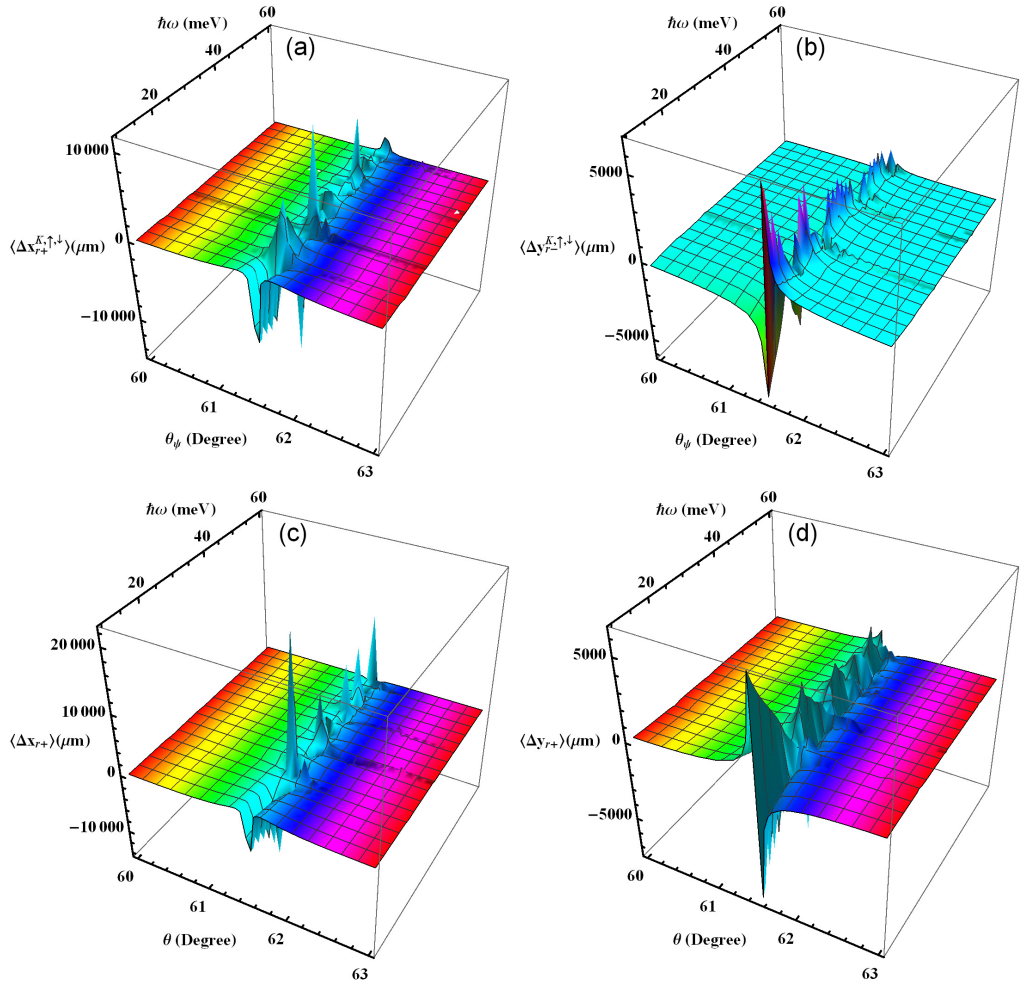

Figure 6.5: Electric field modulated (a) LHCP in-plane and (b) RHCP transverse PSHE in the VSPM state as a function of the incident photon energy and the incident angle for both spins in the K valley. Electric field modulated LHCP (c) in-plane and (d) transverse PSHE in the BI phase. The applied magnetic field is 1 T.

the system goes from the QSHI to the BI state. On the VSPM point $\Delta_z = \Delta_{so}$, the Dirac cones meet at $E_{0,K,\uparrow} = 0$ for the spin up Dirac fermion while the transition gap is equal to $E_{0,K,\downarrow}$ for the spin down in the K valley. Figure 6.5(a) represents the giant LHCP in-plane PSHE as a function of the incident angle and the photonic energy on this particular point. We observe quantized and significantly enhanced spin and valley polarized shifts in this case. The local minima and max-

ima can be seen around the first and second transitions $T_{-10,K,\uparrow} = 18.2$ meV and $T_{01,K,\downarrow} = 27.8$ meV, respectively. According to Figure 6.5(b), the spin and valley polarized RHCP transverse PSHE $\langle \Delta_{y_{r-}}^{K,\uparrow,(\downarrow)} \rangle$ is negative for $\theta_\psi < \theta_B$ and positive for $\theta_\psi > \theta_B$.

Similarly, for the BI state, both $\langle \Delta_{x_{r+}}^{K,\uparrow,(\downarrow)} \rangle$ and $\langle \Delta_{y_{r+}}^{K,\uparrow,(\downarrow)} \rangle$ display a similar tendency and sensitivity to the variance of θ_B as presented in Figures 6.5(c) and (d). The LHCP in-plane spatial shift is negative as expected. At the first magneto-excitation energy, we can see a sharp peak, and the polarity of the shift is changed from negative to positive as shown in Figure. 6.5(c). Similarly, we observe a giant positive transverse spatial shift at the first transition. Furthermore, the magnitudes of transverse spatial shifts are greater than the in-plane shifts in the BI state as shown in Figure 6.5(c). For the BI phase, as depicted in Figures. 6.5(c) and (d) it is clear that the spin-dependent shifts are significantly enhanced.

Chapter 7

Summary and outlook

The current chapter will furnish the reader with the main findings of the work described in previous chapters and the possible future extension of this work.

7.1 Summary

In the first part of the thesis, we started with a brief introduction to quantum materials. In the first chapter, we set the stage for the quantum mechanical description of 2D quantum materials. We reviewed some basic concepts in-band topology. We found that the key role players in topological band theory are the Berry phase and topological invariant. We started from the classical Hall effect and finally derived the quantized Hall resistivity ρ_{xy} and connected it to the topological invariant. We discussed the topological edge states in detail and argued that these topological edge states are robust against backscattering. We noted that these topological helical modes are protected by TRS. We derived the SOC in 2D materials using the Dirac equation. We described how the time-reversal symmetry is useful for the description of 2D and 3D topological insulators. Finally, we introduced 3D hybridized topological insulator ultra-thin films.

In the second chapter, we discussed the electronic properties of the 2D quantum materials, for example, graphene and silicene by deriving their low energy physics utilizing the tight-binding models. We discussed the energy dispersion of the 2DEG in the presence of a magnetic field and found that the energy dispersion of free electrons is a discrete set of highly degenerate LLs. Unlike 2DEG, in the presence of a magnetic field graphene responds differently. The energy dispersion of the Dirac fermions is proportional to the $\sqrt{nB}$. Another striking difference is the existence of the zero-energy LL which remains pinned at the Dirac point.

We also introduced a low-energy specific model for the Dirac fermions in buckled honeycomb 2D lattices possessing spin-orbit interaction. The staggered 2D materials have been predicted to map onto the Kane-Mele Hamiltonian. Additionally, we discussed the energy dispersion of these 2D quantum materials in the presence of the magnetic field. We found that there is only a single contribution from the $n = 0$ levels for each band. The SOC provides mass to the Dirac fermions.

We made use of the electric field as a control knob to close and reopen the band gap in order to drive phase transition between trivial and non-trivial states. Finally, in the same Chapter, we derived the low energy dispersion of TI thin film. The zeroth LL in TI thin film is quantum anomalous: its magnitude is independent of the magnetic field, and its sign depends on the specific Dirac SSs.

In Chapter 3, we focused on the transport properties of these materials. This chapter served as a theoretical framework for the description of the magneto-optic effects. We provided a brief reminder on quantized magneto-transport properties with a focus on the tools that are needed later in this thesis. We started with the introduction of the advance and retarded Green's functions which are the main pillars of the linear response theory. The Kubo formalism is an extremely popular technique in condensed matter physics to calculate linear response in materials.

We provided a comprehensive derivation of the Kubo formula for electronic conductivity. Using the Kubo approach, we then derived the general optical conductivity expression for the 2DEG which is equally suitable for studying quantum transport phenomena in other 2D graphene-based materials.

Using Kubo formalism, we derived the longitudinal and Hall magneto-optical conductivities which were shown to display novel and interesting physics as functions of the incident light frequency Ω, the chemical potential μ_F, temperature T and applied electric and magnetic fields. To better visualize the dependence of these parameters, we plotted the MO conductivities for different magnetic fields and in different topological regimes.

The main results of my work were presented in Chapters 4, 5, and Chapter 6. In Chapter 4, we explored the well-known magneto-optic effects, i.e., the Faraday and Kerr rotations in two different quantum materials. For example, we theoretically demonstrated the transitional MO effect due to the topological phase transition in staggered 2D materials and studied the electric field modulated valley and spin-polarized Faraday, Kerr rotations and ellipticities for three different topological regimes in silicene.

We also observed that if we change the polarization of the incident light or switch from one valley to another, the anti-phase peaks invert with respect to the baseline. We further investigated the magnetic field modulated MOKE for different magnetic fields and found that by increasing the magnetic field, the positions of the valley and spin-polarized FR and MOKE anti-phase peaks move towards higher frequencies, and the magnitude of FR and MOKE rotation is also enhanced. The second part of Chapter 4, reproduced similar results for 3D topological insulators. The most notable result we reported was that the magnitude of the maximum giant Kerr rotation angles for the first two anti-phase pairs exceeds $\approx 15^\circ$ at a

magnetic field of 5 T, which is an exceptionally large rotation for hybridized 3D TI-substrate system as compared to 3D Bi_2Se_3 films with μ_F=30 meV above the Dirac point in the presence of a magnetic field of 7 T [195].

In Chapter 5, we explored the mechanical beam shifts of topological silicene and 3D hybridized topological insulators. The lateral shifts are modulated by electric and magnetic fields and are analyzed in the THz frequency range. We have studied the effect of chemical potential, spin, valley, and incident photon frequency on the silicenic layer, with the particular enhancement of the GH shift in the vicinity of the Brewster angle. Furthermore, we found that the Brewster angle is sensitive to changing magnetic fields and chemical potential. The phenomenon can be used to develop highly tunable solid-state modulators. More interestingly, the valleys and spins indices can be used for the switching of the GH shift from negative to positive and vice versa.

In Chapter 6, we reported on the spin and valley polarized in-plane and transverse PSHE on the surface of the graphene-family substrate system. This formalism includes 2D materials such as silicene, germanene, stanene, and plumbene. Our findings show that both the spatial shifts are quantized and the nature of these spin shifts are oscillatory due to the LL splitting in the presence of the magnetic field. This is true for both the K and K' valleys. Our analysis highlights that the giant PSHE appears away from magneto-excitation energy peaks and offers a practical way to determine the valley and spin-polarized Hall conductivity and LLs by direct optical measurement, for example through quantum weak measurement techniques [176, 194].

7.2 Future Directions

In recent years, a broad family of 2D bilayer semiconducting quantum materials (twisted bilayer graphene and transition metal dichalcogenides) have been fabricated through micromechanical exfoliation [196, 197], having exotic properties and potential applications in electronic and optoelectronic devices. Twisted bilayer graphene (TBG) consists of two graphene sheets that are rotated by an angle called magic angle with respect to each other [198]. In the vicinity of the magic angle, TBG transforms from a weakly correlated Fermi liquid to a strongly correlated 2D quantum system [199]. In TBG the magic angle of 1.1° has been reported, which gives rise to exotic phenomena, including intrinsic superconductivity, quantized anomalous Hall states, magnetism, and interaction-induced correlated insulator states [196, 200, 201].

An interesting follow-up to the present work would be the exploration of these MO effects in other 2D quantum materials i.e. TBG [196] and topological Weyl semimetals [30]. We believe that the MO effects in TBG will open up a new way to design novel chiral topological photonic technologies. Analyzing systems with such exotic magneto-optic materials are expected to be used in many new optoelectronic, spinoptics, spintronics, and valleytronics applications, for example, manipulation of surface plasmons, remote sensing of magnetic fields, modulation of polarization, and other laser applications.

2D ferrovalley materials offer another landscape of 2D quantum materials which are half-metallic and belongs to a new kind of spin-valley coupled 2D material [202, 203]. We aim to determine the full response of 2D ferrovalley materials to electromagnetic fields as a function of frequency in the presence of an external magnetic field.

Recently, the idea of topology has been entered from condensed matter physics

into photonics, and now this burgeoning field of optics is called topological photonics. The topological laser is the hottest topic in topological photonics nowadays. In topological laser, the main driver is topologically protected photonic modes, in which light is topologically protected [204]. Comparing with conventional lasers, topological lasers are more efficient and robust against defects giving rise to a new type of lasing [204, 205]. For future considerations, we aspire to explore the topologically protected photonic edge states in 2D valleytronic materials for lasing applications [206].

References

[1] C. Broholm, I. Fisher, J. Moore, M. Murnane, A. Moreo, J. Tranquada, D. Basov, J. Freericks, M. Aronson, A. MacDonald, *et al.*, "Basic research needs workshop on quantum materials for energy relevant technology," tech. rep., USDOE Office of Science (United States), (2016).

[2] P. Maksym and T. Chakraborty, "Quantum dots in a magnetic field: Role of electron-electron interactions," *Physical Review Letters*, vol. 65, no. 1, p. 108, (1990).

[3] T. Takagahara and K. Takeda, "Theory of the quantum confinement effect on excitons in quantum dots of indirect-gap materials," *Physical Review B*, vol. 46, no. 23, p. 15578, (1992).

[4] F. W. Wise, "Lead salt quantum dots: the limit of strong quantum confinement," *Accounts of Chemical Research*, vol. 33, no. 11, pp. 773–780, (2000).

[5] J. N. Munday, D. Iannuzzi, Y. Barash, and F. Capasso, "Torque on birefringent plates induced by quantum fluctuations," *Physical Review A*, vol. 71, no. 4, p. 042102, (2005).

[6] T. Rappoport, L. Ghivelder, J. Fernandes, R. Guimaraes, and M. Continentino, "Experimental observation of quantum entanglement in low-dimensional spin systems," *Physical Review B*, vol. 75, no. 5, p. 054422, (2007).

[7] D. Basov, R. Averitt, and D. Hsieh, "Towards properties on demand in quantum materials," *Nature Materials*, vol. 16, no. 11, pp. 1077–1088, (2017).

[8] B. Keimer and J. Moore, "The physics of quantum materials," *Nature Physics*, vol. 13, no. 11, pp. 1045–1055, (2017).

[9] G. Blatter, M. V. Feigel'man, V. B. Geshkenbein, A. I. Larkin, and V. M. Vinokur, "Vortices in high-temperature superconductors," *Reviews of Modern Physics*, vol. 66, no. 4, p. 1125, (1994).

[10] E. Dagotto, "Correlated electrons in high-temperature superconductors," *Reviews of Modern Physics*, vol. 66, no. 3, p. 763, (1994).

[11] F. Bergeret, A. F. Volkov, and K. B. Efetov, "Odd triplet superconductivity and related phenomena in superconductor-ferromagnet structures," *Reviews of Modern Physics*, vol. 77, no. 4, p. 1321, (2005).

[12] K. Ishida, H. Mukuda, Y. Kitaoka, K. Asayama, Z. Mao, Y. Mori, and Y. Maeno, "Spin-triplet superconductivity in Sr_2RuO_4 identified by 17 o knight shift," *Nature*, vol. 396, no. 6712, pp. 658–660, (1998).

[13] K. v. Klitzing, G. Dorda, and M. Pepper, "New method for high-accuracy determination of the fine-structure constant based on quantized Hall resistance," *Physical Review Letters*, vol. 45, no. 6, p. 494, (1980).

[14] D. C. Tsui, H. L. Stormer, and A. C. Gossard, "Two-dimensional magnetotransport in the extreme quantum limit," *Physical Review Letters*, vol. 48, no. 22, p. 1559, (1982).

[15] C. L. Kane and E. J. Mele, "Quantum spin Hall effect in graphene," *Physical Review Letters*, vol. 95, no. 22, p. 226801, (2005).

[16] C. L. Kane and E. J. Mele, "Z_2 topological order and the quantum spin Hall effect," *Physical Review Letters*, vol. 95, no. 14, p. 146802, (2005).

[17] C.-Z. Chang, J. Zhang, X. Feng, J. Shen, Z. Zhang, M. Guo, K. Li, Y. Ou, P. Wei, L.-L. Wang, *et al.*, "Experimental observation of the quantum anomalous Hall effect in a magnetic topological insulator," *Science*, vol. 340, no. 6129, pp. 167–170, (2013).

[18] M. König, S. Wiedmann, C. Brüne, A. Roth, H. Buhmann, L. W. Molenkamp, X.-L. Qi, and S.-C. Zhang, "Quantum spin Hall insulator state in HgTe quantum wells," *Science*, vol. 318, no. 5851, pp. 766–770, (2007).

[19] Y. Shimizu, K. Miyagawa, K. Kanoda, M. Maesato, and G. Saito, "Spin liquid state in an organic mott insulator with a triangular lattice," *Physical Review Letters*, vol. 91, no. 10, p. 107001, (2003).

[20] E. Sonin, "Spin currents and spin superfluidity," *Advances in Physics*, vol. 59, no. 3, pp. 181–255, (2010).

[21] M. Z. Hasan and C. L. Kane, "Colloquium: topological insulators," *Reviews of Modern Physics*, vol. 82, no. 4, p. 3045, (2010).

[22] A. Molle, J. Goldberger, M. Houssa, Y. Xu, S.-C. Zhang, and D. Akinwande, "Buckled two-dimensional xene sheets," *Nature Materials*, vol. 16, no. 2, pp. 163–169, (2017).

[23] M. Dávila, L. Xian, S. Cahangirov, A. Rubio, and G. Le Lay, "Germanene: a novel two-dimensional germanium allotrope akin to graphene and silicene," *New Journal of Physics*, vol. 16, no. 9, p. 095002, (2014).

[24] S. Cahangirov, M. Topsakal, E. Aktürk, H. Şahin, and S. Ciraci, "Two-and one-dimensional honeycomb structures of silicon and germanium," *Physical Review Letters*, vol. 102, no. 23, p. 236804, (2009).

[25] B. Cai, S. Zhang, Z. Hu, Y. Hu, Y. Zou, and H. Zeng, "Tinene: a two-dimensional dirac material with a 72 mev band gap," *Physical Chemistry Chemical Physics*, vol. 17, no. 19, pp. 12634–12638, (2015).

[26] K. F. Mak, K. L. McGill, J. Park, and P. L. McEuen, "The valley Hall effect in MoS_2 transistors," *Science*, vol. 344, no. 6191, pp. 1489–1492, (2014).

[27] X.-L. Qi and S.-C. Zhang, "Topological insulators and superconductors," *Reviews of Modern Physics*, vol. 83, no. 4, p. 1057, (2011).

[28] B. Lv, H. Weng, B. Fu, X. P. Wang, H. Miao, J. Ma, P. Richard, X. Huang, L. Zhao, G. Chen, *et al.*, "Experimental discovery of weyl semimetal TaAs," *Physical Review X*, vol. 5, no. 3, p. 031013, (2015).

[29] B. Yan and C. Felser, "Topological materials: Weyl semimetals," *Annual Review of Condensed Matter Physics*, vol. 8, pp. 337–354, (2017).

[30] N. Liu, H. Guo, L. Fu, S. Kaiser, H. Schweizer, and H. Giessen, "Three-dimensional photonic metamaterials at optical frequencies," *Nature Materials*, vol. 7, no. 1, pp. 31–37, (2008).

[31] M. Sajid, J. K. Asbóth, D. Meschede, R. F. Werner, and A. Alberti, "Creating anomalous floquet chern insulators with magnetic quantum walks," *Physical Review B*, vol. 99, no. 21, p. 214303, (2019).

[32] K. S. Novoselov, A. K. Geim, S. V. Morozov, D. Jiang, Y. Zhang, S. V. Dubonos, I. V. Grigorieva, and A. A. Firsov, "Electric field effect in atomically thin carbon films," *Science*, vol. 306, no. 5696, pp. 666–669, (2004).

[33] N. Tombros, C. Jozsa, M. Popinciuc, H. T. Jonkman, and B. J. Van Wees, "Electronic spin transport and spin precession in single graphene layers at room temperature," *Nature*, vol. 448, no. 7153, pp. 571–574, (2007).

[34] A. Kara, H. Enriquez, A. P. Seitsonen, L. L. Y. Voon, S. Vizzini, B. Aufray, and H. Oughaddou, "A review on silicene—new candidate for electronics," *Surface Science Reports*, vol. 67, no. 1, pp. 1–18, (2012).

[35] D. Jose and A. Datta, "Structures and chemical properties of silicene: unlike graphene," *Accounts of Chemical Research*, vol. 47, no. 2, pp. 593–602, (2014).

[36] J. R. Schaibley, H. Yu, G. Clark, P. Rivera, J. S. Ross, K. L. Seyler, W. Yao, and X. Xu, "Valleytronics in 2D materials," *Nature Reviews Materials*, vol. 1, no. 11, pp. 1–15, (2016).

[37] W. J. d. M. Kort-Kamp, "Topological phase transitions in the photonic spin Hall effect," *Physical Review Letters*, vol. 119, no. 14, p. 147401, (2017).

[38] A. Agarwal, M. S. Vitiello, L. Viti, A. Cupolillo, and A. Politano, "Plasmonics with two-dimensional semiconductors: from basic research to technological applications," *Nanoscale*, vol. 10, no. 19, pp. 8938–8946, (2018).

[39] G. Tkachov, *Topological insulators: The physics of spin helicity in quantum transport*. CRC Press, (2015).

[40] B. A. Bernevig, *Topological insulators and topological superconductors*. Princeton university press, (2013).

[41] W. S. Massey, *A basic course in algebraic topology*, vol. 127. Springer, (2019).

[42] M. Sajid, *Magnetic Quantum Walks of Neutral Atoms in Optical Lattices*. PhD thesis, Universitäts-und Landesbibliothek Bonn, (2018).

[43] X.-G. Wen, "Topological orders and edge excitations in fractional quantum Hall states," *Advances in Physics*, vol. 44, no. 5, pp. 405–473, (1995).

[44] D. J. Thouless, M. Kohmoto, M. P. Nightingale, and M. den Nijs, "Quantized Hall conductance in a two-dimensional periodic potential," *Physical Review Letters*, vol. 49, no. 6, p. 405, (1982).

[45] F. D. M. Haldane, "Model for a quantum Hall effect without Landau levels: Condensed-matter realization of the" parity anomaly"," *Physical Review Letters*, vol. 61, no. 18, p. 2015, (1988).

[46] A. P. Schnyder, S. Ryu, A. Furusaki, and A. W. Ludwig, "Classification of topological insulators and superconductors in three spatial dimensions," *Physical Review B*, vol. 78, no. 19, p. 195125, (2008).

[47] Y. Ando, "Topological insulator materials," *Journal of the Physical Society of Japan*, vol. 82, no. 10, p. 102001, (2013).

[48] M. V. Berry, "Quantal phase factors accompanying adiabatic changes," *Proceedings of the Royal Society of London. A. Mathematical and Physical Sciences*, vol. 392, no. 1802, pp. 45–57, (1984).

[49] D. Xiao, M.-C. Chang, and Q. Niu, "Berry phase effects on electronic properties," *Reviews of Modern Physics*, vol. 82, no. 3, p. 1959, (2010).

[50] T. Kato, "On the adiabatic theorem of quantum mechanics," *Journal of the Physical Society of Japan*, vol. 5, no. 6, pp. 435–439, (1950).

[51] A. Messiah, "Quantum mechanics, vol. ii," (1962).

[52] N. Doughty, *Lagrangian interaction: an introduction to relativistic symmetry in electrodynamics and gravitation*. CRC Press, (2018).

[53] N. Zettili, "Quantum mechanics: concepts and applications," (2003).

[54] J. J. Sakurai, *Advanced quantum mechanics*. Pearson Education India, (2006).

[55] J. E. Moore and L. Balents, "Topological invariants of time-reversal-invariant band structures," *Physical Review B*, vol. 75, no. 12, p. 121306, (2007).

[56] L. Fu, C. L. Kane, and E. J. Mele, "Topological insulators in three dimensions," *Physical Review Letters*, vol. 98, no. 10, p. 106803, (2007).

[57] L. Fu and C. L. Kane, "Probing neutral majorana fermion edge modes with charge transport," *Physical Review Letters*, vol. 102, no. 21, p. 216403, (2009).

[58] P. Roushan, J. Seo, C. V. Parker, Y. S. Hor, D. Hsieh, D. Qian, A. Richardella, M. Z. Hasan, R. J. Cava, and A. Yazdani, "Topological surface states protected from backscattering by chiral spin texture," *Nature*, vol. 460, no. 7259, pp. 1106–1109, (2009).

[59] C.-X. Liu, H. Zhang, B. Yan, X.-L. Qi, T. Frauenheim, X. Dai, Z. Fang, and S.-C. Zhang, "Oscillatory crossover from two-dimensional to three-dimensional topological insulators," *Physical Review B*, vol. 81, no. 4, p. 041307, (2010).

[60] H.-Z. Lu, W.-Y. Shan, W. Yao, Q. Niu, and S.-Q. Shen, "Massive dirac fermions and spin physics in an ultrathin film of topological insulator," *Physical Review B*, vol. 81, no. 11, p. 115407, (2010).

[61] J. Wang, A. M. DaSilva, C.-Z. Chang, K. He, J. Jain, N. Samarth, X.-C. Ma, Q.-K. Xue, and M. H. Chan, "Evidence for electron-electron interaction in topological insulator thin films," *Physical Review B*, vol. 83, no. 24, p. 245438, (2011).

[62] H. Cao, J. Tian, I. Miotkowski, T. Shen, J. Hu, S. Qiao, and Y. P. Chen, "Quantized Hall effect and shubnikov–de haas oscillations in highly doped Bi_2Se_3: Evidence for layered transport of bulk carriers," *Physical Review Letters*, vol. 108, no. 21, p. 216803, (2012).

[63] G. G. Guzmán-Verri and L. L. Y. Voon, "Electronic structure of silicon-based nanostructures," *Physical Review B*, vol. 76, no. 7, p. 075131, (2007).

[64] M. Ezawa, "Spin-valley optical selection rule and strong circular dichroism in silicene," *Physical Review B*, vol. 86, no. 16, p. 161407, (2012).

[65] C.-C. Liu, W. Feng, and Y. Yao, "Quantum spin Hall effect in silicene and two-dimensional germanium," *Physical Review Letters*, vol. 107, no. 7, p. 076802, (2011).

[66] Y. Xu, B. Yan, H.-J. Zhang, J. Wang, G. Xu, P. Tang, W. Duan, and S.-C. Zhang, "Large-gap quantum spin Hall insulators in tin films," *Physical Review Letters*, vol. 111, no. 13, p. 136804, (2013).

[67] M. Ezawa, "Photoinduced topological phase transition and a single dirac-cone state in silicene," *Physical Review Letters*, vol. 110, no. 2, p. 026603, (2013).

[68] J. Zhao, H. Liu, Z. Yu, R. Quhe, S. Zhou, Y. Wang, C. C. Liu, H. Zhong, N. Han, J. Lu, *et al.*, "Rise of silicene: A competitive 2D material," *Progress in Materials Science*, vol. 83, pp. 24–151, (2016).

[69] C. Grazianetti, E. Cinquanta, and A. Molle, "Two-dimensional silicon: the advent of silicene," *2D Materials*, vol. 3, no. 1, p. 012001, (2016).

[70] C.-C. Liu, H. Jiang, and Y. Yao, "Low-energy effective Hamiltonian involving spin-orbit coupling in silicene and two-dimensional germanium and tin," *Physical Review B*, vol. 84, no. 19, p. 195430, (2011).

[71] E. Cinquanta, E. Scalise, D. Chiappe, C. Grazianetti, B. van den Broek, M. Houssa, M. Fanciulli, and A. Molle, "Getting through the nature of silicene: An $sp_2 - -sp_3$ two-dimensional silicon nanosheet," *The Journal of Physical Chemistry C*, vol. 117, no. 32, pp. 16719–16724, (2013).

[72] M. Ezawa, "A topological insulator and helical zero mode in silicene under an inhomogeneous electric field," *New Journal of Physics*, vol. 14, no. 3, p. 033003, (2012).

[73] M. Ezawa, "Monolayer topological insulators: silicene, germanene, and stanene," *Journal of the Physical Society of Japan*, vol. 84, no. 12, p. 121003, (2015).

[74] W. Wu, W. Zhang, S. Chen, X. Ling, W. Shu, H. Luo, S. Wen, and X. Yin, "Transitional Goos-Hänchen effect due to the topological phase transitions," *Optics Express*, vol. 26, no. 18, pp. 23705–23713, (2018).

[75] M. Shah and M. S. Anwar, "Magneto-optical effects in the Landau level manifold of 2d lattices with spin-orbit interaction," *Optics Express*, vol. 27, no. 16, pp. 23217–23233, (2019).

[76] M. Tahir and U. Schwingenschlögl, "Valley polarized quantum Hall effect and topological insulator phase transitions in silicene," *Scientific Reports*, vol. 3, no. 1, pp. 1–5, (2013).

[77] A. Zyuzin and A. Burkov, "Thin topological insulator film in a perpendicular magnetic field," *Physical Review B*, vol. 83, no. 19, p. 195413, (2011).

[78] P. Cheng, C. Song, T. Zhang, Y. Zhang, Y. Wang, J.-F. Jia, J. Wang, Y. Wang, B.-F. Zhu, X. Chen, *et al.*, "Landau quantization of topological surface states in Bi_2Se_3," *Physical Review Letters*, vol. 105, no. 7, p. 076801, (2010).

[79] M. Tahir, K. Sabeeh, and U. Schwingenschlögl, "Quantum capacitance of an ultrathin topological insulator film in a magnetic field," *Scientific Reports*, vol. 3, no. 1, pp. 1–5, (2013).

[80] M. Shah, A. Akbar, M. Sajid, and M. S. Anwar, "Transitional Faraday and Kerr effect in hybridized topological insulator thin films," *Optical Materials Express*, vol. 11, no. 2, pp. 525–538, (2021.

[81] R. A. Jishi, *Feynman diagram techniques in condensed matter physics*. Cambridge University Press, (2013).

[82] G. D. Mahan, *Many-particle physics*. Springer Science & Business Media, (2013).

[83] R. Kubo, "Statistical-mechanical theory of irreversible processes. i. general theory and simple applications to magnetic and conduction problems," *Journal of the Physical Society of Japan*, vol. 12, no. 6, pp. 570–586, (1957).

[84] H. Bruus and K. Flensberg, *Many-body quantum theory in condensed matter physics: an introduction*. Oxford university press, (2004).

[85]

[86] V. Vargiamidis, P. Vasilopoulos, and G. Hai, "Dc and ac transport in silicene," *Journal of Physics: Condensed Matter*, vol. 26, no. 34, p. 345303, 2014.

[87] W.-K. Tse and A. MacDonald, "Magneto-optical Faraday and Kerr effects in topological insulator films and in other layered quantized Hall systems," *Physical Review B*, vol. 84, no. 20, p. 205327, (2011).

[88] C. J. Tabert and E. J. Nicol, "Magneto-optical conductivity of silicene and other buckled honeycomb lattices," *Physical Review B*, vol. 88, no. 8, p. 085434, (2013).

[89] T. Stauber and N. Peres, "Effect of Holstein phonons on the electronic properties of graphene," *Journal of Physics: Condensed Matter*, vol. 20, no. 5, p. 055002, (2008).

[90] V. Gusynin and S. Sharapov, "Unconventional integer quantum Hall effect in graphene," *Physical Review Letters*, vol. 95, no. 14, p. 146801, (2005).

[91] V. Gusynin, S. Sharapov, and J. Carbotte, "Anomalous absorption line in the magneto-optical response of graphene," *Physical Review Letters*, vol. 98, no. 15, p. 157402, (2007).

[92] F. H. Koppens, D. E. Chang, and F. J. Garcia de Abajo, "Graphene plasmonics: a platform for strong light–matter interactions," *Nano Letters*, vol. 11, no. 8, pp. 3370–3377, (2011).

[93] I. Crassee, J. Levallois, A. L. Walter, M. Ostler, A. Bostwick, E. Rotenberg, T. Seyller, D. Van Der Marel, and A. B. Kuzmenko, "Giant Faraday rotation in single-and multilayer graphene," *Nature Physics*, vol. 7, no. 1, pp. 48–51, (2011).

[94] A. Ferreira, J. Viana-Gomes, Y. V. Bludov, V. Pereira, N. Peres, and A. C. Neto, "Faraday effect in graphene enclosed in an optical cavity and the equation of motion method for the study of magneto-optical transport in solids," *Physical Review B*, vol. 84, no. 23, p. 235410, (2011).

[95] D. L. Sounas and C. Caloz, "Electromagnetic nonreciprocity and gyrotropy of graphene," *Applied Physics Letters*, vol. 98, no. 2, p. 021911, (2011).

[96] G. Catarina, J. Have, J. Fernández-Rossier, and N. M. Peres, "Optical orientation with linearly polarized light in transition metal dichalcogenides," *Physical Review B*, vol. 99, no. 12, p. 125405, (2019).

[97] R. Suzuki, M. Sakano, Y. Zhang, R. Akashi, D. Morikawa, A. Harasawa, K. Yaji, K. Kuroda, K. Miyamoto, T. Okuda, *et al.*, "Valley-dependent spin polarization in bulk MoS_2 with broken inversion symmetry," *Nature Nanotechnology*, vol. 9, no. 8, p. 611, (2014).

[98] M. Cazalilla, H. Ochoa, and F. Guinea, "Quantum spin Hall effect in two-dimensional crystals of transition-metal dichalcogenides," *Physical Review Letters*, vol. 113, no. 7, p. 077201, (2014).

[99] A. Pospischil, M. M. Furchi, and T. Mueller, "Solar-energy conversion and light emission in an atomic monolayer p–n diode," *Nature Nanotechnology*, vol. 9, no. 4, pp. 257–261, (2014).

[100] S. Wu, S. Buckley, J. R. Schaibley, L. Feng, J. Yan, D. G. Mandrus, F. Hatami, W. Yao, J. Vučković, A. Majumdar, *et al.*, "Monolayer semiconductor nanocavity lasers with ultralow thresholds," *Nature*, vol. 520, no. 7545, pp. 69–72, (2015).

[101] D. Xiao, W. Yao, and Q. Niu, "Valley-contrasting physics in graphene: magnetic moment and topological transport," *Physical Review Letters*, vol. 99, no. 23, p. 236809, (2007).

[102] W. Yao, D. Xiao, and Q. Niu, "Valley-dependent optoelectronics from inversion symmetry breaking," *Physical Review B*, vol. 77, no. 23, p. 235406, (2008).

[103] H. Zeng, J. Dai, W. Yao, D. Xiao, and X. Cui, "Valley polarization in MoS_2 monolayers by optical pumping," *Nature Nanotechnology*, vol. 7, no. 8, pp. 490–493, (2012).

[104] P. M. Mihailovic, S. J. Petricevic, and J. B. Radunovic, "Compensation for temperature-dependence of the Faraday effect by optical activity temperature shift," *IEEE Sensors Journal*, vol. 13, no. 2, pp. 832–837, (2012).

[105] T. Yoshino, S.-i. Torihata, M. Yokota, and N. Tsukada, "Faraday-effect optical current sensor with a garnet film/ring core in a transverse configuration," *Applied Optics*, vol. 42, no. 10, pp. 1769–1772, (2003).

[106] J. W. Dawson, T. W. MacDougall, and E. Hernandez, "Verdet constant limited temperature response of a fiber-optic current sensor," *IEEE Photonics Technology Letters*, vol. 7, no. 12, pp. 1468–1470, (1995).

[107] A. Dolatabady and N. Granpayeh, "Manipulation of the Faraday rotation by graphene metasurfaces," *Journal of Magnetism and Magnetic Materials*, vol. 469, pp. 231–235, (2019).

[108] J.-M. Poumirol, P. Q. Liu, T. M. Slipchenko, A. Y. Nikitin, L. Martin-Moreno, J. Faist, and A. B. Kuzmenko, "Electrically controlled terahertz magneto-optical phenomena in continuous and patterned graphene," *Nature Communications*, vol. 8, no. 1, pp. 1–6, (2017).

[109] A. Grebenchukov, S. Azbite, A. Zaitsev, and M. Khodzitsky, "Faraday effect control in graphene-dielectric structure by optical pumping," *Journal of Magnetism and Magnetic Materials*, vol. 472, pp. 25–28, (2019).

[110] K. N. Okada, Y. Takahashi, M. Mogi, R. Yoshimi, A. Tsukazaki, K. S. Takahashi, N. Ogawa, M. Kawasaki, and Y. Tokura, "Terahertz spectroscopy on Faraday and Kerr rotations in a quantum anomalous Hall state," *Nature Communications*, vol. 7, p. 12245, (2016).

[111] Q. Yang, X. A. Zhang, A. Bagal, W. Guo, and C.-H. Chang, "Antireflection effects at nanostructured material interfaces and the suppression of thin-film interference," *Nanotechnology*, vol. 24, no. 23, p. 235202, (2013).

[112] W. Kort-Kamp, B. Amorim, G. Bastos, F. A. Pinheiro, F. Rosa, N. Peres, and C. Farina, "Active magneto-optical control of spontaneous emission in graphene," *Physical Review B*, vol. 92, no. 20, p. 205415, (2015).

[113] M. Shah, M. Sajid, and M. Shah, "Magnetic field and Fermi energy modulated quantized Imbert-Fedorov shifts in graphene," *JOSA B*, vol. 38, no. 9, pp. 2736–2741, (2021).

[114] M. Oliva-Leyva and C. Wang, "Magneto-optical conductivity of anisotropic two-dimensional dirac–weyl materials," *Annals of Physics*, vol. 384, pp. 61–70, (2017).

[115] T. Low, R. Roldán, H. Wang, F. Xia, P. Avouris, L. M. Moreno, and F. Guinea, "Plasmons and screening in monolayer and multilayer black phosphorus," *Physical Review Letters*, vol. 113, no. 10, p. 106802, (2014).

[116] M. H. Levitt, *Spin dynamics: basics of nuclear magnetic resonance*. John Wiley & Sons, (2013).

[117] H. Funk, A. Knorr, F. Wendler, and E. Malic, "Microscopic view on Landau level broadening mechanisms in graphene," *Physical Review B*, vol. 92, no. 20, p. 205428, (2015).

[118] C. J. Tabert and E. J. Nicol, "Valley-spin polarization in the magneto-optical response of silicene and other similar 2d crystals," *Physical Review Letters*, vol. 110, no. 19, p. 197402, (2013).

[119] N. Ubrig, I. Crassee, J. Levallois, I. O. Nedoliuk, F. Fromm, M. Kaiser, T. Seyller, and A. B. Kuzmenko, "Fabry-perot enhanced Faraday rotation in graphene," *Optics Express*, vol. 21, no. 21, pp. 24736–24741, (2013).

[120] W.-Y. Shan, H.-Z. Lu, and S.-Q. Shen, "Effective continuous model for surface states and thin films of three-dimensional topological insulators," *New Journal of Physics*, vol. 12, no. 4, p. 043048, (2010).

[121] S.-B. Zhang, H.-Z. Lu, and S.-Q. Shen, "Edge states and integer quantum Hall effect in topological insulator thin films," *Scientific Reports*, vol. 5, no. 1, pp. 1–10, (2015).

[122] Y. Xu, G. Jiang, I. Miotkowski, R. R. Biswas, and Y. P. Chen, "Tuning insulator-semimetal transitions in 3D topological insulator thin films by intersurface hybridization and in-plane magnetic fields," *Physical Review Letters*, vol. 123, no. 20, p. 207701, (2019).

[123] X. Xi, C. Ma, Z. Liu, Z. Chen, W. Ku, H. Berger, C. Martin, D. Tanner, and G. Carr, "Signatures of a pressure-induced topological quantum phase transition in $BiTeI$," *Physical Review Letters*, vol. 111, no. 15, p. 155701, (2013).

[124] J. Mutch, W.-C. Chen, P. Went, T. Qian, I. Z. Wilson, A. Andreev, C.-C. Chen, and J.-H. Chu, "Evidence for a strain-tuned topological phase transition in $ZrTe_5$," *Science Advances*, vol. 5, no. 8, p. eaav9771, (2019).

[125] G. Liu, G. Zhou, and Y.-H. Chen, "Modulation of external electric field on surface states of topological insulator Bi_2Se_3 thin films," *Applied Physics Letters*, vol. 101, no. 22, p. 223109, (2012).

[126] J. L. Collins, A. Tadich, W. Wu, L. C. Gomes, J. N. Rodrigues, C. Liu, J. Hellerstedt, H. Ryu, S. Tang, S.-K. Mo, *et al.*, "Electric-field-tuned topological phase transition in ultrathin Na_3Bi," *Nature*, vol. 564, no. 7736, pp. 390–394, (2018).

[127] A. Zyuzin, M. Hook, and A. a. Burkov, "Parallel magnetic field driven quantum phase transition in a thin topological insulator film," *Physical Review B*, vol. 83, no. 24, p. 245428, (2011).

[128] A. Pertsova, C. M. Canali, and A. H. MacDonald, "Thin films of a three-dimensional topological insulator in a strong magnetic field: Microscopic study," *Physical Review B*, vol. 91, no. 7, p. 075430, (2015).

[129] S. K. Chong, L. Liu, T. D. Sparks, F. Liu, and V. V. Deshpande, "Topological phase transitions in a hybridized three-dimensional topological insulator," *arXiv preprint arXiv:2004.04870*, (2020).

[130] W.-K. Tse and A. MacDonald, "Giant magneto-optical Kerr effect and universal Faraday effect in thin-film topological insulators," *Physical Review Letters*, vol. 105, no. 5, p. 057401, (2010).

[131] R. V. Aguilar, A. Stier, W. Liu, L. Bilbro, D. George, N. Bansal, L. Wu, J. Cerne, A. Markelz, S. Oh, *et al.*, "Terahertz response and colossal Kerr rotation from the surface states of the topological insulator Bi_2Se_3," *Physical Review Letters*, vol. 108, no. 8, p. 087403, (2012).

[132] G. S. Jenkins, A. B. Sushkov, D. C. Schmadel, M.-H. Kim, M. Brahlek, N. Bansal, S. Oh, and H. D. Drew, "Giant plateau in the terahertz Faraday angle in gated Bi_2Se_3," *Physical Review B*, vol. 86, no. 23, p. 235133, (2012).

[133] V. Dziom, A. Shuvaev, A. Pimenov, G. Astakhov, C. Ames, K. Bendias, J. Böttcher, G. Tkachov, E. Hankiewicz, C. Brüne, *et al.*, "Observation of the universal magnetoelectric effect in a 3D topological insulator," *Nature Communications*, vol. 8, no. 1, pp. 1–8, (2017).

[134] Y. Shao, K. W. Post, J.-S. Wu, S. Dai, A. J. Frenzel, A. R. Richardella, J. S. Lee, N. Samarth, M. M. Fogler, A. V. Balatsky, *et al.*, "Faraday rotation due to surface states in the topological insulator $(Bi_{1-x}Sb_x)_2Te_3$," *Nano Letters*, vol. 17, no. 2, pp. 980–984, (2017).

[135] X. Li, K. Yoshioka, M. Xie, I. G Timothy Noe, W. Lee, N. M. Peraca, W. Gao, T. Hagiwara, Ø. S. Handegård, L.-W. Nien, *et al.*, "Terahertz Faraday and Kerr rotation spectroscopy of $(Bi_{1-x}Sb_x)$ films in high magnetic fields up to 30 Tesla," *Physical Review B*, vol. 100, no. 11, p. 115145, (2019).

[136] I. O. Nedoliuk, S. Hu, A. K. Geim, and A. B. Kuzmenko, "Colossal infrared and terahertz magneto-optical activity in a two-dimensional dirac material," *Nature Nanotechnology*, vol. 14, no. 8, pp. 756–761, (2019).

[137] A. Stroppa, S. Picozzi, A. Continenza, M. Kim, and A. J. Freeman, "Magneto-optical properties of (ga, mn) as: An ab initio determination," *Physical Review B*, vol. 77, no. 3, p. 035208, (2008).

[138] K. Yang, W. Hu, H. Wu, M.-H. Whangbo, P. G. Radaelli, and A. Stroppa, "Magneto-optical Kerr switching properties of $(CrI_3)_2$ and $(CrBr_3/CrI_3)$ bilayers," *ACS Applied Electronic Materials*, vol. 2, no. 5, pp. 1373–1380, (2020).

[139] F.-R. Fan, H. Wu, D. Nabok, S. Hu, W. Ren, C. Draxl, and A. Stroppa, "Electric-magneto-optical Kerr effect in a hybrid organic–inorganic per-

ovskite," *Journal of the American Chemical Society*, vol. 139, no. 37, pp. 12883–12886, (2017).

[140] M. N. Deeter, "Fiber-optic Faraday-effect magnetic-field sensor based on flux concentrators," *Applied Optics*, vol. 35, no. 1, pp. 154–157, (1996).

[141] M. Shah and M. S. Anwar, "Magneto-optic modulation of lateral and angular shifts in spin-orbit coupled members of the graphene family," *OSA Continuum*, vol. 3, no. 4, pp. 878–892, (2020).

[142] N. P. Butch, K. Kirshenbaum, P. Syers, A. B. Sushkov, G. S. Jenkins, H. D. Drew, and J. Paglione, "Strong surface scattering in ultrahigh-mobility Bi_2Se_3 topological insulator crystals," *Physical Review B*, vol. 81, no. 24, p. 241301, (2010).

[143] C. Li, B. De Ronde, A. Nikitin, Y. Huang, M. S. Golden, A. De Visser, and A. Brinkman, "Interaction between counter-propagating quantum Hall edge channels in the 3D topological insulator bisbtese 2," *Physical Review B*, vol. 96, no. 19, p. 195427, (2017).

[144] A. Taskin, H. F. Legg, F. Yang, S. Sasaki, Y. Kanai, K. Matsumoto, A. Rosch, and Y. Ando, "Planar Hall effect from the surface of topological insulators," *Nature Communications*, vol. 8, no. 1, pp. 1–7, (2017).

[145] S. K. Chong, K. B. Han, T. D. Sparks, and V. V. Deshpande, "Tunable coupling between surface states of a three-dimensional topological insulator in the quantum Hall regime," *Physical Review Letters*, vol. 123, no. 3, p. 036804, (2019).

[146] M. Shah, M. Sajid, and M. S. Anwar, "Quantized Goos-Hänchen shifts on the surface of hybridized topological insulator thin films," *Physica E: Low-dimensional Systems and Nanostructures*, p. 114819, (2021).

[147] F. Goos and H. Hänchen, "Ein neuer und fundamentaler versuch zur totalreflexion," *Annalen der Physik*, vol. 436, no. 7-8, pp. 333–346, (1947).

[148] C. Imbert, "Calculation and experimental proof of the transverse shift induced by total internal reflection of a circularly polarized liwu2011valleyght beam," *Physical Review D*, vol. 5, no. 4, p. 787, (1972).

[149] H. K. Lotsch, "Reflection and refraction of a beam of light at a plane interface," *JOSA*, vol. 58, no. 4, pp. 551–561, (1968).

[150] C. Schaefer and R. Pich, "Ein beitrag zur theorie der totalreflexion," *Annalen der Physik*, vol. 422, no. 3, pp. 245–266, (1937).

[151] J. He, J. Yi, and S. He, "Giant negative Goos-Hänchen shifts for a photonic crystal with a negative effective index," *Optics Express*, vol. 14, no. 7, pp. 3024–3029, (2006).

[152] I. Soboleva, V. Moskalenko, and A. Fedyanin, "Giant Goos-Hänchen effect and fano resonance at photonic crystal surfaces," *Physical Review Letters*, vol. 108, no. 12, p. 123901, (2012).

[153] X. Yin, L. Hesselink, Z. Liu, N. Fang, and X. Zhang, "Large positive and negative lateral optical beam displacements due to surface plasmon resonance," *Applied Physics Letters*, vol. 85, no. 3, pp. 372–374, (2004).

[154] X. Yin and L. Hesselink, "Goos-Hänchen shift surface plasmon resonance sensor," *Applied Physics Letters*, vol. 89, no. 26, p. 261108, (2006).

[155] Y. Huang, Z. Yu, C. Zhong, J. Fang, and Z. Dong, "Tunable lateral shifts of the reflected wave on the surface of an anisotropic chiral metamaterial," *Optical Materials Express*, vol. 7, no. 5, pp. 1473–1485, (2017).

[156] S. Longhi, G. Della Valle, and K. Staliunas, "Goos-Hänchen shift in complex crystals," *Physical Review A*, vol. 84, no. 4, p. 042119, (2011).

[157] S.-Y. Lee, J. Le Deunff, M. Choi, and R. Ketzmerick, "Quantum Goos-Hänchen shift and tunneling transmission at a curved step potential," *Physical Review A*, vol. 89, no. 2, p. 022120, (2014).

[158] T. Hashimoto and T. Yoshino, "Optical heterodyne sensor using the Goos–Hänchen shift," *Optics Letters*, vol. 14, no. 17, pp. 913–915, (1989).

[159] Y. Fan, N.-H. Shen, F. Zhang, Z. Wei, H. Li, Q. Zhao, Q. Fu, P. Zhang, T. Koschny, and C. M. Soukoulis, "Electrically tunable Goos–Hänchen effect with graphene in the terahertz regime," *Advanced Optical Materials*, vol. 4, no. 11, pp. 1824–1828, (2016).

[160] W. Wu, S. Chen, C. Mi, W. Zhang, H. Luo, and S. Wen, "Giant quantized Goos-Hänchen effect on the surface of graphene in the quantum Hall regime," *Physical Review A*, vol. 96, no. 4, p. 043814, (2017).

[161] T. Tang, J. Qin, J. Xie, L. Deng, and L. Bi, "Magneto-optical Goos-Hänchen effect in a prism-waveguide coupling structure," *Optics Express*, vol. 22, no. 22, pp. 27042–27055, (2014).

[162] T. Tang, J. Li, M. Zhu, L. Luo, J. Yao, N. Li, and P. Zhang, "Realization of tunable Goos-Hänchen effect with magneto-optical effect in graphene," *Carbon*, vol. 135, pp. 29–34, (2018).

[163] A. Das and M. Pradhan, "Goos–Hänchen shift for gaussian beams impinging on monolayer-MoS_2-coated surfaces," *JOSA B*, vol. 35, no. 8, pp. 1956–1962, (2018).

[164] G. Ye, W. Zhang, W. Wu, S. Chen, W. Shu, H. Luo, and S. Wen, "Goos-Hänchen and Imbert–Fedorov effects in weyl semimetals," *Physical Review A*, vol. 99, no. 2, p. 023807, (2019).

[165] A. Farmani, A. Mir, and Z. Sharifpour, "Broadly tunable and bidirectional terahertz graphene plasmonic switch based on enhanced Goos-Hänchen effect," *Applied Surface Science*, vol. 453, pp. 358–364, (2018).

[166] Q. Li, B. Zhang, and J. Shen, "Goos-Hänchen shifts of reflected terahertz wave on a CoC-air interface," *Optics Express*, vol. 21, no. 5, pp. 6480–6487, (2013).

[167] X. Li, P. Wang, F. Xing, X.-D. Chen, Z.-B. Liu, and J.-G. Tian, "Experimental observation of a giant Goos–Hänchen shift in graphene using a beam splitter scanning method," *Optics Letters*, vol. 39, no. 19, pp. 5574–5577, (2014).

[168] E. Azarova and G. Maksimova, "Spin-and valley-dependent Goos–Gänchen effect in silicene and gapped graphene structures," *Journal of Physics and Chemistry of Solids*, vol. 100, pp. 143–147, (2017).

[169] Z. Wu, F. Zhai, F. Peeters, H. Xu, and K. Chang, "Valley-dependent brewster angles and Goos-Hänchen effect in strained graphene," *Physical Review Letters*, vol. 106, no. 17, p. 176802, (2011).

[170] D. Brewster, "On the laws which regulate the polarisation of light by reflexion from transparent bodies," *Philosophical Transactions of the Royal Society of London*, vol. 105, pp. 125–159, (1815).

[171] A. Lakhtakia, "Would brewster recognize today's brewster angle?," *Optics News*, vol. 15, no. 6, pp. 14–18, (1989).

[172] Z. Chen, X. Chen, L. Tao, K. Chen, M. Long, X. Liu, K. Yan, R. I. Stantchev, E. Pickwell-MacPherson, and J.-B. Xu, "Graphene controlled brewster angle device for ultra broadband terahertz modulation," *Nature Communications*, vol. 9, no. 1, pp. 1–7, (2018).

[173] S. Grosche, M. Ornigotti, and A. Szameit, "Goos-Hänchen and Imbert–Fedorov shifts for gaussian beams impinging on graphene-coated surfaces," *Optics Express*, vol. 23, no. 23, pp. 30195–30203, (2015).

[174] M. Ezawa, "Valley-polarized metals and quantum anomalous Hall effect in silicene," *Physical Review Letters*, vol. 109, no. 5, p. 055502, (2012).

[175] W. Wu, S. Chen, W. Xu, Z. Liu, R. Lou, L. Shen, H. Luo, S. Wen, and X. Yin, "Weak-value amplification for the optical signature of topological phase transitions," *Photonics Research*, vol. 8, no. 12, pp. B47–B54, (2020).

[176] F. Liu, J. Xu, G. Song, and Y. Yang, "Goos–Hänchen and Imbert–Fedorov shifts at the interface of ordinary dielectric and topological insulator," *JOSA B*, vol. 30, no. 5, pp. 1167–1172, (2013).

[177] H. Da and X. Yan, "Identification of trivial and nontrivial insulators: Enhanced lateral shift in topological insulator-based cavity," *Journal of Applied Physics*, vol. 120, no. 12, p. 125308, (2016).

[178] M. Merano, A. Aiello, M. Van Exter, and J. Woerdman, "Observing angular deviations in the specular reflection of a light beam," *Nature Photonics*, vol. 3, no. 6, pp. 337–340, (2009).

[179] M. Shah and M. S. Anwar, "Quantized and topological photonic spin Hall effects in the graphene family in the presence of magnetic fields," in *Optical Sensors*, pp. STu3D–5, Optical Society of America, (2020).

[180] G. Jia, G. Li, Y. Zhou, X. Miao, and X. Zhou, "Landau quantisation of photonic spin Hall effect in monolayer black phosphorus," *Nanophotonics*, vol. 9, no. 1, pp. 225–233, (2019).

[181] W. Wang, Y. Qu, K. Du, S. Bai, J. Tian, M. Pan, H. Ye, M. Qiu, and Q. Li, "Broadband optical absorption based on single-sized metal-dielectric-

metal plasmonic nanostructures with high metals," *Applied Physics Letters*, vol. 110, no. 10, p. 101101, (2017).

[182] M. Shah and M. S. Anwar, "Valley and spin polarized quantized spin dependent photonic shifts in topological silicene," *Physics Letters A*, p. 127342, (2021).

[183] M. Onoda, S. Murakami, and N. Nagaosa, "Hall effect of light," *Physical Review Letters*, vol. 93, no. 8, p. 083901, (2004).

[184] O. Hosten and P. Kwiat, "Observation of the spin Hall effect of light via weak measurements," *Science*, vol. 319, no. 5864, pp. 787–790, (2008).

[185] O. G. Rodríguez-Herrera, D. Lara, K. Y. Bliokh, E. A. Ostrovskaya, and C. Dainty, "Optical nanoprobing via spin-orbit interaction of light," *Physical Review Letters*, vol. 104, no. 25, p. 253601, (2010).

[186] L. Cai, M. Liu, S. Chen, Y. Liu, W. Shu, H. Luo, and S. Wen, "Quantized photonic spin Hall effect in graphene," *Physical Review A*, vol. 95, no. 1, p. 013809, (2017).

[187] X. Ling, X. Zhou, K. Huang, Y. Liu, C.-W. Qiu, H. Luo, and S. Wen, "Recent advances in the spin Hall effect of light," *Reports on Progress in Physics*, vol. 80, no. 6, p. 066401, (2017).

[188] L. Luo, G. Feng, S. Zhou, and T. Tang, "Photonic spin Hall effect of reflected light in a prism-graphene waveguide," *Superlattices and Microstructures*, vol. 122, pp. 530–537, (2018).

[189] W. Zhang, W. Wu, S. Chen, J. Zhang, X. Ling, W. Shu, H. Luo, and S. Wen, "Photonic spin Hall effect on the surface of anisotropic two-dimensional atomic crystals," *Photonics Research*, vol. 6, no. 6, pp. 511–516, (2018).

[190] L. Sheng, L. Xie, H. Luo, X. Zhou, X. Ling, and Z. Zhang, "Sensitivity enhanced refractive index sensor by reducing the influence of in-plane wavevector in photonic spin Hall effect," *IEEE Photonics Journal*, vol. 10, no. 5, pp. 1–9, (2018).

[191] X. Zhou, L. Sheng, and X. Ling, "Photonic spin Hall effect enabled refractive index sensor using weak measurements," *Scientific Reports*, vol. 8, no. 1, pp. 1–8, (2018).

[192] H. Lin, B. Chen, S. Yang, W. Zhu, J. Yu, H. Guan, H. Lu, Y. Luo, and Z. Chen, "Photonic spin Hall effect of monolayer black phosphorus in the terahertz region," *Nanophotonics*, vol. 7, no. 12, pp. 1929–1937, (2018).

[193] O. J. Santana and L. E. de Araujo, "Direct measurement of the composite Goos–Hänchen shift of an optical beam," *Optics Letters*, vol. 43, no. 16, pp. 4037–4040, (2018).

[194] L. Wu, M. Salehi, N. Koirala, J. Moon, S. Oh, and N. Armitage, "Quantized Faraday and Kerr rotation and axion electrodynamics of a 3D topological insulator," *Science*, vol. 354, no. 6316, pp. 1124–1127, (2016).

[195] Y. Cao, V. Fatemi, S. Fang, K. Watanabe, T. Taniguchi, E. Kaxiras, and P. Jarillo-Herrero, "Unconventional superconductivity in magic-angle graphene superlattices," *Nature*, vol. 556, no. 7699, pp. 43–50, (2018).

[196] X. Zhang, H. Nan, S. Xiao, X. Wan, X. Gu, A. Du, Z. Ni, and K. K. Ostrikov, "Transition metal dichalcogenides bilayer single crystals by reverse-flow chemical vapor epitaxy," *Nature Communications*, vol. 10, no. 1, pp. 1–10, (2019).

[197] C.-J. Kim, A. Sánchez-Castillo, Z. Ziegler, Y. Ogawa, C. Noguez, and J. Park, "Chiral atomically thin films," *Nature Nanotechnology*, vol. 11, no. 6, pp. 520–524, (2016).

[198] E. Y. Andrei and A. H. MacDonald, "Graphene bilayers with a twist," *Nature materials*, vol. 19, no. 12, pp. 1265–1275, (2020).

[199] Y. Cao, V. Fatemi, A. Demir, S. Fang, S. L. Tomarken, J. Y. Luo, J. D. Sanchez-Yamagishi, K. Watanabe, T. Taniguchi, E. Kaxiras, *et al.*, "Correlated insulator behaviour at half-filling in magic-angle graphene superlattices," *Nature*, vol. 556, no. 7699, pp. 80–84, (2018).

[200] J. L. Dos Santos, N. Peres, and A. C. Neto, "Graphene bilayer with a twist: Electronic structure," *Physical Review Letters*, vol. 99, no. 25, p. 256802, (2007).

[201] W.-Y. Tong, S.-J. Gong, X. Wan, and C.-G. Duan, "Concepts of ferrovalley material and anomalous valley Hall effect," *Nature Communications*, vol. 7, no. 1, pp. 1–7, (2016).

[202] X.-W. Shen, H. Hu, and C.-G. Duan, "Two-dimensional ferrovalley materials," in *Spintronic 2D Materials*, pp. 65–93, Elsevier, (2020).

[203] M. A. Bandres, S. Wittek, G. Harari, M. Parto, J. Ren, M. Segev, D. N. Christodoulides, and M. Khajavikhan, "Topological insulator laser: Experiments," *Science*, vol. 359, no. 6381, (2018).

[204] G. Harari, M. A. Bandres, Y. Lumer, M. C. Rechtsman, Y. D. Chong, M. Khajavikhan, D. N. Christodoulides, and M. Segev, "Topological insulator laser: theory," *Science*, vol. 359, no. 6381, (2018).

[205] Y. Zeng, U. Chattopadhyay, B. Zhu, B. Qiang, J. Li, Y. Jin, L. Li, A. G. Davies, E. H. Linfield, B. Zhang, *et al.*, "Electrically pumped topological laser with valley edge modes," *Nature*, vol. 578, no. 7794, pp. 246–250, (2020).